IAEA nuclear fusion

REVIEW

The reversed field pinch

To cite this article: L. Marrelli *et al* 2021 *Nucl. Fusion* **61** 023001

IOP Publishing | International Atomic Energy Agency Nuclear Fusion

Nucl. Fusion **61** (2021) 023001 (75pp) https://doi.org/10.1088/1741-4326/abc06c

Review

The reversed field pinch

L. Marrelli[1,2,*], P. Martin[1,3], M.E. Puiatti[1,2], J.S. Sarff[4], B.E. Chapman[4], J.R. Drake[5], D.F. Escande[6] and S. Masamune[7,8]

[1] Consorzio RFX, Corso Stati Uniti 4, 35127 Padova, Italy
[2] CNR-ISTP, Corso Stati Uniti 4, 35127 Padova, Italy
[3] Dipartimento di Fisica e Astronomia, Università degli Studi di Padova, Padova, Italy
[4] Department of Physics, University of Wisconsin, Madison, WI, United States of America
[5] Royal Institute of Technology KTH, SE-10044 Stockholm, Sweden
[6] Aix-Marseille Université, CNRS, PIIM, UMR 7345, Marseille, France
[7] Kyoto Institute of Technology, Kyoto 606-8585, Japan
[8] Chubu University, 1200 Matsumoto-cho, Kasugai, Aichi 487-8501, Japan

E-mail: lionello.marrelli@igi.cnr.it

Received 28 February 2020, revised 30 September 2020
Accepted for publication 8 October 2020
Published 28 January 2021

Abstract

This paper reviews the research on the reversed field pinch (RFP) in the last three decades. Substantial experimental and theoretical progress and transformational changes have been achieved since the last review (Bodin 1990 *Nucl. Fusion* **30** 1717–37). The experiments have been performed in devices with different sizes and capabilities. The largest are RFX-mod in Padova (Italy) and MST in Madison (USA). The experimental community includes also EXTRAP-T2R in Sweden, RELAX in Japan and KTX in China. Impressive improvements in the performance are the result of exploration of two lines: the high current operation (up to 2 MA) with the spontaneous occurrence of helical equilibria with good magnetic flux surfaces and the active control of the current profile. A crucial ingredient for the advancements obtained in the experiments has been the development of state-of-art active feedback control systems allowing the control of MHD instabilities in presence of a thin shell. The balance between achievements and still open issues leads us to the conclusion that the RFP can be a valuable and diverse contributor in the quest for fusion electricity.

Keywords: magnetic confinement, reversed field pinch, MHD

(Some figures may appear in colour only in the online journal)

1. Introduction

This paper reviews progress in understanding and improving the performance of the reversed field pinch (RFP) toroidal magnetic configuration as a fusion energy concept, covering several decades of research since the last reviews [1, 2]. The development of the RFP has progressed in parallel with other magnetic configurations, and in many respects, it is the third-most developed toroidal configuration next to the tokamak and stellarator, benefiting from well-diagnosed experiments and comprehensive theory and modelling. Significant advances have accrued over the past several decades, and the perspective on the RFP is now very different. This review summarizes these advances with selected emphasis on those that have been most impactful in guiding future research directions on the RFP.

The advances in fusion research over the last few decades have been tremendous, and the grand challenge to achieve a burning plasma in ITER dominates the world's magnetic fusion effort. Carbon-free energy sources are essential to limit global warming and avert climate change, while at the same time it is necessary to increase the abundance of affordable

* Author to whom any correspondence should be addressed.

energy for the benefit of all people in all nations. Nuclear fusion can and should play a central role in achieving a future based on clean, sustainable energy. While the tokamak configuration is most developed and provides the basis for ITER, fusion energy is simply too important to be narrowly constrained to one possible approach. Research on multiple approaches not only increases the possibility for fusion energy to become a reality but also exposes the underlying science more completely and stimulates innovation. The models governing fusion plasmas are largely agnostic to magnetic configuration. Experiments, theory, and modelling that cover a broad range of configurations allow the development of robust, predictive fusion science. In the end, any specific approach to fusion must have a tractable path forward, and at this point in time there are no known showstoppers exposed for the RFP. Some challenges that might have seemed insurmountable 30–40 years ago now have solutions, while others are much better understood and must be resolved with new experiments and advanced modelling. Only few key routes remain mostly unexplored for the RFP, in particular control of the plasma boundary at the material interface and power exhaust.

It has long been appreciated that the RFP offers a high beta, low field approach to fusion with all of the potential benefits that entails. However, the RFP's unique advantage is the opportunity to achieve an ohmically ignited and inductively sustained toroidal fusion plasma, including the possibility for steady-state operation using ac magnetic helicity injection. The RFP is magnetized almost entirely by plasma current, which increases ohmic heating and reduces the demands on magnets. The poloidal current that generates toroidal magnetic field is mostly in the plasma, not in a winding. The elimination of auxiliary heating and current drive is game changing for toroidal plasma confinement. Induction of current is simple, reliable and efficient, accomplished with transformers that are located outside of the blanket. Plasma-facing antennas are absent, and perforations in the neutron shield are minimized. The applied toroidal field in an RFP is small and can even be set to zero, although the toroidal field magnet is valuable as a poloidal current transformer for optimizing inductive control and sustainment. The TITAN reactor study investigated the advantages of a compact, high beta, inductively sustained RFP plasma core, yielding one of the lowest cost-of-electricity projections to date. This study introduced novel design elements, including single-piece maintenance and an integrated blanket-magnet for the toroidal field. New scenarios and requirements have emerged in the intervening years, and updated reactor studies are starting again to affirm the RFP's potential as a low-cost, reliable approach to fusion energy.

As a toroidal plasma, the RFP shares all of the fundamental requirements for fusion related to equilibrium, stability, energy and particle confinement, impurity control, and plasma–wall interactions (PWI) (but sans auxiliary heating). This review describes our current knowledge on these fundamental areas of fusion science for the RFP.

The first main change for the RFP in the last thirty years is that poor confinement from stochastic transport is no longer a barrier. Multiple tearing instabilities can appear (multiple helicity regime, MH), causing the magnetic field to become stochastic, the historic challenge for energy confinement in RFP plasmas. Two approaches show that stochastic transport can be circumvented, one through self-organization towards a single helicity (SH) regime that has a narrow mode spectrum, and one through control of the inductive electric field and the plasma current profile, which directly targets the free energy for instability. Energy confinement as good as for tokamak plasmas of comparable size, magnetic field strength, and heating power has now been demonstrated in RFP plasmas. The scaling of confinement has been better established from work on the largest RFP experiments, RFX-mod and MST; microturbulence from drift waves takes over when stochastic transport is reduced, likely to be the ultimate limit for thermal particle and energy confinement as it is for tokamak and stellarator plasmas. The scaling of energy confinement for larger, hotter, higher current plasmas remains an open question that can only be resolved with new experiments. The magnetic field strength in present-day RFP experiments is still five-times smaller than required for a reactor, bearing in mind $B \sim I_p/a$, where I_p is the toroidal plasma current, and a is the minor radius.

The RFP plasma also suffers instability to multiple ideal kink modes as a consequence of its low safety factor equilibrium, $q < 1$, even in the limit of vanishing thermal pressure. It is therefore essential that the plasma be surrounded by a conducting wall to prevent growth of global modes on an Alfvénic timescale. The finite conductivity of the stabilizing wall translates the instability to resistive wall modes (RWM). Multiple RWMs can be simultaneously unstable, which might have seemed an insurmountable hurdle. A second game changing development for the RFP is active mode control using saddle coils surrounding the wall and plasma, which controls all unstable modes and maintains a precise plasma boundary for pulse durations limited only by power supplies. Moreover, the control encompasses simultaneous magnetic field error correction as well. This pioneering development of active mode control for RFP plasmas has helped improve the prospects for steady-state advanced tokamak plasmas that suffer analogous high-beta kink modes, and it also creates connections to 3D physics shared by stellarator plasmas.

Advanced nonlinear, visco-resistive, 3D MHD models and simulations have been critical to understanding RFP plasmas. The development of major MHD codes now used extensively in magnetic fusion research has roots in the goal to understand the RFP's magnetic self-organization. The knowledge gained from this work has inspired approaches to improve confinement in the RFP. Current profile control was invented in MHD modelling before being tested experimentally. Similarly, the bifurcation towards the single-helicity regime was initially discovered in modelling of high viscosity RFP plasmas and then quasi-helical states emerged in experiments. The latter were better reproduced in simulations by including a helical boundary condition.

Positive trends of temperature and confinement with plasma current have been observed in present experiments, and the upgrade of the RFX-mod device, presently underway, is expected to improve the confidence on such scalings, giving the basis to conceive a future reactor based on the RFP concept.

Advances in understanding the RFP's operational limits for density and beta have also been made. Interestingly, RFP plasmas obey the same empirical density limit as for tokamak plasmas, but the density is large since the plasma current density is large. The ideal beta limit for the RFP is also very large (order 40%), and the limiting behaviour is soft, most likely governed by non-ideal processes. Beta and density-driven fast disruptions are uncommon in RFP plasmas.

Investigation of energetic ions is a new area of research for the RFP in the last several years. Energetic ion confinement is found to be classical, better than the thermal particle confinement, even in the MH regime with a stochastic magnetic field. The energetic ion beta in the core exceeds the projected alpha particle β for a reactor plasma when energetic-particle-driven activity is observed to onset.

An important possibility for the RFP is steady-state current sustainment using inductive current drive. The oscillating field current drive (OFCD) concept was proposed in conjunction with discussions of the conservation of magnetic helicity in relaxed-state plasmas. In OFCD, ac loop voltages inject cycle-average dc magnetic helicity to sustain the plasma current without accumulation of magnetizing flux. Fractional current drive by OFCD of at least 10% has been demonstrated, and nonlinear MHD modelling shows that the underlying dynamics are similar to conventional steady induction. Demonstrating full OFCD sustainment with small ac ripple is one of the key opportunities for a larger, higher current experiment. The development of high temperature superconducting magnet technology could be strongly enabling for OFCD, symbiotic with recent efforts to establish a compact, high-field tokamak demonstration reactor.

While this review is focussed on the fusion context for the RFP, the magnetic self-organization aspects of the RFP that are interesting from a basic science point of view with connections to astrophysics are implicit. Tearing instability relates to magnetic reconnection, and the nonlinear saturation process that regulates tearing relates to the magnetic dynamo process. Non collisional ion heating and energization are particularly strong in RFP plasmas, likely associated with a turbulent cascade, and make excellent connections to similar processes in solar and astrophysical settings. These topics are embedded within the fusion context, with many of the key references provided in the bibliography.

1.1. Chapter contents

Chapter 2 gives an insight into the basic experimental properties of the RFP. The axisymmetric magnetic equilibrium model for the RFP is recalled. The dynamics of the configuration in the two different regimes of MH and quasi single helicity (QSH), characterised by different spectra of tearing modes, are described, and the helical equilibria in QSH states are introduced as well. The helical states with two magnetic axes are QSH double axis (QSH-DAx), while the helical state with a single helical axis is QSH-SHAx.

Chapter 3 summarizes the current understanding of the RFP self-organisation. Taylor's theory of field reversal is recalled. The need of a dynamo process for the RFP sustainment is discussed, together with experimental measurements. The transition from MH to QSH states as the result of a bifurcation process is introduced. A second bifurcation is then described, from a QSH state characterised by two magnetic axes, the unperturbed axi-symmetric one and the axis related to the island of the dominant mode (QSH-DAx state), to a magnetic equilibrium featuring the helical axis only as the result of the expulsion of the magnetic separatrix (QSH-SHAx). The effect of a helical boundary in the simulation of helical states, allowing a better reproduction of the experiments, is discussed. The progress in the understanding of the helical equilibria allows a new vision of the dynamo process (electrostatic dynamo), common for multiple and QSH states.

The complex magnetic dynamics have a crucial impact on the confinement and transport properties in the RFP, which are addressed in chapter 4. In the MH state the overlap of the magnetic islands due to the core resonant dynamo modes causes a broad region of stochastic magnetic field, where the temperature profile is observed to be flat. The experimental results are compared to the Rechester and Rosenbluth (RR) theory of transport in a stochastic field [3]. In QSH states the temperature profile mirrors the magnetic topology: a small hot island is observed when the magnetic topology is characterized by the presence of two magnetic axes in QSH-DAx states. A wider region with high temperature, involving most of the plasma core and encompassed by strong gradients, is instead observed in QSH-SHAx states, which are characterized by improved transport and confinement properties. Studies about the impact of microturbulence in regimes of reduced stochastic transport, performed by gyrokinetic simulations, are also reported. A large number of experiments and simulations have been dedicated to edge transport and turbulence, and to fast ion and electron confinement as well. This is also reviewed in chapter 4.

The approach to improved confinement in the RFP based on current profile control is described in chapter 5. MHD modelling demonstrated that tearing fluctuations responsible for magnetic field stochasticization could be reduced or even eliminated with a suitable modification of the current profile. Several approaches to inductive current profile control have been studied in experiments and simulations. Temporal variations in the toroidal and/or poloidal magnetic field are used to control the inductive electric field, called pulsed poloidal (or parallel) current drive (PPCD). The dynamo electric field during PPCD is observed to become very small, so that the resistive term in the Ohm's law is balanced by the applied electric field. This coincides with a large reduction of magnetic fluctuations and a ten-fold improvement in energy and thermal particle confinement time, with substantial enhancement of the electron and ion temperatures.

Chapter 6 deals with the limits to plasma pressure. RFPs share with tokamaks and stellarators a high density limit, traditionally described by the Greenwald empirical limit (or by the Sudo limit in the case of stellarators). This chapter describes the experimental and modelling efforts to explain such a limit, thus contributing to the understanding of a still open issue for all magnetic configurations. The β limit is different in the RFP with respect to the tokamak: the ideal β limit is much higher in the RFP. In MST values of total β as high as 26% have been measured, consistent with the Connor–Taylor scaling [4] and exceeding the Mercier criterion governing the interchange stability [5]. High beta values are also associated to neoclassical bootstrap current effects.

During the last 15 years RFP devices have become very attractive laboratories to study state-of-the-art active feedback control of MHD stability. To these studies is dedicated chapter 7. Theoretical studies on the stabilization of RWMs are described together with the experimental demonstration of their control. The focus is on EXTRAP-T2R and RFX-mod experiments, which are devices equipped with sophisticated active control systems. The chapter also deals with tearing modes, which in the RFP are ruled by nonlinear MHD (in contrast to RWM). The constructive interference due to phase-locking of the $m = 1$ and $m = 0$ tearing modes produces a toroidally localized helical deformation of the plasma column (slinky or locked mode, LM). Several control algorithms have been developed and tested to mitigate the local deformation of the magnetic field, mainly in RFX-mod, ultimately leading to a very effective reduction and slow rotation of LM.

As in other magnetic configurations, plasma-wall interactions (PWI) play a crucial role in determining the plasma behaviour and performance, in particular through the control of plasma density and impurity contamination. In the RFP PWI is related to the magnetic topology through the three-dimensional edge magnetic fields. This is discussed in chapter 8.

Chapter 9 summarizes the experimental and modelling studies made on a quasi-steady-state method of inductive current sustainment, called OFCD, based on the application of oscillatory toroidal and poloidal loop voltages, resulting in the generation of a dc current via the nonlinear relaxation processes. Fractional current drive of at least 10% has been demonstrated, and nonlinear MHD modelling reveals the dynamics of relaxation. The scaling for the concomitant ac ripple in the equilibrium magnetic field is reviewed, which can be used to project the experimental requirements for full sustainment by OFCD.

Chapter 10 summarizes system studies for an RFP based reactor and neutron source, and concluding remarks are given in chapter 11.

1.2. The RFP devices

Since the 1990s, several RFP devices have been in operation, listed in table 1. The largest one is RFX-mod, designed to reach 2 MA maximum current, (formerly RFX, [6]) at Consorzio RFX in Padova, with major radius $R = 2$ m and minor radius $a = 0.459$ m. It is equipped with a thin copper shell with $\tau_w = 100$ ms ($\tau_w = \mu_0 a\delta\sigma$, where a is the minor radius, δ is the wall thickness and σ is the wall conductivity) and a network of actively controlled saddle coils for thin shell operations [7].

The MST device, located at the University of Wisconsin Madison, USA [8] ($R = 1.5$ m, $a = 0.50$ m) can operate up to 0.6 MA plasma current. The MST's 5 cm thick aluminium shell serves as both the vacuum chamber as well as the toroidal and poloidal equilibrium field magnet. The shell has a minor radius of 0.52 m with graphite plasma limiters. The inductive current profile control technique was originally developed on MST. The facility includes a 1 MW, 25 keV, 20 ms neutral beam injector to study energetic ion confinement and stability.

EXTRAP-T2R [9], in operation at the Royal Institute of Technology, Stockholm, Sweden ($R = 1.24$ m, $a = 0.18$ m, maximum plasma current = 0.3 MA), is equipped with a copper shell with shell time 12 ms and focuses its experimental activity on the development of advanced tools for the feedback control of plasma MHD instabilities.

The TPE-RX device [10, 11] ($R = 1.72$ m, $a = 0.45$ m) had a multiple layer construction composed of a close fitting thin shell (1 mm copper) ($b/a = 1.08$) and a thick shell (5 cm aluminium). It operated from 1998 up to 2007 [12].

RELAX is a low aspect ratio RFP [13] ($R = 0.51$ m, $a = 0.25$ m, maximum plasma current = 0.12 MA) operated at the Kyoto Institute of Technology, Japan and is mainly dedicated to the study of single helicity plasmas. RELAX is exploring MHD stability and the possibility of generating bootstrap current at a low aspect ratio [14].

KTX [15–17] started its operation in 2015 at the University of Science and Technology in Hefei, China, ($R = 1.4$ m, $a = 0.4$ m). It has a magnetic boundary similar to that of RFX-mod and is foreseen to produce a plasma current of 0.5 MA in phase I and 1 MA in phase II, with an MHD active control system. KTX is somewhat smaller in size than MST, but it utilizes an air core, like RFX, in order to achieve higher plasma current levels. The unique double-C design of the KTX vacuum vessel allows access to the interior of the machine for rapid first-wall (FW) modifications and investigations of power and particle handling. The KTX device provides a platform to develop diagnostic tools [18] and to investigate the fluctuation induced transport in high temperature plasmas.

An upgrade of RFX-mod machine assembly has been designed (dubbed RFX-mod2) and is presently being implemented [19–21]. The primary goal of the upgrade, discussed in chapters 4 and 7, is to modify the magnetic front-end in order to reduce the amplitude of tearing modes and thus mitigate the magnetic chaos and the localized PWI due to wall-locking).

2. Experimental properties of the RFP configurations

2.1. The axisymmetric RFP equilibrium

The RFP equilibrium is a paramagnetic configuration: the plasma currents arrange in a way to ensure MHD equilibrium and generate most of the toroidal flux. The amount of toroidal flux converted from the poloidal flux by the dynamo process (explained in section 3.3) is proportional to the plasma current: the inverse of the proportionality constant is the figure of merit that the RFP configuration shares with all pinch configurations,

Table 1. Main parameters of present RFP devices and the large TPE-RX device that operated until 2007. Cross sections of devices are shown in figure 1.

	RELAX	EXTRAP-T2R	TPE-RX	MST	KTX phase1 (phase2) (projected)	RFX-mod
R/a (m)	0.5/0.25	1.24/0.18	1.72/0.45	1.5/0.5	1.4/0.4	2/0.459
Shell time τ_w (ms)	5	12	300	1100	40	100
Max I_p (MA)	0.12	0.3	0.45	0.6	0.5 (1)	2
Pulse length (ms)	3.5	100	80	100	2	500
Max T_e (keV)	0.3	0.3	1	2.0	0.3 (0.8)	1.5
n_e range 10^{19} m^{-3}	0.2–3	0.5–2	0.5–1	1–4	1–10	1–8

hence the name *pinch parameter* Θ:

$$\Theta = \frac{B_\theta(a)}{\langle B_\phi \rangle} \tag{2.1}$$

where $\langle B_\phi \rangle$ is the cross section averaged toroidal magnetic field and a is the plasma minor radius. The distinguishing feature of the RFP is the reversal of the toroidal field at the edge: its magnitude, normalized to the toroidal flux is defined as the *reversal parameter F*:

$$F = \frac{B_\phi(a)}{\langle B_\phi \rangle} \tag{2.2}$$

These two externally measurable parameters are used to characterize the RFP operations and allow comparing experiments of different sizes. The magnetic safety factor at a is proportional to the ratio of F and Θ, $q(a) = (a/R)(F/\Theta)$. Experimentally, F and Θ are correlated and follow some trajectory in the (F, Θ) plane [22]. At the beginning of the setting-up phase of a plasma pulse $F = 1$ and $\Theta = 0$; as plasma current is initiated and increased due to the induced loop voltage, the plasma begins to generate toroidal flux, so that F decreases as Θ increases; in particular, above a Θ threshold F becomes negative.

The axisymmetric part of the parallel current profile $\mu = \mu_0 \mathbf{J} \cdot \mathbf{B}/B^2$ measured in experiments (see e.g. in figure 1b of [1], or figure 42) is often approximated in a cylindrical geometry by the following family of functions

$$\mu(r) = \mu(0)\left(1 - \frac{r}{a}\right)^\alpha \tag{2.3}$$

characterized by a maximum current at the magnetic axis decreasing to zero at the edge [23, 24]. The exponent α allows to parametrize how much the current profile is peaked. This model is used to derive the internal magnetic profiles and to perform linear stability analysis. A toroidal version of this model has been developed [25] and has been benchmarked with the axisymmetric version of VMEC adapted for the RFP [26]. A toroidal equilibrium reconstruction code MSTFIT that solves the Grad-Shafranov equation (analogous to EFIT widely used for tokamak research) has been also developed for MST and adapted for other RFP experiments [27].

The toroidal and poloidal components of the RFP magnetic field are of comparable amplitude, in contrast with the tokamak where a stabilizing toroidal magnetic field larger than the poloidal one is needed. This is shown in figure 2, where the radial profiles of the poloidal and toroidal components of the magnetic field (normalized to the on-axis magnetic field) are reported for cylindrical RFP and tokamak configurations.

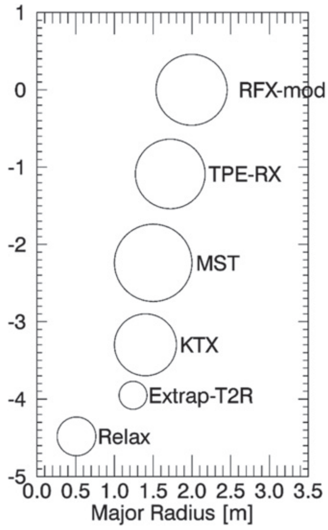

Figure 1. Cross sections of the RFP devices listed in table 1.

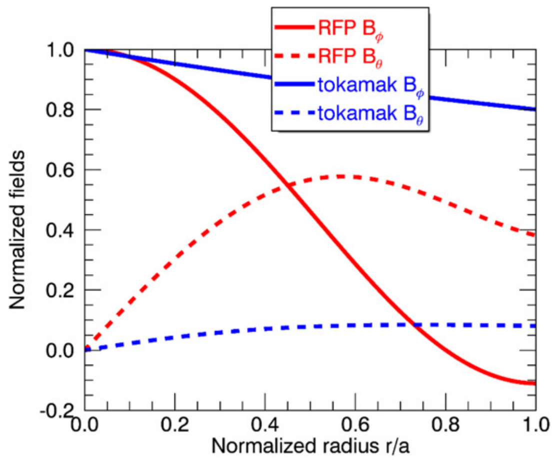

Figure 2. The toroidal (B_ϕ) and poloidal (B_Θ) magnetic field profiles in RFP and tokamak.

When including the flow term in the axisymmetric magnetic equilibrium, the plasma toroidal velocity in RFX-mod plasmas changes sign towards the edge [28], consistent with experimental observations [29–31].

The RFP cylindrical safety factor $q(r) = rB_\phi/RB_\theta$ is strongly sheared, with $q(0) \approx a/2R$ at the magnetic axis and decreasing with minor radius such that $q(a) \leqslant 0$, where a

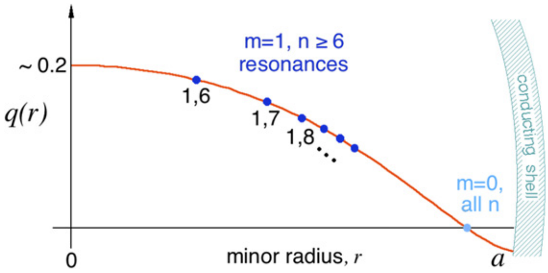

Figure 3. Axisymmetric safety factor profile $q(r) = rB_\phi/RB_\theta$ for a typical RFP with an aspect ratio $A = 3$. The location of the $m = 1$ and of the $m = 0$ resonant surfaces are shown.

and R are the minor and major radius respectively (figure 3). The toroidal field at the plasma surface is therefore directed opposite to the core, giving the RFP configuration its name. This has profound consequences in terms of plasma magnetohydrodynamic (MHD) stability. In addition to ideal kink modes, which become RWM due to the finite conductivity of the shell, there are many resonant surfaces for $m = 1$ tearing modes with $n \geq 2R/a$, where m and n are the poloidal and toroidal mode numbers of the usual Fourier decomposition, and the $q = 0$ surface is resonant for $m = 0$ modes.[9]

2.2. The dynamics of the RFP configuration: from multiple helicity to quasi single helicity

Two widely different regimes, characterized by different $m = 1$ and $m = 0$ magnetic fluctuation spectra, have been observed in RFP experiments especially as long as higher plasma currents, and consequently higher electron temperatures, have been obtained. These regimes have been defined as multiple helicity (MH) and quasi single helicity (QSH), according to the shape of the measured spectrum of the $m = 1$ and of the $m = 0$ Fourier harmonics of the magnetic field measured at the edge of the experiments. They are largely dependent on the device magnetic boundary parameters such as aspect ratio, thickness of the conducting shell and its distance from the wall. Experimentally, MH states are characterized by the presence of many $m = 1$ Fourier components of the magnetic field with comparable amplitude. In the QSH states one single $m = 1$ Fourier component grows up becoming dominant over the other 'secondary' modes, whose amplitude is smaller than in MH.

2.2.1. Multiple helicity regime. In both early RFP experiments [32] and 3D MHD computations [33–35], the Fourier modes measured at the edge had poloidal mode number $m = 1$ and a range of toroidal mode numbers, n, resonant in the plasma core given the q profile (figure 3).

When in the setting-up phase of the plasma discharge the profile of the safety factor, initially flat, evolves through a series of non-monotonic profiles (until the field reversal), the local minimum at the edge is a source of kink instability [36]. The series of current-driven modes with $m = 1$ and increasing n occurring as soon as the mode resonance appears, generate the poloidal current required to create the toroidal flux [37]. This process bears some similarity with the Kadomtsev reconnection model in the tokamak [38].

[9] Due to the chosen conventions of the orientation of the coordinate system and of the 2D Fourier decomposition, and due to the relative orientation between the toroidal field and the plasma current, in RFX-mod and in EXTRAP-T2R internally resonant tearing modes toroidal numbers are negative, so that $n \leqslant -2R/a$.

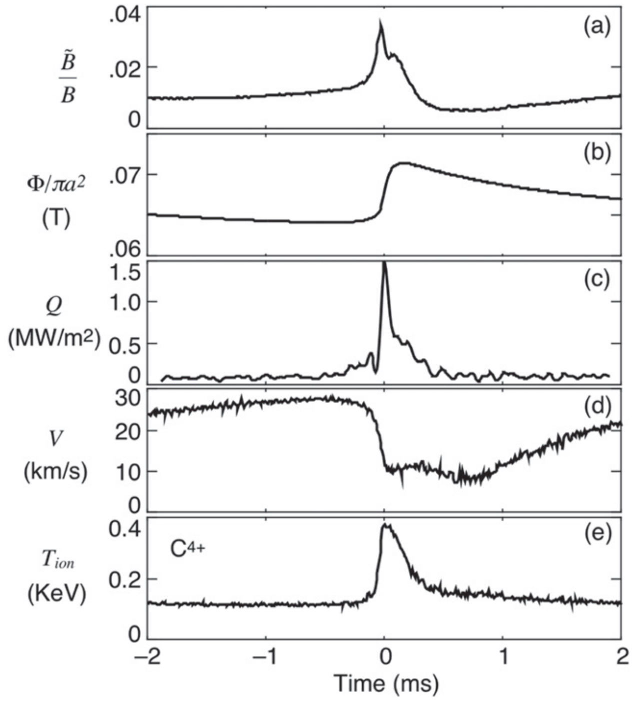

Figure 4. Prototypical RFP sawtooth, ensemble averaged from a large number of similar events recorded on the MST RFP. Time $t = 0$ is a marker at the peak of sawtooth activity. Each panel represents the change in a key parameter during a sawtooth event. (a) Relative amplitude of magnetic fluctuations, illustrating tearing mode growth; (b) toroidal magnetic flux density, illustrating RFP dynamo activity; (c) heat flux, indicative of magnetic stochastic transport; (d) plasma flow, indicative of momentum transport; and (e) ion temperature, demonstrating ion heating.

In the sustainment phase, toroidal flux generation is observed to occur either continuously or in discrete events [39, 40] referred to as sawtooth crashes [41], dynamo reconnection events or discrete reconnection events (DREs) in different contexts and papers (an example is shown in figure 4). The impulsive features of these events have been reproduced and studied in visco-resistive MHD simulations [42–45]. The frequency of such events depends on the pinch parameter Θ [41, 46] and on the magnetic boundary. Experimental observations showed such events as associated to large amplitude bursts of $m = 1$ and $m = 0$ low n modes (figure 4(a)) [47–52]. The cyclic relaxation of the current profile has been measured via Faraday rotation, which shows repetitive flattening of $\mu(r)$ inside the $q = 0$ surface and peaking near the plasma edge [53]. The generation of the toroidal flux is a local, toroidally asymmetric phenomenon as a consequence of the nonlinear phase alignment [54]. Toroidally localized, magnetic field aligned current sheets have been measured in RFX-mod [55] and in MST [56, 57].

The global impact of DREs depends on the nonlinear interaction between $m = 1$ modes resonant in the core and

$m = 0$ modes resonant near the plasma surface. For 'non reversed' plasmas with $F = 0$ (vanishing toroidal field at $r = a$), the $m = 0$ resonance is removed from the plasma, and the global impact of reconnection events is muted [58]. Operation with $F \approx 0$ is an empirical control that helps stimulate QSH, likely a consequence of reduced coupling between $m = 1$ and $m = 0$ modes.

While visco-resistive MHD describes well the sawtooth relaxation dynamics as a consequence of tearing instability, flattening of the current profile has also been modelled as a kinetic effect related to magnetic chaos [59, 60]: in the radial domain of chaotic magnetic field, transport is fast and equilibrium almost force-free, so that $\boldsymbol{J} = \mu(r)\boldsymbol{B}$, where μ may be radius dependent. Setting this in $\nabla \cdot \boldsymbol{J} = 0$ implies $\nabla\mu(r) \cdot \boldsymbol{B} = 0$, which shows that μ must be constant along the field lines.

The scaling of magnetic fluctuation amplitudes with the Lundquist number S has been studied in a number of RFP devices in the MH regime [61–64]. The Lundquist number S, that in RFPs is usually $\gg$1 is defined as the ratio of the resistive diffusion time $\tau_R = \mu_0 L^2/\eta$ (being $\eta \propto Z_{\text{eff}}/T_e^{3/2}$ the plasma resistivity and L the scale of the system) to the Alfvén time $\tau_A = L/V_A$, where $V_A = B/\sqrt{\mu_0\rho}$ is the Alfvén velocity and ρ the mass density. The magnitude of magnetic fluctuations decreases with S in RFP plasmas, so this scaling is important to characterize transport related to magnetic stochasticity. A sufficiently strong scaling is necessary so that RFP plasmas are not limited by stochastic transport.

The generation of the toroidal flux through the nonlinear interaction of the tearing modes is a local, toroidally asymmetric phenomenon [54].

During DREs, the radial profile of the toroidal plasma rotation can change rapidly and spontaneously, representing a rapid radial transport of toroidal momentum. This effect is about two orders of magnitude more rapid than what would be expected from classical viscosity and it is explained by nonlinear interactions involving triplets of tearing modes producing internal torques that redistribute momentum and therefore lead to flow profile flattening [68].

An important consequence of the nonlinear coupling of tearing modes is the formation of a toroidally localized deformation called slinky (inspired by the kink shape formed when a slinky toy is twisted), or locked mode (LM) in RFP literature. The nonlinear interactions related to mode coupling have been analysed using bi-spectral analysis techniques [65–67]. Such phenomenon of phase-locking has been reported in many RFP experiments: OHTE [69], TPE-1RM15 [46], Reversatron II [70], MST [48, 50], TPE-1RM20 [71], TPE-RX [72], EXTRAP-T2R [73], RFX [74, 75] and RFX-mod [76, 77]. The LM has been observed to rotate in the laboratory frame or to *wall-lock*, depending on the level of plasma current, on the amplitude of magnetic fluctuations and on the properties of the device magnetic boundary (resistivity of the conducting shell, presence of error fields, shell–plasma distance).

Wall locking leads to negative local effects, such as enhanced plasma-wall-interaction (PWI), overheating of the first wall [78, 79], increased impurity influxes and total radiation [80]. On the other hand, wall locking also affects

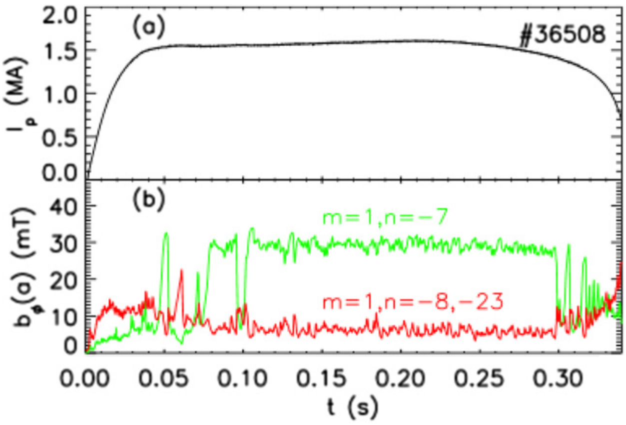

Figure 5. Example of a spontaneous long-lasting QSH in RFX-mod; (top) time evolution of plasma current; (bottom) amplitude of dominant $m = 1$, $n = -7$ tearing mode (red) and averaged amplitude of secondary modes. Reproduced courtesy of IAEA. Figure from [348]. © 2015 EURATOM.

global quantities, such as increase of loop voltage, increased fuel recycling with subsequent difficult control of density. Details of the physics of phase and wall locking of tearing modes together with mitigation techniques will be described in chapter 7, while the effect of the LM on PWI will be discussed in chapter 8.

2.2.2. The QSH regimes: QSH-DAx and QSH-SHAx states. Since 1993, transient QSH states, i.e. periods in which one mode dominates over the other secondary modes in the spectrum, were detected in all large RFP devices. Examples from EXTRAP-T2R [66, 71], TPE-1RM20 [81], MST [82], RFX [83, 84] and RFX-mod [77, 85, 86] have been published.

Plasmas with long lasting QSH states over the whole current flat-top phase were present in the RFX data base at about 1 MA plasma current [87, 88].

After the observation of long lasting QSH states in RFX and RFX-mod (see an example in figure 5), experimental studies on such regimes were extended in all other RFP devices. QSH states have been found in MST [89–91], in TPE-RX [92], in EXTRAP-T2R [93] and in RELAX [94]. In TPE-RX, long-lasting highly reproducible QSH states were obtained by applying a delayed reversal of the toroidal field at the edge [95], and were systematically triggered by applying a small positive pulse in the initially weakly reversed edge magnetic field [96]. The end of the QSH phase came with a distortion of the $m = 0$ magnetic island chain, and the occurrence of a chaotic region, expelling energy at the location of the LM [97]. In RELAX, QSH states lasting above 30% of the flat-top duration can be obtained [98].

The conditions to observe QSH states are similar in all RFP experiments: they occur at shallow reversal (i.e. F near 0) and the dominant mode typically resonates near the magnetic axis [96, 98–100]. Moreover, there is a higher probability to obtain QSH spectra with higher plasma current [65, 89, 101, 102], and their persistence (i.e. the overall fraction of the flat-top characterized by QSH states) increases with current too. In RFX-mod at plasma current above 1.5 MA the latter can exceed 90%

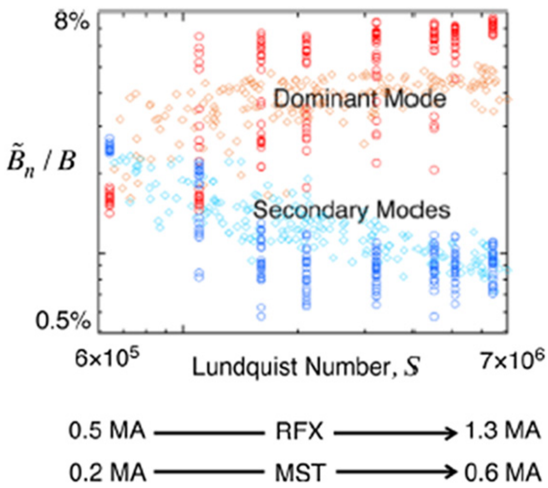

Figure 6. Magnetic fluctuation amplitude versus Lundquist number for both RFX-mod (diamond symbol) and MST (circle symbol). The range of plasma current, I_p, for both experiments is also noted. Data from RFX-mod extending the current range to 2 MA are not shown. Reproduced courtesy of IAEA. Figure from [105]. Copyright 2013 IAEA.

of the plasma current flat-top [102, 103]. The amplitude of the dominant mode and that of the secondary modes scale in opposite ways with the current and with the Lundquist number S, as observed both in RFX-mod and in MST and reported in figure 6 [104, 105]. Long lasting QSH states observed in RELAX, despite the low plasma current, suggest that a low aspect ratio configuration could be a favourable condition, due to the scarcer density of the central $m = 1$ tearing modes in this case [98, 99].

Two kinds of QSH states have been observed. When the amplitude of the dominant magnetic mode is up to a few percent of the central magnetic field, and several times that of the other secondary modes [90, 106] the magnetic field topology displays two magnetic axes (figure 7(*a*)). The first one corresponds to the unperturbed equilibrium one while the second axis is related to the island O-point [107]. Such QSH states are termed double axis (QSH-DAx[10]) states [108].

In the highest RFX-mod plasma current regimes, where secondary modes reach the lowest amplitudes, QSH states with the expulsion of the magnetic separatrix between the helical island corresponding to the dominant mode and the axisymmetric field have been observed [107, 109]. The initially small magnetic island related to the dominant mode in QSH-DAx is replaced by a large helical structure without separatrix (see figure 7(*b*)). These QSH states featuring a single helical magnetic axis are dubbed QSH-SHAx[11] states. QSH-SHAx states were obtained either spontaneously, at plasma current above $\approx$ 1.4 MA [110], or stimulated by an external magnetic perturbation, or triggered by oscillating poloidal current drive (OPCD) [107, 111]. In [112] it was predicted that the disappearance

[10] In all RFP literature this is usually only indicated as DAx. In order to help the reader we use in this review the prefix QSH, to indicate that this is a particular kind of QSH state.

[11] As before, in the RFP literature these are usually defined SHAx, but here they will be defined QSH-SHAx.

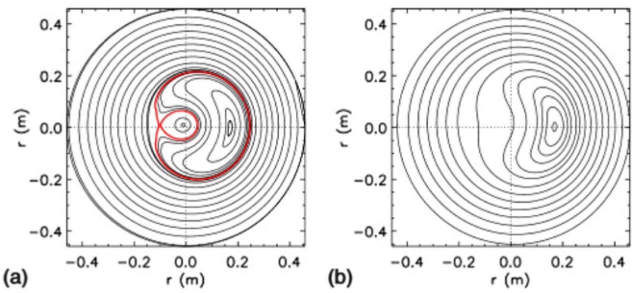

Figure 7. Magnetic topology reconstructed using only the axisymmetric fields and the radial profile of the magnetic field of the dominant mode: (*a*) QSH-DAx with a magnetic island; (*b*) QSH-SHAx state. Reprinted from [111], with the permission of AIP Publishing.

of the magnetic separatrix in QSH states corresponds to chaos healing.

QSH-SHAx states also occur in MST, at similar Lundquist number S despite lower plasma currents (about 0.5 MA) than in RFX-mod, with the dominant $m = 1$, $n = 5$ mode as large as 8% of the axisymmetric field [91, 105, 113].

Both QSH-SHAx and QSH-DAx periods end by sawtooth crashes, similar to the ones typical of the MH regimes, where the amplitude of secondary modes increases and the dominant mode decreases (figures 5(*b*) and 16(*c*)), but the system goes back immediately to QSH. Moreover, a small sawtooth-like activity still occurs during long lasting QSH states in RFX-mod, characterized by small crashes not leading to a back-transition to MH states [114].

2.2.3. QSH states stimulated by a helical boundary. The possibility to increase the duration of QSH phases with the application of a stationary or rotating magnetic perturbation (MP) to a prescribed slow (up to 50–100 Hz) frequency has been investigated in MST, EXTRAP-T2R and in RFX-mod. MST adopted a pre-programmed approach as in resonant magnetic perturbation (RMP) or resonant field amplification (RFA) experiments (see e.g. [115] or [116, 117]), where the currents flowing into the control coils are pre-programmed. Instead in RFX-mod the measured radial field is feedback controlled at a prescribed reference level [118]. As a result, the application of an $m = 1$, $n = -7$ field in plasmas with shallow reversal, strongly increases the persistence of the helical state [119], provided that the reference amplitude is above some threshold. Furthermore, QSH states can be obtained at higher densities ($n/n_G \approx 0.5$, (with n_G [10^{20} m^{-3}] = I_p [MA]/πa^2 Greenwald density)) than in the spontaneous case [120]. While first RFX-mod experiments with the application of an external 3D field resulted in a significant increase (up to 50%) of the loop voltage necessary to sustain the plasma current, such effect has then been minimized with a proper tailoring of the radial field [121]. In EXTRAP-T2R, an increase of the persistence of QSH periods up to 10% of the discharge and larger helical core structures occurred by applying a feedback controlled RMP with the corresponding helicity [122].

As predicted by numerical simulations [123], by providing a corresponding helical boundary condition in RFX-mod, it is

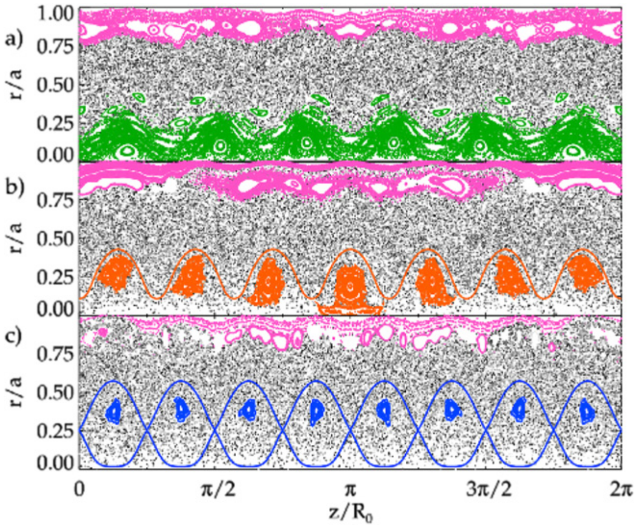

Figure 8. Poincaré maps from simulations at $\theta = 0$ with a 2% MP as boundary condition; (top) MP with helicity $m = 1$, $n = -6$, non resonant; (middle) MP with helicity $m = 1$, $n = -6$; (bottom) MP with helicity $m = 1$, $n = -8$. The $n = -6$ case shows larger areas of conserved surfaces. Reproduced courtesy of IAEA. Figure from [125]. © 2017 EURATOM.

possible to excite non internally resonant QSH $n = 6$ states [124]. When a non-resonant boundary condition is applied the area with well conserved magnetic surfaces is larger and the transport of magnetic field lines is reduced (figure 8) [125]. This has been related to the existence of Cantori, encompassing the region characterized by conserved magnetic surfaces, which act as barriers to transport of magnetic field lines [126].

The application of 3D fields to improve the properties of the configuration is not unique to the RFP configuration. The motivations for introducing the 3D magnetic fields include plasma confinement and stability optimization (stellarators), plasma control (tokamak edge-localized modes and tokamak and RFP resistive wall instabilities) and engineering/economic constraints (limited number of toroidal field coils, asymmetrical particle/energy sources and non-uniform ferrous steel structure near the plasma). A survey of common tools developed in the stellarator community can be found in [127].

2.3. The helical equilibria for the QSH-SHAx and QSH-DAx states

The internal topology of the magnetic field is reconstructed with several approaches. The first one is a perturbative approach. Marginally stable eigenfunctions [128, 129] were matched to the edge magnetic fluctuation spectrum and implemented in field line tracing codes [130, 131]. This has been done in several RFP devices [101, 132, 133]. Such codes have also been benchmarked with the NEMATO tool, which solves the magnetic field line equation on a 3D grid in a volume preserving integrator scheme [134]. In QSH-DAx Poincaré plots were displaying magnetic islands emerging out of stochastic domain closely corresponding to independently measured ‘bean’-like hot structure featuring strong electron temperature gradient at the edges (see figure 9)

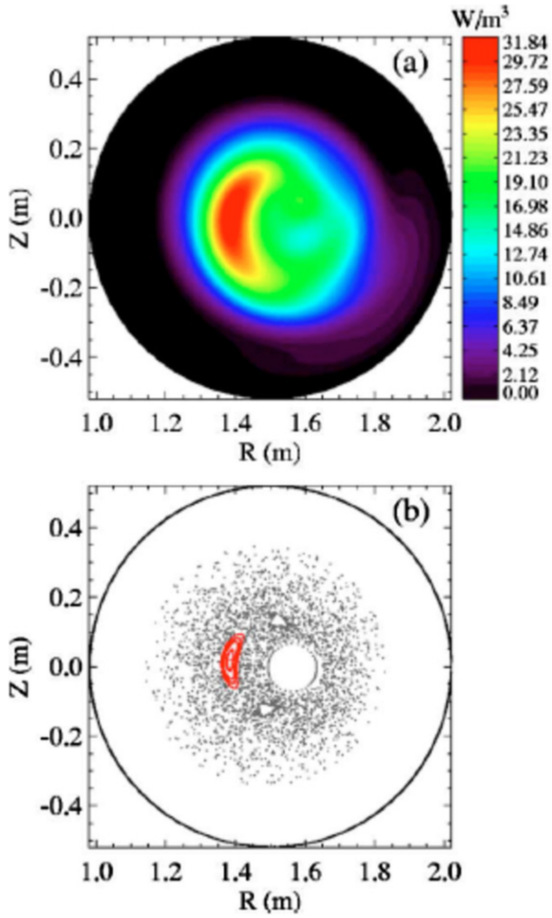

Figure 9. (*a*) Tomographic reconstruction of the SXR emissivity and (*b*) Poincaré plot of the magnetic-field lines from the ORBIT code for a ($m = 1$, $n = 6$) island during a QSH state in a standard shot (no. 1020709059). Reprinted from [135], with the permission of AIP Publishing.

[87–90, 135]. In Poincaré plots of QSH-SHAx states, wider regions separated from outer stochastic domain appear into the core.

A much faster way to reconstruct internal topology is based on the SHEq code [136], where a system of helical flux coordinates is implemented by considering only the dominant mode radial profile as a perturbation on the axisymmetric equilibrium. The magnetic field reconstruction by SHEq has been compared with a direct measurement of the internal magnetic field in MST [91, 113]. In RFX-mod, the reconstructed equilibrium shows that the electron temperature and density are constant along the helical magnetic flux surfaces, see figure 10 [109].

These helical equilibria have also been reconstructed with the VMEC equilibrium code, originally developed in the stellarator community, and applied and enhanced in order to deal with the reversal of the toroidal field [26, 137]. The resolution of the equilibrium reconstruction has been then improved by coupling VMEC with the V3FIT code [138], able to include internal and external measurements as constraints. As an example, figure 11 shows the improvement of the magnetic reconstruction when the pressure profile is included as a constraint.

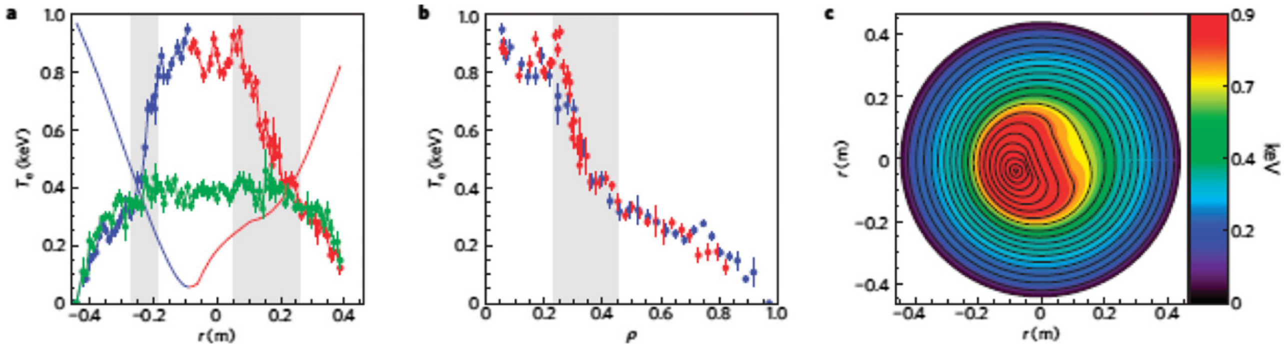

Figure 10. In RFX-mod, mapping of measured electron temperature T_e on helical flux surfaces. (a) T_e profile as measured by Thomson scattering, with the continuous line corresponding to the helical flux coordinate ρ, (b) T_e profile mapped on the helical flux coordinate ρ; (c) 2D map of T_e on the poloidal plane, with helical flux surfaces superimposed. Reprinted by permission from Springer Nature Customer Service Centre GmbH: Springer Nature, Nature Physics [109], Copyright 2009.

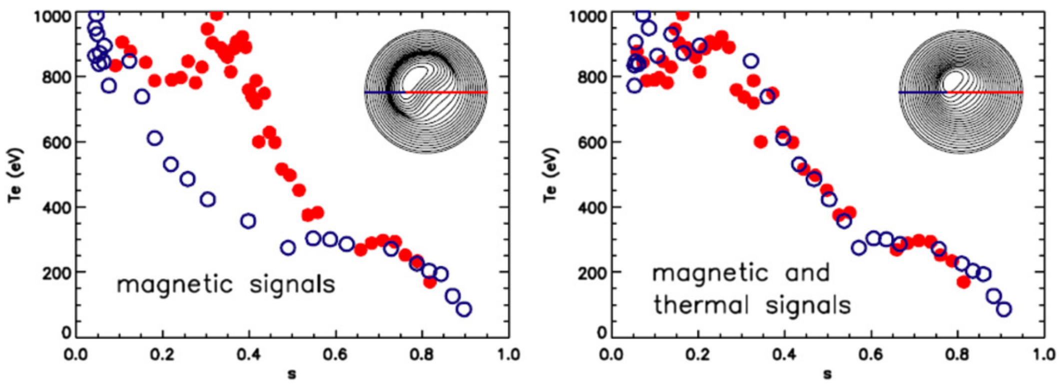

Figure 11. Remapping of electron temperature measurements on magnetic flux surfaces (see small plots) as obtained by the V3FIT code. Empty and full circles refer to different sides with respect to the helical axis. Left plot: force-free equilibrium obtained using only magnetic measurements. Right plot: equilibrium with pressure consistent with temperature and density measurements. Reproduced courtesy of IAEA. Figure from [138]. Copyright 2013 IAEA.

A fundamental property of QSH-SHAx equilibria is that the q profile is non-monotonic: it goes through a maximum located in the vicinity of the temperature gradient region, as shown in figure 12(b). Non-monotonic q profiles have also been found in numerical SH simulations by the SPECYL code [139, 140]. As the maximum value of the helical q is lower than the axisymmetric one, the innermost resonant mode of the axisymmetric safety factor ($m = 1, n = -7$ in RFX-mod for example) is not resonant anymore according to the helical q profile (therefore, in RFX-mod, the innermost resonant mode becomes $m = 1, n = -8$).

The magnetic topology of both QSH-SHAx and QSH-DAx states of RFX-mod can be reproduced by a one parameter fit of a minimally constrained equilibrium model using only five parameters in a two-domain generalization of Taylor's theory (that will be summarized in section 3.1). Both states appear as a consequence of the formation of a transport barrier in the plasma core, in agreement with experimental results [141].

It is worth mentioning that helical core equilibria states are also found in tokamaks, associated to the non-monotonic q profile occurring in hybrid mode operations, as obtained in 3D equilibrium calculations [142, 143].

3. Magnetic self-organization in the RFP

The first experimental evidences of a RFP configuration as an example of self-organization dates back to the toroidal pinch research in the 1960s, with the observation of the quiet periods in the ZETA machine [144, 145]: low magnetic turbulence periods associated to the reversal of the toroidal field near the plasma edge.

The toroidal field reversal is the key ingredient for the ideal stability of internal modes, combined to a sufficiently close fitting shell for suppressing external $m = 1$ modes [36, 146]. Later linear ideal and resistive MHD stability analysis with more realistic profiles [23] and boundary conditions [147] confirmed and enhanced these findings.

The emergence of a quiet and ordered configuration out of the turbulent discharge setting-up was considered an example of a self-organized process, as defined by Hasegawa [148]. A weakly dissipative continuous medium in which energy and one or more other quantities are conserved in absence of dissipation, evolves towards an ordered quasi-stationary state, obtained by a constrained minimization. According to the Taylor's conjecture in [149], magnetic helicity is the other conserved quantity.

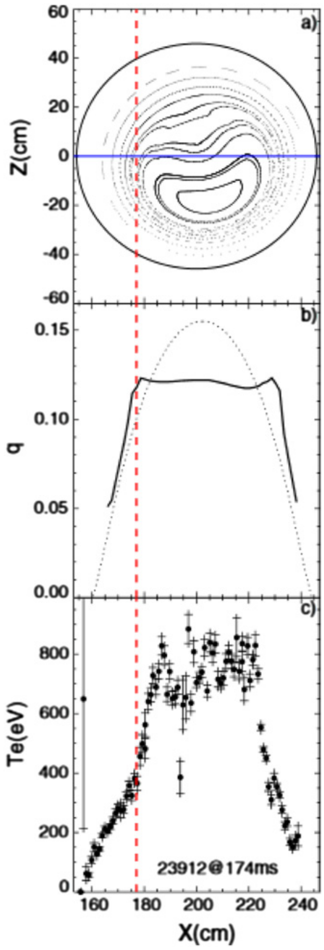

Figure 12. For a QSH-SHAx in RFX-mod: (*a*) Poincaré plot of magnetic surfaces; (*b*) safety factor profile (plain line) compared to the axisymmetric case (dashed); (*c*) temperature profile from Thomson scattering as measured along a diameter (blue line in plot (*a*)). Reprinted figure with permission from [139], Copyright 2011 by the American Physical Society.

The self-organization process is not unique to the RFP configuration and occurs in other current carrying fusion plasmas as well, e.g. in disruptions or hybrid operations in tokamak [143, 150] and spheromak plasmas [151, 152]. And indeed self-organization in fusion or laboratory plasmas shares several similarities with magnetic reconnection in space plasmas [153].

In this chapter, the first sections deal with the need for a dynamo electric field in the ohmic sustainment of the RFP and describe how the dynamo is related to magnetic field and flow fluctuations (sections 3.1–3.3). In the first 3D numerical simulations the dynamo field was interpreted as due to many nonlinearly interacting tearing modes, consistent with the MH state experimentally observed at that time (section 3.4). From the '90s, exploiting advanced computing potentialities, 3D simulations discovered a bifurcation of the magnetic configuration from the MH to the SH state ruled by the plasma dissipation, coming parallel to the initial experimental observations of QSH states (section 3.5). The agreement between theoretical predictions and experiments improved when a helical boundary was included in the simulations. Section 3.6 summarizes the experimental measurements of MHD dynamo and the evidences of a two-fluid contribution from the Hall dynamo, while flow and momentum transport studies are recalled in section 3.7. Finally, section 3.8 presents a new interpretation of the MHD dynamo as an electrostatic dynamo able to unify the description of both multiple and SH plasmas. Section 3.9 summarizes further theory aspects.

3.1. Taylor's theory of the RFP

The first attempt to explain the reversal of the toroidal field was performed within the Taylor's theory [149, 154] as being due to some unspecified MHD turbulence. Such a turbulence in a weakly resistive plasma causes reconnection of magnetic field lines so that the plasma rapidly relaxes towards a minimum energy state on ideal MHD time scales (of the order of the Alfvén time), which are faster than the classical resistive diffusion time scales.

The mathematical properties of this state are obtained by a variational argument, i.e. by minimizing the magnetic energy subject to the conjecture that, in presence of weak resistivity, the conservation of the total helicity is a constraint to be satisfied. The motivation behind Taylor's conjecture is that the finite plasma resistivity causes reconnection of magnetic field lines and breaks the conservation of the infinity of helicity invariants of the ideal magnetohydrodynamics found by Moffatt [155]. For an isolated plasma, enclosed in a perfectly conducting wall, this minimization leads to a force free equilibrium field [156].

Despite the appeal of the Taylor conjecture, there is as yet no rigorous justification for it, although various heuristic arguments have been advanced [157]. Still, it has been successfully used as a framework for the interpretation of the RFP experimental and numerical behaviour of the RFP, especially during the DREs [158]. For example, from global magnetic measurements combined with equilibrium modelling, the magnetic energy and helicity have been inferred in the MST during DREs [24], revealing that the helicity changes relatively little while magnetic energy reduction is significant.

In Taylor's relaxation theory the magnetic field was found to obey the force-free equilibrium equation

$$\nabla \times \boldsymbol{B} = \mu \boldsymbol{B} \tag{3.1}$$

where μ is constant throughout the whole plasma. This implies that the plasma current density $\boldsymbol{J}$ is aligned to magnetic field $\boldsymbol{B}$. In cylindrical geometry, solutions of the force free equation (3.1) are Bessel functions (hence the name Bessel function model, BFM) and the (F, Θ) parameters describe a unique set of relaxed state equilibria similar to experimental observations. The theory predicts that, above a certain Θ value, an equilibrium with reversed toroidal field occurs.

On the other hand, in the light of visco-resistive MHD simulations performed from 90s, several aspects of Taylor's theory have been criticized [159]. Among them: the states predicted by the theory do not exist, neither experimentally, nor numerically; the timescale of relaxation turns out to be intermediate between ideal and resistive; the fluctuations involved in these processes are large scale (tearing and resistive modes). Also,

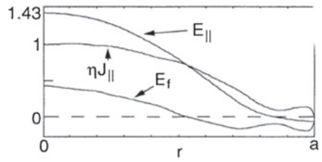

Figure 13. Parallel electric field profiles for the RFP from a 3D visco-resistive MHD simulation. $E_{\|}$ is externally applied, E_f is the MHD dynamo, and $\eta J_{\|}$ is the resulting ohmic electric field. Reprinted figure with permission from [177], Copyright 1989 by the American Physical Society.

the predicted saturation of the pinch parameter at $\Theta = 1.56$ is not observed in experiments, and unlike Taylor's theory, the relationship between Θ and F is somewhat different than defined by the BFM model [160]. Furthermore, Taylor theory assumes a closed system, while the RFP is an open ohmic system.

3.2. The need of a dynamo for the RFP

While Taylor's theory approximately describes the properties of the RFP discharges, it is not a self-contained theory that describes all of the detailed processes generating field reversal, i.e. the reconnection and relaxation mechanisms. Moreover, even though the axi-symmetric RFP is a steady equilibrium, its ohmic sustainment by an induction toroidal field cannot occur in axi-symmetric geometry [37], and therefore a steady-state axisymmetric solution should not exist. This is a result of the Cowling anti-dynamo theorem, which states that a symmetric magnetic field configuration cannot be maintained against resistive diffusion by a symmetric velocity field [161, 162]. The nearest stationary axisymmetric ohmic equilibrium is the force free paramagnetic pinch [146, 163] with a null toroidal field at the edge. The process that generates the poloidal current consistent with the experimentally observed toroidal field reversal is defined as *dynamo*, in loose analogy with astrophysical and geophysical settings. Without the dynamo process, the axisymmetric magnetic field would resistively diffuse and reversal would be lost [164].

Figure 13 shows the radial profile of the parallel component of the mean applied electric field $E_{\|} = \boldsymbol{E} \cdot \boldsymbol{B} / |\boldsymbol{B}|$ and compares it with the $\eta J_{\|}$ term, clearly showing that the axisymmetric Ohm's law is violated. In particular in the core the applied electric field is larger than required ($E_{\|} > \eta J_{\|}$), while in the edge it is less and even directed in the opposite direction. The dynamo process generates an additional parallel current required to balance the Ohm's law.

At the beginning of the 90s' two possible mechanisms underlying the RFP dynamo were investigated, partially supported by experimental observations [1, 160, 165]. The first one was based on the MHD dynamo, which relied on the local mean-field single fluid Ohm's law, in which the coupling of velocity and magnetic fluctuations generated an average electric field $\mathbf{E}_f$ sustaining the plasma current against resistive diffusion.

A second approach was based on the current due to the free streaming of electrons along stochastic field lines, the so called kinetic dynamo theory (KDT) [59]. The measurement of fast electrons at the edge of several RFP devices was the evidence suggesting this possibility. However, further theoretical studies and experimental investigations ruled out this interpretation (see section 4.8).

3.3. The MHD dynamo

Borrowing concepts from geophysical and astrophysical turbulent dynamo theories [162], the fields and currents are separated into mean ($\langle \mathbf{B} \rangle, \langle \mathbf{E} \rangle, \langle \mathbf{J} \rangle$) and fluctuating components ($\tilde{\mathbf{b}}$,$\tilde{\mathbf{v}}$), where the angle brackets represent a mean-field flux surface average, which leads to an additional mean field term $\langle \tilde{\mathbf{v}} \times \tilde{\mathbf{b}} \rangle_{\|}$ in the parallel to $\langle \mathbf{B} \rangle$ components of Ohm's law [166]:

$$E_{\|} + \langle \tilde{\mathbf{v}} \times \tilde{\mathbf{b}} \rangle_{\|} = \eta J_{\|} \tag{3.2}$$

In particular, this term, called in subsequent RFP literature *MHD dynamo*, can be non-zero at the reversal surface, where the induction electric field is zero, and can drive the required poloidal current. As the velocity and magnetic field dynamics are coupled through the Lorentz force, the determination of the MHD dynamo term is a nonlinear problem. In [166] a simplified statistical approach was adopted based on mean-field electrodynamics [162]. The MHD dynamo term was assumed to be proportional to the mean field through the free parameter α (the α-*dynamo* approach [167]) and under some assumptions the equilibrium field was found to obey the force-free condition with constant μ, as in equation (3.1).

Self-consistent investigations on the dynamics of the fluctuations were based on 3D nonlinear visco-resistive MHD computations. Sykes and Wesson showed robust field reversal in a single fluid MHD simulation using a $14 \times 14 \times 13$ grid [168]. They identified the basic mechanism of field reversal as the quasi-periodic nonlinear evolution of an $m = 1$ global kink instability in the presence of an externally applied toroidal voltage. An intuitive explanation of this result can rely on a simple *toy model*, which consists in a current-carrying resistive wire initially placed on the axis of a cylindrical flux conserver, whose spontaneous kink leads to the reversal of the edge axial magnetic field, and not to a 'disruption' [169, 170].

This mechanism was confirmed by subsequent numerical simulations, based on the elementary cylindrical visco-resistive compressible nonlinear MHD model in the constant-pressure, constant-density approximation with a forced SH [33, 35, 171–173].

3.4. The standard paradigm: the MHD dynamo is inherently multiple helicity

The initial numerical 2D SH states were deemed too far from the experimentally observed MH plasmas. When computational physicists, taking advantage of the increase of the power of computers, began to deal with the full 3D problem, the parameters of initial numerical simulations led them into the MH state. The MHD dynamo term was inherently due to several nonlinearly interacting global tearing modes. Fully 3D MHD numerical simulations with multiple helicities were able to reproduce field reversal and the quasi-periodic RFP sawtooth dynamics (see section 2.2) [42, 160, 173–176].

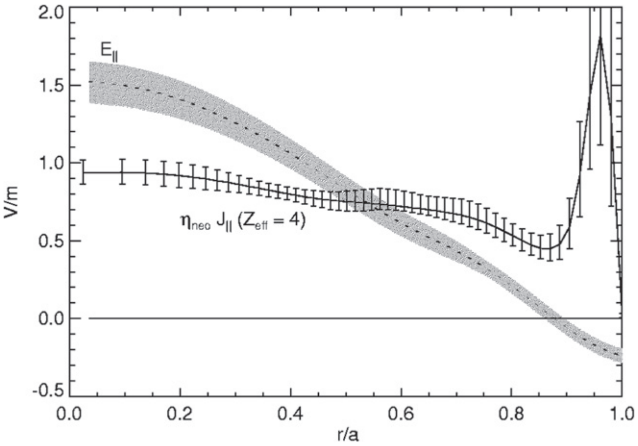

Figure 14. Results from an equilibrium reconstruction illustrating that $E_\parallel \neq \eta J_\parallel$ in standard multiple-helicity RFP operation. In particular, the existence of a radial location with zero applied electric field and finite current density makes clear the need for dynamo drive. Reprinted from [178], with the permission of AIP Publishing.

An example of the radial profiles of the MHD dynamo electric field $E_{f\parallel} = -\langle\tilde{\mathbf{v}} \times \tilde{\mathbf{b}}\rangle \cdot \mathbf{B}/|\boldsymbol{B}|$ is shown in figure 13 along with all the terms of the Ohm's law for a quasi-stationary solution of a 3D visco-resistive MHD simulation [177]. Figure 14 shows the terms $E_\parallel$ and $\eta J_\parallel$ derived from an experimental equilibrium reconstruction [178]. The parallel Ohm's law becomes $E - E_{f\parallel} = \eta J_\parallel$. Both the applied $E_\parallel$ and parallel MHD dynamo field $E_{f\parallel}$ modify the parallel current profile $J_\parallel$ which, in turn, determines the stability and the level of dynamo fluctuations. By itself, the applied $E_\parallel$ would create a peaked $J_\parallel$ profile and could not sustain a reversed magnetic field (note that $E_\parallel$ near the edge is in a direction to suppress $J_\parallel$). The positive values of $E_{f\parallel}$ near the axis suppress parallel (axial) current, i.e. act as an anti-dynamo, while negative values of $E_{f\parallel}$ near the edge drive parallel (mostly poloidal) current.

The competition between these two processes has been used to interpret the common observation of the DREs, described in section 2.2. From linear theory [23, 160], the peaked $E_\parallel$ causes a gradient in $J_\parallel$ that destabilizes tearing modes. The parallel dynamo field $E_{f\parallel}$ generated by the tearing modes and their associated flow fluctuations tend to flatten the $J_\parallel$ profile, and in so doing, sustain the reversed toroidal field. Therefore, nonlinear saturation of the tearing instability is interpreted as a balance between these two competing processes, and an equilibrium is maintained near marginal stability.

The nonlinear interaction between $m = 1$ and $m = 0$, low n resonant modes was investigated in [42], by implementing a post-processing energy diagnostic to identify the path taken in Fourier space by the poloidal magnetic field energy as it is converted to axial magnetic field energy by the dynamo process. Such coupling was subsequently verified experimentally (see section 2.2.1).

Numerical simulations performed with a Lundquist number close to the experimental ones in [179] highlighted the presence of toroidally localized dynamo current sheets generated during reconnection events, which are toroidal in the core (anti-dynamo) and mainly poloidal in the edge.

3.5. The transition from multiple helicity to single helicity

Since 1990 and before QSH experimental observations, 3D numerical simulations revealed a bifurcation of the magnetic configuration from the MH state to the SH state, occurring when viscosity is increased and coming with magnetic order [179–182].

An appropriate rescaling of time and velocity in the MHD equations shows that, for given radial distributions of plasma resistivity η and viscosity ν, the dynamics is ruled by the magnetic Prandtl number $P = \nu(0)/\eta(0)$ and by the dissipation of the system $d = \eta(0)\nu(0)$, also quantified by the Hartmann number $H = d^{-1/2}$, a classical dimensionless number in conductive fluid MHD. Dissipation is the dominant parameter when the inertia term becomes negligible, which happens for a large range of simulation parameters [183]. These simulations indicate d (or H) as the control parameter independently of P and Θ. Therefore, the previous high viscosity simulations turned out to be in reality high dissipation (or small H) simulations. As usual in nonlinear dynamics, an increase of dissipation is favourable to a laminar behaviour of the system. Depending on the initial conditions, two nearby different helicities were found to be selected by the plasma when relaxing to SH [183, 184].

Incidentally, it has to be mentioned that, while in the first simulations the plasma current and the axial magnetic flux were taken as constant, which implies the constancy of the pinch parameter Θ ([184] and references therein), from 2008 on simulations with the SpeCyl and PIXIE3D codes were performed with a constant loop voltage instead of a constant Θ [185, 186].

3.5.1. The intermediate regime: the QSH states. As d decreases, the pure helix (single helicity, SH) develops a toroidally (axially) localized bulging (slinky); this bulged helix is interrupted by longer and longer intermittent phases, in which secondary modes with other helicities show up in the Fourier spectrum. The bulged helix corresponds to a QSH state where secondary modes are not zero but smaller than the dominant one. When at least two modes have similar amplitudes, the plasma switches to the MH state. With decreasing d, the duration of the QSH phases decreases, as well as the percentage of time where QSH dominates, and after a transition region corresponding to $10^3 \leqslant H \leqslant 10^4$, the system reaches a non-stationary MH regime [183]. This is shown in figure 15 where the energy of the $m = 0, n \neq 0$ modes is used as an order parameter for the SH–QSH–MH transition; indeed these modes vanish in the SH state, since they result from the beating of at least two different helicities. It is important to note that magnetic chaos sets in progressively during the transition.

3.5.2. The role of the helical boundary conditions in MHD simulations. Though MHD simulations were able to predict QSH states, in the first SpeCyl calculations they had a temporal behaviour different from the experimental one. The reason is that the former had a vanishing radial magnetic field at the edge, while the latter correspond to a finite one, since in experiments the time discretization of a digital feedback

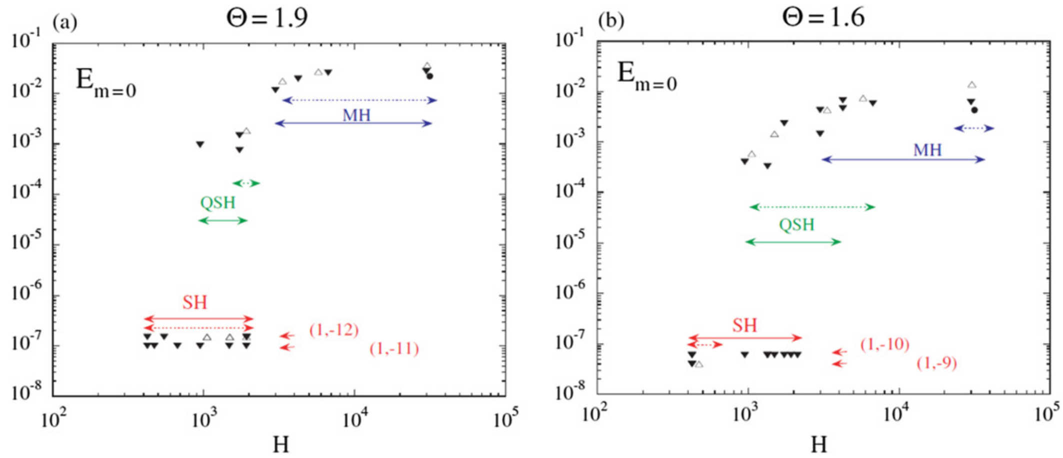

Figure 15. Transition diagrams at two values of the pinch parameter: *(a)* $\Theta = 1.9$, *(b)* $\Theta = 1{:}6$. $E_{m=0}$ is the time averaged magnetic energy of the $m = 0$ modes and H is the Hartmann number. The open triangles correspond to $S = 3.3 \times 10^3$ with P in the range [0.012, 50], black triangles to $S = 3.0 \times 10^4$ with P in the range [1, 5000], and black circles to $S = 10^5$ with $P = 10$. The vanishing SH $m = 0$ modes energy is represented as a finite conventional value with different offsets associated to the different preferred helicities. Reproduced from [184].

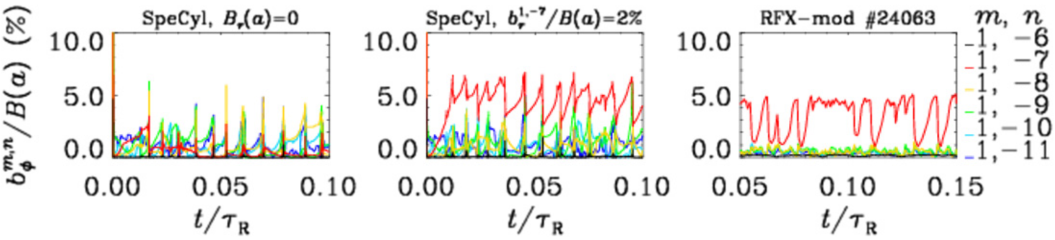

Figure 16. Simulation of the time evolution of the $m = 1$ tearing modes by the Specyl code; (left) with ideal boundary conditions; (middle) with 2% edge magnetic perturbation; (left) comparison with an RFX-mod experiment. The Lundquist number in the simulation is about the experimental one (107). Reproduced courtesy of IAEA. Figure from [271].

control system prevents the achievement of zero radial field at plasma radius [187]. A good agreement with the experimental QSH dynamics was in fact obtained in simulations including a small $m = 1$, $n = -7$ boundary condition (MP) with an amplitude similar to the experimental one (about 1.5% of the central magnetic field) and with $S = 10^7$, consistent with experimental Lundquist number [188]. An example is shown in figure 16. A more recent work, including simulations of both spontaneous and driven experimental QSHs (see section 2.2.3), shows that the similarity with experiments bears on several features [189]: (i) the dependence of the quasi-periodic behaviour of QSH states and of its amplitude on the MP amplitude, (ii) the dependence on the MP amplitude of the position of the shear reversal and maximum q, (iii) the fact that the amplitude of the dominant mode is independent of dissipation, whereas the amplitude of secondary modes decreases with increasing inverse resistivity and viscosity (Lundquist and viscous Lundquist numbers). Numerically, a stationary state is reached for an MP of 10%.

Very recent extended analysis including a large set of simulations actually shows that in presence of a finite radial magnetic field at the edge, a second low dissipation region exists where SH states also develop [126].

3.5.3. Necessary condition for field reversal of the single helicity ohmic state. The SH ohmic state can be described analytically as a small helical perturbation of an axisymmetric ohmic pinch with small edge axial magnetic field and conductivity. This description uses the pinch–stellarator equation, which shows how the axial field of a cylindrical SH RFP evolves radially because of the pinch effect and of a stellarator contribution due to the helical deformation of the plasma [182, 190, 191]. Reversal is due to the edge stellarator contribution, which is more efficient when the edge pinch contribution is weak. The latter condition corresponds to a resistive edge plasma. Furthermore, simulations performed with a flat resistivity profile display a reduction of the dynamo action, which brings to marginally-reversed or even non-reversed equilibrium solutions [192–195]. This occurs because with a larger resistivity at the edge, the electrostatic field is larger too, in order to balance parallel Ohm's law. The electrostatic drift due to such larger electrostatic field provides an enhanced dynamo action, which is sufficient to sustain the reversed configuration [192]. The edge resistivity of RFPs is high enough for the reversed axisymmetric part of the toroidal field to be rather constant in the reversal domain after a steady decrease in the non-reversed one. The pinch-stellarator equation enables the derivation of a necessary criterion for the reversal of the edge axial field [191], which in combination with MHD simulations with a small RMP shows that a finite edge radial magnetic field of given helicity is favourable for field reversal. The criterion is found to be satisfied in RFX-mod when a finite edge radial magnetic field is applied, but only marginally in spontaneous QSH states [191].

3.6. Measurements of the MHD dynamo

The MHD dynamo has been measured both in MH and in QSH plasmas in several RFP devices. Experimental tests of the MHD dynamo theory have been performed by measuring terms of the mean field Ohm's law equation. For conciseness we write here the two fluid version, following [39]:

$$\mathbf{E} + \mathbf{v} \times \mathbf{B} = \eta \mathbf{J} + \frac{\mathbf{J} \times \mathbf{B}}{ne} - \frac{\nabla p_e}{ne} - \frac{m_e}{e}\frac{d\mathbf{v}_e}{dt} \tag{3.3}$$

where $\mathbf{v}_e$ is the electron fluid velocity, $\mathbf{v} \approx \mathbf{v}_i$ (the ion fluid velocity), p_e is the electron pressure, n is the plasma density, m_e is the electron mass, and e is the electron charge. The last three terms on the right-hand side of equation (3.3) are the Hall term, the gradient of electron pressure, and the electron inertia: they represent effects beyond standard single-fluid MHD.

By splitting the quantities in equation (3.3) into mean and fluctuating parts, averaging over an axisymmetric flux surface, and taking parallel components, the generalized parallel Ohm's law becomes

$$\eta J_{\parallel} = E_{\parallel} + \langle \tilde{\mathbf{v}} \times \tilde{\mathbf{b}} \rangle_{\parallel} - \frac{\langle \tilde{\mathbf{j}} \times \tilde{\mathbf{b}} \rangle_{\parallel}}{ne} \tag{3.4}$$

where the last term on the right-hand side is referred to as the *Hall dynamo*. Note that the electron inertia term is usually neglected as small, and the parallel component of the pressure gradient term vanishes upon axisymmetric poloidal and toroidal averaging. In the parallel two-fluid Ohm's law $\boldsymbol{v}_i$ and $\boldsymbol{v}_e$ are combined in the usual relations for the fluid velocity $\boldsymbol{v} = (m_i\boldsymbol{v}_i + m_e\boldsymbol{v}_e)$ and current $\boldsymbol{J} = en(\boldsymbol{v}_i - \boldsymbol{v}_e)$ [196]:

$$\eta J_{\parallel} - E_{\parallel} = \langle \left(\tilde{\mathbf{v}} - \frac{\tilde{\mathbf{j}}}{ne} \right) \times \tilde{\mathbf{b}} \rangle_{\parallel} \approx \langle \tilde{\mathbf{v}}_e \times \tilde{\mathbf{b}} \rangle_{\parallel} \tag{3.5}$$

The appearance of only electron velocity in the rhs is the consequence of the fact that Ohm's law in two fluids MHD represents the force balance equation for the electron fluid.

The Hall dynamo term is a two-fluid MHD effect: it arises when the ion flow does not follow electron flow, which implies that electrons and ions experience different forces and therefore the electron pressure force can drive flows only in electrons [167]. The effect of electron pressure fluctuations can be made explicit, so that it can be related to local measurements. Extracting the perpendicular component of the electron flow velocity and inserting it into equation (3.4), two terms which can be measured by insertable probes become apparent:

$$\eta J_{\parallel} - E_{\parallel} = \langle \tilde{\mathbf{E}}_{\perp} \cdot \tilde{\mathbf{b}}_{\perp} \rangle_{\parallel} + \langle \nabla_{\perp} \tilde{P}_e \cdot \tilde{\mathbf{b}}_{\perp} \rangle_{\parallel} \tag{3.6}$$

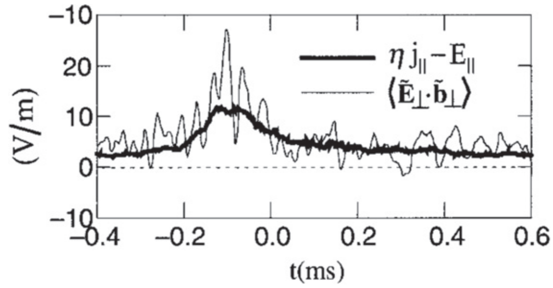

Figure 17. Comparison of the dynamo electric field $\langle \tilde{E}_{\perp} \cdot \tilde{b}_{\perp} \rangle$ to $\eta \boldsymbol{J}_{\parallel} - E_{\parallel}$ from an ensemble of sawtooth relaxation events in the MST RFP. Time $t = 0$ is a reproducible time marker for aligning individual sawtooth events during ensemble averaging. Reprinted from [196], with the permission of AIP Publishing.

The first term arises from the fluctuating $\boldsymbol{E} \times \boldsymbol{B}$ drift and is called the MHD dynamo, and the second term is a two fluid effect called the *diamagnetic dynamo*, related to the electron diamagnetic drift. The diamagnetic dynamo is therefore a manifestation of the Hall dynamo. In the single-fluid limit where ions and electrons drift together, the Hall dynamo is absent.

3.6.1. Edge measurements of MHD dynamo. The first direct measurements of the dynamo were made in the REPUTE RFP edge [197], and later in the MST edge [39], by directly correlating fluctuations in the electric and magnetic fields. In REPUTE, the measured dynamo electric field was far below that required to balance resistive dissipation, suggesting that two-fluid effects could have an impact. However, the measurements in MST revealed a dynamo electric field of direction and magnitude consistent with current sustainment, i.e. balancing parallel Ohm's law. It is interesting to highlight that MHD dynamo effects were measured in a spheromak using a similar technique [198].

The Hall dynamo term was also directly measured by correlating current density and magnetic field fluctuations using probes in MST plasmas. It was found to be small in the far edge [199], but it increases and is sufficient to balance Ohm's law near the reversal surface [200], showing that two fluid dynamics are important in the relaxation process.

Figure 17 shows the dynamo electric field measured in the edge of the MST MH plasma ($r/a = 0.9$), compared to the other terms in Ohm's law, where the resistivity η is calculated from measured local electron temperature T_e and with estimated effective charge $Z_{eff} = 2$ (the effective charge Z_{eff} is defined as $Z_{eff} = \sum_i n_i Z_i^2 / \sum_i n_i Z_i$, with i ranging over all the ionic species present in the plasma). The dynamo electric field increases during the sawtooth event to overcome the inductive back reaction produced by rapid changes in the plasma current profile.

Measurements performed in TPE-1RM20 edge over a wide range of electron collisionality, (defined by the ratio of electron mean free path to the plasma radius) shed light on the different results [201]. Depending on the collisionality regime, the MHD dynamo dominates in the collisionless region, and the diamagnetic dynamo dominates in the collisional regime,

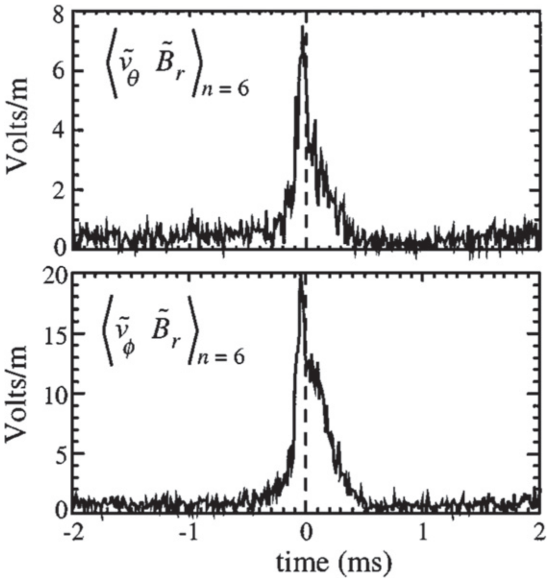

Figure 18. Two $m = 1$, $n = 6$ components of the dynamo, both of which suppress parallel current in the core of MST. The velocity and magnetic fluctuations reach peak coherence at the sawtooth event ($t = 0$) and are nearly in phase, maximizing the dynamo product. Reprinted from [205], with the permission of AIP Publishing.

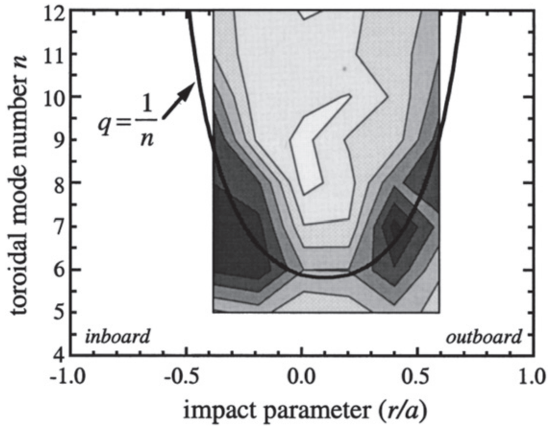

Figure 19. Amplitude contours of the mode-resolved poloidal velocity fluctuation $\left\{\sqrt{\tilde{v}_\theta^2}\right\}_n$. The velocity fluctuation amplitude for a particular n-mode peaks approximately at the impact parameter where that mode is expected to be resonant (estimated from the q profile). Reprinted from [205], with the permission of AIP Publishing.

indicating that diamagnetic drift controls the electron flow's correlation with the magnetic field. This finding explains the original result from REPUTE [196]. The results from these measurements, performed in MH states, imply that the (turbulent) dynamo effect causes helicity transport and overall helicity is conserved [202].

Fast, direct and local measurements of ion velocity fluctuations $\tilde{\mathbf{v}}$ were obtained by an insertable optical probe in MST [203]. The probe collected light from two perpendicular lines of sight limited by view dumps to produce radial localization of the measurements to 2–3 cm. The correlation analysis highlighted the contribution to the MHD dynamo of individual resonant tearing modes. The two lines of sight of the optical probe provided simultaneous measurements of the radial and toroidal components of the plasma velocity, $\tilde{v}_r$ $\tilde{v}_t$, which are the quantities arising in the parallel component of $\langle \tilde{\mathbf{v}} \times \tilde{\mathbf{b}} \rangle_\parallel = \langle (\tilde{v}_r \tilde{b}_t \rangle$-$\langle \tilde{v}_t \tilde{b}_r \rangle)$. To obtain the complete dynamo product, the velocity fluctuations $\tilde{v}_r$ $\tilde{v}_t$ were correlated with the local measurements of the magnetic fluctuations $\tilde{b}_t$ and $\tilde{b}_r$, respectively. The parallel current profile $J_\parallel$ was obtained using an insertable Rogowski coil [48] and the toroidal field profile was determined by an additional insertable magnetic pickup coil. Ensembles over repeatable plasma discharges $I_p = 210$ kA, with density $n_e = 1 \times 10^{19}$ m^{-3} were considered.

The main finding of this work is that the MHD dynamo electric field balances the Ohm's law in the outer region of the MST plasma up to the reversal surface, (qualitatively consistent with the former edge measurements), but not inside, where the Hall dynamo from two fluid dynamics becomes important [200, 204]. Correlation analysis with tearing modes also reveals that the edge structure of velocity fluctuations is mainly related to $m = 0$, low n harmonics, which are correlated to tearing modes resonant at the reversal surface. A small dynamo field is measured also between crashes, confirming the continuous nature of the single-fluid MHD dynamo (at least at the edge).

3.6.2. Mode resolved core measurements of MHD dynamo. Core ion flow fluctuations have also been measured, initially by line-integrated passive spectroscopy [205] and subsequently with charge exchange recombination spectroscopy (CHERS) [206], allowing more localized observations of the flow fluctuations and of the single fluid MHD dynamo electric field. Correlation analysis with tearing modes extracted the single fluid MHD dynamo term and allowed a more detailed determination of its spatial distribution. Throughout the sawtooth cycle, the core fluctuations have been found to be mainly correlated with internally resonant modes ($m = 1$, $n = 5$–7 in MST). Figure 18 is an example of two components of the $\langle \tilde{\mathbf{v}} \times \tilde{\mathbf{b}} \rangle$ dynamo produced by the core-resonant $m = 1$, $n = 6$ tearing mode. This work also indicated that the velocity fluctuation eigenfunctions involved in the MHD dynamo were peaked at the rational surfaces, with widths similar to the ones expected for the islands related to tearing modes (figure 19).

3.6.3. Measurements of flow fluctuations and MHD dynamo in QSH states. The MHD dynamo in QSH states was first measured in MST [90]. Main results are: (i) the magnetic and velocity fluctuation spectrum have the same dominant wave number. (ii) The corresponding component of the velocity extends throughout the plasma volume and couples with magnetic fluctuations, producing a significant MHD dynamo electric field. (iii) The radial profile of this component is consistent with the one obtained in QSH runs of the SpeCyl MHD code [184]. A similar study performed in RFX-mod [207] showed that a helical plasma flow forms an $m = 1$ convective cell which in turn creates a localized sheared flow outside the region of high temperature gradient (figure 20). However, the experimental pattern revealed the maximum flow shear more external

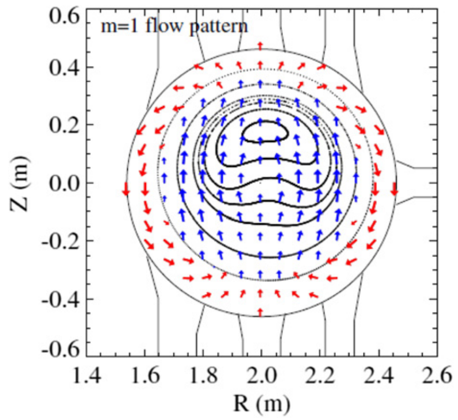

Figure 20. 2D reconstruction of the flow pattern in RFX-mod from multichord Doppler shift measurements. Data refer to a 1.2 MA plasma discharge. The flow is radially directed towards the helical magnetic axis in the core and changes the sign moving to the edge. The helical axis is represented by the reconstructed helical magnetic surfaces. Reproduced courtesy of IAEA. Figure from [207]. Copyright 2011 IAEA.

with respect to the predictions of 3D MHD simulations, possibly due to an ambipolar component of the helical electric field on top of the MHD one.

Localized flow measurements in MST [206] show that poloidal flows associated with the $n = 6$ mode during QSH intervals are larger and broader than in MH, but they do not dominate the flow spectrum over the entire radius, in contrast to the magnetic spectrum. The $n = 7$–12 modes, in fact, maintain a similar flow structure during QSH while all tearing mode flows remain peaked near their resonant surfaces.

Even weak external 3D fields, used to stimulate QSH states (section 2.2.3) can modify significantly the flow profile and in particular its shear [119]. In RFX-mod, in fact, the edge flow displays a QSH modulation [208]. Probes have been used in low current discharges (up to 0.45 MA) of RFX-mod, enabling the observation in stimulated QSH states of a modulation of the perpendicular components of the flow [209] concomitant with the density modulation along the toroidal angle [210, 211].

3.6.4. Mode resolved measurements of the Hall dynamo. In MST the Hall dynamo term has been measured in the plasma core using an eleven-chord laser Faraday rotation diagnostic and correlating the current and magnetic field fluctuations over an ensemble of several sawtooth cycles [212]. The Hall dynamo is found to be spatially localized in the region of the resonant surface, while an additional dynamo mechanism may be required to balance the induced electric field elsewhere. Such a picture is qualitatively consistent with two-fluids quasilinear theory [213] which predicts a localized Hall dynamo and a more diffuse MHD dynamo away from the resonant surfaces. The Hall dynamo term is found to become large (up to 40 V m^{-1}) during the sawtooth crashes.

3.7. Plasma flow and momentum transport

Experimentally, during a DRE rapid momentum transport is found as a flattening of the radial profile of the toroidal and poloidal rotation, as mentioned in section 2.2.1 [68]. Such flattening has been explained by the generalization of Taylor's relaxation theory to two-fluids, in which context both the electron and ion helicities are conserved separately [214, 215]. In the resulting relaxed state, the spatial constant $\mu = J_\parallel/B$ is recovered from the standard MHD analysis and represents the dynamics of the electrons. Additionally, a new spatial constant appears, $nV_\parallel/B$, representing the dynamics of the ions and describing the relaxed state of the parallel plasma momentum profile.

Momentum transport is tightly linked to MHD dynamo process. In fact, the mean-field parallel momentum balance equation is

$$\rho\frac{\partial v_\parallel}{\partial t} = \langle\tilde{\mathbf{j}}\times\tilde{\mathbf{b}}\rangle_\parallel - \rho\langle\tilde{\mathbf{v}}\cdot\nabla\tilde{\mathbf{v}}\rangle_\parallel \tag{3.7}$$

where the left-hand side represents ion inertia with ρ as the mass density. On the right-hand side are the fluctuation-induced Maxwell and Reynolds stresses, respectively. Note that both the Maxwell stress term in equation (3.7) and the Hall dynamo one in equation (3.5) contain the term $\langle\tilde{\mathbf{j}}\times\tilde{\mathbf{b}}\rangle_\parallel$, indicating that the dynamics of the parallel current and parallel flow are coupled when two fluid effects are important. In MHD simulations, the relaxation of the parallel momentum profile is driven by the same reconnection events causing relaxation of the parallel current profile [216]. Experiments in MST confirmed such a tight coupling: MST measurements using probes in the edge and Faraday rotation in the core identified large Reynolds and Maxwell stresses associated with fluctuations at the tearing mode scale. The force densities from these stresses are large compared to the plasma inertia, but they tend to oppose each other [200, 212] so that their effect is negligible.

Recent two-fluid computations [44, 45, 217] show that there is a significant contribution from the Hall dynamo and coupling to momentum relaxation. The total dynamo is a smooth superposition of MHD and Hall effects that together balance Ohm's law, but each component varies considerably across the plasma radius, with each vanishing locally at particular locations. This is similar to the behaviour measured in MST plasmas.

3.8. A new interpretation of the MHD dynamo: the electrostatic dynamo

Both in SH and MH states, the spatially fluctuating component of the velocity may be seen as an electrostatic drift velocity related to an electrostatic field which is spatially modulated [218–220]. This is the basis for many of the probe measurements of the dynamo described above [39, 196, 197]. The electrostatic drift comes quite natural in SH. In fact, the helical displacement of magnetic surfaces produces a modulation of the parallel current density along each flux tube, which requires the build-up of a helical electrostatic potential producing the dynamo flow as an electrostatic drift (laminar MHD dynamo). This statement is supported by an elementary calculation in cylindrical geometry in [220]: in the parallel Ohm's law (scalar product of equation (3.3) with $\boldsymbol{B}$), the $\boldsymbol{v}\times\boldsymbol{B}$ term and the Hall term $\boldsymbol{J}\times\boldsymbol{B}$ bring vanishing contributions. The gradient of electron pressure vanishes too, because it is perpendicular to magnetic surfaces. Moreover, electron inertia is generally neglected in the RFP. If the magnetic field is known, the parallel Ohm's law enables the calculation of the electrostatic potential ϕ since $\mathbf{E} = E_0\widehat{\boldsymbol{e}_z} - \nabla\varphi$, with E_0 the inductive (loop) electric field. Finally, the full Ohm's law equation (3.3) yields the velocity field, which turns out to be slaved to the magnetic field. In the plasma core, the contribution from the applied electric field $E_\parallel$ is larger than that from the mean parallel current density, but it is smaller in the edge, as shown in figure 13. The difference is balanced by the electrostatic term, which provides an anti-dynamo contribution in the core and a dynamo contribution in the edge. The same interpretation can be applied to the MH case, where the electrostatic field is due to charge separation patterns produced by the periodic relaxation events and is again the main contributor to the fluctuating velocity field [218, 219, 221].

The pinch velocity leads to a build-up of the plasma density on the helical axis in MHD simulations where density is free to evolve [193]. This does not occur in a genuine plasma, where the central density profile is flat. This inconsistency was avoided in [222] by adding a diffusive term in the continuity equation for the density.

It is worth noting that a dynamo conversion of poloidal flux to toroidal flux, analogous to the RFP one, is invoked to explain the nonlinear saturation of the $m = 1$, $n = 1$ mode, i.e. the helical core observed in the hybrid mode of operation of the tokamak [143, 223]. This type of dynamo is also present in a flux rope configuration susceptible to the kink instability [224].

3.9. Further theoretical aspects

3.9.1. Toroidal effects. When performed in toroidal geometry, 3D nonlinear visco-resistive MHD simulations show that toroidal coupling prevents the system from reaching a pure SH state when dissipation increases, but that magnetic chaos due to toroidal coupling stays limited close to SH states for the aspect ratios of the largest present RFP's [225]. This is confirmed by toroidal simulations with the PIXIE3D code, also showing an $m = 0$ island chain induced by the toroidal coupling at the $q = 0$ reversal surface [124]. Incompressible 3D nonlinear visco-resistive MHD simulations show that, in contrast to the cylindrical case, the toroidal one presents a double poloidal recirculation cell with a shear localized at the plasma edge [226].

3.9.2. Two fluids effects on single helicity states. Analytical calculations in [220] show that (i) the SH state is the same on using single or two-fluid Ohm's law, which backs up a numerical result (section VA of [227]); (ii) the SH mode amplitude is insensitive to S, which backs up experimental [104] and numerical results in a two-fluid context [227]. Adding gyroviscosity in the force balance equation enables to get the experimental ratio of secondary to primary modes, while it is twice too large otherwise [227]. More analytical results can be found in the course [228].

3.9.3. Role of anisotropic resistivity. QSH states were obtained in simulations performed with an anisotropic thermal conductivity and using a multiple-time-scale analysis. In these simulations, the temperature distribution indicates the existence of closed magnetic surfaces, and there is a hot confined region [229]. When resistivity increases steeply at the edge, SH states are obtained for parameters similar to the case without thermal transport [230, 231].

3.9.4. Aspect ratio scaling of single helicity. The aspect ratio scaling law for the toroidal mode number of experimental QSH states was shown to be close to the one corresponding to the optimal electromagnetic response of the toroidal shell surrounding the plasma [232]. In [233] it is shown that the observed scaling with the aspect ratio and reversal parameter for the dominant mode in the single helical states can be obtained by minimizing the distance of the relaxed state described in [234] from a state which is constructed as a two region generalization of Taylor relaxation model [235].

3.9.5. Shear stabilization of $m = 1$ couplings in multiple helicity. Recently, a new MHD approach was proposed to explain why high current is favourable to QSH-SHAx states, why the innermost resonant $m = 1$ mode is the spontaneous dominant mode and why there are crashes of this mode. It invokes the shear stabilization associated with the 3D structure of the dominant mode to interrupt the nonlinear mode–mode coupling occurring in the MH regime [236]. This kind of ideas had been first introduced in [237]. The crashes can also be interpreted as the consequence of pressure-driven resistive modes, which introduce a feedback between transport and the MHD stability of the system [238].

4. Transport and confinement in the multiple helicity and quasi single helicity RFP

Energy and particle transport in RFP plasmas are strongly influenced by the presence and magnitude of tearing instabilities. Multiple magnetic islands can overlap and cause the magnetic field to be stochastic in a large volume of the plasma. Not surprisingly, the role of stochastic transport has been thoroughly examined in RFP plasmas. The well-known test-particle transport model for parallel streaming in a stochastic field works well, apart from nuances. However, QSH states and the application of current profile control both have reduced tearing instability, allowing confinement that is not limited by stochastic transport. Microinstability associated with several branches of drift waves plays an important role when tearing is suppressed.

In QSH states, the healing of magnetic surfaces allows hot regions to form inside the helical island structure. A transport barrier forms at the boundary of the helical core, and thermal transport is locally reduced. Microinstability from ion temperature gradient (ITG) and/or microtearing (MT) is dominant in the transport barrier. Trapped electron modes (TEM) are the dominant microinstabilities with current profile control, as discussed in chapter 5.

Impulsive DREs (aka sawteeth) that appear in MH plasmas as well in QSH plasmas during back-transitions to MH impart strong effects on transport and heating. The amplitudes of magnetic fluctuations burst in these events, which cools electrons, in addition to regulating magnetic flux generation and dynamo sustainment. A significant fraction (10%–30%) of the stored magnetic energy is released abruptly in a sawtooth crash, but much of this released energy remains confined as ion thermal energy through a powerful non-collisional heating process. Ion heating occurs simultaneously with electron cooling, and the sustained ion temperature is a large fraction of the electron temperature, even when collisional coupling of the species is weak.

Neutral beam injection (NBI) experiments have allowed assessment of energetic (or fast) ion confinement and stability. Importantly, energetic ion confinement in the RFP is classical, even in the MH regime with strong magnetic stochasticity. This is related to the drift orbits of fast ions. The energetic ion confinement is also good in QSH states, provided secondary modes remain sufficiently small. The fast ion beta in the core of MST plasmas reaches 8%, by which point energetic particle and Alfven eigenmodes are observed that limit the fast ion population. The relatively weak but strongly sheared magnetic field in the RFP generates a distinct Alfven continuum and provides a complementary environment to tokamak and stellarator plasmas for the study of fast ion driven instabilities.

In the following, core heat and particle transport properties are described in sections 4.1 and 4.2, both in MH and QSH states. An overview of the studies of the effect of microinstabilities on transport in RFPs is also given in section 4.3; ion heating and the effect on transport during DREs (sawtooth cycle) are discussed in section 4.4. The main features of transport in the edge region are reported in section 4.5. Section 4.6 gives a short summary of the isotopic effect in the RFP. Finally, sections 4.7 and 4.8 summarise the observations related to fast particle confinement in the RFP.

4.1. Core heat transport and confinement

In standard MH plasmas, strong temperature and density gradients are observed nearby the $q = 0$ toroidal field reversal surface [239–241], which naturally distinguishes two domains in describing transport: a core region inside the reversal surface, and an edge region from the reversal surface to the wall/limiter.

In the edge, transport is strongly influenced by a chain of $m = 0$ magnetic islands developing at the reversal surface [242, 243], and forming in fact a transport barrier corresponding to the $q = 0$ surface. The local pressure gradient is large, and the magnetic stochasticity is small compared to the core. Microinstabilities also play a role in the edge.

In the core, stochastic transport is dominant when magnetic islands created by multiple tearing modes are overlapped. The degree of magnetic stochasticity is quantified by the Chirikov stochastic instability parameter s, defined as [244]

$$s = \frac{1}{2}\frac{|W_{mn} + W_{m'n'}|}{|r_{mn} - r_{m'n'}|} \tag{4.1}$$

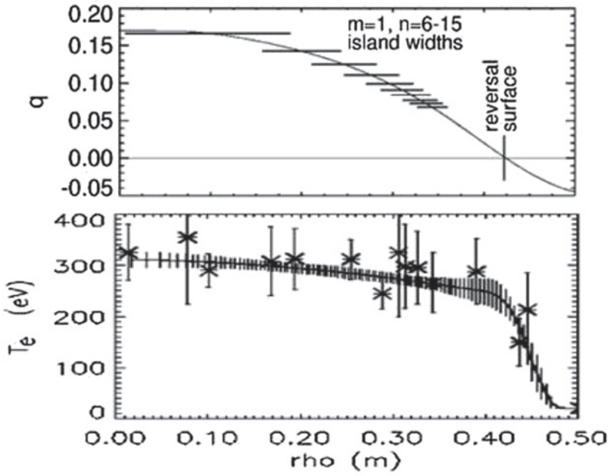

Figure 21. (Top) the $q(r)$ profile for an $I_p = 385$ kA MH plasma in MST. The horizontal lines indicate the typical magnetic island widths for the largest $m = 1$ tearing modes, centred on their resonant surfaces; (bottom) the electron temperature profile measured by Thomson scattering. The solid line is the fit from a toroidal equilibrium reconstruction. Adapted figure with permission from [239], Copyright 2003 by the American Physical Society.

where m and m' (n and n') are the poloidal (toroidal) mode numbers, W_{mn} is the width of the magnetic island related to the (n, m) mode, and r_{mn} the radial location of the resonant surface. Overlap of neighbouring magnetic islands occurs when $s > 1$, and the field becomes fully stochastic when $s \gg 1$.

In a domain where $s \gg 1$, transport caused by parallel streaming in a stochastic magnetic field can be large, as proposed by Rechester and Rosenbluth (RR) [3]. According to RR, the thermal diffusivity χ_{RR} depends on the magnetic fluctuations as:

$$\chi_{RR} = v_{th} D_m = v_{th}\left(\tilde{b}_r/B\right)^2 L_{ac} \tag{4.2}$$

where D_m is the stochastic magnetic field diffusion coefficient, $\tilde{b}_r$ is the magnetic fluctuation amplitude radial to unperturbed magnetic surfaces, B is the equilibrium field, v_{th} is the particle thermal speed, and L_{ac} is an auto correlation length characterizing the random diffusion of magnetic field lines. Stochastic transport is not inherently ambipolar, and the particle flux is given by [245]

$$\Gamma = -D\nabla n + v \cdot n \tag{4.3}$$

where D is the stochastic particle diffusion coefficient, and v is the convective velocity. Assuming thermal energy loss is dominated by electrons due to their high mobility ($T_i \approx T_e$), the ambipolarity constraint leads to $\chi_{RR}/D = \left(m_i/m_e\right)^{1/2}$.

Since stochastic heat transport scales as $\chi_{RR} \sim \left(\tilde{b}_r/B\right)^2 L_{ac}$, it is small if $\tilde{b}_r$ is small, or if the field is weakly disordered (small effective L_{ac}). The region near the $q = 0$ surface has large magnetic shear and densely packed $m = 1$ resonant surfaces. This encourages island overlap, but if the fluctuations are small, stochastic diffusion is small. As an example, the minimum heat diffusivity in high current pulsed poloidal current drive (PPCD) plasmas ($\chi_e \sim 2$ m^2

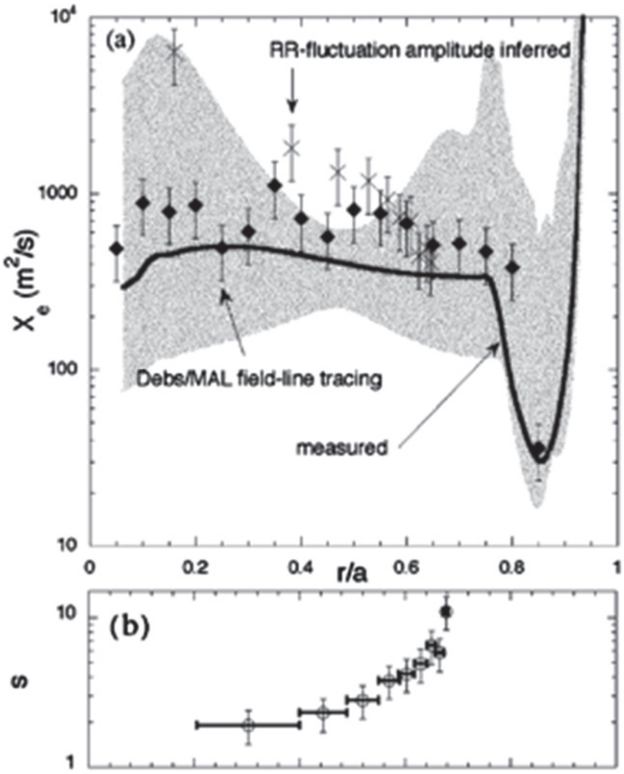

Figure 22. (a) Measured profile of electron thermal diffusivity, χ_e, in MST (solid line), compared with stochastic diffusion from field line tracing (diamonds) and with the analytic RR formula equation (4.2) (crosses). The shaded region represents uncertainty in the measured χ_e. (b) The Chirikov stochasticity parameter, s, corresponding to figure 21 (top). Adapted figure with permission from [239], Copyright 2003 by the American Physical Society.

s^{-1}, [246]) is in this region that likely remains stochastic. Moreover, weakly chaotic regions with $s \sim 1$ have small thermal leakage and act as confining structures [247, 248].

4.1.1. Multiple helicity regime. The broad spectrum of $m = 1$ and $m = 0$ tearing modes in the MH regime allows for the appearance of many magnetic islands on resonant surfaces that span the minor radius of the plasma. As an example, the top panel of figure 21 shows the safety factor profile, $q(r)$, for a typical MH plasma in MST, with the widths of the largest $m = 1$ magnetic islands indicated by horizontal lines, each centred on its resonant surface, r_{mn}. The bottom panel shows the electron temperature profile measured at a time between discrete relaxation events, which is flat in the core. The island widths are estimated using the amplitudes of the radial magnetic fluctuations, $b_{r,mn}(r_{mn})$, calculated by the nonlinear 3D MHD code DEBS [174] but scaled to match the fluctuation amplitudes measured at the plasma surface. The amplitudes in the simulations are larger than in the experiment by a factor $\sim$1.7 [239].

The electron heat diffusivity, $\chi_e(r)$, in the plasmas represented by figure 21 was measured using global power balance [239], shown as the solid line in figure 22(a). Two comparisons with the predicted stochastic heat diffusivity, $\chi_{RR}(r)$, are overlaid. Analytic values of χ_{RR} using equation (4.2) based on $b_{r,mn}(r_{mn})$ and fixed correlation length, L_{ac}, are shown as crosses at the resonant surfaces, r_{mn}, for the largest $m = 1$ modes. These analytic values of χ_{RR} agree reasonably well with χ_e near midradius, $r/a \geqslant 0.6$, but they significantly overestimate the heat diffusivity near $r = 0$. The points plotted as diamonds are for a more native calculation of $\chi_{RR} = v_{e,th}D_m$ based on the magnetic diffusion, $D_m = \Delta r^2/2\Delta L$, determined from an ensemble of direct field line tracings in the 3D field provided by the DEBS simulations noted above. Magnetic diffusivity, D_m, measures the average radial excursion, Δr, of field line trajectories over length, ΔL, along the field. This direct evaluation of χ_{RR} agrees well with the measured $\chi_e(r)$. The analytic RR formula assumes the magnetic field is fully stochastic. This requires large values for the Chirikov parameter, s, which are shown in figure 22(b) for the data corresponding to figure 21. Evidently, $s > 5$ is required for an accurate estimate using equation (4.2), which is why the analytic values fail for $r/a \leqslant 0.6$ where $s \approx 1$. These comparisons highlight that it is local island overlap that regulate magnetic diffusion. As another example of this, since the magnetic fluctuation amplitudes of modes resonant in the edge region of MST plasmas are small, stochastic transport vanishes in the outer region near the $q = 0$ surface [249], despite a sizeable MP from modes resonant deep in the core that can advect field lines but do not cause them to become stochastic.

The radial profile of the electron thermal diffusivity χ_e has been analysed in various experiments by expressing $\chi_e \propto (\tilde{b}/B)^{\alpha}$, as inspired by the RR scaling: while a dependence on magnetic fluctuations has been confirmed in all devices, the α exponent has not always been found to be 2 as in equation (4.2). In RFX and RFX-mod, where electron and ion temperatures are close [85], steady state analyses of the electron thermal transport adopted a single fluid approach. An effective thermal diffusivity χ_{eff} has been calculated, whose dependence on the magnetic fluctuations has been found to be $\chi_{eff} \propto (\tilde{b}/B)^{1.4}$ [63, 64]. This result has been interpreted by a model taking into account the effect of mode spectrum on field line stochasticity [250].

A perturbative approach was applied to evaluate the thermal diffusivity in the TPE-RX device, based on the analysis of the radial propagation of a cold pulse during pellet injection [251]. In the scaling with magnetic fluctuations $\alpha \sim 1$.

Nonlinear MHD computations of the electron energy transport in a stochastic field were also applied to characterize energy confinement in MH RFPs. When using the classical parallel electron thermal diffusivity to estimate the parallel heat diffusion, the experimental energy confinement scaling was well reproduced [252–254].

Analysis of ion energy transport is complicated by the fact that ion heating from magnetic reconnection and turbulence is very powerful in RFP plasmas. In both MST and RFX plasmas, the ion temperature is a large fraction of the electron temperature. In MST the ion temperature can even exceed the electron temperature during sawtooth relaxation events, which is not expected for collisional relaxation of an ohmically heated plasma [255]. Non-collisional ion heating is discussed further in section 4.4.

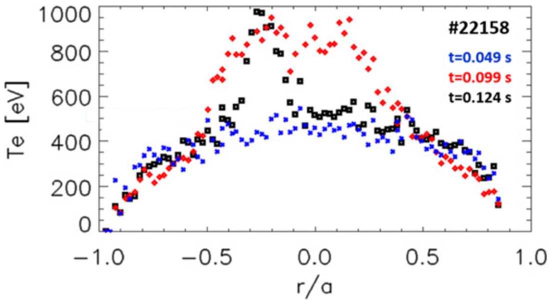

Figure 23. Comparison of the electron temperature profile in RFX-mod QSH (black squares QSH-DAx, red diamonds QSH-SHAx states) and MH (blue squares) plasmas.

4.1.2. Quasi single helicity states. To highlight the effect of the magnetic equilibrium, figure 23 compares the electron temperature profiles measured by the Thomson scattering diagnostic in MH, QSH-DAx and QSH-SHAx in an RFX-mod plasma. Data refer to three times during the same plasma discharge. As described in section 2.3, the QSH-DAx state (black squares) corresponds to the development of a hot island involving a small fraction of plasma radius. When the magnetic separatrix is expelled and the transition to a QSH-SHAx state occurs, the hot island becomes wider and encompassed by strong electron temperature gradients (red diamonds), establishing an electron thermal transport barrier (eITB) [102, 108, 109, 256, 257]. In agreement with the theoretical description [112], a threshold has been found for the occurrence of the transition QSH-DAx/QSH-SHAx, which is observed when the dominant mode amplitude, normalized to the edge magnetic field, is larger than about 3%–4%. The amplitude of secondary modes is another important parameter that determines the appearance of wide helical structures. In particular, the widest thermal structures are found at the lowest amplitudes of the two innermost secondary modes resonant according to the helical safety factor: i.e. the $m = 1$, $n = -8$ and $m = 1$, $n = -9$ in RFX-mod, as can be seen in figure 24 [258].

In RFX-mod QSH-DAx states the heat diffusivity in the temperature gradient region ranges between 6 and 35 $m^2\ s^{-1}$, approaching the tokamak range. Despite the small size of the island, the global electron confinement time τ_E is higher than in MH states (by about a factor 2), about 1.3 ms [259]. Simulations of test ion and electron transport show the average diffusion coefficients inside the helical core to be about one order of magnitude lower than those found in MH plasmas [260]. When QSH-DAx states are stimulated by a helical edge magnetic field (see section 2.2.3), the magnetic chaos decreases too, involving the region outside the island, and allowing for a global enhancement of confinement by about 50% [261]. Indications of improved electron energy confinement have been found in TPE-RX [262].

The thermal diffusivity inside a magnetic island $m = 1$, $n = 6$ close to the axis (QSH-DAx) has been measured in MST, showing flat temperature profiles with rapid parallel heat conduction along helical magnetic field lines in-between the reconnection events. Instead, just after a DRE, a temperature gradient develops inside the $m = 1$, $n = 5$ island, when the $m = 1$, $n = 5$ mode may briefly come into resonance near the magnetic axis. This suggests local heating and relatively good confinement within the island [263].

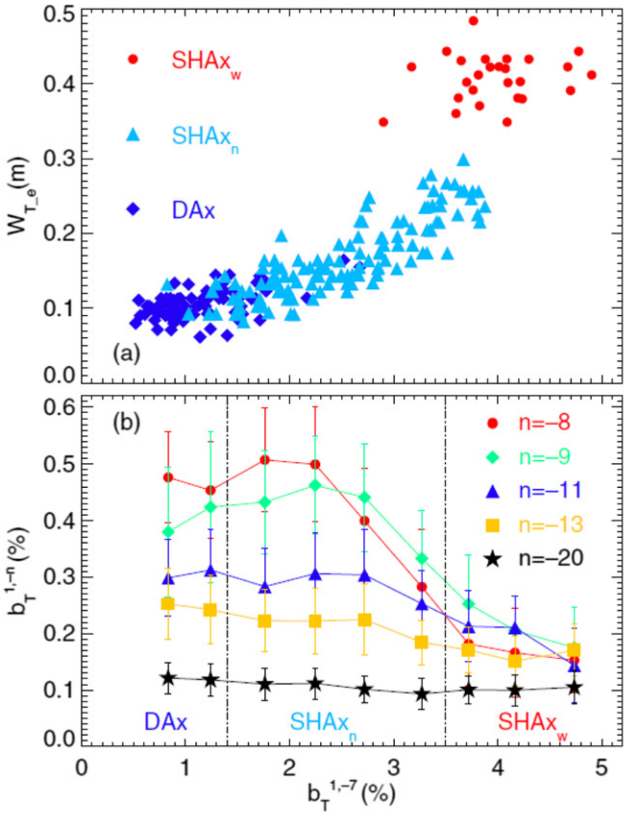

Figure 24. (*a*) Thermal structure width versus the dominant mode amplitude $b_T{}^{1,-7}$. (*b*) Ensemble-averaged amplitude of selected secondary modes versus $b_T{}^{1,-7}$. Reprinted figure with permission from [258], Copyright 2016 by the American Physical Society.

Regarding the confinement in QSH-SHAx states, in MST the global energy confinement improves by about 50%. A three-fold improvement in confinement is obtained by forcing a slow decay of the plasma current [105]. In RFX-mod, where extensive experiments and analysis involving QSH-SHAx states have been carried out, the eITBs encompassing the wide central island are characterized by an electronic thermal diffusivity lower than 20 $m^2\ s^{-1}$, with minimum values as low as 2 $m^2\ s^{-1}$. Such a value of χ_e, though still higher than the classical one (under 1 $m^2\ s^{-1}$), is much lower than outside the barrier or in MH states, where it ranges around 100 $m^2\ s^{-1}$ [264–266]. Both thermal diffusivity and electron temperature gradient length scale with the total amplitude of the secondary $m = 1$ modes [257, 267]. So does the inverse of the maximum electron temperature gradient [103, 267]. These scalings indicate a strong link between the level of magnetic chaos and the strength of the barrier.

The DKES/PENTA codes [268, 269], developed for stellarators, have been applied to the RFP for local neoclassical computations of the thermal diffusion coefficients with electron density and temperature profiles typical of an RFX-mod QSH-SHAx plasma. A comparison with power balance estimates shows that residual chaos due to secondary tearing modes and small-scale turbulence still contributes to drive anomalous transport in the barrier region [137].

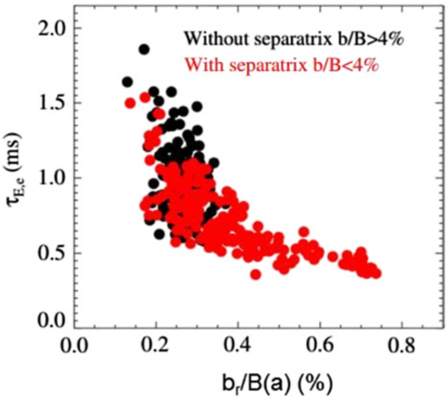

Figure 25. Electron energy confinement time as a function of average secondary mode amplitude in RFX-mod; black points correspond to QSH-SHAx states, red points to QSH-DAx states. Reproduced courtesy of IAEA. Figure from [272]. Copyright 2009 IAEA.

It has to be mentioned, though, that in helical states the electron temperature gradients show a time behaviour not necessarily related to the dynamics of secondary modes [265]. The highest gradients (above keV m^{-1}) occur in the rising phase of the QSH state, and start decreasing (0.5–1 keV m^{-1}) before the destabilization of secondary modes [103]. Despite this intermittent behaviour of eITBs, there are examples of long-lasting eITBs, up to 18 ms in deuterium plasmas, in particular with QSH stimulated by 3D MPs externally applied [121].

In RFX-mod, in QSH-SHAx states the highest τ_{Ee}'s values are obtained. This is shown in figure 25, where a clear relation between the electron energy confinement time and the secondary mode amplitude appears [103, 104, 270–272]. This is also found in a three parameter fit of the energy confinement time with plasma current, average density and amplitude of secondary modes b_{r}, which yields a scaling $\tau_{\mathrm{Ee}} \approx I^{0.81\pm0.02} \langle n_{\mathrm{e}} \rangle^{0.28\pm0.02} b_{\mathrm{r}}{}^{-0.88\pm0.0}$ (figure 26) [273]. This result strongly motivates the upgrade of the RFX-mod magnetic front-end presently under implementation [20], whose main aim is to obtain a decrease of b_{r} by moving the plasma edge closer to the thin shell.

As yet, spontaneous helical states are observed at relatively low plasma densities, $n/n_{\mathrm{G}} \leqslant 0.35$ [274]. Such a limit has been related to the effect of an anomalous viscosity due to microturbulence which can act outside the reversal region [211, 271, 275].

To interpret the flat temperature profile of the hot region encompassed by the temperature gradients in QSH-SHAx states, transport related to self-consistently generated vortical drift motions due to electrostatic turbulence was proposed in [276].

4.2. Particle transport and confinement

In the RFX device, an interpretative analysis of the electron density profiles measured by the 13 chord two colour interferometer [277] in MH plasmas yields a particle diffusion coefficient of $\approx$10–20 $m^2\ s^{-1}$ in the core decreasing to about 5 $m^2\ s^{-1}$ towards the edge. The same analysis also indicates the presence of a particle outward pinch, necessary to

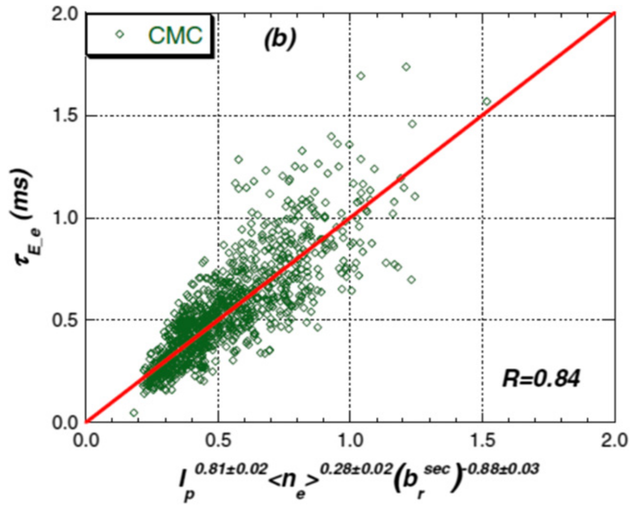

Figure 26. Electron energy confinement time scaling laws for RFX-mod discharges. Three-parameter fit with plasma current, average density and amplitude of radial field modes ($m = 1$, $n = -15$ to -8) measured at the plasma edge. Reproduced courtesy of IAEA. Figure from [273]. Copyright 2009 IAEA.

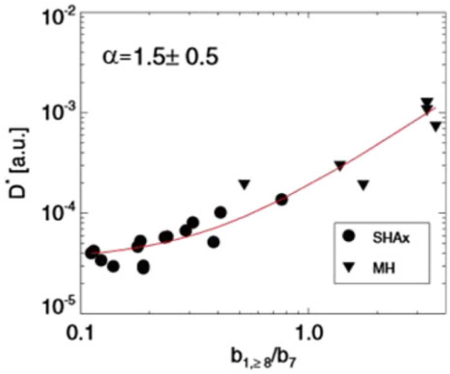

Figure 27. Effective core particle diffusivity normalized to the ion thermal velocity as a function of the ratio between secondary and dominant modes. Reproduced courtesy of IAEA. Figure from [279]. © 2015 EURATOM.

reconstruct the hollow or flat experimental profiles [278]. The ratio of thermal to particle diffusivities turns out to be consistent with RR theory in the core. A subsequent analysis carried out in RFX-mod both in MH and QSH plasmas also yields $\chi/D = \left(m_{\mathrm{i}}/m_{\mathrm{e}}\right)^{1/2}$ and a dependence $D^* \propto (\tilde{b}\big/B)^{1.5}$ (with D^* core diffusivity normalized to the thermal velocity) [279]. This implies that, though residual magnetic chaos remains the main drive for particle transport also in QSH plasmas, the diffusion coefficient is lower, as expected, due to its dependence on magnetic fluctuations: figure 27 shows that the same power law is able to describe the behaviour of D^* in both MH and SHAx states, with $\alpha = 1.5$ in equation (4.2).

The fact that in RFX and RFX-mod the scaling of particle diffusivity is weaker than in RR theory has been related to a sub-diffusive nature of transport. In [280, 281] the ORBIT code [130] is applied, showing that the velocity in equation (4.3) can be interpreted as a sub-diffusive correction to the diffusive evaluation of fluxes. Indeed, in RFX-mod the magnetic field is chaotic, but not much above the stochastic threshold, so that hidden structures are anyway present and the RR assumption of random phase approximation and fully isotropic stochasticity might be questionable.

Simulations in [282] predict a strong improvement of particle confinement in QSH with respect to MH. This has been experimentally confirmed in several devices: in TPE-RX, the transition from MH to QSH came with an enhancement of the particle confinement time τ_p by about 30% [283]. The improvement was confirmed in RFX-mod, in particular by using pellet injection [26]. A pellet entering the central hot region in a QSH-SHAx plasma induces a higher density with a possibly peaked profile, which triggers both an enhancement of τ_{Ee} by a factor 2 to 3, and an increase of τ_p, with a maximum value of 12 ms obtained at 1.5 MA [26].

Single particle trajectory numerical studies applied to RFX-mod plasmas show that, while passing particles are confined for a very long time, particle trapping dominates transport across the helical structure at the rather low collisionality of QSH regimes. The neoclassical diffusion coefficient is one order of magnitude larger than the classical one [260, 284, 285]. When trapped particles drift out of the helical core, at $r/a \approx 0.6$, they become almost passing without being lost, because the helical distortion decreases when going outwards. This results in a very low population of superbanana particles at the experimental levels of helical magnetic field (about 10% of the total) [286]. Therefore, transport is proportional to the collision frequency, in contrast with unoptimized stellarators where the lower bound of transport scales inversely with this frequency [286]. The diffusion coefficients computed by this approach were confirmed by local neoclassical transport calculations including the radial electric field.

The computation of single particle trajectories exhibits a different influence of helical states on main gas and impurity transport [260]. Several studies of impurity transport have been carried out, both in MST and in RFX and RFX-mod (see for example [287–290]). In MH regimes the experimental impurity diffusion coefficient is around 10–20 $m^2\ s^{-1}$, and the convective term in equation (4.3) is outward, in both experiments. An example for RFX-mod is given in figure 28. These values are larger than those predicted by the stochastic model (also shown in the figure). The analysis of impurity behaviour in RFX-mod QSH states shows that inside the core region the confinement of impurities does not increase, which makes unlikely their central accumulation [272]. A core impurity diffusivity one order of magnitude higher than at the edge has been estimated [291], with an outwardly directed pinch velocity over the whole plasma featuring a strong maximum around the core/edge transition point of the diffusivity, much wider than in MH.

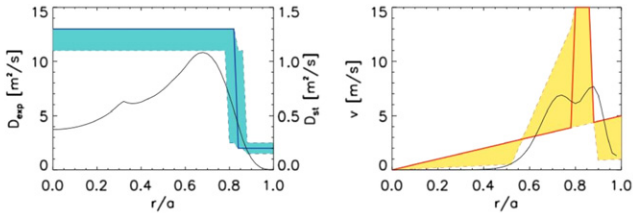

Figure 28. Carbon diffusion coefficient (left) and pinch velocity (right) in RFX-mod MH; blue and red lines are the experimental values, obtained by the combination of measurements with the simulation by a collisional-radiative 1D transport code; coloured areas are the estimated uncertainties in the determination. Black solid lines are the values computed according to the stochastic theory. Reproduced from [287]. © 2015 EURATOM.

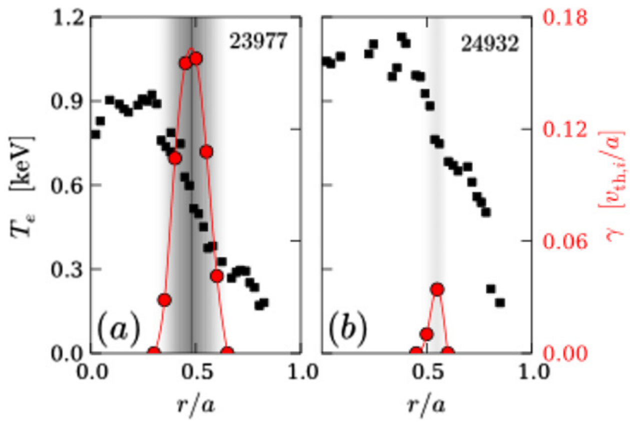

Figure 29. Growth rate of the most unstable MT mode as obtained for two RFX-mod plasmas by the GS2 code modified to include the RFP geometry. The grey tone corresponds to the mode growth rate. Reprinted figure with permission from [298], Copyright 2010 by the American Physical Society.

4.3. Effect of microinstabilities

Gyrokinetic numerical simulations and analytical analyses have been applied to study the role of microturbulence as a driving mechanism of transport in the RFP. In axisymmetric configurations, the ITG mode threshold is larger than in the Tokamak by a factor R/a, due to a strong Landau damping related to short field connection lengths of plasmas acting in low-q configurations [292–294]. In addition, non-linear calculations show that in axisymmetric plasmas the impact of residual zonal flow, beneficial in controlling ITG, can be strong [295]. The threshold for ITG stability decreases in helical states, because of the enhancement of temperature gradients in the outer part of the helical deformation where magnetic surfaces are close-packed [295]. Therefore, ITG turbulence might be an important contributor to the total heat transport in helical states, also in combination with a decreased impact of the stochastic transport related to magnetic chaos. The stability of ITG modes might be further decreased in the presence of strongly outwardly peaked impurity profiles [296]. However, quasilinear and nonlinear three-species simulations of ITG turbulence prove that the inward impurity flux corresponding to a strong ITG would not be compatible with the measured positive impurity peaking [297].

Linear gyrokinetic simulations of RFX-mod QSH-SHAx states show that microtearing modes are unstable at the eITB, as shown in figure 29. For the strongest eITB's, quasi-linear estimates of the associated transport show MT-driven thermal transport to be comparable to the experimental one [298]. It has to be noted that MT modes have actually been experimentally observed in RFX-mod helical states, with amplitude well correlated to the electron temperature gradient [299].

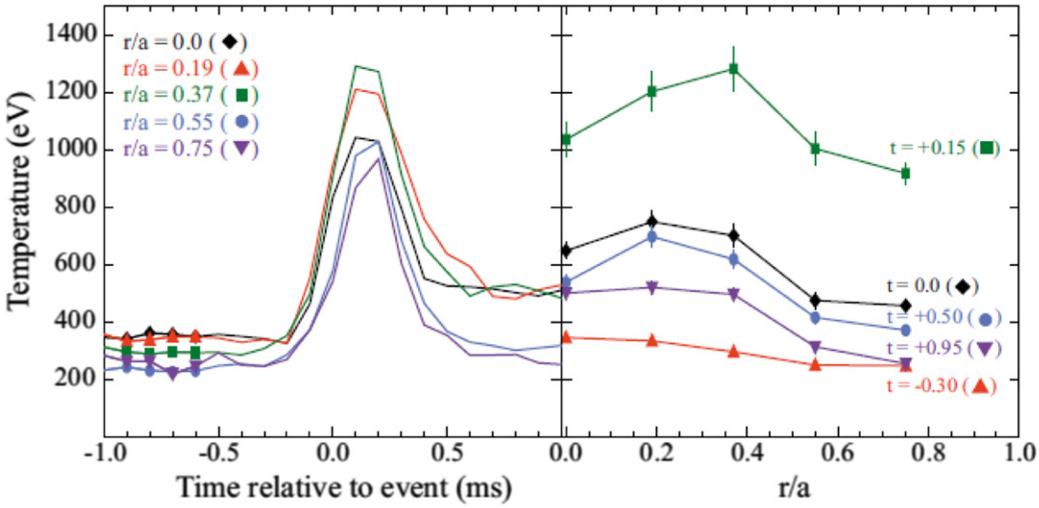

Figure 30. The impurity ion (C^{6+}) temperature measured by CHERS in MST plasmas during a reconnection event ($I_p = 390$ kA, $n_e = 10^{19}$ m^{-3}): (left) time evolution relative to the sawtooth crash time ($t = 0$) at five radial locations; (right) radial profiles of the ion temperature at five different times during the sawtooth cycle, showing that the heating is global. Reprinted from [307], with the permission of AIP Publishing.

Microturbulence has been modelled for MST plasmas with a focus primarily on plasmas with inductive current profile control (PPCD) [300–302]. The ITG and MT channels have been analysed, and the role of finite β, already well known in the tokamak [303], has been elucidated for the RFP, with ITG unstable at low β (vanishing around $\beta = 6\%–10\%$) and MT unstable at high β. For PPCD plasmas, density-gradient-driven trapped-electron modes (TEM) are the dominant microinstabiliy, shown to be in good agreement with experimental measurements. This is discussed in chapter 6.

The occurrence of collisionless MT instabilities has been studied in RFX-mod [304] and MST [301], indicating that the high magnetic drifts in the RFP could favour such microinstabilities.

4.4. Non-collisional ion heating and effect of discrete reconnection events

As described in chapter 2, DREs occur in both MH and in QSH plasmas, and in the latter they correspond to a back transition to the MH state. In MST plasmas, the stored magnetic energy released during a DRE is 10%–30%, with an instantaneous power that can exceed 10 MW. Recently, the same kind of evaluation has been made for RFX-mod back transitions QSH/MH, where it is estimated that 30%–40% of the stored magnetic energy is released during reconnection and does not contribute to ohmic plasma heating [114].

A large fraction of the magnetic energy released during reconnection events is converted into ion thermal energy, heating the ions to high temperature 1–3 keV [255, 305–307]. An example of the time behaviour of ion temperature during a DRE in MST is given in figure 30. Detailed studies of ion heating in MST plasmas reveal that it is charge and mass dependent [308, 309] anisotropic in space with $T_{i,\perp} > T_{i,\|}$ [310] and an energetic ion tail forms spontaneously with a power-law distribution [310].

Several theories have been proposed to explain the ion heating and acceleration mechanisms. The leading candidates are ion cyclotron damping in a turbulent cascade [311, 312], and stochastic heating [308]. Both mechanisms tend to heat anisotropically with $T_{i,\perp} > T_{i,\|}$, a key heating characteristic. The turbulent cascade, driven by large-scale tearing, exhibits non-collisional dissipative features suggestive of a kinetic process consistent with the observed ion heating [313, 314]. While the drive is MHD tearing, the cascade exhibits drift waves and is not purely Alfvénic, either through nonlinear coupling or independent drift instability [315]. The RFP's turbulent cascade, coupled to strong ion heating, represents a grand challenge for multiscale modelling that spans self-organization on the global scale to non-collisional dissipation at the microscale. Viscous heating has also been evaluated, but it is more difficult to make rapid, and therefore powerful [316]. The energetic ion tail is formed, in part, due to runaway ion acceleration [317, 318]. A large inductive electric field accompanies the flux change driven by reconnection, which exceeds the Dreicer electric field for ions.

Temperature profiles as measured by multi-chord SXR tomography in MST tend to peak before and flatten after the crash [41, 319]. In the crash phase an outward propagating heat pulse is detected, allowing to quantify the presence of stochasticity due to the multiple $m = 1$ modes [320].

In order to investigate the effect of DREs on electron thermal transport, a time dependent model has been applied to RFX-mod and EXTRAP-T2R MH plasmas [321, 322]. The χ_e radial profile is divided into three regions: (a) the core, where $\chi_e = k_1(\tilde{b}/B)^{1.4}$ is assumed; (b) the reversal region, with $\chi_e = k_0$; (c) the edge region, where a much higher diffusivity is assumed. Figure 31 shows an example of the χ_e profile reconstructed before and after a DRE [321], with enhanced core thermal diffusivity just after the DRE. The same model also gives good agreement with the experiments when applied to the EXTRAP-T2R MH plasmas [321]. Experimentally, as

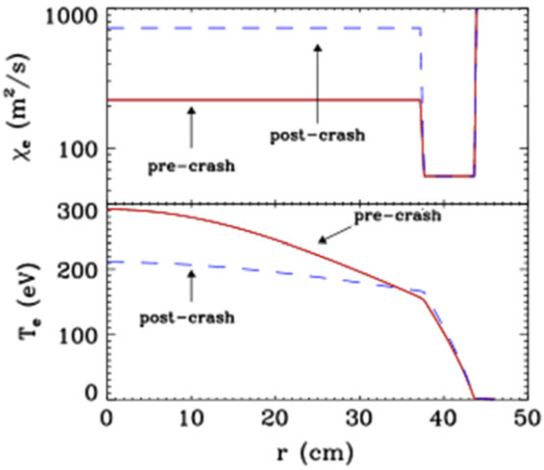

Figure 31. Simulation of electron temperature and thermal diffusivity profiles before and after a DRE in RFX-mod. Reproduced courtesy of IAEA. Figure from [321]. Copyright 2008 IAEA.

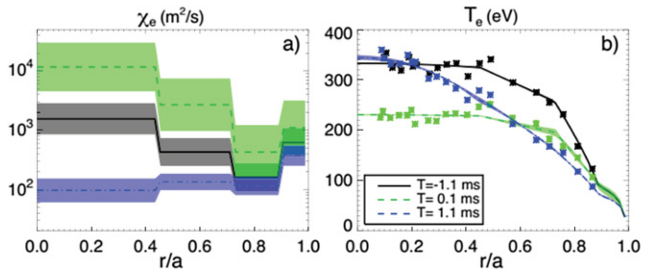

Figure 32. Electron thermal diffusivity (*a*) and temperature (*b*) in MST at three times. Black: 1.1 ms before a DRE, green: 0.1 ms after DRE; blue: 1.1 ms after DRE. Reprinted figure with permission from [323], Copyright 2011 by the American Physical Society.

reported in [51], enhanced non axisymmetric particle losses are observed in RFX-mod during DRE localized at the toroidal angle where MHD tearing modes lock in phase and to the wall.

The analysis by Biewer described in section 4.1.1 was performed for a time point midway between reconnection events. Later the analysis was applied to the full evolution of the sawtooth cycle [323], summarized in figure 32. This included a large ensemble of DEBS simulations that matched experimental parameters as closely as possible. The best agreement between experiment and modelling includes a neoclassical enhancement ($\sim 2\times$) of the parallel electrical resistivity associated with trapped electrons. The inboard-outboard mirror in a toroidal RFP equilibrium is comparable to that for tokamak plasmas of similar aspect ratio [62], but drifts are mostly in-surface for the RFP, and perpendicular neoclassical transport enhancement is negligible [324, 325]. Since trapped electrons are not free to travel long distance along field lines, the stochastic heat conductivity is reduced, $\chi_e = f_c v_{th,e} D_m$, where f_c is the fraction of passing particles, and D_m is the previous stochastic magnetic diffusivity. This reduction in heat transport is likely important in astrophysical plasmas that contain turbulent magnetic field.

The thermal diffusivity inside a magnetic island close to the axis has been measured in MST, showing flat temperature profiles with rapid parallel heat conduction along helical magnetic field lines in-between the DREs. Instead, just after a DRE,

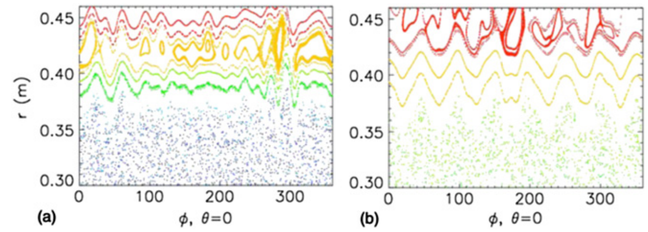

Figure 33. Poincaré plot in the r–ϕ plane of the magnetic field lines in RFX-mod MH (*a*) and QSH (*b*) plasmas. Reproduced courtesy of IAEA. Figure from [243]. Copyright 2009 IAEA.

a temperature gradient develops inside the island, suggesting reduced thermal transport [263].

Magnetic fluctuation induced particle transport and density relaxation in the core of MST plasmas was measured using advanced interferometry-polarimetry [326]; the particle flux is non-ambipolar in the DRE, which implies the formation of zonal flow [327, 328].

4.5. Edge transport and turbulence

The $m = 0$ island chain which develops at the field reversal surface strongly influences the edge transport, both in the MH and QSH state. Tearing modes, which are certainly detrimental for confinement when producing intense magnetic chaos in the $q > 0$ region, have also a secondary positive effect, allowing for the formation of good magnetic surfaces close to $m = 0$ islands, which indeed act as a transport barrier and have a direct impact on plasma pressure profile [242, 281]. An example is given in figure 33.

The change in the pressure profile, whose gradient increases when the magnetic shift is outward [329], influences the edge turbulence. In particular in RFX-mod it is found that the radial correlation length of the fluctuations increases with the characteristic radial pressure length, indicating that the latter drives the radial dimension of turbulent structures [329].

In fact outside the reversal surface transport is mainly driven by electrostatic turbulence and, similar to tokamak and stellarator, is characterized by a highly sheared $v_{E\times B}$ flow [30, 31, 249, 330–332]. The heat transport driven by electrostatic fluctuations was measured in the REPUTE experiment in the region $a/2 < r < a$ [333] and in the edge region of MST [334]. In both devices, it was found that the energy transport driven by electrostatic fluctuations was relatively small with respect to the total heat loss, though in MST the particle flux were found to be comparable to the total particle loss. In particular, in [333] an evaluation of the particle and energy flux driven by stochasticity was given, which was subsequently interpreted by a model calculating the ion and electron fluxes under the ambipolar constraint [335]. Experiments on the EXTRAP-T2R device showed that Reynolds stress, driving the $E \times B$ flow against anomalous resistivity, features a high gradient in the edge region where the flow shear is large, and is mainly related to the electrostatic component, despite the high magnetic fluctuations in this region [336, 337]. Coherent structures emerge as bursts in the turbulent background, with rotation direction determined by the local velocity shear: in RFX and EXTRAP-T2R they have been identified as dipolar and monopolar vortices, contributing by about 50% to the radial diffusivity [338]. The statistical properties of such turbulence share common features with other magnetic configurations [339].

The edge electromagnetic turbulence measured in RFX-mod when operated as an RFP and as a tokamak has been compared [340, 341]. Electrostatic fluctuations in both configurations reveal a strong degree of intermittency with very similar scaling of the shape of the PDF of fluctuation increment, while magnetic fluctuations behave differently, with a lower degree of intermittency in the tokamak case, consistent with the lower β. In particular, the study of turbulence in the scrape off layer of RFX-mod when operated as a tokamak allowed the validation of the GIBS code [342, 343].

The edge electrostatic properties are strongly related to the underlying magnetic topology. When 3D non-axisymmetric MPs are applied in RFX-mod to stimulate QSH states (section 2.2.3), though they have a main $m = 1$ periodicity, at the edge the flux induced by electrostatic turbulence results to be modulated by an $m = 0$ magnetic island, with an enhancement close to the O-point and a reduction at the X-point; transport is due to fluctuations propagating in the electron diamagnetic drift direction [344]. Also, the connection length to the wall of the edge magnetic field L_{cw} is the result of the interaction between the applied dominant $m = 1$ and the $m = 0$ modes and has a complex structure, responsible for an impure $m = 1$ behaviour observed for floating potential, electron pressure, perpendicular flow, high frequency magnetic turbulence [210]. The edge flow pattern in presence of an MP has been reconstructed and shows a convective cell structure, with the toroidal flow moving to an outer region when the deformation related to the MP (Δ_{MP}) is positive (outwards) and to a more internal one when $\Delta_{\mathrm{MP}} < 0$ [345].

As in the core, at the edge the reduction of tearing mode amplitude is related to an improved confinement: the temperature gradient, which scales almost linearly with plasma current, increases at low secondary mode amplitude, and so does the thermal diffusivity, as shown in figure 34 [243].

Recent research in RFX-mod [346] points out the crucial role of the secondary modes in influencing the plasma performance in QSH (electron temperature and confinement time, particle influx and PWI, radiated power). In QSH plasmas with a well-formed helical state, despite secondary mode amplitude is kept low by the feedback system, a deformation related to a non-stationary locked mode (LM) remains present, similar to MH plasmas [78], though with a strongly reduced size of the displacement (<1 cm). In figure 35 such an LM is observed as an interference pattern (panel (*b*), black curve), which corresponds to two dips of the magnetic field connection length to the wall, L_{cw} (see panel (*a*)). These 'holes' can be seen as homoclinic lobes ('fingers') at two toroidal positions ($\phi \approx 110°$ and $\phi \approx 133°$) [346]. The analysis of RFX-mod data suggests a threshold of $\approx$0.3 in terms of the ratio between secondary locking size and displacement of the helical structure, $S_k = \Delta_{\mathrm{sec}}/\Delta_{1,7}$ to completely avoid the detrimental effect of the secondary mode locking, which is

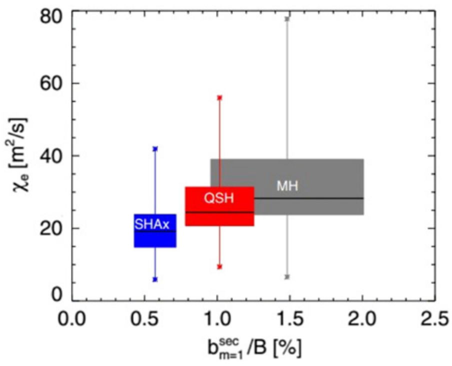

Figure 34. Edge electron thermal conductivity as a function of secondary modes amplitude in RFX-mod; boxes encompass the 25% and 75% percentile of the statistical population of the measured values; bars indicate the minimum and maximum values. Reproduced courtesy of IAEA. Figure from [243]. Copyright 2009 IAEA.

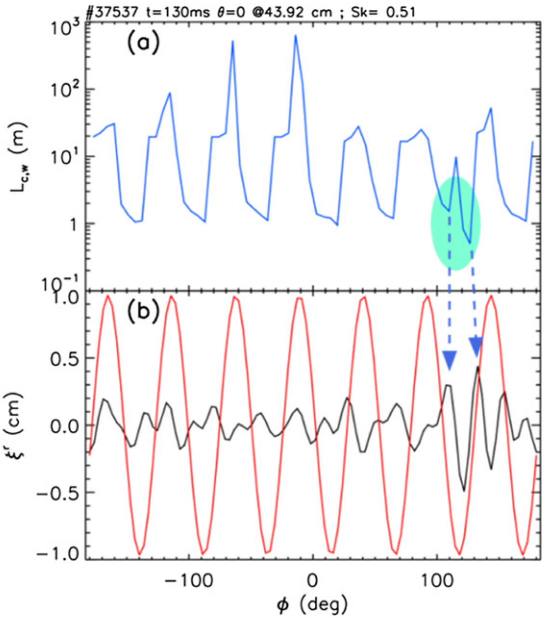

Figure 35. From an RFX-mod QSH discharge: (*a*) magnetic field connection length in the edge (in metres, logarithmic plot) as a function of the toroidal angle; (*b*) displacement of the dominant (red) and secondary modes (black). The arrows indicate the interference pattern at the locking angle. Reproduced courtesy of IAEA. Figure from [346]. © EURATOM 2019.

important in perspective of the RFX-mod upgrade, where a reduction by a factor $\sim$2 in secondary mode amplitude is expected [347].

4.6. Isotopic effect

The comparison of plasmas with hydrogen and deuterium as filling gas carried out in RFX-mod has shown a positive isotopic effect on the confinement of SHAx states similar to the one in tokamaks. For plasma currents around 1.5 MA, the energy confinement time scales as ${m_{\mathrm{i}}}^{0.3}$; the particle influx is significantly reduced and the particle confinement time scales as ${m_{\mathrm{i}}}^{0.45}$. The effect on confinement is mainly due to

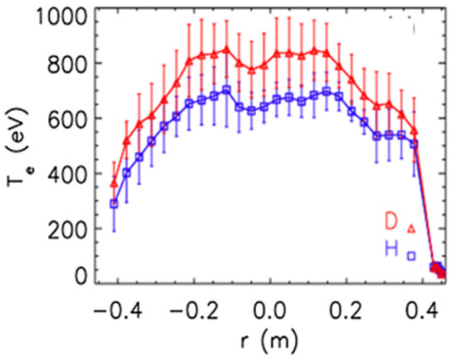

Figure 36. Example of electron temperature measurements obtained in RFX-mod discharges with hydrogen (blue) and deuterium (red) as filling gas at the same electron density. In deuterium, the temperature is higher up to $r \approx 0.365$ m ($r/a = 0.8$). Reproduced courtesy of IAEA. Figure from [348]. © 2015 EURATOM.

the mitigation of transport at the edge [348]. In deuterium plasmas, the electron temperatures are higher by about 0.2 keV over most of the plasma volume ($r \approx 0.365$ m, corresponding to $r/a < 0.8$), as shown in figure 36; the numerical calculation of particle orbits shows that the loss time in QSH regimes is about 1.3 times higher in deuterium than in hydrogen for both spontaneous and induced helical states [121].

4.7. Energetic ion confinement and stability

The confinement of energetic ions is fundamental to fusion energy. A tangential NBI system on MST has allowed detailed investigation of energetic (aka fast) ion confinement and stability in both MH and QSH plasmas. The NBI sources 25 keV, H or D neutrals (varied mixture) with an effective current $\leqslant$40 A and power $\leqslant$1 MW. The NBI pulse is $\leqslant$20 ms. The energetic ion confinement is measured using the 'beam blip' technique, in which a population of fast ions are created in a short NBI pulse, and the decay in d–d fusion neutron emission is observed using scintillation detectors [349]. An advanced neutral particle analyser measures the fast deuterium and hydrogen distributions simultaneously, which reveals dynamics associated with energetic particle driven instabilities [350].

The energetic ion confinement time is consistent with classical slowing down ($\sim$20 ms) and an order of magnitude larger than the thermal particle confinement time ($\sim$1 ms) [349, 351]. Drifts of the fast ion guiding centres carry them off the magnetic field such that they do not experience the magnetic field's stochasticity, even in the MH regime. The drift is quantified using a generalization of the safety factor based on the fast ion guiding centre velocity [349]. The fast ion safety factor is larger than the magnetic safety factor, thus avoiding resonance with the dominant core tearing mode. Interestingly, the fast ion safety factor helps explain stochastic diffusion of fast ions in tokamak plasmas when an $m = 1$, $n = 2$ neoclassical tearing mode is present [352, 353].

For longer duration NBI, classical heating [354] and current drive [355] are observed until the fast ion population reaches a critical threshold at which point both energetic particle modes (EPM) [356] and magnetic-island-induced Alfven

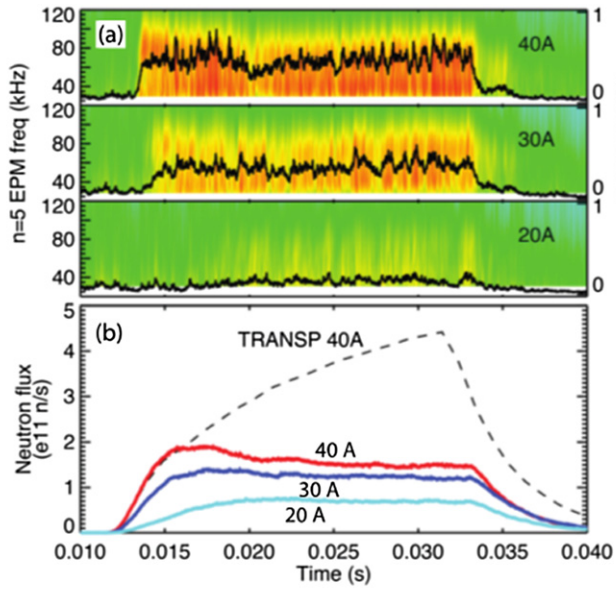

Figure 37. (a) Magnetic fluctuations associated with an $n = 5$ EPM for varying NBI. The injector turns on at 12 ms with fast rise time $\sim$2 ms. (b) The d–d neutron emission corresponding to the cases in (a). The dotted line is the TRANSP-NUBEAM prediction for classical slowing down. Reproduced courtesy of IAEA. Figure adapted from [362]. Copyright 2019 IAEA.

eigenmodes (MIAE) [357, 358] are triggered by saturation of a wave-particle resonance condition [359]. Example behaviour is illustrated in figure 37: the NBI current is increased in steps and onset of EPM activity occurs when the NBI current is >20 A (0.5 MW). The fast ion distribution is modelled using the NUBEAM module in the TRANSP code [354, 360]. The curve labelled 'TRANSP' in figure 37(b) is the expected d–d neutron emission for maximum NBI without loss of fast ions. Density and magnetic field fluctuations measured by an interferometer-polarimeter show that the energetic particle driven modes are nonlinearly coupled and lead to flattening of the fast ion profile during 'fishbone' type bursts, resembling predator–prey dynamics [361]; toroidal Alfven eigenmodes are possible in an RFP plasma, but the beam energy for MST is too low to access the bandgap.

The fast ion profile has been measured using a columnated neutron detector [362]. The corresponding fast ion beta profile is shown in figure 38, with $\beta_{\rm fi}(0) \sim 8\%$. The onset of EPM activity occurs for a critical gradient in the fast ion beta. The profile in figure 38 is the quasi-steady state profile at marginal stability and full beam power. The limit to the fast ion beta is believed to result from the onset of the EPM and MIAE activity, which redistributes the fast ions outward in radius where they are subject to stochastic transport [351, 362]. Central $\beta_{\rm fi} \sim 8\%$ is comparable to the alpha beta expected in a reactor plasma. Also, the 25 keV fast ions in MST ($B < 0.5$ T) have a normalized gyroradius, $\rho_{\rm fi}/a \sim 0.1$, similar to alpha particles in a reactor plasma with $B \sim 5$ T, so the dynamics observed in MST plasmas are likely representative of expectations for alpha particles.

The fast ions have a stabilizing influence on the tearing mode resonant closest to the magnetic axis where the fast ion density is large [357, 363]. This delays the transition from MH

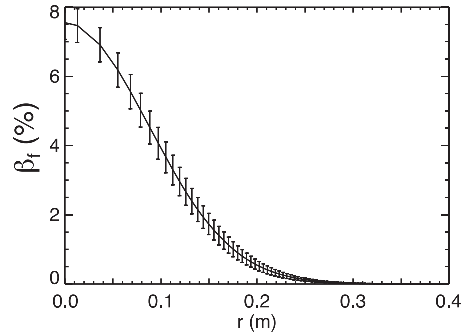

Figure 38. The quasi-stationary fast ion beta profile at marginal stability, measured at $t = 30$ ms for conditions as in figure 26 with full beam power (40 A) in 300 kA MST plasmas. Reproduced courtesy of IAEA. Figure from [362]. Copyright 2019 IAEA.

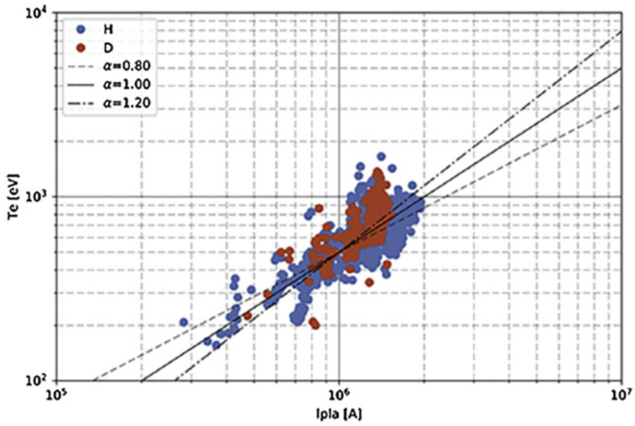

Figure 39. Central electron temperature as a function of plasma current in RFX-mod. Red points refer to deuterium plasmas. Reprinted from [376], Copyright 2018, with permission from Elsevier.

to QSH, and the fast ion confinement is degraded if the secondary mode amplitudes are not reduced [364]. With QSH, the fast ions are born over a larger region in the core as a result of the helical distortion, making them more susceptible to stochastic transport in the mid-radius region. However, if the secondary modes are reduced, which is a key feature of the best performing QSH states, then the fast ion confinement recovers its classical behaviour [351, 365].

4.8. Fast electrons and the kinetic dynamo theory (KDT)

In many RFP experiments, fast electrons have been measured at the plasma edge with parallel energies characteristic of the central temperature [366–370]. In some cases, these electrons carry most of the edge equilibrium current.

The KDT [59] predicts that these electrons can provide the current required to sustain the field reversal if a pre-determined stochastic magnetic field is assumed and transport is given by the RR expression. Self-consistent numerical simulations have shown that kinetic dynamo could sustain a stationary RFP configuration [371], with the fast electrons providing a substantial contribution to the poloidal current in the edge [372].

The presence of fast electrons at the edge is not a unique feature of KDT. Indeed, due to the relatively low edge temperature, the electric field generated by the MHD dynamo can produce significant deviations of the electron distribution from the classical Spitzer–Harm distribution, as measured in the edge of RFX, significantly affecting Langmuir probe measurements [373, 374]. The main difference is that the KDT predicts the suprathermal tails to be much more robust at the edge and less so in the core compared to the MHD dynamo. In RFX the trajectory deflection of frozen hydrogen pellets has been used as a diagnostic of suprathermal electrons in the plasma, showing that the pellet trajectories are better reproduced assuming the distorted electron distribution function consistent with an MHD dynamo electric field than with the fast electron population consistent with KDT modelling [371].

Runaway electrons (i.e. electrons with energies greater than 100 keV) are observed during QSH states in MST, due to their emission of bremsstrahlung hard x-ray photons: the magnetic island provides a region of reduced stochasticity where high-energy electrons are generated and well confined [375].

4.9. Perspectives in the next future

As described in previous sections, both in MH and QSH states the quality of the confinement in an RFP is strictly related to the amplitude of magnetic fluctuations. Moreover, a clear dependence of temperature on current has been documented as in figure 39 [102, 376], though the experiments at the highest current values in RFX-mod have not been carried out in optimized conditions. Based on these facts an upgrade of the RFX-mod device, RFX-mod2, is presently underway, aiming at the experimental study of an RFP plasma at 2 MA with an optimized magnetic front-end (section 7.3), i.e. in condition of reduced effect of tearing modes [114]. Experimentally QSH states, though more persistent at high current, have never been obtained as a stationary equilibrium. Moreover, QSH are more likely to occur and produce transport barriers at low density: still open question is if this is related to a poor control of particle recycling, related to a strong PWI at high current. Due to a milder magnetic boundary, experiments on RFX-mod2 are expected to allow more stationary helical states at higher density and to clarify the effect of microinstabilities in conditions of reduced magnetic chaos.

5. Current profile control

Typically, RFP plasmas are formed and sustained using toroidal induction by the transformer linking the torus. The parallel electric field is therefore peaked in the core, and this destabilizes tearing modes. Nonlinear saturation of the tearing instability creates a dynamo electric field that keeps the current profile close to marginal stability in either the QSH or MH regimes. Since tearing instability results from the peaked electric field, adding current drive in the outer region allows the possibility to attain a tearing-stable current profile. This is referred to as current profile control and involves the addition of one of several possible current drive sources: (1) external field coils, (2) insertable electrostatic current sources, and (3) edge-localized radio frequency (RF) current drive.

The inductive approach using external field coils as transformers has been most successful, leading to a strong reduction in magnetic stochasticity and large improvement of energy confinement in RFP plasmas. Microturbulence emerges when tearing instability is suppressed, suggesting RFP confinement might ultimately be limited by microinstability as it is in tokamak and stellarator plasmas. These advances have been very important for the development of the RFP and for the advancement of toroidal fusion science, e.g., by extending the reach of gyrokinetic modelling.

The theoretical and experimental foundations for current profile control are described in section 5.1. In section 5.2 we describe four inductive techniques, and in section 5.3 we describe measurements of the modified current profile and fluctuation reduction. Improvements in RFP fusion performance and work towards fusion parameter scaling are described in sections 5.4 and 5.5. The emerging role of microturbulence is described in section 5.6. Results with insertable current sources and RF antennas are described in section 5.7. Section 5.8 contains other related routes to improved confinement, and section 5.9 discusses questions and future directions.

5.1. Foundations for current profile control

Comparison between experiment and nonlinear MHD established that the multiple core-resonant modes are current-gradient-driven tearing fluctuations (or resistive kinks), well described by resistive MHD [37, 165], which can stochasticize the magnetic field in the core.

MHD computations demonstrated that these tearing fluctuations could be reduced or even eliminated with a suitable modification of the current profile [158, 377–379]. The essential idea is captured in figure 40 showing results from the DEBS code. On the left are profiles of the plasma current flowing parallel to B. The standard profile corresponds to steady toroidal induction, while the controlled one results from the addition of current in the plasma edge, implemented in the simulations as a localized *ad-hoc* electron force profile. The additional current drive leads to dramatic changes in the core-resonant tearing mode amplitudes, such that stochasticity, is substantially reduced, see figures 40(*b*) and (*c*). The fact that a change to the edge current profile can affect core-resonant tearing modes stems from the global character of these modes, such that they are sensitive to the shape of the current profile everywhere in the plasma. The added current can either be stabilizing or destabilizing, depending on its magnitude and profile (stabilizing in the case of figure 40). The added current drive can be thought of as replacing the dynamo electric field, allowing fluctuations to be reduced or eliminated.

5.2. Inductive techniques

Four approaches to inductive current profile control have been studied experimentally and, in most cases, computationally. All entail temporal variations in the toroidal and/or poloidal magnetic field. Two of them are transient techniques: pulsed poloidal (or parallel) current drive (PPCD) primarily entails a ramp down of the toroidal magnetic field, and self-similar current decay (SSCD) entails a ramp down of both fields.

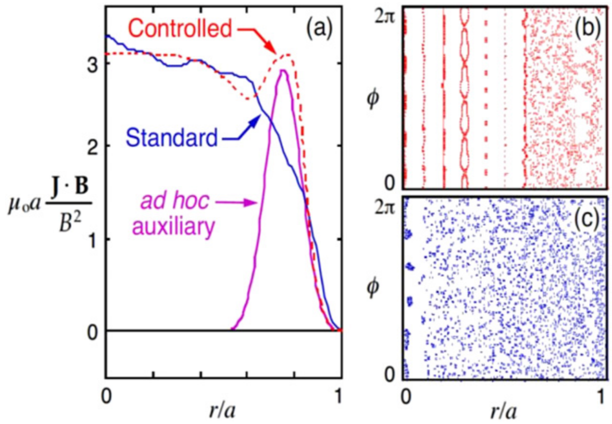

Figure 40. From DEBS code: (*a*) $J_{\|}/B$ radial profile in the standard steady toroidal induction case (blue) compared to the controlled case (red) with an auxiliary ad hoc parallel electron force (magenta). Poincaré plot of magnetic field line in controlled (*b*) and standard (*c*) cases. Adapted from [158].

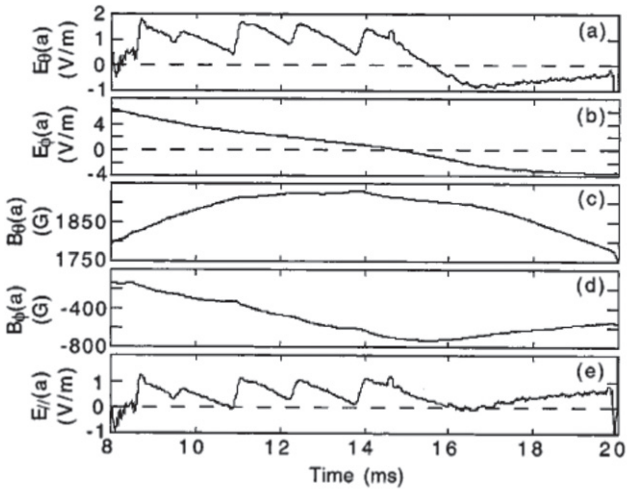

Figure 41. MST 500 kA plasma with PPCD: time evolution of (*a*) poloidal and (*b*) toroidal electric fields, (*c*) poloidal and (*d*) toroidal magnetic fields and (*e*) parallel electric field. PPCD is applied at 8.5 ms. Reprinted from [383], with the permission of AIP Publishing.

The other two techniques are quasi-steady-state. OPCD entails oscillation of the toroidal magnetic field, and OFCD entails oscillation of both fields. The most thoroughly developed of these techniques is PPCD. Hence, PPCD is the primary focus of this chapter. Though less developed than PPCD, OFCD has potentially very interesting implications for an RFP based fusion reactor; it will be separately described in chapter 9.

The PPCD technique was first studied experimentally on MST [380] and computationally in DEBS soon thereafter [378] and in later work [381, 382]. Electric and magnetic field waveforms from one of the highest-performance MST PPCD plasmas are shown in figure 41. Sustained reduction of both $m = 1$ and $m = 0$ fluctuations was found to require $E_{\|} \geqslant 0$, where $E_{\|} = E_{\|}(a) = \mathbf{E}{\cdot}\mathbf{B}/|\mathbf{B}| = (E_\theta B_\theta + E_\phi B_\phi)/|\mathbf{B}|$ is the surface parallel electric field, and the subscripts θ and ϕ refer to the poloidal and toroidal direction [383]. $E_{\|} > 0$ is maintained initially through E_θ via a ramp down in B_ϕ. Later in time, E_ϕ is reversed in order to prolong the control period. The ramp down in B_ϕ brings about a rather extreme RFP equilibrium, with the toroidal field reversal parameter, F, reaching about -2 and the pinch parameter, Θ, reaching about 3.5. In addition to the $E_\parallel$ criterion, the production of high-quality PPCD plasmas is subject to a number of other conditions, e.g., avoiding an overly large E_θ [384], providing a well-conditioned plasma-facing boundary and sufficiently low initial plasma density [383, 385, 386], avoiding sawtooth crashes at the initiation of PPCD [383], and assuring a good control of magnetic error fields and of the LM [383, 387].

The SSCD technique was first considered in two independent theoretical studies [388, 389] in which it was recognized that a particular prescribed self-similar temporal ramp-down of both B_θ and B_ϕ can yield an inductive electric field that maintains an MHD stable current profile. The self-similar solutions are space–time separable such that the equilibrium profiles are stationary in time, while the magnetic flux decay sustains the current with $E_\parallel = \eta J_\parallel$ (no dynamo). The ramp-down rate is proportional to the instantaneous value of the resistive diffusion time, close to the global *L*/*R* timescale. Nonlinear, 3D simulations with SSCD programing yield essentially complete tearing stabilization [390]. The loop voltage programing required for SSCD, originally dubbed 'catching' [388], was first attempted on the HBTX device at Culham, but the results were never published.

The OPCD technique was first tested experimentally on RFX [391] and later examined with a 1D model simulating magnetic field profiles [392]. Entailing a sinusoidal oscillation of B_ϕ, half of each OPCD cycle is PPCD-like in the trajectory of B_ϕ, and magnetic fluctuations can be reduced in an oscillatory fashion.

5.3. Current profile modification and fluctuation reduction

In this section, some examples are provided of the experimental current profile control and of fluctuation responses to current profile control, primarily from PPCD plasmas but also from SSCD. Direct internal measurements of the current profile during PPCD were made possible on MST by a combination of laser polarimetry [393] and 2D RFP equilibrium reconstruction [27]. Figure 42 compares profiles of $\mu = \mu_0 a(J_\parallel/B)$ during PPCD (μ is the same quantity plotted in figure 40) to profiles before and after sawtooth crashes, each of which leads to flattening of the current profile in steady-induction plasmas [53, 394]. Measured with approximately 0.08 m spatial resolution, μ during PPCD falls between the pre-crash and post-crash profile for $r > 0.3$ m, while the PPCD profile is more peaked than either profile in the centre of the plasma. Such peaking was also observed in MHD modelling of PPCD plasmas in RFX with the SpeCyl code [395], showing that during PPCD a significant reduction of MP is accompanied by a shrinking of the magnetic profiles. Measurements of the current profile were also made in the outer 10% of MST plasmas by an inserted probe [396] with 0.01 m spatial resolution. In this region μ *decreases* when PPCD is applied. This result was interpreted as being due to measured drops in the dynamo electric field and the electrical conductivity, the latter resulting from a drop in the electron temperature. Overall, the change in the μ profile is fairly modest with PPCD, but additional measurements in MST showed that there are much larger changes to the inductive electric field profiles [397, 398]. Hence, there is a much greater change in the current drive than in the current density profile, consistent with marginal tearing stability.

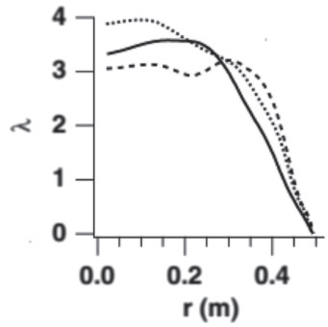

Figure 42. Radial profiles of $\mu = -\mu_0 a J_\parallel/B$ in MST; (solid line) 0.25 ms before a sawtooth crash; (long dashed line) 0.25 ms after a sawtooth crash; (short dashed line) during PPCD. Reprinted figure with permission from [53], Copyright 2002 by the American Physical Society.

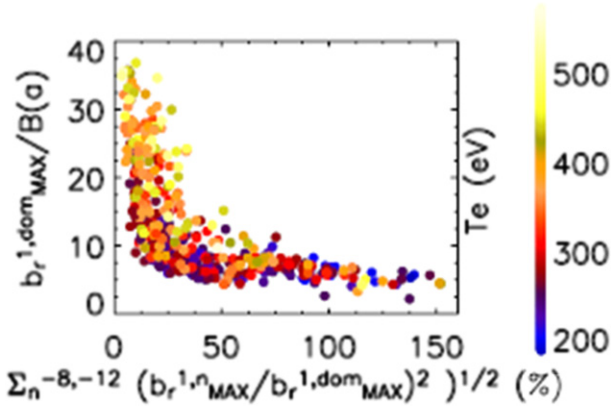

Figure 43. Maximum of the dominant mode as a function of the ratio between the maximum of secondary modes to the maximum of the dominant one (from RFX-mod OPCD discharges. The behaviour of electron temperature is also reported. Reprinted figure with permission from [261], Copyright 2007 by the American Physical Society.

Fluctuation measurements with current profile control are numerous and show a significant drop in magnetic fluctuations. Figure 43, representing data from RFX-mod OPCD plasmas, shows that the innermost resonant (i.e. $m = 1$, $n = -7$) mode gradually increases while the remaining $m = 1$ modes with higher-n decrease, which also corresponds to higher electron temperatures [261]. The reduction of higher-n modes is a feature of plasmas with improved global confinement [397, 399]. While most measurements of magnetic fluctuations are restricted to magnetic sensing coils at the plasma boundary, the polarimeter in MST allowed for first time the measurement of the fluctuation reduction in the core [394, 400] which has been found to be broadband and substantial.

Ohm's law in steady-induction RFP plasmas is balanced by the dynamo electric field, see chapter 3. In plasmas with

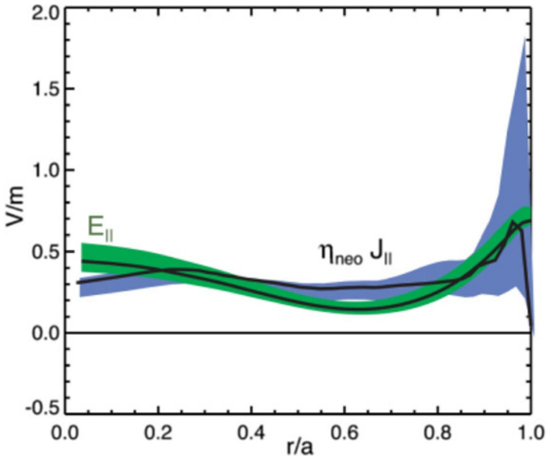

Figure 44. From an MST plasma with PPCD, profile of inductive parallel electric field and product of neoclassical resistivity and parallel current. Reprinted from [398], with the permission of AIP Publishing.

substantial dynamo fluctuation reduction, such as with PPCD, the dynamo electric field becomes small. This was demonstrated by measurements in PPCD plasmas in MST, figure 44 [178, 398]. In this figure, the electric field and resistive current terms in parallel Ohm's law are shown to be approximately equal over the entire plasma, implying that these plasmas are dynamo free. Consistent with the discussion earlier in this section, the $\eta_{\rm neo}J_{\|}$ term does not change much between steady-induction and PPCD plasmas, but $E_{\|}$, along with the dynamo electric field, changes substantially [178, 398].

With the drop in the core-resonant magnetic fluctuations, changes occur in the behaviour of other fluctuating quantities. For example, in the core of MST PPCD plasmas, density fluctuations, measured with interferometry and a heavy ion beam probe, are found to drop significantly [401–403]. Potential fluctuations drop as well, both in the core [403] and in the edge [404]. This is not unexpected given the previously measured correlation between core-resonant magnetic fluctuations and edge-localized potential fluctuations in steady-induction plasmas in the EXTRAP-T1 RFP [405]. There is also a more localized tapering of the fluctuations in MST correlated with a region of strong flow shear (the flow shear is addressed further in section 5.8). Measurements in the edge plasma of MST during PPCD also reveal that higher-frequency magnetic turbulence is much less intermittent and has a statistical behaviour typical of self-similar turbulence, as expected in systems exhibiting self-organized criticality [406]. A similar conclusion was drawn for both magnetic and potential fluctuations in the edge of TPE-RX PPCD plasmas [407].

The reduction in core-resonant tearing fluctuations also brings about an important change to the core magnetic topology. Tomographic x-ray measurements in the core of MST PPCD plasmas revealed two discrete, non-overlapping islands, corresponding to the two innermost resonant $m = 1$ modes [135, 408]. This is shown in figure 45 and is a direct evidence of decreased stochasticity in the core. High-energy runaway electrons also emerge in these plasmas, as described in more detail in the next section, further indicating that stochasticity no longer dominates core transport.

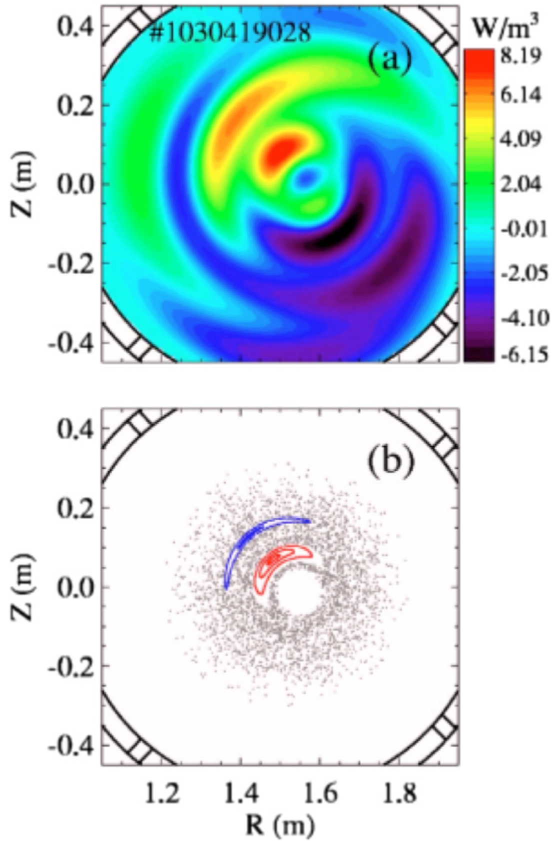

Figure 45. During an MST PPCD plasma showing (*a*) SXR emissivity tomographic reconstruction showing ($m = 1$, $n = 6$) and ($m = 1$, $n = 7$) islands appearing simultaneously in the core and (*b*) the corresponding reconstruction of the magnetic field lines by the ORBIT code. Reprinted from [135], with the permission of AIP Publishing.

5.4. Improved fusion performance

This section describes improvements in fusion performance brought about by SSCD, OPCD and PPCD. Most of the results are from plasmas with PPCD, and with only two exceptions, noted below, the results described here are from ohmically heated plasmas. The papers cited herein contain results from both hydrogen and deuterium plasmas.

The only published test of SSCD occurred in RFX-mod [409]. The simultaneous decay of B_θ and B_ϕ is provided primarily by actively reversing the sign of the surface toroidal voltage. This affects both the toroidal and poloidal current flowing in the plasma. As magnetic fluctuations drop, poloidal beta, $\beta_{\rm p} = 2\mu_0\langle p\rangle/B_\theta^2(a)$ increases by approximately 50% along with the global energy confinement time. A crude approximation of SSCD was also tested on MST without programmable power supplies, with the decay of B_θ and B_ϕ provided passively by the external poloidal field circuit. The energy confinement time in such plasmas is estimated to triple.

The quasi-steady OPCD technique was tested in both RFX [391, 410, 411] and RFX-mod [261]. One signature of OPCD is an oscillation in the central electron temperature, which increases in the PPCD-like half of OPCD cycle and then decreases in the other half. In plasmas with OPCD during the

PPCD-like phase, a transition to a QSH state occurs. A helical T_e structure emerges and the maximum ∇T_e corresponds to an electron thermal diffusivity χ_e of about 10 m^2 s^{-1}. The global energy confinement time increases by about 60% [261].

The PPCD technique has been the most widely applied and studied of the inductive approaches, and it has brought about the most substantial improvements in RFP fusion performance. PPCD has been tested in MST, RFX, RFX-mod, EXTRAP-T2R, and TPE-RX, and it has led to (1) improvements in energetic electron and ion particle confinement and in thermal electron particle confinement, (2) large values of the normalized electron density, substantially exceeding the Greenwald limit, (3) classical confinement of impurity ions, (4) RFP-record values of electron and ion temperature, with a simultaneous reduction in ohmic heating power, (5) an RFP-record beta that exceeds the Mercier criterion, (6) an RFP-record tokamak-like energy confinement time, and (7) the emergence of two new regimes for the RFP, with the prominence of micro-instability in lower-β plasmas and pressure-driven macro-instability in higher-β plasmas. We expand upon these results in what follows.

One of the key PPCD results was the observation of runaway electrons in the core of MST plasmas [412]. In a stochastic magnetic topology, the rate of electron transport increases with the electron velocity. Hence, while the Dreicer criterion for runaway electrons can easily be satisfied in low density RFP plasmas, electrons are lost more and more quickly as they accelerate. Figure 46 contains x-ray bremsstrahlung emission from PPCD and steady-induction plasmas. The rate of overall electron diffusion coefficient to bulk thermal electron diffusion coefficient is $\sim(v_{\|}/v_{\mathrm{th}})^{\alpha}$, where $v_{\|}$ and v_{th} are the parallel and thermal electron velocities, respectively. $\alpha = 1$ corresponds to a diffusion model consistent with stochastic magnetic transport; $\alpha = 0$ allows no energy dependence to the diffusion coefficient, suggestive of diffusion driven by electrostatic fluctuations. The experimental x-ray energy spectrum from steady-induction plasmas is well fitted by an exponential curve with $\alpha = 1$, while the spectrum from PPCD plasmas is well fitted with $\alpha = 0$, indicating that stochastic transport is no longer playing an important role.

High-energy (20 keV) beam-injected ions may also be modestly better confined during PPCD [413]; however, it has to be mentioned that beam ions are already well confined in steady-induction MST plasmas [349].

Thermal electron particle confinement is also improved with PPCD. From measurements in MST, the particle flux decreases everywhere in the plasma, with a drop of almost two orders of magnitude in the core. Correspondingly, the global particle confinement time is estimated to improve eightfold [401, 402]. The rate of particle diffusion also drops by about a factor of two in RFX plasmas [395]. The combination of PPCD and frozen-deuterium pellet injection in TPE-RX brought about an estimated five-fold improvement in the global particle confinement time [414]. Absent pellet injection, the global confinement time improved in TPE-RX by an estimated factor of ten [407, 415].

Frozen pellet injection allows a substantial increase in the density attainable in PPCD plasmas, while retaining reduced fluctuations and improved confinement. Raising the density with edge-deposited fuelling techniques such as gas puffing bring about increased fluctuations and degraded confinement [246, 414, 416, 417]. Pellet injection can fuel the plasma core without substantially impacting the edge or degrading confinement. The synergy between pellet injection and PPCD was first noted in RFX [395, 418], where the density doubled, reaching about 4×10^{19} m^{-3}. Pellet injection into TPE-RX brought about a similar doubling of the density [414], and injection into MST plasmas initially quadrupled the density, surpassing the Greenwald density limit [246, 416, 417]. Shown in table 2 are central densities and densities normalized to the Greenwald limit in MST. Subsequent injection of larger pellets in MST has resulted in an absolute density up to 9×10^{19} m^{-3} and a normalized density up to $\sim$2 [100, 419].

The confinement of impurity ions also improves. In steady-induction RFX plasmas, the impurity particle diffusion coefficient profile drops from 20 m^2 s^{-1} in the core to 1 m^2 s^{-1} in the outer 10% of the plasma. With PPCD, the lower diffusivity region widens to encompass the outer 20% of the plasma [411]. In EXTRAP-T2R, the rate of impurity diffusion decreases by about a factor of two in the core with no change

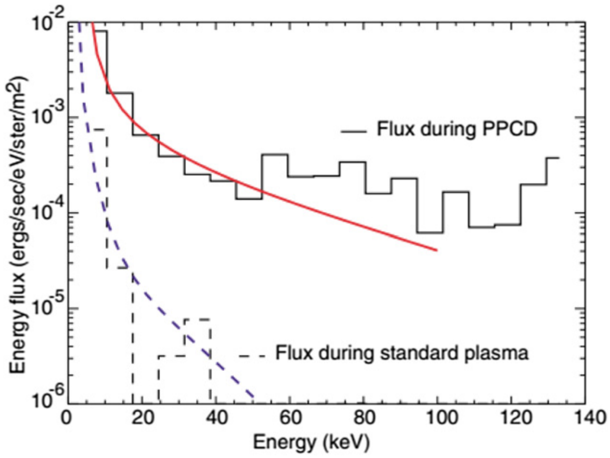

Figure 46. X-ray measurements in MST PPCD and steady induction plasmas. Curves are fits of data with electron diffusion coefficients independent of (PPCD) and proportional to (steady induction) the parallel electron velocity. Reprinted figure with permission from [412], Copyright 2003 by the American Physical Society.

Table 2. PPCD plasmas in MST with and without pellet injection at low (columns 1 and 2) and high (columns 3 and 4) plasma current. Reproduced courtesy of IAEA. Table from [246]. Copyright 2009 IAEA.

	w/o pellets	With pellets	w/o pellets	With pellets
I_p (MA)	0.21	0.17	0.53	0.48
$n_e(0)$ (10^{19} m^{-3})	0.9	3.5	1.2	4
$\langle n_e \rangle / n_G$	0.26	1.2	0.13	0.66
P_{oh} (MW)	1.0	2.2	2.3	4
$T_e(0)$ (keV)	0.6	0.17	1.9	0.7
$T_i(0)$ (keV)	0.18	0.19	1.3	0.6
β_{tot} (%)	15	26	10	17
τ_E (ms)	10	>5	12	7

in the edge [420]. In MST, impurity transport drops down to the classical value [289, 324, 325]. Dominated by Coulomb collisions rather than neoclassical particle drift effects, impurity ions are convected outward, and the impurity density profile, along with the Z_{eff} profile [421], become hollow, consistent with the temperature screening mechanism of classical transport.

One common feature of PPCD plasmas is an increase in the central electron temperature, e.g., [82, 422–426]. This is in spite of the fact that the ohmic heating power commonly drops, e.g., [380, 427]. The largest central $T_{\mathrm{e}} \sim 2$ keV was achieved in MST, table 2 [428]. Neutral beam heating has also been applied to PPCD plasmas in MST, increasing the central electron temperature by about 100 eV [354].

In contrast to electron temperature, the evolution in the ion temperature in low-density PPCD plasmas is typically fairly small. The only localized measurements of the ion temperature in the core of PPCD plasmas were made in MST using neutral-beam-based charge-exchange-recombination spectroscopy. Initial measurements in low density plasmas showed that the central T_{i} changes very little between steady-induction and PPCD plasmas, with a value of about 300 eV in the core of plasmas with a central $T_{\mathrm{e}} > 1$ keV [383]. The ohmic heating power channelled from the electrons to the ions is quite small. A roughly four-fold increase in the ion temperature, to about 1.3 keV (table 2), was achieved by triggering large amplitude sawtooth crashes shortly before the start of PPCD [428]. The ion heat generated during the crashes is trapped in the plasma with the onset of PPCD and the ion energy confinement time is estimated to improve ten-fold. With pellet injection and substantially higher density, the ion temperature increases with time during PPCD plasmas in MST [416]. This is due both to a larger ohmic input power and a larger rate of energy transfer from the electrons to the ions.

Another common feature of PPCD plasmas is an increase in β. There are examples of this from RFX, TPE-RX, EXTRAP-T2R, and MST, e.g. [83, 424, 429, 430]. This will be discussed in detail in chapter 6.

In PPCD plasmas, an increase in the global energy confinement time is observed in all RFP devices. The confinement time in RFX and EXTRAP-T2R as much as doubled [83, 430], while in TPE-RX it increased as much as five-fold [251, 426]. The largest increase in confinement, as well as the largest absolute RFP confinement time was produced in MST. The energy confinement time increased by more than ten-fold, reaching about 12 ms [246, 428]. The global electron thermal diffusivity drops to about 5 $\mathrm{m^2\ s^{-1}}$, with a local minimum of about 2 $\mathrm{m^2\ s^{-1}}$ in the region of large ∇T_{e}. The values of confinement times reached in MST are tokamak-like [397, 399, 428]. This is illustrated in figure 47, where MST standard and PPCD confinement data are compared to a tokamak reference that has the same plasma size, magnetic field strength, and heating power as determined by the IPB98(y,2) empirical confinement scaling for ELMy H-mode tokamak database [431]. This comparison is not meant to imply that tokamak scaling applies equally well to the RFP. Rather it demonstrates that the best RFP energy confinement is comparable to that expected for a tokamak plasma that has the same size and magnetic field.

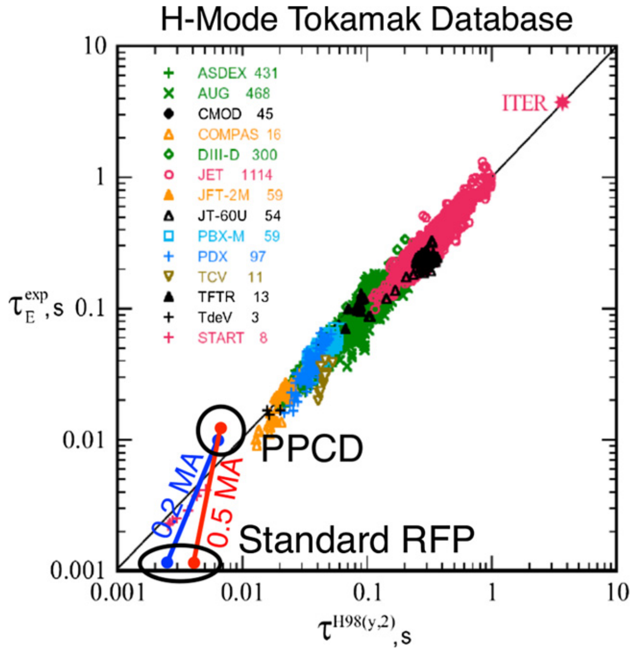

Figure 47. MST confinement time compared to a reference tokamak plasma having the same size, same field strength, and same heating power as specified by the IPB98(y,2) ELMy-H mode empirical scaling. Reproduced from [428].

5.5. Confinement scaling

Considering plasmas with PPCD, for which there are results from multiple RFP devices, there is not as yet a firmly established universal scaling for energy confinement time, although basic parameters such as plasma minor radius very likely play a role. As suggested by figure 40(*b*), even with current profile control there may be regions of the plasma where stochasticity still plays a role in energy transport. In addition, as discussed in the next section, in lower-density (lower-β) PPCD plasmas, micro-scale fluctuations due to instabilities like the TEM may be important, while, as described in the next chapter, in higher-β PPCD plasmas, macro-scale pressure-driven tearing may play a role.

As reported in figure 48, for low-density and high-density PPCD plasmas in MST, the improved energy confinement fell above, and in one case well above, the empirical Connor–Taylor scaling [4] which was based on the best standard-plasma confinement results from a variety of RFP devices [383, 417, 424]. Hence, PPCD plasmas represent a break from the previous trend.

The dependence on the dimensionless Lundquist number S, which was introduced in chapter 2 and varies as $I_{\mathrm{p}} T_{\mathrm{e}}^{3/2}/n_{\mathrm{i}}^{1/2}$, was examined based on data from RFX [63, 64]. While magnetic fluctuations were smaller (and the energy confinement time larger) in RFX PPCD plasmas, the fluctuations exhibited the same amplitude scaling with S as steady-induction plasmas.

The factor by which the energy confinement time improves with PPCD in *low-density* TPE-RX, RFX, and MST plasmas, including results up to 2002, was found to be well represented

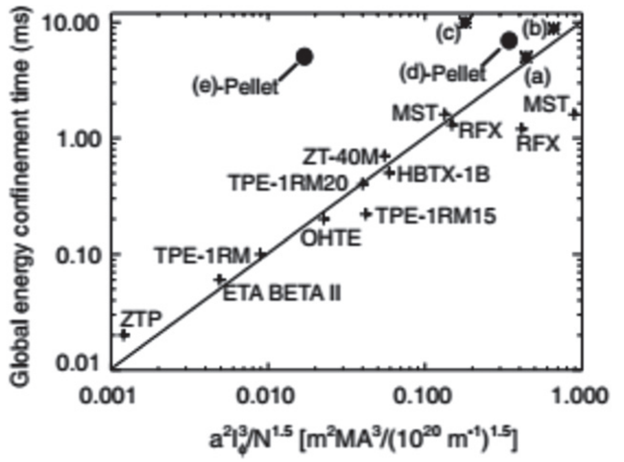

Figure 48. Connor–Taylor scaling of confinement for various RFP devices including steady induction plasmas (+) and PPCD plasmas at low (*) and high (•) density. Reproduced courtesy of IAEA. Figure from [417]. Copyright 2009 IAEA.

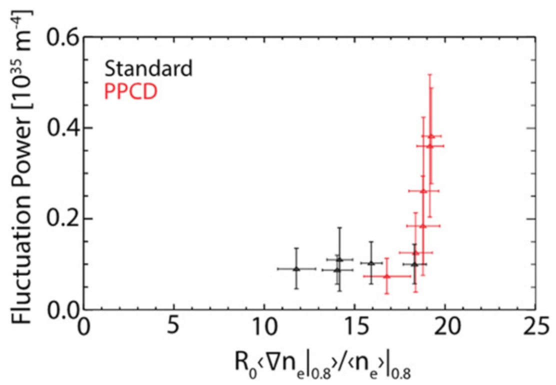

Figure 49. Line-integrated density fluctuations, $\langle\tilde{n}_e^2\rangle$, measured by FIR far-forward scattering at $r/a = 0.86$ versus the normalized inverse density gradient scale length evaluated at $r/a = 0.8$. The emergent TEM fluctuations with PPCD exhibit a critical-gradient threshold close to the value predicted by GENE. The local density gradient is relatively small in standard plasmas, which is why the fluctuation amplitude for standard plasmas is lower than for PPCD. Reprinted from [436], with the permission of AIP Publishing.

by the change in the parameter $\gamma = (1 - F)/\Theta$ from the beginning to the end of PPCD [83, 426, 429]. This parameter is linked to the shape of the current profile and hence MHD stability. Later work included additional TPE-RX data and data from EXTRAP-T2R and found that an empirical scaling including a Θ^3 dependence encompassed fairly well all of the PPCD results from various devices [432].

The scaling of various RFP confinement-related parameters was evaluated numerically for generic current profile control with single-fluid resistive MHD modelling [433, 434]. An auxiliary electric field profile was applied in the model in the place of tearing fluctuations on the resistive time scale. The energy confinement time scales as $196\Theta^{-1.0}a^{1.5}M_i^{0.25}Z_{\rm eff}^{-0.50}(I/N)^{0.50}I^{0.50}$, where M_i is the fuel-ion to proton mass ratio, and N is the line density.

5.6. Emergence of microturbulence in PPCD plasmas

When tearing modes are sufficiently reduced it is plausible that microturbulence might ultimately govern energy and particle transport in RFP plasmas, as it does in tokamak and stellarator plasmas. The non-stochastic confinement properties of energetic electrons described above provided the initial indication this might be the case for PPCD plasmas. The role of microinstability in QSH plasmas was already discussed in section 4.3.

Density fluctuations measured by FIR forward scattering in MST's standard RFP plasmas are strongly correlated with the magnetic fluctuations associated with tearing modes [435]. These fluctuations are also greatly reduced with PPCD, consistent with the large reduction in magnetic fluctuations. The spectral shape of the density fluctuations changes with PPCD, and a higher frequency peak emerges around 50 kHz, identified as density-gradient-driven TEM. The fluctuations have $k_\perp\rho_i \approx 0.1$–$0.2$ and propagate in the electron diamagnetic drift direction [436].

As shown in figure 49, the onset of the TEM density fluctuations exhibits a clear critical-gradient threshold, $R/L_n \approx 20$, where $L_n = n_e/|\nabla n_e|$ is the density gradient scale length. This agrees with linear gyrokinetic modelling (GENE) predictions [300, 437]. The critical gradient threshold is larger than for tokamak plasmas by roughly the aspect ratio, R/a, owing to the difference in magnetic field scale length. Nonlinear GENE modelling shows a large Dimits-like shift from exceptionally strong zonal flows that suppress the TEM turbulence to near zero. This was initially a surprise, but it was discovered that a small magnetic perturbation, e.g., a remnant tearing mode, disrupts the zonal flows, as shown in figure 50. With weaker zonal flows, the turbulence saturates at larger amplitude, comparable to the level measured in MST [300, 302]. An intriguing prospect emerges: as tearing is further suppressed, either through further improvements in profile control or towards pure SH states, anomalous transport might be uniquely small in RFP plasmas.

A zonal flow has been identified experimentally in MST plasmas. Measurements using two probes with capacitive electrodes separated 180° toroidally that measure the plasma potential directly observe a zonal flow, most likely associated with the TEM turbulence [438]. Such direct observations of zonal flows are rare in fusion research, despite their underlying importance in the formation of transport barriers.

The impurity flux associated with the TEM turbulence has also been measured using a novel linearized correlation method of active spectroscopy [439]. The spectral method could be used to investigate turbulent transport that limits impurity accumulation in the core of high-performance, metal–wall tokamak and stellarator experiments.

5.7. Towards non-inductive (dc) current profile control

Three additional efforts were undertaken on MST with the goal of non-inductively (non-transiently) modifying the current profile and will be briefly summarized in this section: driving current via electrostatic current sources inserted into the

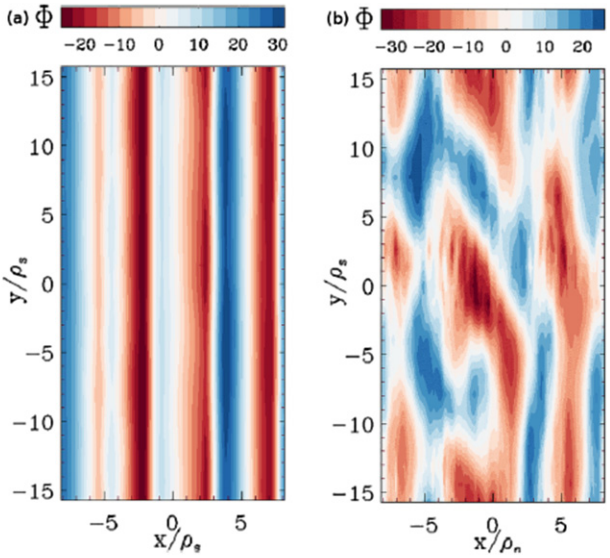

Figure 50. Electrostatic potential contours Φ (in units of $\rho_s e/R_0 T_e$) in the radial–toroidal plane for TEM turbulence in nonlinear GENE simulations. In the absence of residual tearing fluctuations (*a*), TEM instability leads to very strong zonal flow formation and the complete suppression of turbulent heat and particle transport. With residual tearing fluctuations (*b*), the zonal flow is weaker, and the turbulence saturates at larger amplitude. Reprinted from [302], with the permission of AIP Publishing.

plasma edge and launching lower-hybrid (LH) and electron-Bernstein waves (EBWs) from RF antennas.

Edge electrostatic current drive was tested with 16 miniature plasma sources inserted into the outer 10% of the plasma [440]. When the sources were inserted but inactive, they caused a perturbation leading to an estimated 50% drop in particle and energy confinement. When biased negatively to emit electron current, each source injects roughly 0.5 kA, and when the current is injected parallel to the background edge parallel current, magnetic fluctuations are reduced, and the particle and energy confinement are restored to approximately their unperturbed values. The restoration of confinement is linked to a time-averaged drop in magnetic fluctuation amplitude, due primarily to an increase in the time between sawtooth crashes. Although the plasma sources did not prove a viable means of achieving a net confinement improvement, they did demonstrate the principle of current profile control.

The foundation for LH wave injection stemmed in part from theoretical studies [441, 442]. The aim is to generate an RF current drive profile similar to the ad hoc electron force profile shown in figure 40. It was predicted that the location of the driven current can be controlled by choice of parallel wave number and RF frequency, and that the predicted efficiency of current drive is sufficient for tearing suppression with 1–2 MW of RF power. Experimentally, an interdigital-line antenna mounted on the inner surface of MST launched the correct $n_{\parallel}$ spectrum and was well loaded by the plasma [443, 444]. With the source of RF power exceeding 200 kW, substantial x-ray emission from the plasma was observed [445]. However, robust operation at this high source power did not prove feasible, implying that a large number of antennas would be required to inject sufficient power to affect tearing mode stability.

The foundation for the injection of the EBW was laid in part by computational studies showing that there is a directional component to the absorption of the wave, which can be controlled by the poloidal angle at which the wave is launched, so that directed current drive is possible [446]. The conversion of Bernstein waves generated within the plasma to electromagnetic waves was confirmed by measurements of thermal emission at the plasma boundary [447]. By reciprocity, this implies that externally launched electromagnetic waves can couple to the Bernstein mode. Starting with very low power (<10 W), coupling of RF was studied experimentally with a waveguide antenna and found to agree with full-wave modelling [448]. Coupling efficiency exceeding 80% was observed under certain conditions, though coupling can be degraded by effects such as edge density fluctuations [449]. The available power for injection was increased to several hundred kW, and electron energization in the plasma is evident from x-ray emission [450]. However, recent modelling with a Fokker–Planck, RF-altered electron distribution coupled into a single-fluid MHD simulation indicates that much larger power (∼10 MW) would be needed to produce an observable effect on the tearing modes [451].

5.8. Other routes to improved confinement

In addition to current profile control and helical states, there are other routes to improved confinement in the RFP that do not entail active control, *per se*. We mention these here, given an observed partial synergy with and partial similarity to PPCD plasmas in MST.

In both TPE-1RM20 and MST, spontaneous periods of improved confinement were observed in conjunction with strong toroidal magnetic field reversal and a relatively large pinch parameter. In such regimes, dubbed 'improved high theta mode' in TPE-1RM20 [452] and ultimately 'enhanced confinement' (EC) periods in MST [453, 454], magnetic fluctuations drop, and both the electron temperature and the energy confinement increase, doubling in TPE-1RM20 and tripling in MST. Improved confinement was also observed in TPE-RX, corresponding to discharges with slow decay (towards zero) of the edge toroidal field [455].

The EC periods in MST are characterized in part by regularly occurring bursts of $m = 0$ mode activity. Each burst causes a temporary degradation of confinement [57]. Such bursts can also occur in PPCD plasmas, with a similar effect on confinement [319]. The hottest, highest confinement PPCD plasmas are entirely free of such bursts [424], with reduction of both $m = 1$ and $m = 0$ occurring almost immediately after the start of PPCD [383]. This immediate reduction occurs when an EC period is produced leading into the start of PPCD. In fact a possible explanation of the lower effect of PPCD in RFX and RFX-mod with respect to MST has been ascribed to a lower reduction of $m = 0$ modes. Furthermore, EC periods can terminate with very large amplitude sawtooth crashes, contributing to the pre-PPCD ion heating described above [428]. Initiating PPCD with (EC-like) strong toroidal magnetic field reversal also led to the best PPCD performance in EXTRAP-T2R [430].

The physics of these spontaneous periods of improved confinement, and the $m = 0$ bursts occurring in EC and PPCD plasmas in MST, is not well understood. However, based on the fact that the bursts bear some resemblance to edge-localized modes in tokamak H-mode plasmas [57, 456], it was hypothesized that $E \times B$ flow shear could play a role. In the PPCD case, this would not be overly surprizing given the emergence of tokamak-like microinstabilities. Actually strong flow shear was measured in the edge of both EC and PPCD plasmas [404, 454]. Later modelling of the impact of various flow profiles on tearing stability showed that the flow shear in EC and PPCD plasmas could play a role in governing the $m = 0$ bursts [457]. Modifications to $E \times B$ flow shear were also measured during PPCD in RFX [458, 459]. Finally, it is worth mentioning that biasing the edge of MST brought about a reduction of electrostatic fluctuations and an improvement in particle confinement [460]. Electrostatic fluctuations and the edge particle flux were also affected by biasing in RFX [461].

5.9. Open questions and future directions

There are many questions in the realm of current profile control. For example: (i) what is the optimal inductive $E(a)$ waveform for sustained fluctuation reduction and improved confinement, and can the degree and duration of improved confinement be increased? (ii) How does the improved energy confinement time scale with parameters like the plasma current? (iii) What would be the impact of an advanced, low-recycling boundary on plasmas with current profile control? (iv) How are PPCD/OPCD plasmas associated to the onset of QSH states? (v) What is the role of $m = 0$ modes? Though the comprehension of these plasmas has significantly progressed, further computational and experimental work is required to fully address these points.

While MHD computation provided the foundation for current profile control, experimental progress to date has been almost entirely empirical. This is due in part to the fact that fully nonlinear simulations of RFP plasmas require considerable raw computing power, the need for which increases, for example, with S. The most recent modelling of PPCD with the NIMROD MHD code was conducted with $S < 10^4$ [382], much lower than in the hottest PPCD plasmas in MST. The importance of $m = 0$ bursts in MST plasmas was described above, but such bursts are not typically observed in MHD computation, implying unrealistic input parameters or missing physics.

Gyrokinetic modelling is also likely to be important. The potentially missing physics noted above might be related to micro-instability. Hence, understanding present day experimental results and projecting to the future will likely require both MHD and gyrokinetic work.

In present-day RFP devices, current profile results have for the most part stemmed from simple, passive power supplies comprised of capacitors and inductors. The future of current profile control lies in digitally programed, feedback-controlled power supplies, which are in use on RFX-mod and are being developed on MST. In agreement with the modelling described just above, the power supply waveforms can be adjusted in real time based on measurements of the MHD dynamo, or at least the constituent fluctuations. But additional inductive and/or non-inductive control may also be needed for micro-scale fluctuations.

The scaling laws found in present-day devices need to be assessed at higher I_p, which might also allow for non-inductive control techniques like RF.

With respect to power and particle handling, RFP devices have to date operated with primitive boundaries that would be irrelevant in a reactor setting. While substantial progress in fusion performance has nonetheless been possible, it was noted above that a crucial requirement for high-quality PPCD plasmas is a 'well-conditioned boundary,' meaning minimized contamination by atmospheric impurities and low recycling. Indeed MHD modelling showed that changing the edge resistivity changes magnetic fluctuation amplitudes [462]. It is customary to think of current profile control in terms of changing the inductive electric field, but the current profile can be altered equally well by a change in resistivity. Together with the already mentioned possible effect of the $m = 0$ modes (section 5.8), also the need for low recycling in PPCD may explain in part the fact that the confinement improvements in TPE-RX and MST were greater than that in RFX and RFX-mod: with full graphite coverage of the plasma-facing boundary, RFX and RFX-mod had large recycling, in contrast to the other two devices with their metallic boundaries.

In this chapter and in the previous ones two ways of reducing stochasticity and improving the performance of RFP plasmas have been presented: the helical states and the current profile control. Still an open issue is whether current profile control could effectively act in QSH states. An extended experimental investigation has not been done yet. In RFX-mod at plasma current $I_p < 1$ MA, OPCD favoured the development of QSH leading to an enhancement in confinement by $\approx$50% [261]. At high current QSHs spontaneously develop, so that their time phasing and duration with OPCD is difficult to control. New insights into the combined effect of QSH and OPC/PPCD will come from RFX-mod2, where more stationary helical states are expected to occur.

6. Density and β limit

The high-density limit is nearly the same for the RFP and the tokamak, associated to a radiation barrier. It is traditionally described by the empirical Greenwald limit [463] for both configurations, suggesting that the same mechanism is behind such behaviour. Instead in the stellarator, where a high density limit exists as well, it is described by the Sudo scaling [464]. More recently, a power balance model accounting for neutrals and impurity radiation has been developed and successfully describes the high density limit in the stellarator, RFP and L-mode tokamak [465, 466]. While the RFP has the same empirical density limit as for the tokamak, the absolute value of density is large because the current density is large. An RFP reactor plasma would operate below the empirical limit, as illustrated in the TITAN power plant study (see chapter 10).

At variance with the density limit, the β limit is different in tokamaks and RFPs. In the tokamak, the total β is basically limited by ideal stability, which sets a disruptive limit around 5%, depending on current and aspect ratio. In addition, limitations of achievable β related to neoclassical pressure driven resistive tearing modes have been observed in several devices, and compared to theory, see for example [467–469]. In the stellarator, ideal interchange modes are a major concern for high β plasma production, leading to a non-disruptive limit similar to the tokamak one [470, 471], though violations of the Mercier criterion [5] have been observed in some experiments and interpreted as a local effect [472, 473].

Instead, plasmas characterized by high β values are a feature of the RFP configuration, where, due to edge magnetic field being nearly poloidal, the total β is almost equal to the poloidal one. As reported in papers as [36, 474], the ideal limit is much higher than in tokamaks, $\beta_p = 50\%$ for $m = 0$ instabilities and $\beta_p = 100\%$ for $m = 1$. However, current experiments achieve β values that, though high compared to the tokamak and stellarator, are still well below the ideal stability limit.

6.1. Density limits

Since 80s, the operational range of RFP experiments has been found to be limited both at low and high electron density [50, 475]. The low-density limit was related to the acceleration of runaway electrons and to the growth of the magnetic fluctuations. In RFX-mod the longest durations of helical states featuring ITBs have been obtained when the careful design of the magnetic boundary and the consequent reduction of the edge radial field by a proper tuning of the feedback MHD control system (clean mode control, see section 7.2) has allowed the extension of the density operational range towards the lower values [121].

Similar to tokamaks, the high density limit in RFPs has been associated to a radiation barrier, dependent on plasma current [476]. In RFX-mod, the high density limit was compared to the tokamak empirical Greenwald limit [463]:

$$n_e \left[10^{20}\ \mathrm{m}^{-3}\right] < n_G = I_p[\mathrm{MA}]/\pi a^2 \tag{6.1}$$

with n_e average plasma density, I_p plasma current. It was found that in the RFP as in the tokamak the upper boundary of the density operating space is limited by the Greenwald density n_G [477]. The same empirical limit was also observed in the MST RFP in standard plasmas [417], see figure 51. The fact that the same representation, based on averaged global plasma quantities, matches well data from devices characterized by different size, performances, magnetic topology and transport quality suggested that a common physics could underlie the phenomenology of the Greenwald limit. Indeed, the point of view of the RFP configuration has been compared to those of the tokamak and stellarator, significantly contributing to the general understanding of the high density limit [478]. A theory based model able to describe the density limit in RFPs, L-mode tokamaks and stellarators has been proposed, simply based on a radiative limit and taking into account the radiation from impurities and neutrals [465, 466]. The model leads to a constraint for the edge density, ruled by radiation losses from light impurities. For the ohmic tokamak and the RFP, the limit scales linearly with the plasma current, as the empirical Greenwald one. The auxiliary heating adds a further dependence, scaling with the power as $P^{0.4}$, in agreement with L-mode tokamak experiments. Compared to previous works with a similar approach and applied to ohmic tokamaks [479], this model is able to take into account profile-dependent terms.

In RFX-mod, when the density approaches the Greenwald value, the temperature decreases, while the density increases at the edge [274]. Such edge density accumulation takes place after a back transition from the QSH to the MH regime, which occurs at $n/n_G \approx 0.35$ [208]. Due to the edge density accumulation radiation increases, in the shape of a poloidal radiating belt [477, 480], which resembles the MARFE phenomenology observed in tokamaks (with poloidal and toroidal coordinates exchanged due to the poloidal nature of the magnetic field in the RFP edge) [481] or Serpens in LHD stellarator [482].

An important difference between RFPs and tokamaks is that the density limit is not disruptive in the RFP: when the Greenwald density is approached, due to plasma cooling and resistivity increase, the toroidal flux decreases, resulting in the shrinking of the current profile with soft decrease of plasma current. Indeed, in the RFP when density increases, the input power necessary to sustain the discharge increases as well, so that the density limit can be regarded as a power limit, governed by the volt-seconds stored in the magnetizing circuit of the device [274].

Only in some circumstances, at high current and density, fast terminations have been observed in RFX, RFX-mod and MST [417, 483]. In particular, in RFX-mod, where they occur mainly at very high current and in conditions of saturated graphite wall, they have been related, to strong localized PWIs in the region of wall mode locking, where severe power loads are dissipated, leading to a sudden particle release, locally enhanced radiation and temperature drop.

Dedicated experiments in RFX-mod led to the interpretation of the density limit based on the relation between the above-mentioned localized accumulation process and the $m = 0$ mode magnetic topology. The main experimental observations are summarized in figure 52 as a function of the normalized toroidal angle $\varphi - \varphi_{\mathrm{lock}}$ where φ_{lock} is the angle corresponding to the maximum deformation of the $m = 1$ mode bulge due to wall mode locking (LM) [484]. The maximum H_α emission corresponds to the maximum $m = 1$ mode deformation, (green and red lines in panel (*d*)) thus indicating at that location the main particle source. At the edge, black line in panel (*a*) shows the Poincaré plot of the $m = 0, n = 1$ island; the plasma flow, measured by the gas puffing imaging diagnostic [485] corresponds to the blue line and reverses at the X-point of such island. This indicates that particles are carried from the source toroidal position to a stagnation point where density accumulates (panel (*c*)) and, correspondingly, radiation is enhanced (panel (*b*)). The understanding of these observations relies on the application of the guiding-centre code ORBIT [130], upgraded to include the effect of a recycling wall [484]. The whole process is triggered by a charge separation, induced

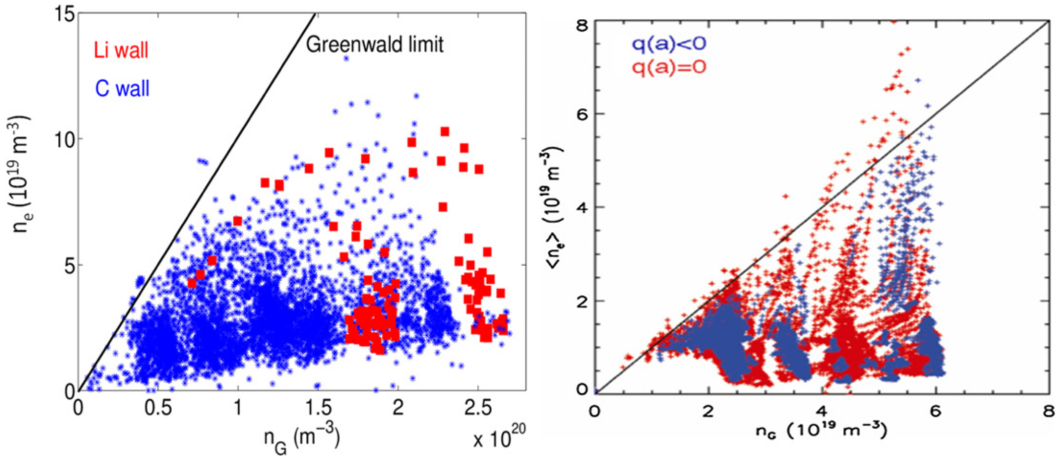

Figure 51. Greenwald plot in RFX-mod (left) and MST. (Right) Reproduced courtesy of IAEA. Figure from [100]. Copyright 2015 IAEA.

by a differential diffusion between ions and electrons, which at high density leads to small order ($\approx 10^{14}$ m^{-3}) electron accumulation at the $m = 0$ island X-point. To ensure ambipolarity, a radial electric field develops, which originates a convective cell, ultimately producing the macroscopic density accumulation (order 10^{20} m^{-3}). In [486] the model has been generalized: it is shown that in any kind of device if a perturbation breaks the toroidal symmetry with a drift depending on the gyroradius (larger for ions than electrons), an ambipolar potential, with the same symmetry as the perturbation, is produced to balance the drifts.

It is well known that in tokamaks the Greenwald limit has been exceeded in several conditions, in particular including additional heating and peaking of density profile in enhanced transport regimes and the modification of the source (pellet injection, strong NBI, supersonic molecular beam), as for example reported in [463, 487]. The same is true for RFPs, where also plasmas with $n/n_G > 1$ have been produced in several conditions.

In RFX-mod, where the operation at the highest densities is limited by the power available in the plant, the Greenwald value can be often exceeded at low current levels ($\leqslant$0.3 MA) [275]. Discharges with He as filling gas have been found to be favourable for $n/n_G > 1$ plasmas [477]. This finding, similar to what previously observed in ASDEX-Upgrade [488], is attributed to a less localized PWI in the region of LMs and, in the case of He, to a different edge flow pattern [489].

The injection of hydrogen/deuterium pellet did not allow overcoming the Greenwald limit in RFX-mod: this has been ascribed to the available pellet sizes, too large to penetrate into the plasma without destroying the helical core or too small to reach the plasma centre before the complete ablation. Pellets have rather been injected in RFX in order to study particle transport, comparing different plasma regimes, and in particular characterizing the enhanced particle confinement time in QSH states (from $\approx$3–4 ms in MH to $\approx$12 ms in QSH) [26] and with pulse poloidal current drive [418].

Instead, as discussed in chapter 5, in MST $n/n_G = 1.4$ ($n_e = 0.9\,10^{20}$ m^{-3}) has been observed at $I_p = 0.5$ MA in pellet-fuelled PPCD phases [100, 417]; also, in discharges with gas puffing through a high throughput valve $n/n_G = 1$ has been achieved [417].

The radiative limit is not the only high-density boundary in RFPs: a soft density limit has been observed both for the PPCD and for QSH state development. The former ([417, 430]), weakly increasing with plasma current, is related to the onset of bursty $m = 0$ activity, and in MST requires to start the current drive with a density below 0.8–1.1 10^{19} m^{-3} in the current range 0.2–0.5 MA [383]. The latter is also linked to a threshold in $m = 0$ mode amplitude and requires $n/n_G \leqslant 0.35$ for the spontaneous development of QSH states [211].

Given the relationship between $m = 0$ modes and upper density limit, the effect of the reversal parameter F has been studied too, both in RFX-mod and MST. As predicted in [179], the magnetic equilibrium plays an important role in governing the $m = 0$ modes. Their amplitude is lower when the field reversal is shallow. In fact, in RFX-mod the operation at high current is compatible with higher densities when the F parameter is close to zero, which corresponds to reduced $m = 0$ mode amplitude and milder PWI [208]. Therefore, the operation at shallow F is the preferred one to perform discharges at high current, since it helps in operating just below the density threshold for spontaneous QSH states. On the other hand, in such condition the distance of the reversal from the wall is small and the islands easily overlap the wall, which makes more difficult the control of the density and easier the onset of the radiative instability [274]. In MST, results reported in [100, 417] show a modestly larger density limit with $F \approx 0$.

6.2. High β plasmas

Experimentally, high beta values are usually related to high density and low fluctuation (i.e. low transport) regimes. In the TPE-1RM20 RFP, in the so-called improved high theta mode the highest $\Theta = B_\theta(a)/\langle B_\Phi \rangle \approx 2$ has been found to correspond to increased densities and temperatures, and therefore to the highest values of $\beta_p \approx 18\%$ [452]. This regime was related to a reduction of dynamo activity, measured as a large reduction of magnetic fluctuation power around 70 kHz. Similar β_p values have been measured in TPE-RX when the electron density was increased by fast gas puffing [490]. Indeed, in

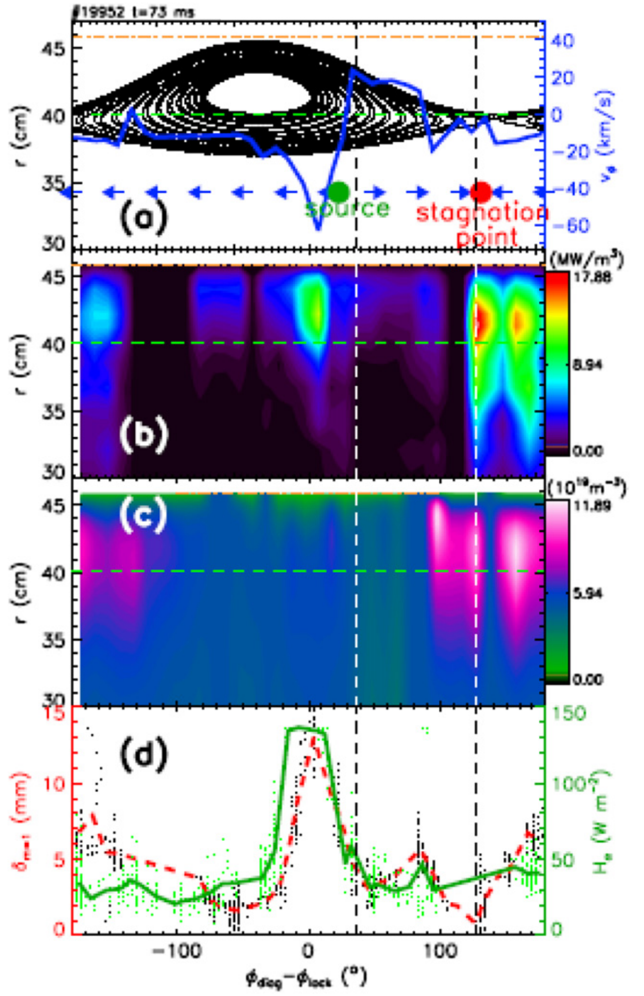

Figure 52. In an RFX-mod discharge with $n/n_G = 0.8$, from top to bottom (*a*) plasma flow as a function of the normalized toroidal angle, $\varphi - \varphi_{lock}$ (zero = maximum of the LM, i.e. the $m = 1$ bulge). The Poincaré plot of the island associated with the $m = 0, n = 1$ mode is also shown; (*b*) tomographic map of total radiation (minor radius as the *y*-axis); (*c*) map of electron density obtained from a multichord interferometer; (*d*) H_α emissivity (solid) and $m = 1$ deformation (dashed). The stagnation point for the plasma flow corresponds to the X-point of the island and to the maximum radiation and density, the other null point (=the source) corresponds to the peak of the influxes. The dashed, horizontal line in panels (*a*)–(*c*) corresponds to the reversal surface, where $B_\varphi = 0$. Reproduced courtesy of IAEA. Figure from [484]. Copyright 2012 IAEA.

most RFPs increasing density in improved regimes by pellet injection or fast gas puffing has been applied as a means to improve confinement and achieve record β values. In RFX-mod, the highest poloidal beta values of ≈15% have been observed when n/n_G approaches 1 [491]. A statistical analysis in terms of global parameters and assuming ion temperature as a constant fraction of the electron temperature, yields $\beta_p \approx I_p^{-0.23}\,(n/n_G)^{0.58}$, which indicates a small degradation of β_p with plasma current and a more significant increase with n/n_G [273]. Instead, 3D resistive MHD simulations by the DEBSP code, based on stochastic transport scalings [253] predict a dependence of β_p on I_p more negative than the experimental RFX-mod data ($\beta_p \approx I_p^{-0.56}(n/n_G)^{0.56}$). In MST

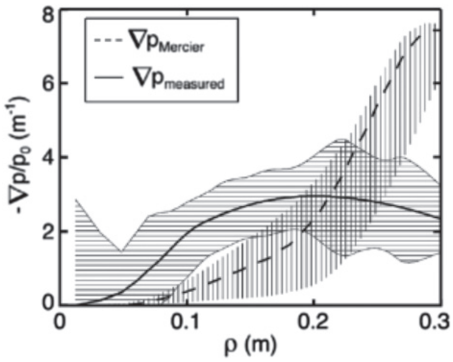

Figure 53. Profile of the measured pressure gradients (solid line) in an MST discharge with pellet injection where $\beta = 26\%$ is achieved. Dashed line is the critical Mercier pressure gradients, which is exceeded in the core plasma. Shaded regions indicate the uncertainties. Reproduced courtesy of IAEA. Figure from [246]. Copyright 2009 IAEA.

also a modest decrease of β_p with the current, $\beta_p \approx I_p^{-0.23}$ at high n/n_G, was reported in [62].

In several RFP devices the maximum achieved β has been transiently enhanced by the combination of high-density plasmas and active control of the current profile (see chapter 5). In RFX, when an OPCD was applied, β_p was enhanced by a factor 50% [492]. In the TPE-RX device, double β_p (13%) and β (11%) values have been measured during PPCD with respect to standard plasmas. In MST, the application of PPCD leads to enhanced total β of 11%–15% (depending on plasma current), to be compared to 5%–9% in standard plasmas [399]. When during PPCD phases deuterium pellets were injected, thus increasing density and its gradient, record β values have been obtained [246].

The TPE-RX experiment achieved increased density operation with improved confinement and β_p up to the record value ≈34%, by the injection of a deuterium pellet during PPCD [12].

In MST, dedicated studies on β limit have been performed, optimizing pellet parameters in PPCD plasmas in order to produce its ablation in the core and maximize β [100, 417]. In these experiments, as introduced in chapter 5, while density increases the electron temperature decreases, and a large fraction of ohmic power (higher at higher density) is collisionally transferred to ions. The larger stored energy leads to high beta values, $\beta \approx 26\%$, corresponding to a $\beta_p \approx 40\%$. The latter β value coincides with the prediction by the Connor–Taylor scaling, $\beta \approx (m_e/m_i)^{1/6}$ (m_e and m_i electron and ion mass respectively), which gives 25.4% for MST [417]. In such plasmas, pressure gradients exceeding the Mercier limit have been produced [246, 417], see figure 53, similar to what observed in stellarators (see for example [471, 493]).

The Mercier criterion governs the interchange stability, and can be expressed as:

$$r\frac{B_\phi^2}{2\mu_0}\left(\frac{q'}{q}\right)^2 + 4p'\left(1-q^2\right) > 0 \qquad (6.2)$$

with the first term related to the stabilizing effect of the magnetic shear and the second one to the destabilizing effect of pressure gradient when $q < 1$.

Theoretical computations by the DEBS code have shown that in these high β regimes both pressure-driven interchange modes and tearing modes are linearly unstable [246]. In MST high β plasmas, interchange modes have not been observed (possibly due to limits of the diagnostics), so that an open issue remains whether the driving modes are interchange or global tearing modes. In [494] it is found that at low β the parity of pressure driven modes is the tearing parity. At β values around 20% the interchange modes appear and become dominant around 40%. Indeed in RFX-mod the observed edge magnetic fluctuations corresponding to linearly unstable pressure driven modes have the tearing parity, though they were in a first time interpreted as g-modes [495].

A disruptive limit of β does not occur, even when the control of the current profile with the related reduction of current driven modes and increase of β leads to a destabilization of pressure driven modes: at very high β a 'soft' degradation of confinement is observed, likely related to increased fluctuations at high density [417].

At variance with tokamaks, shaping effects have not been found in RFPs to enhance the β limit for both ideal [496] and resistive β modes, due to a poloidal mode coupling stronger than in the circular topology (produced by the variation of the poloidal field along the poloidal angle) and to the development of multiple trapping regions [497].

6.3. Neoclassical bootstrap current at high β

The bootstrap current J_{BS} depends on temperature and pressure normalized profiles and on the trapped particle fraction:

$$\langle \mathbf{J}_{\mathrm{BS}} \cdot \mathbf{B} \rangle = L_{31}\left[\frac{p_{\mathrm{e}}'}{p_{\mathrm{e}}} + \frac{1}{Z}\left(\frac{p_{\mathrm{e}}'}{p_{\mathrm{e}}} + \alpha\frac{T_{\mathrm{e}}'}{T_{\mathrm{e}}}\right)\right] + L_{32}\frac{T_{\mathrm{e}}'}{T_{\mathrm{e}}} \qquad (6.3)$$

with p_{e} electron kinetic pressure L_{31}, L_{32}, α functions depending on the trapped particle fraction and on the magnetic equilibrium [498, 499]. In an axisymmetric RFP, the fraction of trapped particles in the core is similar to the fraction in a tokamak with the same aspect ratio, while it becomes lower at the edge, depending on the current profile [62]. The corresponding bootstrap current is instead much lower than in tokamaks, due to the higher poloidal field. In [284], it has been calculated by two different codes (RFXTOR, based on RFX-mod magnetic measurements [25] and FLOW, solving a generalized version of Grad–Shafranov equation [500]). The result is shown in figure 54 and confirms that in present day circular RFPs only a negligible additional current can be provided by the bootstrap mechanism [28]. The total fraction of trapped particles increases in the presence of a helical structure, as in RFP QSH states, basically due to an additional field ripple introduced by the helical geometry, evaluated from 30% in the axisymmetric case to 40% in the helical configuration in [284]. This suggests a modest increase of the bootstrap current. The shaping effect is also related to some increase of the fraction of bootstrap current: in [497] it is evaluated to be of the order of 10%–30%, which maintains the total fraction very low.

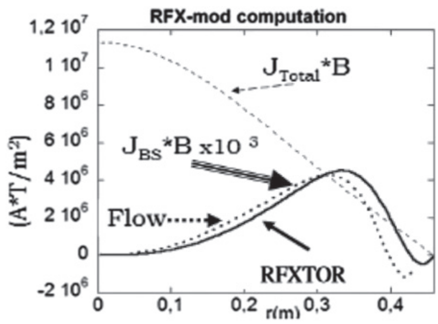

Figure 54. Total and bootstrap parallel current profiles calculated for RFX-J_{BS} is multiplied by 10^3. Reprinted from [284], with permission from JSPF.

A more relevant effect is instead expected in a low aspect ratio equilibrium, mainly due to enhanced neoclassical viscosity [501]. More specifically, in [502] it has been found that, in a reactor relevant range of parameters with an aspect ratio 2, ellipticity 1.4 and triangularity 0.4, if the pressure profile is flat and thanks to a decreased magnetic shear, an equilibrium with 94% bootstrap current and extremely high values of $\beta = 63\%$ stable to ideal kink and Mercier localized modes could be maintained.

6.4. Summary and possible developments

As indicated by experimental scaling laws, the confinement in the RFP scales favourably with electron density, which makes high-density regimes particularly attractive in this sense. Unfortunately, due to the low particle confinement time the density enhancement (with consequent confinement increase) induced by pellet injection is transient, so that stationary high-density regimes are reached with high rates of gas puffing. This produces edge peaked density profiles, which results in enhanced radiation, decreased temperature and enhanced request for ohmic power to sustain the current. In fact, as discussed in section 6.2, in MST the combination of PPCD with pellet injection allows the achievement of high values of confinement and β, also exceeding the Mercier criterion, but in a transient way. On the other hand, in RFX-mod, though when pellet penetrates the helical core in QSH states the particle confinement is enhanced, the effect is anyway transient as well. Future developments could be linked to a more efficient multi-pellet injection, capable of injecting several pellets throughout the plasma discharge, coupled to a low recycling wall (see chapter 8): this could allow the development of more core-peaked profiles, avoiding the MARFE-like structures at the edge while maintaining higher $n_{\mathrm{e}}T_{\mathrm{e}}$ product in the core.

7. Active control of MHD stability

7.1. Resistive wall modes

In the past, the limitation to pulse length imposed by RWM instabilities was considered a serious issue for the future of the RFP configuration. In order to characterize the dynamics

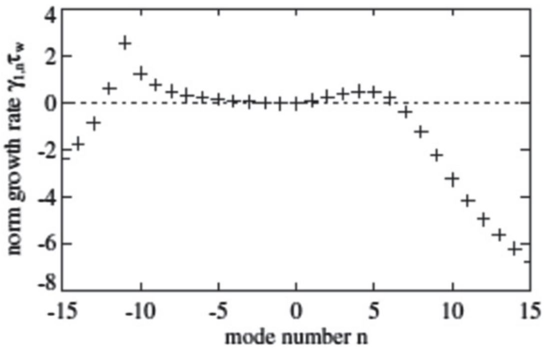

Figure 55. RWM growth rates normalized to the long wall time constant $\gamma^{m,n}\tau^{m,n}$ for $m = 1$ modes as a function of the toroidal mode number n. Reproduced from [531].

of RWMs, several RFP experiments were fitted with resistive walls, sometimes referred to as thin shells, with wall time constants shorter than the discharge pulse length. These early RFP experiments with resistive walls were commissioned in the late 1980s and included the OHTE device at General Atomic [503, 504], the Reversatron at the University of Colorado [505], the HBTX-1C device at Culham [506] and REPUTE-I [507, 508].

A convincing experimental demonstration of the RWM instability was achieved in the HBTX-1C experiment. The wall time constant $\tau_w = \mu_0 a\delta\sigma$ (where a is the minor radius, δ is the wall thickness and σ is the wall conductivity) for HBTX1C was 1 ms. The discharge was sustained for about 4 ms. Nonresonant ideal kinks (RWMs) were observed with growth rates about a factor of three times the wall time constant, consistent with theoretical studies assuming typical current profiles. Even though REPUTE-1 was affected by error fields, it detected a marginally nonresonant mode consistent with the stability limit of an ideal internal $m = 1$ kink mode [507]. The OHTE experiment did not report evidences of RWMs [504], while the EXTRAP-T2R experiment (based on OHTE but without helical coils), rebuilt in 1999–2000 with a resistive wall, actually did show clear RWMs [509].

The wall penetration time for EXTRAP-T2R was selected to be 12 ms, which was relatively long compared to the earlier resistive shell experiments in OHTE; the observed growth rates of the RWMs were on the time scale as the wall penetration time: the normalized RWM growth rates spectrum $\hat{\gamma}^{m,n} = \tau_w\gamma^{m,n}$ for a typical RFP EXTRAP-T2R equilibrium are shown in figure 55.

Shortly after the experimental evidence for the existence of RWMs the first attempt of a simple active feedback experiment was performed in HBTX-1C [510]. Two helically wound coils (sine and cosine configuration) outside the outer shell of the vessel were incorporated in order to control the ($m = 1$, $n = 2$) mode. When the mode amplitude reached a pre-set value (below the level corresponding to discharge termination), the helical coil with the correct phase was activated to suppress the growth. With this feedback algorithm, the targeted mode was suppressed below the pre-set level. Although the early demonstration of active feedback of a single RWM in HBTX-1C was noteworthy, suppression of only one RWM mode did not substantially improve the RFP performance and the extension to multiple modes would have been technically challenging.

7.1.1. Theoretical studies on RWM stabilization. Theoretical studies of RWM instability properties were carried out to determine the requirements for active control. In [511] the effect of shell resistivity and distance of the boundary on linear stability of RWMs was investigated. Analytical studies developed further the stability analysis of the RWMs, taking into account rotational stabilization and wall distance [512, 513], and supported the conclusion that active feedback was necessary for long pulse operation in the RFP.

The DEBS code was modified to include resistive wall boundary conditions and investigate nonlinear aspects of RWM stability. Nonlinear numerical simulations of an RFP with the RFX geometry performed by this code provided estimates of performance degradation due to an increase in fluctuation amplitudes [514], both due to RWMs and tearing modes, on time scales longer than the shell time. The code was further modified adding a 'virtual' set of helical coils in order to perform multiple RWM stabilization studies [515]. Each virtual helical coil was independently acting on a different Fourier harmonic, a feedback algorithm named *mode control* (MC), because each mode was independently controlled with a different gain. This algorithm has been implemented and tested experimentally, as it will be described in section 7.1.3. An extensive scan of parameters for DEBS runs showed that the external kinks are always unstable if the wall surrounding the plasma is not ideal. The instability was found independently of the initial condition, the plasma equilibrium or the plasma physical conditions.

A significant finding was that the external kinks are well described within the linear theory: their nonlinear interactions are, in fact, almost negligible during their growth phase. More generally, linear theory gives a good prediction for the $m = 1$ spectrum, eigenfunctions and growth rates. As far as feedback control is concerned, feedback stabilization of external kink modes is possible, if carefully chosen gains are simultaneously set on 4 or 5 unstable modes. An experimental verification of the linear RWM behaviour was obtained in EXTRAP-T2R [509], further experiments performed in RFX-mod [516] confirmed the linear behaviour of the RWMs.

Different from tokamaks [517], the stability of internally and externally non-resonant modes in RFPs is not affected by plasma rotation, except if the plasma rotation velocity becomes comparable to the Alfven velocity [513, 518]: the latter is larger than the natural rotation velocity in current RFPs. Hence, based on the above linear theory active feedback is definitely needed for a long pulse RFP. Despite these differences, studies of resistive wall instability physics for RFPs and for tokamaks are complementary, and the physical model for MHD stability for both configurations with a thin (resistive) wall has many similarities [519].

7.1.2. The intelligent shell geometry. As an alternative to helical coils, a concept for feedback stabilization of the RWM instabilities called the *intelligent shell* (IS) or *virtual shell* (VS) was proposed by Bishop [520] at about the same time as the experiments on HBTX-1C were carried out. The IS is composed by a set of saddle coils that surround the plasma. The amount of current driven in each coil is determined by sensors located at the same position as the coil and with an identical shape. From a control theory point of view, this scheme consisted of a series of independent single input single output circuits. The aim of the IS concept is to 'freeze' the magnetic flux linking the powered coil, i.e. the system of coils mimics eddy currents and behaves as a perfectly conducting shell. The array includes a finite number of control coils in the poloidal direction, M_c, and in the toroidal direction N_c. In Bishop's paper, the voltage detected by the sensor coil due to the change of the flux is fed to an amplifier that drives current in the corresponding saddle coil aiming at reducing the measured flux.

The finite number of control coils sets a first limitation of the IS scheme: unstable modes with wavelengths shorter than the actuator coils spacing (i.e. with toroidal mode number $n > N_c/2$) would be largely unaffected.

A more stringent criterion on the minimum number of coils arises when multiple modes are simultaneously unstable. An early semi-analytical study by Fitzpatrick and Yu [521] modelled the linear RFP RWM feedback stabilization with an ideal proportional control in the IS scheme (i.e. flux sensors of the same geometry of saddle loops). A successful stabilization of multiple modes was possible if the number of coils in the toroidal direction N_c was greater than, or equal to, the range of toroidal mode numbers Δn of the multiple intrinsically unstable RFP RWMs. This is because a discrete saddle coil system always generate toroidal harmonics n together with toroidal sidebands $n + hN_c$ (where h is an integer number) whose amplitudes are not independent: the aforementioned criterion $N_c > \Delta n$ states that if n characterizes an unstable mode, then no sideband, in particular the first one $n + N_c$, should correspond to another unstable mode. A clear illustration of the violation of this criterion was obtained in initial EXTRAP-T2R active feedback operations with a limited number of active coils [522]: two unstable modes were, in fact, observed to grow with phases aligned in such a way to generate zero flux below the control coils.

The conceptually simple IS feedback approach cannot be directly implemented in a toroidal device, because it interferes with the control of plasma position and equilibrium by means of an applied external vertical field, which corresponds to an $m = 1$, $n = 0$ harmonic of the radial field. In order to circumvent this basic limitation, the feedback system needs the implementation of a multiple input multiple output scheme: a centralized digital controller [523, 524] is necessary in order to process simultaneously in real-time all signal inputs and to generate the required references for the currents in the control coil. In the variants of the IS (named *selective virtual shell* (SVS) [76] or *wise shell* [525]), the feedback variables are 'virtual' measurement $\tilde{b}^{i,j}$ (where the indices i, j refer to the spatial location of the sensor). Such 'virtual' measurements are obtained by inverse Fourier transforming a suitably modified version $\tilde{b}^{m,n}$ of the Fourier coefficients of raw measurements. For example, in order to remove the vertical field, $\tilde{b}^{m,n}$ is equal to the input $b^{m,n}$ for all (m, n) except the (1, 0) coefficient, which is instead set to 0. SVS was also used to let selected unstable (m, n) modes grow uncontrolled while keeping all others at negligible levels [77, 526].

7.1.3. The mode control algorithms. Based on nonlinear feedback studies recalled in previous sections, a feedback system with a realistic geometrical description of the coils and of the sensors was studied in [527], by applying standard control theory techniques as previously adopted for tokamaks [528]. The geometry of the IS was adopted (i.e. a finite and equal number of sensors and active coils, both in poloidal and toroidal directions), but the control scheme was different. In this scheme (dubbed *mode control* (MC)), the feedback variables $b^{m,n}$ are the Fourier coefficients of the flux loop sensor signals $b^{i,j}$, while the current harmonics $I^{m,n}$ correspond to the coefficients of the Fourier decomposition of the currents flowing into the control coils. The current flowing on each control coil is determined by an inverse Fourier transform of the spectrum of $I^{m,n}$ current harmonics, which is proportional to the corresponding feedback variable. This mode of operation was also defined *targeted-mode control* [525]. Due to the linearity of the Fourier transform, the mode control feedback scheme is equivalent to the IS if the same gains are set for all modes in mode control or for all positions in IS. In mode control a different gain for each mode can be applied, and in particular it can be set to 0 in order to let the corresponding harmonic uncontrolled. As Fourier coefficients are complex numbers, mode control gains can be complex. Experiments have been performed with the proportional component set to complex values [76, 516]. This technique has been used to induce slow rotations of MHD modes (both TM and RWMs).

7.1.4. Influence of control coil field sidebands and their aliasing on MHD control. Due to its finite number, whenever the control coil system generates an (m, n) harmonic aimed at cancelling a corresponding unstable plasma mode, it also creates sidebands with helicity $(m + kM_c, n + hN_c)$ where k and h are integer numbers. If the number of sensors is equal to the number of coils (as in the IS geometry) all of the sidebands are aliased into the (m, n) coefficient of the discrete Fourier transform of the measurements $b^{m,n}$. In other words, measured harmonics are polluted by the field generated by control coils. Equivalently, the perfect cancelation by the feedback coils of the sensor fluxes does not correspond to the cancelation of the plasma or error field harmonics. This effect was simulated for RWM control in [521] and in [527] and determined the optimal number of actuator and sensor coils. Both studies indicated that, when using a control system with the same number of sensors and actuators (i.e. with an IS geometry), the first sideband should not correspond to an unstable mode. This determines the choice of the number of coils. Given that the RWM spectrum of poloidal modes in the RFP corresponds to $m = -1$, 0 and 1, at least $M_c = 3$ coils in poloidal direction are necessary, but practical mechanical considerations suggest adopting $M_c = 4$. As far as the toroidal number N_c is concerned, for the aspect *ratio* $R/a = 4$, as in RFX, the minimum number of coils is 24, in order to avoid the generation of a sideband in the tearing mode part of the spectrum while stabilizing an RWM. In RFX-mod, in order to increase the stable operation window

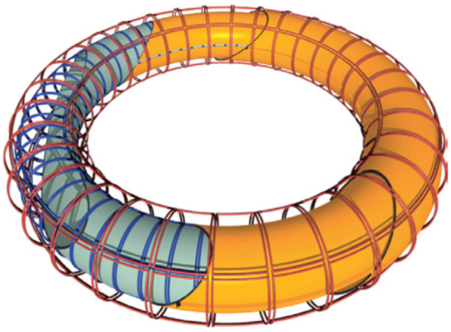

Figure 56. EXTRAP-T2R illustration showing the vacuum vessel (grey), the copper resistive wall (orange), the radial magnetic field sensors placed between the vessel and resistive wall (blue) and the active coils outside the resistive wall (red). Reproduced courtesy of IAEA. Figure from [545]. Copyright 2013 IAEA.

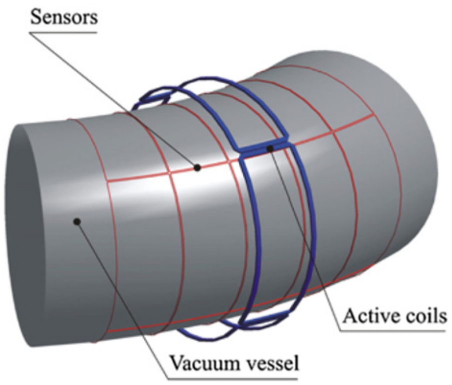

Figure 57. A section of the RFX-mod mechanical and magnetic front end, highlighting active saddle coils (blue) and magnetic sensors (red). In each toroidal location there are 4 active coils and 4 radial field sensors, for a total of 48 toroidal locations. Reproduced courtesy of IAEA. Figure from [646]. Copyright 2011 IAEA.

for radial sensors without overlapping coils, N_c was increased to 48.

A different approach to deal with sidebands aliasing, dubbed *clean mode control* (CMC) [529] and developed for RFX-mod in the context of the control of tearing modes (see next section 7.2), was successfully applied to the current driven $q(a) < 2$ tokamak RWM [530].

7.1.5. Experimental demonstrations of RWM stabilization. Two RFP experiments, EXTRAP-T2R in Stockholm and RFX-mod in Padua, were specifically rebuilt to provide platforms to address experimental studies of active feedback to suppress RWM instabilities. RFX-mod was equipped with a thin copper shell (with $\tau_w = 100$ ms), which replaced the thick aluminium shell of RFX, while the copper shell wall time constant of EXTRAP-T2R was $\tau_w = 12$ ms. As far as feedback was concerned, both experiments implemented the IS geometry: EXTRAP-T2R (figure 56) had $M_c = 4, N_c = 32$ saddle coils and corresponding saddle loop sensors, while RFX-mod was equipped with a matrix of $M_c = 4, N_c = 48$ (figure 57) active coils and sensors.

First experiments on simultaneous stabilization of multiple RWMs in the RFP have been performed with a limited number of active coils in EXTRAP-T2R, i.e. $N_c = 16$, $M_c = 4$ [522], i.e. half of the installed ones (figure 58). In order to reduce power supply requirements, four coils at each toroidal position were hard-wired into two pairs forming $m = 1$ active coils. The sensor coil array was ($N_s = 32$, $M_s = 4$) and the four sensor coils at each toroidal position were also hard-wired forming $m = 1$ sensors [525]. With this configuration, mode coupling of n and $n + 16$ modes due to the sidebands generated by the coil array could be partially resolved by the sensors coils, although not controlled by the active coils. The IS experiments clearly illustrated the effect of the violation of the stabilization criterion $N_c > \Delta n$ derived in [521]: the flux through all the sensors could be maintained at zero although two unstable modes, separated by $\Delta n = 16$, were not zero but with phases aligned to compensate for each other at actuator locations.

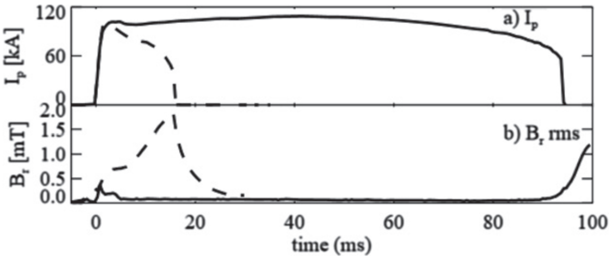

Figure 58. EXTRAP-T2R pulse showing the discharge current and total radial field amplitude at the sensor coil array for a discharge without control (dashed line) and with active control (line).

After the upgrade of the coil power supply system to $M_c = 4$, $N_c = 32$, complete stabilization of the unstable spectrum of RWMs was achieved in EXTRAP-T2R [531, 532] With the optimized feedback parameters, pulse lengths of 90 ms, limited by power supplies [533], were achieved corresponding to about ten resistive wall times (figure 58).

The RFX-mod device resumed operations after the substantial modifications to RFX in 2005 [7] and it also reported clear evidences of unstable RWMs when operating without feedback [77].

Since the beginning, in RFX-mod feedback operations exploited the full coverage by the saddle coil array with $N_c = 48$ and $M_c = 4$, 192 independently controlled coils. The same hardware and the same control algorithms developed for the EXTRAP-T2R device were adopted. Initial operations, based on the selective VS approach, allowed extending the RFX-mod discharge duration from 150 ms to more than 300 ms, with a significant loop voltage reduction, as reported in [85]. Different from EXTRAP-T2R, RFX-mod (as previously RFX) was affected by the wall-locking of tearing modes (as will be described in next section 7.2): therefore, the feedback system was also limiting the radial field penetration of wall locked tearing modes.

RFX-mod has also been operated as a circular ohmic tokamak with toroidal field of 0.5 T. Its particular combination of the copper shell and of the Inconel vacuum vessel geometry is able to convert the $m = 2$, $n = 1$ external ideal current-driven kink that always occurs when $q(a) < 2$ into a RWM. The number of actuator coils was not designed to satisfy the stabilization criteria of this mode: in fact, the standard mode control scheme that was successful for RFP RWMs proved insufficient for the $q(a) < 2$ RWM in the tokamak [530], no matter what gain was used. A simple stabilization criterion for standard mode control has been derived in [534]. Once the clean mode control feedback algorithm was put in place (see section 7.2.3), the RWM was routinely kept at a negligible level for the whole duration of the discharge.

7.1.6. Advanced topics in RWM control. The demonstration of feedback stabilization of RWM instabilities was very important for the RFP concept. After RWM stabilization became routine for the RFX-mod and EXTRAP-T2R RFP experiments, the comprehensive and flexible control systems have been used for a range of additional technology and physics developments of general interest for RWM physics in fusion experiments.

Resonant field amplification (a.k.a. plasma response): the capability of resolving and targeting modes using the control system opened up the possibility to study RFA [535]. A broad spectrum of field errors is ubiquitous and field error harmonics are present in the range of the RWM spectrum. In particular, it was experimentally observed that the spectrum of RWMs, both in amplitude growth rate and in phase, was very reproducible when active control was not operating. This implied the existence of a reproducible field error spectrum, acting as a reproducible seed to the RWM dynamics. The observed growth rate spectrum was not as theoretically predicted: in particular, low n modes $n = \pm 1, \pm 2$, which according to theory were marginally stable, had high growth rates. The field error spectrum contains low n modes associated with shell gaps, leakage flux from the iron core or lack of symmetry in toroidal coil positioning, which should result in RFA. Because the mode growth and phase were reproducible, separate modes could be targeted using an open loop configuration. Transient external control field harmonics were produced and the response of the plasma–shell system was analysed. The growth and the damping rate of modes could be distinguished from the RFA effects and evaluated, giving good agreement with the theoretical predictions.

An important issue in all magnetic configurations is the assessment of error fields during plasma operation, which can be significantly different from error fields measured in vacuum conditions [536]. This was fulfiled by using the reference output tracking capability to produce a simulated external static field error harmonic with controlled amplitude and phase and, simultaneously, the same harmonic rotating with controlled amplitude and phase. The effect of the rotating harmonic on the static field error harmonic depends on the relative phase difference. As the phase of the rotating harmonic passes the phase of the static harmonic, growth and suppression produce an oscillation in the measured amplitude, which can be used to estimate the phase and amplitude of the field error harmonic.

RWM control with partial coverage: a general issue is the development of a control system when the number and placement of control coils is limited for technical reasons. The RFX-mod and EXTRAP-T2R experiments have full active coil coverage but the reduction of coverage can be simulated in the control algorithm software. Furthermore, both devices have well developed control models, so that extensive studies of partial or few-coils coverage can be performed numerically. In RFX-mod, control with reduced coil coverage in the RFP was studied and compared with simulations using the flight simulator with encouraging results [537, 538]. Similar studies were performed in RFX-mod tokamak discharges: as low as six active coils located in the outboard midplane were sufficient to stabilize the current driven $m = 2$, $n = 1$ unstable mode that occurs when $q(a)$ decreases below 2 [537]. In EXTRAP-T2R an attempt to address RWM stabilization with few coils and low coverage was made incorporating the empirically derived model-based control to simulate the control with reduced coverage [539]. Full control was not achieved in these first attempts, though the capability for studies was demonstrated.

Modelling of the control system: an example of the integration of the control system in the demanding technology of a fusion device has been performed at RFX-mod [540], by the adaptation of the CarMa code [541]. This allowed to study the influence on the control system performance of the 3D passive structures surrounding the plasma using the finite element electromagnetic code Cariddi and a 2D model for RFP plasma stability (MARS-F) [541, 542]. In this way, the MHD stability analysis includes the effects of the 3D conducting structures on the control fields. Alternatively to this model-based approach (white box), empirical data have been experimentally collected and a model created for the case without plasma (black box model) [543]. A further advancement in the capability to simulate experimental conditions was the development of a full dynamic flight simulator which includes the features of the CarMa code and a model of the RFX-mod control system [538].

Advanced system identification methods (SIM): the characterization of the RWM dynamics has been performed either theoretically by MHD modelling, or experimentally by observing the mode evolution without feedback control. An alternative approach has been actively developed in EXTRAP-T2R: the RWM dynamics is probed during the feedback-stabilized operations in the real system by simultaneously and exciting the RWM spectrum with pseudo-random spatial patterns (dithering). A minimal physics-based linear model is assumed to represent the data while all parameters (such as the RWM growth rates and the vacuum field penetration time) are extracted from the measurements [544, 545]. The model includes also a prescribed number of aliased side-bands. An important aspect of this kind of technique is that it allows constructing a model that captures the dynamics of the plasma system, including the real 3D wall effects. At the same time, it naturally gives a reasonably small state space [546] representation that can be implemented in real time. An example of the estimated RWM spectrum is shown in figure 59.

The use of closed-loop system identification techniques to enable experimental modal analysis derived solely from empirical data was extended in an experimental study in RFX-mod [547]. Contrary to EXTRAP-T2R, the stabilization diagram for RFX-mod showed unstable activity in the eigenvalue range corresponding to tearing modes. This could be attributed to

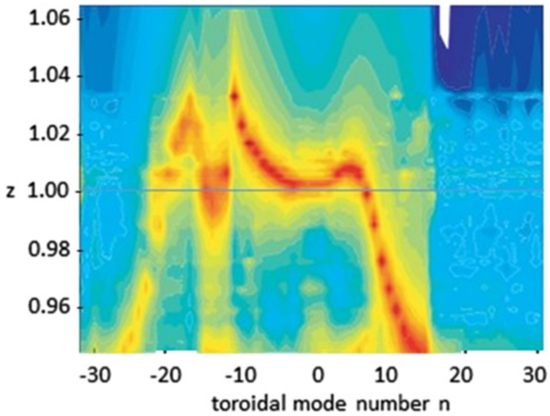

Figure 59. Empirical RWM dispersion relation for T2R. Red colour indicates high modal density (highly probable location of the plasma response eigenvalues; $z < 1$ indicates stability, $z > 1$ indicates instability. Reproduced courtesy of IAEA. Figure from [545]. Copyright 2013 IAEA.

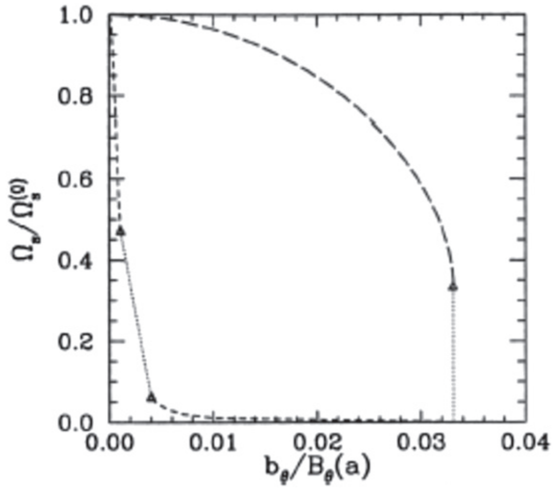

Figure 60. The toroidal angular phase velocity Ω_s of the characteristic tearing mode (normalized to the corresponding velocity $\Omega_s(0)$ in the absence of vacuum vessel eddy currents) as a function of the associated perturbed poloidal magnetic field b_θ seen at the Mirnov coils [normalized with respect to the edge equilibrium magnetic field $B_\theta(a)$] calculated for MST (longdashed line) and RFX (short-dashed line). Reprinted from [550], with the permission of AIP Publishing.

the fact that tearing modes are typically not rotating in RFX-mod. Therefore, the corresponding radial fields (that are well described by a nonlinear dynamic model, as will be shown in next section) are detected by the sensor system and negatively affect the parameters estimate of the linear control model.

The estimated SIM model enables the synthesis of a controller that implements the multiple input multiple output capability of the system. A further refinement based on modern control theory is the development of a model predictive control (MPC) methodology which employs the SIM model for prediction and computes in real time optimal control inputs that satisfy a performance criterion [548]. Since the control model is updated in real time, MPC could have advantages for long pulse operation where discharge parameters, such as equilibrium profiles, change in time.

7.2. Control of tearing modes in the RFP

The issue of wall and phase locking of tearing modes (TM) has been intensively addressed both theoretically and experimentally. In particular, several mitigation approaches have been developed, which are described below. Once major error fields are reduced by careful design or by active coils, the ultimate cause for wall-locking of TM is the conductivity of the nearest closed shell facing the plasma. Based on the experience gained in the RFP devices and in RFX-mod in particular, a modification of the RFX-mod device (named RFX-mod2) is being implemented, as will be described at the end of this chapter.

7.2.1. Wall and phase locking of tearing modes. A basic quasi-linear phenomenological analytical model of the mechanism of wall locking of a single rotating tearing mode was described in [549] for the case of tokamak geometry. An adaptation for the $m = 1$ modes in the RFP has been described in [550, 551], in order to explain the different plasma current threshold for the observed wall-locking of TMs in MST and RFX.

The model assumes that the phase dynamics of a single TM depends on the balance between the electromagnetic torque, produced by the eddy currents on the first resistive conducting wall surrounding the plasma, and a phenomenological viscous torque tending to restore the natural rotation frequency of a tearing mode when it is not wall locked.

With a passive boundary, a bifurcated behaviour occurs, as shown in figure 60. The locking of the mode phase to the wall occurs above a certain mode amplitude while unlocking is found at a significantly lower threshold. The absolute value of the mode amplitude for the locking threshold depends on the resistivity of the closest continuous conducting structure surrounding the plasma. In fact, even though both RFX and MST were equipped with a thick aluminium stabilizing shell, RFX plasma was contained by a vacuum vessel made by Inconel 625 alloy [6]. The significantly higher vessel resistivity was at the origin of a lower mode amplitude threshold for wall locking (short dashed line in figure 60). The behaviour of wall locking in the TPE-RX device was intermediate between RFX and MST. In fact, despite its carefully designed magnetic front-end, with an external thick aluminium shell and an internal thin copper shell, the plasma was contained by an AISI 316L stainless steel vacuum vessel whose resistivity is half than Inconel [10].

Error fields play an important role in the tearing modes wall locking process [552]. They are non-axisymmetric magnetic fields generated, e.g., by eddy currents induced in the non-homogeneous conductors surrounding the plasma due to the gaps in the shells (necessary to allow the penetration of the vertical field) [553] or by a static misalignment of external coils. When the component of an applied error field resonant with tearing modes is above a certain threshold, wall locking is forced because tearing mode braking due to eddy currents is more effective when error fields are present [554, 555]. In RFX-mod, EXTRAP-T2R and MST, thanks to active control coils it was possible to study the braking of plasma rotation when controlled external perturbations are applied [556]. In particular it was possible to measure the dependence of the perpendicular viscosity on the magnetic fluctuation amplitude [557] and compare it with the predicted rate of stochastic field line diffusion [558].

The locked modes phenomenon (introduced in section 2.2.1) i.e. the phase alignment among different TMs, has been modelled by a quasi-linear approach in terms of electromagnetic torques due to three wave nonlinear coupling among $m = 1$ and $m = 0$ tearing modes [552, 554, 559, 560]. The aim of the analytical model was to investigate the formation and breakup of the LM in the RFP, in order to complement 3D non-linear visco-resistive MHD simulations. The electromagnetic torque in the region near a given resonant surface is ascribed to the modification of the linear δJ and δB caused by the three-wave nonlinear coupling among (1, n), (1, n + 1) and (0, 1) modes. In the analysis, the $m = 1$ modes are assumed to be saturated at some level: therefore, their amplitude is considered a fixed parameter. Instead, the $m = 0$ modes are taken as intrinsically stable and only driven by the nonlinear interaction of the $m = 1$ modes. The model predicts that when the amplitude of two coupled tearing modes exceeds a critical value (locking threshold) the two modes phase-lock, while when they are below a much lower critical value (unlocking threshold) their phases are not coupled anymore. In between the two thresholds, both locked and unlocked solutions can occur, depending on the initial conditions.

A thorough analysis of RFX magnetic measurements to characterize the tearing mode spectrum along with the experimental features of the phase-locking phenomenon was documented in [75] and compared with both the Fitzpatrick analytical theory and nonlinear numerical visco-resistive simulations. A partial agreement between the analytical theory and experimental data was found: the residual discrepancy was ascribed to the $m = 0$ modes, which were linearly unstable in RFX due to the large shell/plasma distance $b/a = 1.18$.

A refined theory of mode locking was proposed in [554]: at high mode amplitudes the various tearing modes phase-lock together minimizing the magnitude of the electromagnetic torques exerted at the mode rational surfaces. In particular, the relative phase of $m = 0$ modes was assumed to remain constant in time at the value observed experimentally and that was found to correspond to the minimum absolute value of the electromagnetic torque.

7.2.2. Mitigation techniques of the locked mode. In RFX [561, 562] and in MST [117], the intrinsic error fields were reduced by analog magnetic feedback systems using local saddle coils. Passive reduction of error fields, by means of an overlap of the shell edges, was implemented in TPE-RX [10] and in RFX-mod [563].

In RFX the active control of the position of the wall locked tearing modes was obtained by means of an external non axi-symmetric $m = 0$ magnetic field, obtained by modulating the currents in the toroidal field coils [423], thanks to the non-linear coupling between the $m = 0$ and the $m = 1$ TMs [554].

In RFX-mod, the active feedback by saddle coils allowed a significant mitigation the effects of wall locked tearing modes.

A first improvement compared to RFX and to passive RFX-mod operations [77], was obtained during initial operations with the VS algorithm [76]. Nonetheless a significant toroidally localized PWI was still occurring [79], due to the unrecognized sidebands aliasing described in section 7.1.4. Several forced rotation algorithms were therefore implemented [76], taking advantage of the direct coupling of each ($m = 1$, n) TM with the corresponding field harmonic generated by the control coils. Slow tearing mode rotations up to 40 Hz were observed, together with a slow rotation of the PWI region. Due to the sidebands' aliasing systematic error (section 7.1.4), the VS control algorithm only partially reduces the edge amplitudes of tearing modes, as illustrated by the Fourier spectra shown in figure 61. In a VS controlled discharge, in fact, the Fourier spectrum of radial sensor measurements is significantly low, but these harmonics do not correspond to the real amplitude of tearing modes as they are polluted by coils sidebands. Red bars show instead the clean harmonics corresponding to the real amplitudes of tearing modes, which are much higher and explain the observed PWI. The clean harmonics are obtained by a de-aliasing algorithm: the measured currents flowing into the control coils are used in a vacuum cylindrical model to obtain the time behaviour of the relevant sidebands to be subtracted from the raw harmonics (details are described in [529]).

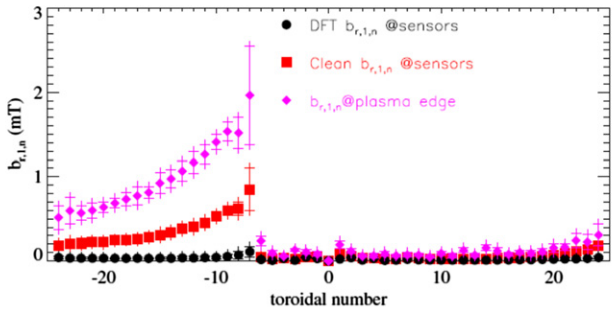

Figure 61. Ensemble averaged spectra of the radial field for the $m = 1$ harmonics: (circles) DFT harmonics of the measurements; (squares) clean Fourier harmonics; (diamonds) harmonics extrapolated at plasma radius. A set of reproducible VS discharges is considered. Averages are taken during plasma current flat-top times, $60 < t < 120$ ms, $I_p = 0.79 \pm 0.04$ MA, $n_e = 2.1 \times 10^{19} \pm 0.2 \times 10^{19}$ m^{-3} and similar equilibrium. Reproduced from [118].

7.2.3. Spontaneous rotation of tearing modes with clean mode control. A second significant improvement of RFX-mod discharges was obtained by the implementation in real-time of the clean mode control de-aliasing algorithm [118] and allowed RFX-mod to reach the design current of 2 MA.

The correction of the aliasing error revealed that control of tearing modes exhibit a non-linear behaviour: with clean mode control, it is possible to reduce the edge amplitude of each wall-locked tearing mode down to a minimum value, by properly increasing the corresponding proportional gain (figure 62(*b*)) [529]. Any further increase of gains generates a rotation of increasing frequency (figure 62(*a*)). On the other hand, active feedback with clean mode control was found to remove the bifurcated behaviour of the wall locking of tearing modes as described in section 7.2.1. During optimization experiments of He discharges with very low plasma current (I_p < 150 kA a regime that was never investigated in RFX) the spontaneous rotation of tearing modes was observed (figure 63) [564]. On the one hand, such a low wall-locking threshold was expected, due to the high resistivity of Inconel vessel. On the other hand, a new unexpected feature of these RFX-mod experiments was the observation that the natural rotation locking threshold correspond to the unlocking one. As in RFX-mod tearing mode amplitudes scale almost linearly with plasma current I_p, the reversibility of the locking threshold with plasma current reflects a reversibility with mode amplitude: this is a marked difference with respect to the hysteresis observed in all other passive RFP experiments.

7.2.4. Modelling of tearing mode phase dynamics under feedback control. The rotation of tearing modes subject to clean mode control was initially reproduced by a stationary nonlinear model [529], based on the same physics mechanisms describing the single TM wall locking in RFX as in [554]. The active control coils are modelled as a harmonic error field whose amplitude and phase are determined by a prescribed feedback law. By assuming a time-constant mode amplitude at the resonant surface, above the wall-locking threshold, in the absence of feedback the mode would be strictly wall-locked. Instead, by applying feedback, the model shows the existence of equilibrium solutions, corresponding to uniform rotations of the mode with frequencies larger than $1/\tau_w$, for gains above a threshold value. These rotations establish with low edge amplitude: this is the advantage of the feedback with respect to feed-forward techniques to induce LM rotations.

Subsequently, a time dependent code including nonlinear phase coupling among multiple $m = 1$ tearing modes, dubbed RFXLocking, was developed [565]. In this code the $m = 0$ low n modes are assumed to be always phase locked, consistent with the experimental RFX findings. As in previous wall-locking studies, the model evolves the mode edge amplitudes and phases under the action of the feedback coils, while the mode amplitudes at the resonant surface are estimated from the experimental measurements.

Thanks to a modified version of RFXLocking, implementing the multiple-shell structure of RFX-mod, a model-based optimization has been performed [566], in order to find an optimal gain set and reduce the edge radial magnetic field amplitude of each tearing mode to the lowest possible value compatible with the tearing mode dynamics.

RFXLocking also reproduces rather well the tearing mode dynamics as a function of the feedback gains. The effect of the proportional gain on the ($m = 1$, $n = -7$) mode angular

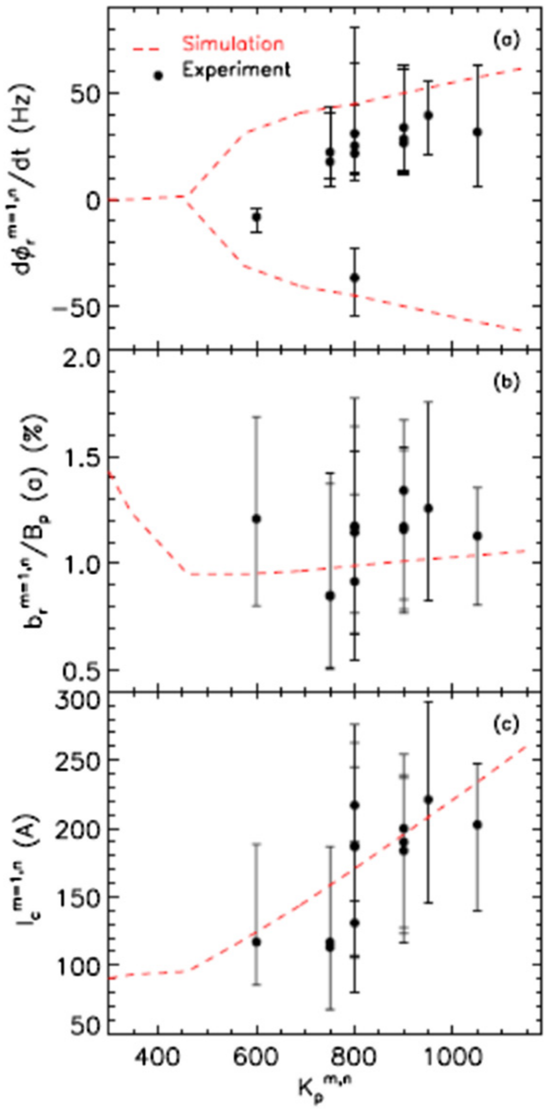

Figure 62. Effect of a proportional gain scan on (*a*) the $m = 1$, $n = -7$ mode angular frequency, (*b*) the (1, −7) normalized edge radial magnetic field and (*c*) the $m = 1$, $n = -7$ coil current amplitude. Each point represents a flattop average and the experimental points are from a set of 1.4 MA reproducible discharges. The error bars are 25th and the 75th percentiles of the data. They represent the variation of the above quantities due to the natural mode dynamics, not measurement errors. The red dashed curve represents the RFXLocking core prediction. Reproduced courtesy of IAEA. Figure from [566]. Copyright 2010 IAEA.

frequency, the normalized edge radial magnetic field and the coil current is shown, for example, in figure 62. The experimental data (full circles) are compared with the model prediction for the same type of discharges (red dashed line). Each point represents a time average over the discharge flattop. A reduction in the total edge radial magnetic field has been obtained with the model-based set, with respect to the empirically optimized one.

The RFX-mod CMC experiment has shown some limitations in the possibility of reducing the edge radial field even when using the radial field harmonics extrapolated at the plasma surface [118] as the feedback variable. The edge radial field cannot be reduced below a minimum non-zero value for

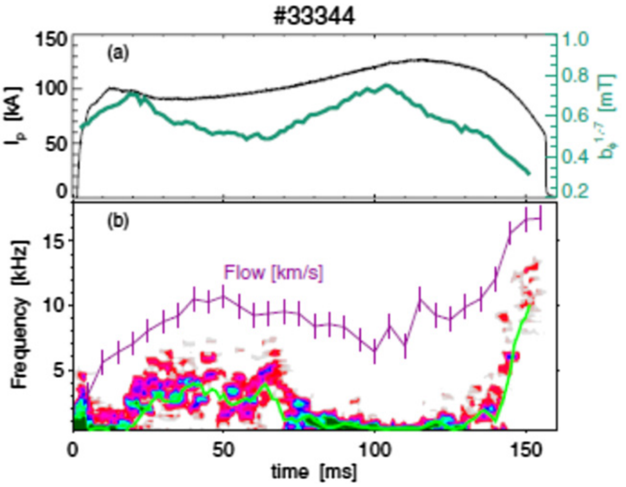

Figure 63. Time traces from shot 33 344 for the $m = 1$, $n = -7$ TM. Top: time traces for plasma current (black line) and toroidal field harmonic amplitude (green line). Bottom: spectrogram of the mode frequency (the light green line is the estimated time behaviour) and line-averaged plasma flow toroidal velocity from spectroscopic measurements (purple line). Reproduced courtesy of IAEA. Figure from [564]. © 2014 EURATOM.

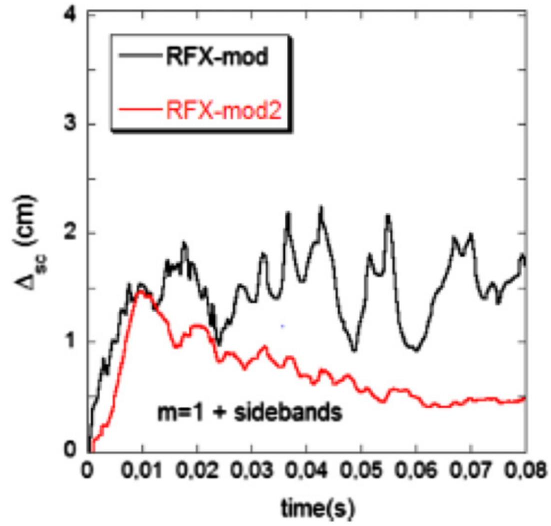

Figure 64. Deformation of the LCMS, with the vacuum vessel removed (red) and with vacuum vessel (black). Reproduced courtesy of IAEA. Figure from [347]. Copyright 2017 IAEA.

each tearing mode. This limitation is not related to the coils' amplifiers, but is physically based, as it can be reproduced by the RFXLocking code that shows the existence of a minimum radial field in an optimum gain region [534]. More precisely, simulations with RFXLocking showed that the ultimate CMC possibilities are fixed by the plasma–shell proximity: no matter the radius where the virtual sensors are located, the actively controlled radial field is always higher than the one obtained by an ideal shell that replaces the resistive one.

7.3. Future perspectives: the design of RFX-mod2

Based on the aforementioned understanding of the interplay between passive conductive boundaries and tearing modes in an RFP, an upgrade of the RFX-mod machine assembly has been designed, dubbed RFX-mod2, and it is now being implemented [19–21, 114]. Main aim of such upgrade is to modify the resistivity and proximity of the magnetic front-end. This will allow reducing the saturated level of tearing modes, and subsequent magnetic chaos, due to increased proximity of the shell to the plasma. Moreover, it will decrease the non-axisymmetric deformation of the last closed magnetic surface (LCMS), due to the phase locked tearing modes. Finally, the plasma current threshold for the wall locking will increase, allowing a better plasma start-up phase.

In RFX-mod2, the stainless steel vacuum vessel containing the RFX-mod plasma will be removed, and the copper shell will become the first conductive surface for the plasma. The vacuum barrier will be provided by the properly modified toroidal support structure. The shell/plasma proximity will be reduced from $b/a = 1.11$ to $b/a = 1.04$. This design choice implies challenging modifications of the components of the machine close to the plasma, while maintaining the existing magnetic coil system. Innovative solutions have been conceived to fulfil vacuum and electrical requirements of the in-vessel components, in particular to ensure their reliability during the operation also in presence of abnormal events.

According to model simulations, this magnetic configuration will reduce the deformation of the LCMS by a factor about 2–3 with respect to RFX-mod, see figure 64 [347]. Moreover, the 3D nonlinear MHD Specyl, including realistic boundary conditions, predicts a reduction of the energy of unstable modes by about 30% [114].

8. Plasma–wall interactions

As in other magnetic confinement devices, in the RFP the PWI plays a crucial role in determining plasma behaviour and performance through the control of plasma density and impurity contamination. In RFPs, PWI is strictly dependent on the magnetic topology, being strongly influenced by the three-dimensional edge magnetic fields related to the wall locking of tearing modes also define locked mode (LM) that produces a localised deformation of the LCMS. When such bulge of the LCMS is wall locked, a large power is deposited onto a relatively small region of the wall, with uncontrolled release of main fuel and impurity particles.

8.1. Effect of magnetic topology on plasma–wall interaction

The LM drives large localized power fluxes onto the wall in the region intersected by the distorted magnetic surfaces. An example of the footprint on the first wall in an RFX discharge is shown in figure 65, compared with the reconstruction of the plasma surface deformation.

In RFX (and in RFX-mod afterwards), the plasma wall is fully covered by polycrystalline graphite tiles, to protect the Inconel vacuum vessel and avoid metal contamination [6]. Though local field errors introduced by the insulating poloidal gap (allowing for the penetration of the magnetic field) were reduced by a local active control system, LMs still produced a

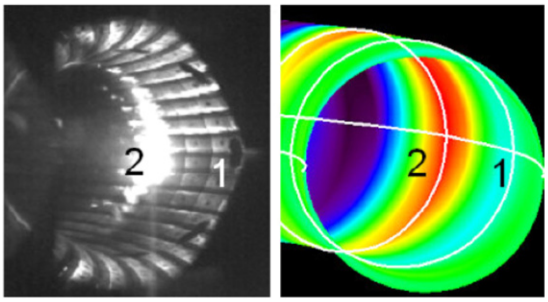

Figure 65. (Left) footprint of the perturbation associated to the LM in an RFX-mod discharge as observed by a CCD camera; (right) magnetic reconstruction of the perturbation. Colour code refers to the distance between the non-axisymmetric plasma and the wall. Reprinted from [79], Copyright 2007, with permission from Elsevier.

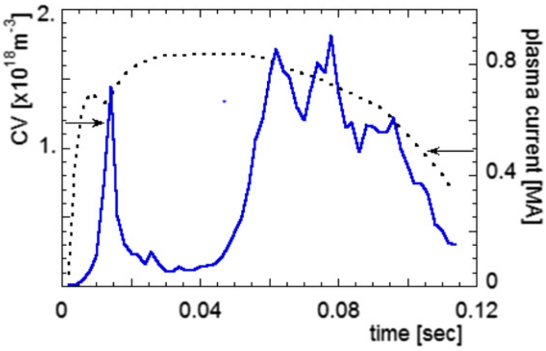

Figure 66. Time evolution of plasma current (dashed) and CV density in an RFX discharge with carbon blooming, manifesting as a strong carbon enhancement and corresponding current decrease.

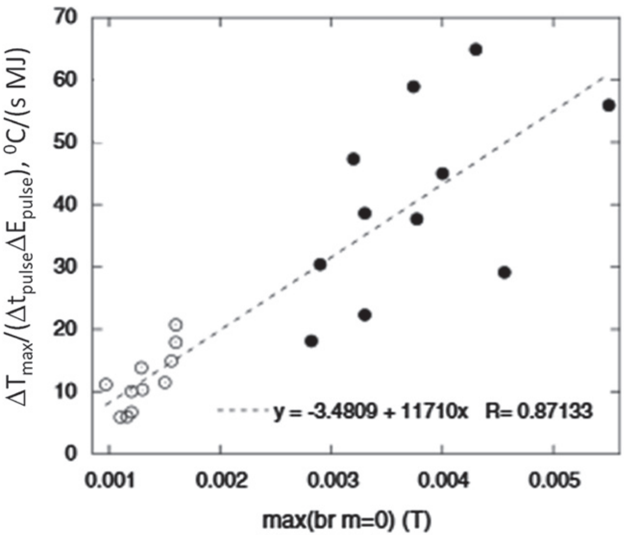

Figure 67. Evolution of maximum wall temperature in RFX-mod as a function of $m = 0$ maximum radial field. Empty circles: with feedback; black circles: without feedback. Reprinted from [79], Copyright 2007, with permission from Elsevier.

large radial displacement of $\approx$2 cm [567], determining power loads locally as high as $\approx$100 MW m^{-2} in the region where the bulge intercepted the wall [80]. This was associated to local enhancement of electron density and density fluctuations, suggesting a continuous ionization and loss of neutrals, and to increased transport and impurity influxes [568]. Carbon and oxygen influxes from the LM region were estimated to be of the order of 20%–40% of the total; however, tomographic measurements of total radiation showed that, due to the relatively small region of interaction, the radiation enhancement produced by LM was a fraction of the total input power of the order of $\approx$10%, leading to the conclusion that the main loss term is due to the local increase of transport and particle fluxes [80]. With plasma current approaching 1 MA, in proximity of LM the graphite tiles reached the carbon radiation enhanced sublimation temperature, producing carbon blooming processes, observed as sudden increase of carbon, radiation and electron density. Such strong particle release locally cooled the plasma, leading to the loss of density control and to the premature decay of the plasma current [78, 569–571]. An example of carbon behaviour when such blooming processes occurred is given in figure 66. A rather crude means to mitigate PWI and carbon blooming was found by applying a toroidally rotating $m = 0$ perturbation, thus forcing a rotation of the bulge associated to LM [423] (section 7.2.2). This technique increased the amplitude of $m = 0$ modes, with associated confinement loss, but the enhanced interaction region was distributed in time over all toroidal angles, allowing reproducible operation up to 1.1 MA. A different approach to mitigate PWI in RFX was adopted by increasing the power radiated at the edge by impurity seeding (in particular neon) [572]. This operational scenario did not affect confinement properties, while both poloidal and toroidal asymmetries of radiated power were reduced, in particular in the high-density regime.

Despite all these issues related to the strong PWI induced by the presence of the LM, in RFX quite low effective charge values were observed, $Z_{\mathrm{eff}} \approx 1.5$ (except for very low density regimes, where the bremsstrahlung measurements become anyway difficult), independent of plasma current. This result has been interpreted as due to a screening mechanism, modelled by a Monte Carlo calculation, associated to a low ratio between impurity ionization length and Larmor radius, and to the presence of a radial electric field which points inward at the wall and outward in the edge plasma [573].

In RFX-mod, TM mitigation techniques, described in section 7.2, allowed obtaining a smoother PWI, compared to RFX. Moreover, the shape of carbon tiles in RFX-mod was optimized in order to avoid strong interactions at their edges [7].

The ratio between the maximum wall temperature increase and the total energy input times the discharge duration $\Delta T_{\mathrm{max}}/(\Delta t_{\mathrm{pulse}}\Delta E_{\mathrm{pulse}})$ has been taken as an indicator of PWI intensity in [79]. This indicator has been found to be correlated with the maximum of the radial field associated to $m = 0$ modes (figure 67), thus implying a dependence of the edge properties on $m = 0$ tearing modes.

Similarly, in the EXTRAP-T2R device before the active stabilization of RWMs, spectroscopy and collector probe measurements showed large metal emissions (Mo and Cr), and arcing was identified as an important contributor to metal

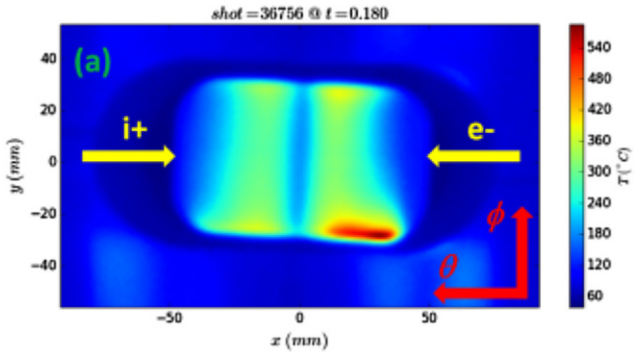

Figure 68. Graphite temperature by an IR camera in RFX-mod; the *x* axis corresponds to the poloidal direction, the *y* axis to the toroidal one. Reprinted from [579], Copyright 2017, with permission from Elsevier. CC BY-NC-ND 4.0.

release [574]. Such effects were mitigated with the application of the active feedback control and allowed a strong improvement of the performance [522].

In the RFX-mod QSH states, the plasma edge is modulated by a helical ripple, thus wetting the wall over a helical region much larger than in the MH state. In such regimes, edge plasma parameters are helically modulated too [208]. In QSH, the power density deposited in the portion of the wall wetted by the helix is ≈5 MW m^{-2} also at the highest current [575], and the plasma radiation is globally more symmetric than in MH [576]. On average, in QSH states the locking region accounts for ∼18% of the total radiated power, which corresponds to a PWI improvement by at least a factor of three with respect to the MH states and the former RFX [346].

Even in good QSH states, in RFX-mod there is still a residual PWI associated with the phase locking of the secondary modes. Correspondingly, the magnetic connection length to the wall presents a strong decrease ('hole') with increased PWI (by a factor ranging between 2 and 10), which is not stationary thanks to the feedback control system. In the RFX-mod2 upgrade it has been calculated that secondary mode locking and associated PWI could be completely avoided [346].

It has to be mentioned that in RFPs the footprint of PWI also shows a poloidal asymmetry between ion and electron drifts, with electron and ion flows separately intercepted by the wall, due to the surface distortion [366, 367, 577, 578]. An example is shown in figure 68. Such asymmetry is more pronounced at low density, indicating that at low density a significant fraction of the poloidal current is due to suprathermal electrons [579]. The separate interception of ion and electron flows at the LM, is at the origin of halo currents which in RFX flowed into the Inconel vessel with intensity up to 25 kA [580], dissipating ≈4%–5% of the total power input.

8.2. Recycling control

In devices with carbon wall as RFX or RFX-mod, the value of plasma density is determined by wall desorption rather than by the fuelling rate. In fact graphite is shot by shot saturated with trapped hydrogen/deuterium, so that the plasma density after the breakdown is completely sustained by atoms released by the wall, with a recycling coefficient *R* which can be greater than 1 [211, 578]. The number of released particles depends both on the number of atoms stored in the graphite and on the power load on the wall, which makes density control very difficult, especially at high current. On the other hand, in RFPs, in addition to gas puffing, the only central fuelling is by pellet injection (no continuous direct core fuelling by neutral beams is applied), and the particle confinement times are relatively low (of the order of 10 ms, see for example [26]). Therefore, very low recycling regimes cannot be sustained. In summary, a good density control can be obtained with *R* close to 1 with a not saturated first wall, which is an equilibrium more difficult to achieve in devices with a full graphite wall: indeed, when in EXTRAP-T2R the carbon armour was replaced by molybdenum limiters, the density control improved [9].

In order to guarantee such conditions, in particular avoiding uncontrolled strong release of particles in high current discharges, effective wall conditioning treatments have been applied, including glow discharge cleaning (GDC), pulse discharge cleaning (repetition of short, low energy plasma discharges), operation with hot wall, boronization, lithization. GDC has been applied in devices with graphite wall (EXTRAP-T2, RFX, RFX-mod), mainly with helium as working gas, to remove trapped hydrogen or deuterium; only occasionally GDC in H has been used to remove impurities [581, 582]. In RFX-mod, the effect of such kind of treatment has been characterized [582], showing a toroidal non-uniformity with respect to the positions of the electrodes: the ion flux to the wall features a distribution ±30° wide around the electrodes.

In RFX, to ensure the operation with a non-saturated graphite as plasma facing material, the wall temperature has been raised up to 280 °C in some plasma sessions. A lower effective recycling characterized such pulses, but the wall response was still more unpredictable, with frequent sudden density build-ups and current quenches. This was associated with an easier overheating of graphite tiles in presence of highly localized power loads, up to the carbon sublimation temperature [583]. Such uncontrolled events were instead avoided soon after a boronization. Boronization has been applied with different techniques on several RFP devices, including EXTRAP-T2 ([584]), MST ([585–587]), RFX([588, 589]) and RFX-mod [575]. A common result in all the experiments is that boronization is effective in reducing recycling, for a number of plasma shots that is dependent on the applied technique and boron layer thickness, on plasma regimes and on carbon redeposition rates. The analysis of samples exposed to the boronization treatments showed that a crucial issue to ensure a good behaviour of a boronized wall is to obtain the deposition of a uniform layer [587, 590, 591]. In carbon wall devices where boronization is periodically performed, as RFX and RFX-mod, its lifetime is mainly limited by carbon erosion and redeposition processes, decreasing with increasing power loads [592].

Two examples of the positive effects obtained in MST and RFX are given in figures 69 and 70, respectively. Figure 69 shows how after boronization the same plasma density is sustained by a higher gas puffing [587], while figure 70 displays

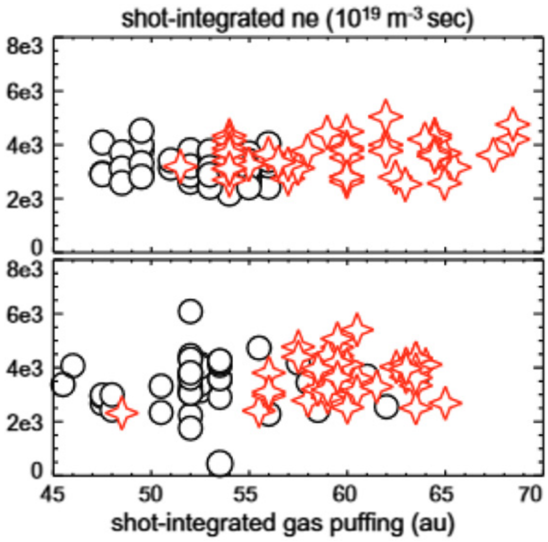

Figure 69. Electron density integrated during the current flat-top as a function of the total number of particles puffed in the MST device before (black circles) and after (red stars) boronization. Reprinted from [587], Copyright 2013, with permission from Elsevier.

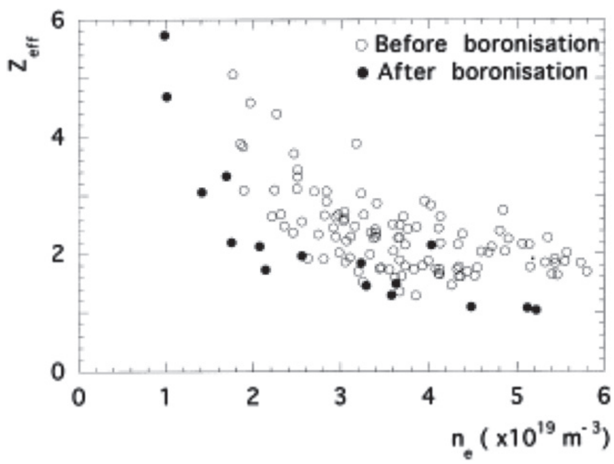

Figure 70. Effect of boronization on Z_{eff} in the RFX device. Reprinted from [573], Copyright 1999, with permission from Elsevier.

a reduction of the plasma effective charge with boronization [573, 593]. In MST, it has also been found that the operation with boronized wall can be associated to discharges featuring prolonged phases (up to 20 ms) without DREs. In such phases, which are believed to be related to a lower plasma resistivity, the energy confinement time increases by a factor 3 [453].

Following the experience of several tokamaks (see for example [594–596]) and stellarators [597], conditioning by lithization has been implemented in RFX-mod by a lithium capillary–pore system [575, 598] and lithium pellet injection [117, 599]. A significant decrease of oxygen and carbon influxes and emissivities (carbon and oxygen are by far the prevailing impurities in RFX) has been found, for carbon in particular more pronounced than with boronization. The important effect was the improvement of density control, which was the main aim of these experiments and allowed operation at high current ($\geqslant$1.5 MA) with higher density, up to

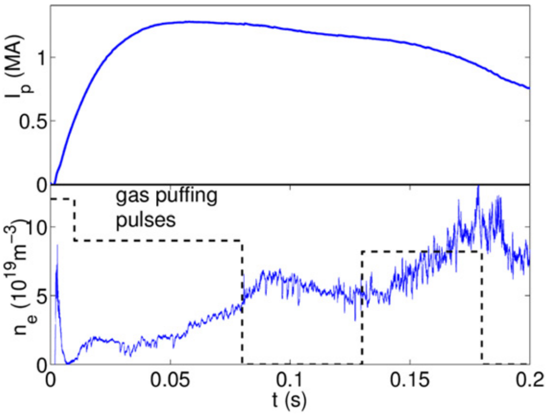

Figure 71. Time evolution of plasma current (top) and electron density (bottom) after lithization in RFX-mod. Pulses of puffed gas are superimposed (dashed), showing the good response of density. Reproduced courtesy of IAEA. Figure from [575]. Copyright 2013 IAEA.

$n/n_G \approx 0.5$: an example is shown in figure 71. Despite a slight peaking of density profiles, confinement was not significantly improved.

Also in the case of lithization, a main issue remains the uniformity of Li deposition, though a more uniform layer has been obtained by multi-pellet injection [599]. An additional operational issue is related to the fact that, when the machine is vented and opened for maintenance, the formation of Li_2CO_3 (difficult to remove in a device lacking of a direct access to the first wall) must be prevented by a long boronization with argon flushing and careful minimization of the opening time [575].

8.3. Dust particles

Dust particles (small loose particles agglomerates, sized from tens of nanometres to millimetre) can be an issue in fusion plasma devices, as they potentially represent a safety hazard, an impurity source and a cause of surface damaging. In this respect, their behaviour has been extensively studied in tokamaks (see for example [600]), while only few papers addressing this issue and related to the EXTRAP-T2 and T2R device have been produced. Main results of such experimental and modelling studies can be summarized as follows:

(a) The preferential origin of dust formation is related again to the high power load deposited in the LM region, where small agglomerates are ejected. In EXTRAP-T2R, in discharges without active feedback more dust particles have been captured (by silica aerogel collectors) than in discharges with active feedback [601, 602];
(b) Post-mortem measurements indicate that most of dust particles are spheroids covered by deposits with granular morphology (figures 72(*b*) and (*c*)) and coated by corrugated layers containing Mo and stainless steel components, indicating that re-mobilization is an important element of intrinsic metal dust dynamics [603];
(c) Some particles elongated and aligned with plasma flow have been detected, (less than 20% of the total, see figure 72(*a*)) suggesting a relevant effect of ion drag [602, 603].

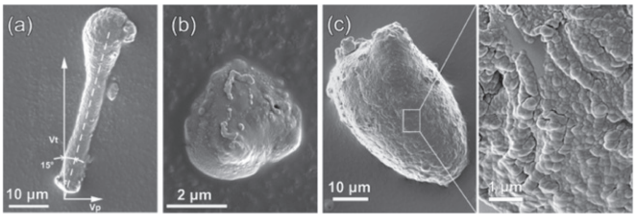

Figure 72. Examples of SEM analysis of dust particles collected post-mortem in EXTRAP-T2R.by adhesive tape. Particles are mainly spheroids covered by deposits (*b*) with granular morphology (*b*) and (*c*). Few elongated particles also observed (*a*). Reproduced from [603].

8.4. The problem of the power exhaust and future directions

Due to the necessity of a close-fitting conducting wall, the RFP devices presently in operation are not equipped with divertors. In the past some studies and experiments on small size devices have been produced in order to explore the impact of a divertor (poloidal and toroidal) on plasma stability and its capability in particle control [604–607] and heat control [608]. Results, though not conclusive because obtained in devices not equipped with effective MHD control systems, showed sometimes some positive effects (decrease of light impurities), but also significant worsening of plasma performance, with increased fluctuations at the X-point and early termination of the discharge.

As an alternative to divertors, the vented pump limiter has been proposed for the RFP as a means for actively controlling neutral particles at the wall [589]. The concept of the vented pump limiter, as applied in the Tore Supra tokamak [609], is to provide a limiter head designed in such a way to be transparent (slots between blades) to recycled neutrals, which enter the limiter and can be extracted. A system of this kind has never been experimentally applied to RFP devices so far. The weak point was the capability of the blades in sustaining power loads that can be locally very high. Another important drawback is that the edge topology is not stationary in time neither uniform along the poloidal and toroidal angles, which indeed makes any tool designed for a tokamak of difficult application in an RFP.

A more viable solution seems to exploit the similarity of the 3D field structures of RFPs and stellarators. In fact, an interesting possibility, proposed in [610], exploits the peculiar topology of the RFP to produce a magnetic configuration resembling the island divertor of the stellarator [611]. The concept is based on the chain of $m = 0$ magnetic islands that in QSH-SHAx states develop at the reversal surface with the same helicity as the dominant mode. In principle, in an RFP device with sufficiently low secondary mode amplitudes, the LCMS could not intercept the wall, while the X-points of $m = 0$ islands would act as the X-point of a divertor. Divertor plates with pumping could be placed in such regularly spaced regions of interaction. The drawback is again that this technique requires stationary $m = 0$ modes, not observed so far, but in principle achievable, given their strict phase relation with $m = 1$ modes, which can be feedback controlled.

As mentioned in section 8.1, the injection of neon in the edge of RFX produced a more symmetric distribution of the radiation without neither penetrating into the core nor affecting the confinement properties. Therefore, though these experiments have not been subsequently investigated in RFX-mod or in other RFPs, they could be promising for future devices and should be further explored, for example in RFX-mod2, as a means to control the power exhaust.

Though the ameliorated magnetic boundary expected in RFX-mod2, according to model predictions, should reduce by a factor 2–3 the radial extent of the deformation of the LCMS (section 7.3) and strongly mitigate the PWI, the power exhaust remains a crucial issue for a future RFP reactor, requiring further modelling and experiments.

9. Current sustainment by oscillating field current drive

One of the most important attributes of the RFP configuration is large ohmic heating from its relatively large plasma current. This creates the possibility for ohmic ignition [612] and eliminates the need for auxiliary heating. Inductive current drive via a transformer is robust and efficient, and it does not introduce special plasma–boundary requirements related to RF launchers or require perforations in the blanket and shield.

The principal drawback of inductive current drive is that it is not strictly steady state as a consequence of Faraday's law of induction. While there is no fundamental reason why a pulsed-reactor concept cannot work, studies show that pulsed operation tends to increase system size and cost [613]. Indeed, a large emphasis in advanced tokamak research is placed on the development of steady-state scenarios that maximize the self-driven neoclassical bootstrap current and minimizes auxiliary current drive, and stellarator research aims to minimize or eliminate plasma current at the expense of toroidal symmetry.

A quasi-steady-state method of inductive current sustainment, called OFCD, has been identified that creates an ohmic, steady-state sustainment scenario for the RFP. In OFCD, audio-range oscillatory toroidal and poloidal loop voltages are applied to the plasma, and the plasma's nonlinear self-organization process generates a dc current. Accumulation of magnetizing flux is avoided, and the plasma current can be sustained indefinitely since the loop voltages have zero time-average. A remnant inductive ac ripple appears in the equilibrium magnetic field, but the amplitude of the ac ripple is projected to be only a few percent for a reactor plasma that has low electrical resistance. This creates an attractive, steady-state method for current sustainment that maintains the simplicity, robustness, and high efficiency associated with inductive current drive. The TITAN fusion power plant study employed OFCD to attain a steady-state, compact fusion power core based on the RFP (see chapter 10).

The theoretical basis for OFCD has greatly matured as part of the development of nonlinear visco-resistive MHD modelling of RFP plasmas. The physics basis and modelling specific to OFCD are reviewed in sections 9.1 and 9.2. Several

OFCD experiments have been conducted on RFP plasmas that are consistent with theoretical and modelling expectations, which are reviewed in section 9.3. Unfortunately, a demonstration of full current drive by OFCD is not expected to be possible in present day RFP devices due to the scaling for the ac ripple that sets a limit on the equilibrium excursion during an OFCD cycle. Plasmas with larger Lundquist number, i.e., larger size and temperature, are necessary to test full current drive by OFCD.

There have been a couple of experimental studies of OFCD on tokamak plasmas which are not discussed here in detail. The first was performed on the small Caltech tokamak without evidence for current drive [614]. There was also an attempt on the DIII-D tokamak using modulation of the plasma elongation to oscillate the toroidal flux, also without evidence for current drive [615]. Relaxed-state modelling shows OFCD is less effective at high safety factor [616], in addition to the concern that tokamak plasmas might not access instabilities that govern plasma relaxation.

9.1. Introduction to oscillating field current drive

The OFCD current drive method derives from the principle of a relaxed state, where (see chapter 3) the magnetic energy is minimized subject to the constraint of conserved total magnetic helicity, K. The relaxed-state magnetic equilibrium satisfies $\nabla\times\mathbf{B} = \mu\mathbf{B}$, with $\mu =$ constant. Conservation of magnetic helicity motivates a helicity balance, given by $\partial K/\partial t = 2V_{\mathrm{T}}\Phi - 2\int \eta\mathbf{J}\cdot\mathbf{B}\mathrm{d}V$, where V_{T} is the toroidal loop voltage at the plasma surface and Φ is the toroidal magnetic flux embedded within the plasma. The first term is the rate of helicity injection, and the second term is ohmic dissipation of helicity resulting from the plasma's finite resistivity, η. Conventional induction injects magnetic helicity (and drives current) through a pulse of toroidal loop voltage generated by the transformer that links the torus.

There is a close correspondence between magnetic helicity, plasma current, and the Poynting theorem for electromagnetic energy [617]. Bevir and Gray [618] recognized that, if the toroidal and poloidal loop voltages are sinusoidal, then net cycle-average helicity injection is possible, i.e., $\partial K/\partial t = \left(\hat{V}_{\mathrm{T}}\hat{V}_{\mathrm{P}}/\omega\right)\sin\,\delta$, where ω is the oscillation frequency, δ is the relative phase between the loop voltages, and the over-hat identifies the ac amplitude of the toroidal and poloidal loop voltages. Note that the poloidal loop voltage $V_{\mathrm{P}} = -\mathrm{d}\Phi/\mathrm{d}t$, so there is a concomitant oscillation in the applied toroidal magnetic field. If the phase, $\delta = \pi/2$, then the rate of helicity injection is maximized. This corresponds to driving a net dc plasma current using purely ac loop voltages, hence the terminology 'ac helicity injection' or OFCD. Note that phase $\delta = -\pi/2$ permits anti-drive, which is used experimentally to induce a current ramp-down and study the dependence on the relative phase. The frequency, ω, must be faster than the inverse resistive diffusion time, $\tau_{\mathrm{R}}^{-1} = \eta/\mu_0 a^2$, but slower than the process that governs magnetic relaxation, i.e., for the RFP, the resistive-Alfvénic hybrid timescale ($\sqrt{\tau_{\mathrm{R}}\tau_{\mathrm{A}}}$) associated with magnetic reconnection from tearing instability, typically in the audio frequency range. At audio frequency, the OFCD inductive current drive has Spitzer conductivity. The principal concern for OFCD may be the impact on energy confinement, since the relaxation process happens through fluctuations. The scaling of these fluctuations is important as it is for conventional pulsed induction.

The formal connection between helicity injection and current drive has been developed in detail [617, 619] and includes dc helicity injection using electrodes which link magnetic flux. This is the basis for coaxial helicity injection (CHI) used extensively for spheromak formation [152, 620] as well as non-inductive start-up of low aspect ratio tokamaks [621, 622]. It also applies to 'localized helicity injection' using compact plasma sources inserted into the plasma. This approach was used on MST as a means for current profile control [460, 623] and has been further developed on the PEGASUS low aspect ratio tokamak as an alternative to CHI for tokamak start-up [624]. A version of ac helicity injection termed 'steady inductive helicity injection' is also being investigated to sustain spheromak plasmas, which aims to minimize the ac ripple by using loop voltages sources that are not toroidally symmetric [625, 626].

9.2. Modelling and scaling predictions

While nonlinear MHD as discussed in chapters 3 and 5 provides a first-principle description for OFCD, a simplified limit is described first in which a global electromagnetic power balance is applied to a plasma that is assumed to maintain a relaxed-state instantaneously. The 3D dynamics are not resolved, but important effects on the magnetic equilibrium are revealed. This demonstrates OFCD on the basis of energy conservation and makes predictions for the evolution of a relaxed-state plasma. Because this approach resembles circuit analysis, it has also been referred to as zero-dimensional modelling [616, 627, 628].

The distinctive feature of a relaxed-state plasma is a rigid (normalized) parallel current profile, $\mu_{\|}(r) = \mu_0\mathbf{J}\cdot\mathbf{B}/B^2$, independent of varying electrical boundary conditions. Small amplitude fluctuations are assumed to provide a turbulent emf in just the right amount at each radius to maintain the relaxed profile. Any partially relaxed state that is time-space separable as $\mu_{\|}(r,t) = \lambda_0(t)\Lambda(r)$ is appropriate for this modelling, where λ_0 is the magnitude of $\mu_{\|}(t)$ at $r = 0$ and $\Lambda(r)$ is the spatial form of the rigid profile. The tendency for fixed $\Lambda(r)$ is the hallmark characteristic of relaxation dynamics in an RFP plasma. For example, the profiles of MST plasmas have $\Lambda(r) \approx 1 - \left(r/a\right)^4$ over a range of operating conditions. The gradient $\mathrm{d}\Lambda/\mathrm{d}r$ is proportional to the free energy for current-driven tearing instability, and dynamically there is a tendency to maintain marginal tearing stability at each instant in time via nonlinear feedback from the dynamo-like emf, $\langle\tilde{\mathbf{V}}\times\tilde{\mathbf{B}}\rangle_{\|}$, in Ohm's law.

The evolution of a relaxed-state plasma is fully determined by a global magnetic energy balance. The Poynting theorem applied to a cylindrical relaxed-state plasma with radius, a, and length, $l = 2\pi R$, can be written with dimensionless quantities as [629]

$$\frac{\partial W}{\partial \lambda_0}\frac{\partial \lambda_0}{\partial t} = 2\Phi\left(\frac{a}{R}\Theta V_\mathrm{T} - FV_\mathrm{P}\right) - S^{-1}P_\Omega \tag{9.1}$$

where W is the magnetic energy, Φ is the toroidal flux, Θ is the pinch parameter, F is the reversal parameter, V_T is the toroidal (axial) loop voltage, V_P is the poloidal loop voltage, S is the Lundquist number, and P_Ω is the ohmic dissipation power. The resistivity profile is important for ohmic dissipation and must be included based on knowledge of the electron temperature's dependence on parameters like the plasma current and density [62, 273]. To simulate OFCD, the drive frequency, amplitudes, and relative phase of the loop voltages are specified, as well as values for the Lundquist number and aspect ratio. Equation (9.1) is time advanced until a steady-state time-average is attained. This yields a dc plasma current with a superposed ac ripple.

The ac ripple in the equilibrium magnetic field derives primarily from the plasma's inductance since the resistive impedance is small, i.e., $V_\mathrm{T} \approx L\mathrm{d}I_\mathrm{p}/\mathrm{d}t$ with $L \approx \mu_0 R$. Hence $\hat{V}_\mathrm{T} \approx \mu_0 R\omega\hat{I}_\mathrm{p}$, where the over-hat identifies the ac amplitude. Equating the time-average ac helicity injection rate in OFCD to the steady-induction helicity injection rate for the same plasma equilibrium yields a scaling prediction for the fractional ac ripple

$$\frac{\hat{I}_\mathrm{p}}{\langle I_\mathrm{p}\rangle} \sim S^{-1/4}\Omega_\mathrm{MHD}^{-1/2}\left(\hat{V}_\mathrm{T}/\hat{V}_\mathrm{P}\right)^{1/2}(R/a)^{-1/2} \tag{9.2}$$

where $\langle I_\mathrm{p}\rangle$ is the cycle-averaged plasma current and $\Omega_\mathrm{MHD} = \omega\sqrt{\tau_\mathrm{R}\tau_\mathrm{A}}$ is the frequency normalized to the MHD tearing timescale. This relationship is obeyed reasonably well in relaxed state modelling, for example the scaling with Lundquist number shown in figure 73(*a*). The scaling with S reveals the trend that the ac ripple decreases slowly with Lundquist number making it impractical to demonstrate 100% current sustainment by OFCD in present-day moderate-S experiments. Figure 73(*b*) shows the projection for a large ripple in F unless S is large, noting that $|F| < 0.5$ is typical for plasmas sustained by conventional induction.

A first-principle model for OFCD has been studied at moderate $S = 10^5$ using 3D, nonlinear, resistive MHD simulations (DEBS code). The formalism is the same as for simulations of RFP plasmas sustained by conventional induction, but the boundary conditions include oscillating loop voltages. The evolution of the plasma current is shown in figure 74 for a case where OFCD is applied to a simulation that had reached steady conditions with conventional induction. When OFCD in initiated, the current settles into a new steady-state after a transition that lasts a couple of cycles. The simulations show that the current profile does not relax instantaneously, as represented by the cycle in F–Θ space. Instantaneous relaxation has a nearly linear F–Θ trajectory (see [629]. These simulations establish a sound theoretical basis for OFCD dynamics, even if limited by moderate S such that the magnitude of the ac ripple is large.

Analysis of Ohm's law provides insight into key differences between current drive with OFCD versus conventional induction. Consider the limit of single-fluid MHD, for which Ohm's law is $\mathbf{E} + \mathbf{V}\times\mathbf{B} = \eta\mathbf{J}$. At low beta the current profile is governed by the component parallel to the mean-field $\mathbf{B}_0$, i.e., $E_\| + \langle\tilde{\mathbf{V}}\times\tilde{\mathbf{B}}\rangle_\| = \eta J_\|$ where the angle brackets represent an average over a mean-field flux surface. The instantaneous alignment between $\mathbf{E}_0$ and $\mathbf{B}_0$ varies over an OFCD cycle, and the cycle average of parallel Ohm's law has non-zero $E_\|$, despite the loop voltages being oscillatory. An equivalent approach is to treat quantities instantaneously, in which case the OFCD mean-field current drive is represented by $\langle\mathbf{V}_0\times\mathbf{B}_0\rangle = \langle\hat{\mathbf{E}}_0\cdot\hat{\mathbf{B}}_0\rangle/B$, where the over-hat identifies the driven ac component. Figure 75(*a*) shows the profile of the OFCD mean-field drive, which peaks in the outer region. For conventional induction, $E_\|$ peaks at $r = 0$. The turbulent emf averaged over both the mean-field flux surface and OFCD cycle is shown in figure 75(*b*). For OFCD, the cycle-average relaxation process transports current from the outer region towards the core. This is dynamically opposite to conventional induction, for which current in the core is transported to the outer region of the plasma. Despite this opposite tendency, the shape of the parallel current profile is similar in both cases, consistent with the profile remaining close to marginal stability for current-driven tearing.

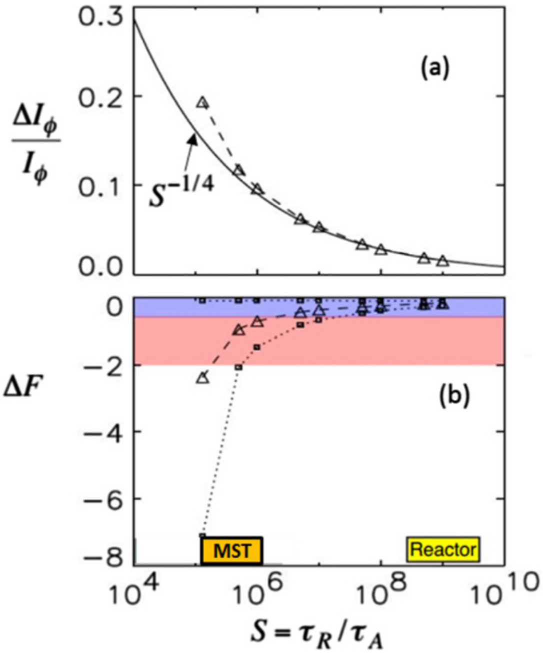

Figure 73. In OFCD plasmas, (*a*) fractional axial current and (*b*) F parameter variation as a function of S. Triangles in (*b*) are time averaged mean values, squares on dotted curves F-oscillation extremes. The red region identifies the PPCD parameter space, the blue region the standard space. S ranges relative to MST, and the extrapolation to the reactor are highlighted. Adapted from [629], with the permission of AIP Publishing.

9.3. Experimental demonstrations of current drive by OFCD

The first OFCD experiments for RFP plasmas were conducted on the ZT-40M device at LANL in the 1980s [630]. High-

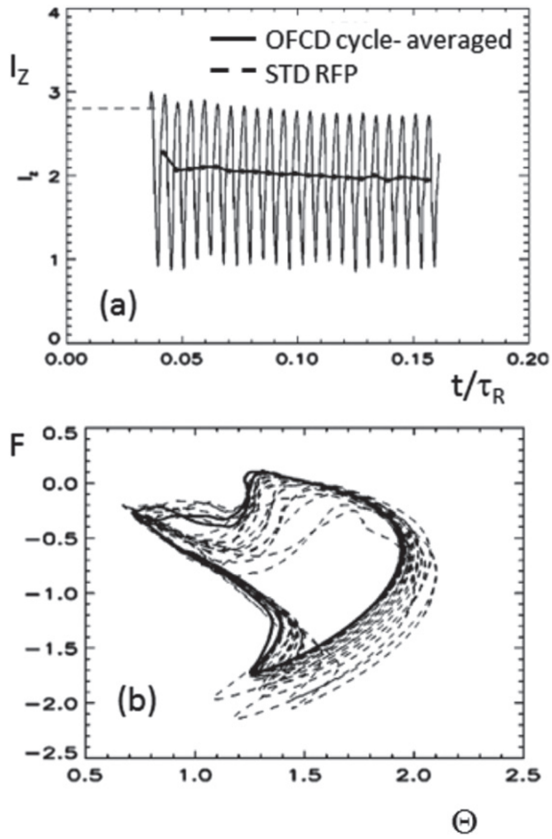

Figure 74. (a) Toroidal current and (b) F–Θ trajectory for OFCD sustained plasma; simulation with $S = 5 \times 10^5$. The solid curve shows the F–Θ limit cycle. Adapted from [629], with the permission of AIP Publishing.

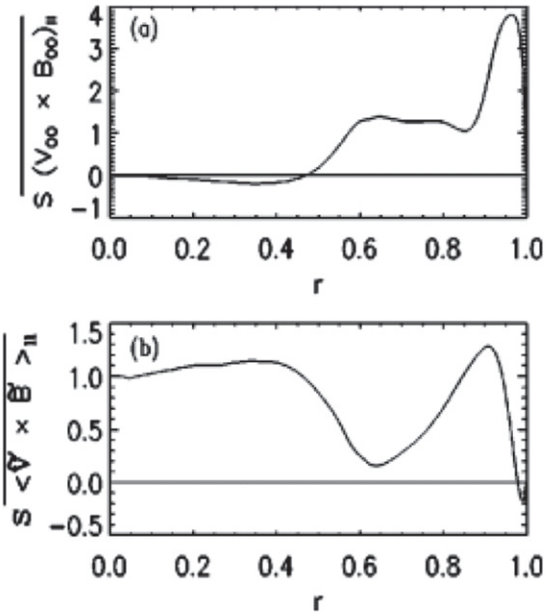

Figure 75. Cycle-averaged dynamo terms from (a) symmetric oscillations and (b) asymmetric tearing dynamo terms $\langle \tilde{\boldsymbol{v}} \times \tilde{\boldsymbol{B}}_{\|} \rangle$. Adapted from [629], with the permission of AIP Publishing.

power oscillators based on power triodes were developed that quickly ramped to full amplitude to turn on OFCD rapidly after plasma formation. The frequency was adjustable, $\omega/2\pi =$ 750 Hz to 2 kHz, and the relative phase of the oscillators was tunable so that OFCD drive and anti-drive could be tested. Since full sustainment was not possible for ZT-40M's low S plasma, the background steady induction was fixed, and the change in plasma current associated with the applied ac voltages was monitored. Experiments were conducted for varied plasma current $I_{\mathrm{p}} = 50$–180 kA. The response to drive and anti-drive phasing behaved as predicted, and probe measurements showed that the current profile was relaxed throughout the ac cycle. At 50 kA a small net increase in the plasma current was observed, consistent with ZT-40M's low S plasma. There were no limiters on the Inconel wall, allowing influx of metal impurities that increased the plasma resistance. At 180 kA, the increased resistance negated net current drive, but the drive and anti-drive phase dependence held at all current levels.

The most extensive experimental tests of OFCD have been performed on the MST device. The minor radius and plasma temperature for MST plasmas are both significantly larger than for ZT-40M, which reduces the plasma resistance. High-power oscillators based on ignitron plasma-closing switches were developed that allowed turn-on at full oscillation amplitude [631]. As for ZT-40M, the background steady induction was fixed, and the change in plasma current was monitored. The oscillator phasing was adjustable to examine the phase dependence in greater detail than in the ZT-40M experiments. Most of the experiments were performed with frequency $\omega/2\pi =$ 280 Hz, since the oscillators were based on resonant tank circuits that were cumbersome to change. Experiments were conducted over a range of plasma current, but detailed studies were performed at 250 kA plasma current where the fractional drive by OFCD was maximum. The amount of OFCD-driven current is most sensitive to the oscillator voltages and frequency, and the added/subtracted current did not depend strongly on the background current over MST's range $I_{\mathrm{p}} = 250$–500 kA.

The OFCD drive and anti-drive result from MST that is analogous to the ZT-40M experiment is shown in figure 76 [632]. The added current reaches 20 kA by the end of the current flattop. Note that the current rises continuously during the flattop period of the pulse, which is a consequence of the plasma's inductive back reaction, $L/R \approx 30$ ms. If the pulse duration were longer, the anticipated OFCD-driven current would saturate at $\Delta I_{\mathrm{p}} \approx 40$ kA, which is 15% of the total current.

The maximum OFCD-driven current in MST plasmas occurs for oscillator phasing $\delta = \pi/8$. The fractional increase in plasma current versus phase is shown in figure 77. There is a more structure in this phase dependence than expected for a global helicity balance. The measured amplitude of magnetic fluctuations associated with tearing instabilities is also phase dependent, as shown in figure 78. Interestingly, the cycle-average amplitude for poloidal mode $m = 0$ is somewhat smaller than for conventional flattop induction (dotted lines), with the minimum amplitude occurring for $\delta \approx \pi/8$.

The evolution of the magnetic equilibrium was studied [633] using a combination of toroidal equilibrium reconstructions [27] and relaxed-state modelling. Time-resolved evalu-

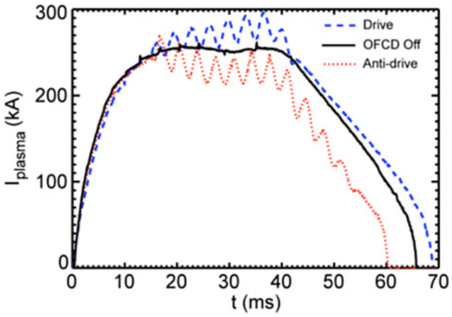

Figure 76. Time evolution of plasma current in MST discharges with OFCD (drive and antidrive) compared to the case without OFCD. Reprinted figure with permission from [632], Copyright 2006 by the American Physical Society.

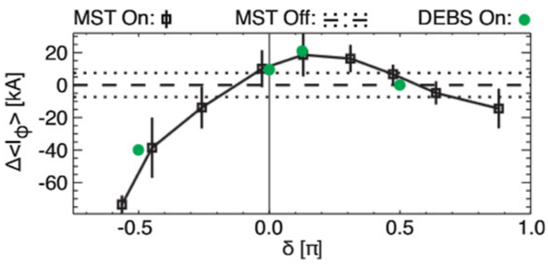

Figure 77. Phase dependence of the plasma current change (cycle averaged) in MST OFCD experiments (squares) compared to a DEBS numerical simulation (green circles) and to the case without OFCD (dashed line with dotted uncertainties). Reprinted from [633], with the permission of AIP Publishing.

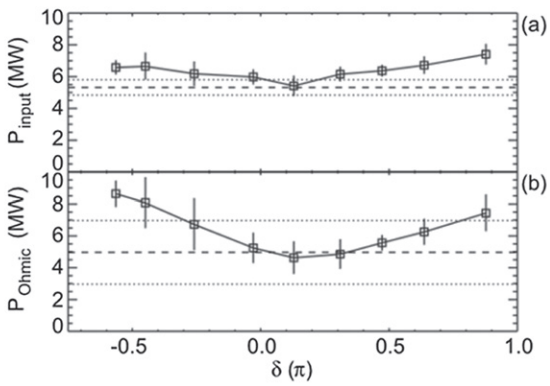

Figure 78. During an MST OFCD pulse: phase dependence of $m/n = 0/1–4$ (*a*) and $m/n = 1/6–15$ (*b*) tearing mode amplitude during the OFCD discharges. Error bars indicate the pulse-to-pulse variability. The OFCD off case is shown for comparison (dashed lines, with dotted lines pulse-to-pulse variability). Reprinted figure with permission from [632], Copyright 2006 by the American Physical Society.

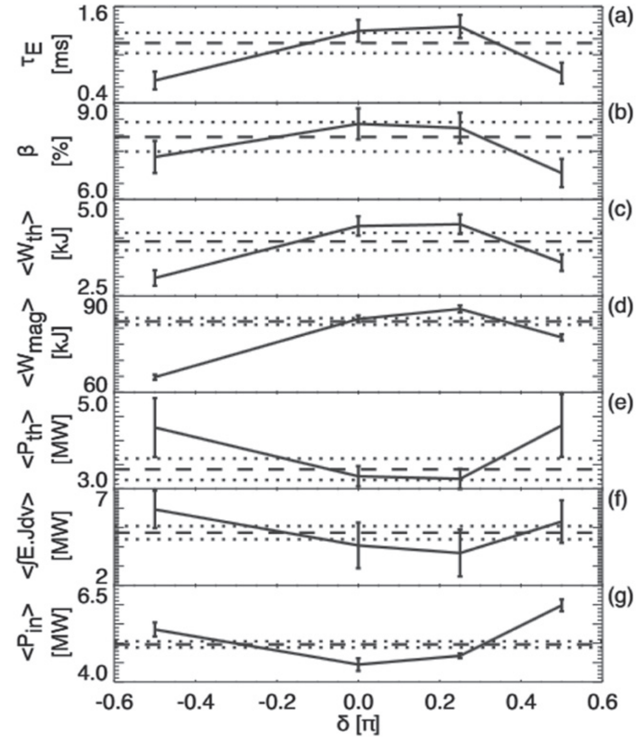

Figure 79. In MST, phase dependence of (*a*) energy confinement time, (*b*) plasma thermal pressure, (*c*) thermal energy, (*d*) magnetic energy, (*e*) thermal input power, (*f*) power transfer from magnetic field, (*g*) total input power for discharge ensembles with OFCD (solid) and without (dashed, with dotted uncertainties). All quantities are cycle averages. Reprinted from [633], with the permission of AIP Publishing.

ations of the magnetic energy and helicity balance were also performed. Key quantities for the energy balance with varied phasing are summarized in figure 79. An important observation in the magnetic helicity balance (not shown) was a measured increase in helicity dissipation for $\delta = \pi/2$, negating the helicity injection added by OFCD.

Nonlinear, 3D, resistive MHD simulations with fractional OFCD current drive were performed to compare with the MST experimental results [633]. The green data points in figure 77 show that the fractional current drive in the simulations has a similar dependence on the relative phase. The lack of maximum current drive at $\delta = \pi/2$ is attributed to an increase in the dissipation of magnetic helicity. The experiments show an important additional effect in that the energy confinement is phase dependent, and not surprisingly maximum for $\delta \approx \pi/8$ (figure 79). The simulations used a fixed resistivity profile without evolution of the thermal energy, so they could not make predictions regarding changes in confinement. Nevertheless, the good agreement between the simulations and experiment provide confidence that the OFCD physics basis is sound.

Since OFCD tends to drive current in the outer region of the plasma (figure 75) while conventional induction peaks in the core, their mixture has a flatter current drive profile. This creates a form of current profile control, which has been studied for optimization in nonlinear MHD modelling [634]. The MST experiments have such a mixture, and the reduction in $m = 0$ tearing amplitude for $\delta = \pi/8$ phasing (figure 78) together with the cycle-averaged improvement in energy confinement (figure 79) are evidence for this control.

A few OFCD experiments have also been conducted on RFX-mod [635]. The ac loop voltages were small in comparison to those used on MST, and the projected current drive from zero-dimensional energy balance was only 0.4% for

800 kA plasmas, making the detection of net current challenging. Measurements of MHD behaviour suggested that the plasma relaxation process was nevertheless affected.

9.4. Future directions

In summary, the visco-resistive, 3D MHD modelling together with experiments from MST and ZT-40M have substantially improved the physics basis for OFCD. While the basic expectations hold, the dynamics associated with relaxation and confinement must be better understood to fully establish the OFCD concept. It is also necessary to test OFCD in RFP plasmas with larger size and temperature, i.e., at larger Lundquist number. Figure 73(*b*) illustrates the gap between MST and a typical reactor plasma. The ac ripple in the equilibrium magnetic field, indicated by the modulation in the reversal parameter, F, exceeds the range of normal operation for $S \lesssim 5 \times 10^7$. Hence, 100% current drive by OFCD in MST (or RFX-mod2) would have excessive equilibrium excursions. The ac ripple is not a subtle physics effect rather the expected response for an ac electric field applied to a circuit that has inductance. The scaling for the ac ripple allows a projection of the size and current for a next-step RFP experiment needed to demonstrate 100% current sustainment by OFCD.

The tendency for RFP plasmas to enter the quasi-single-helicity (QSH) regime at high Lundquist number (chapters 2 and 3) could have a substantial impact on the viability and efficacy of OFCD. This is especially true for a development path that relies on the QSH regime to achieve sufficient energy confinement. The detailed relaxation dynamics with OFCD are different than for conventional induction, and this could change access to and stationarity of QSH. Computational studies with OFCD boundary conditions at very high Lundquist number could begin to address such questions, but such simulations are already state-of-the-art with modest Lundquist and magnetic Prandtl numbers. Fractional OFCD current drive experiments in RFX-mod2 at 2 MA could probe the compatibility and impact of and on QSH. Such experiments might require significant upgrades to the power supplies.

10. RFP reactor studies

Several fusion power plant studies based on the RFP configuration were undertaken in the 1980s with a goal to identify compact, high-power-density options as the basis for fusion reactors with mass power density competitive with fission reactors [636, 637]. The TITAN reactor concept [638–641] was the most detailed of these studies for the RFP. More recently, based on the results of recent experiments and on the expected advancements by RFX-mod2, new studies on the RFP as a neutron source for a fusion–fission hybrid reactor have been undertaken [376, 642].

10.1. The TITAN system study

The high β, high density RFP plasma makes it well suited for high power density. Small size is also enabled by its relatively small field strength at the magnets, i.e., the engineering beta is very high. The possibility for ohmic ignition [612] eliminates major complications related to auxiliary heating and current drive. The TITAN study introduced several novel features in fusion reactor design, including steady-state using inductive current drive via OFCD, single-piece maintenance for high availability, high core radiation to distribute the heat load, and an integrated-blanket-coil concept that allowed the lithium blanket circuit to serve as the toroidal field magnet, since the toroidal field for the RFP is small. The primary magnets were permitted to be normal conducting, which reduced shielding requirements. Superconducting windings were only used for the vertical field equilibrium coils.

The TITAN design is for a 1 GWe class power plant, and the fusion power core is very compact. The key power plant design parameters are given in table 3. The system analysis showed a strong correlation between the neutron wall load (I_w) and the mass power density (MPD), i.e., the ratio of the net electric power to the mass of the fusion power core, about 800 kWe/tonne for the chosen design. The large $I_w = 18$ MW m^{-2} operating point was selected, in part, to bolster the concept of single-piece maintenance for a high plant availability of 85%. Single-piece maintenance was considered possible for a neutron wall load $I_w > 10$ MW m^{-2} [639].

The study's analysis showed that the projected COE decreases with both MPD and neutron wall load with a formal minimum value at $I_w = 18$ MW/m^2, which was taken to be the TITAN operating point. However, the COE flattens for neutron wall load starting around 5 MW m^{-2}, and the design purposely targeted very high MPD. An update to TITAN's costing was later performed by Miller [643], replacing the original costing model with those used in the ARIES tokamak studies, culminating in the ARIES-AT advanced tokamak design [644]. The update also incorporated the level of safety assurance passive-safety cost credits introduced by the ESECOM, and the blanket was updated to a modern configuration used in the ARIES-CS compact stellarator study [645]. The COE versus neutron wall load for the updated analysis is shown in figure 80, revealing a new formal minimum at $I_w = 13$ MW m^{-2} and still flat COE above 5 MW m^{-2}. The figure details the ranges of operating points for different aspect ratios (all with circular cross section).

A neutron wall load $I_w > 5$ MW m^{-2} is today considered very challenging and perhaps beyond material feasibility. The 1 GWe class ARIES studies based on tokamak and stellarator configurations all settled on values $I_w < 5$ MW m^{-2}. While the TITAN study shows a compact fusion power core based on the RFP is possible, it should not be viewed as defining the RFP target. A more general goal of the study was to assess the merits of high power density, and few magnetic configurations allow the possibility for extreme compactness. In a contemporary context, the TITAN study provides support for a compact RFP power core with lower net electric output that might be better suited for today's energy market, and it also provides support for a 1 GWe reactor having $I_w < 5$ MW m^{-2} without a large cost penalty by maintaining the simplicity of ohmic ignition, inductive sustainment, and minimal field strength at the magnets, while eliminating auxiliary heating and current drive.

Table 3. Operating parameters of the TITAN fusion power core. There are two design versions with differing structural materials, TITAN-I with vanadium alloy and TITAN-II with ferritic steel, each with separate cooling methods. Adapted from [639], Copyright 1993, with permission from Elsevier.

Major radius (m)	3.9
Minor radius (m)	0.6
Plasma current (MA)	17.8
Toroidal field at plasma surface (T)	0.36
Poloidal beta	0.23
Plasma ohmic heating at operating point (MW)	30
Neutron wall load (MW m^{-2})	18
Radiation heat flux on first wall (MW m^{-2})	4.6
Fusion power (MW)	2301 (I), 2290 (II)
Total thermal power (MW)	2935 (I), 3027 (II)
Net electric power (MW)	970 (I), 900 (II)
MPD (kWe/tonne)	757 (I), 806 (II)

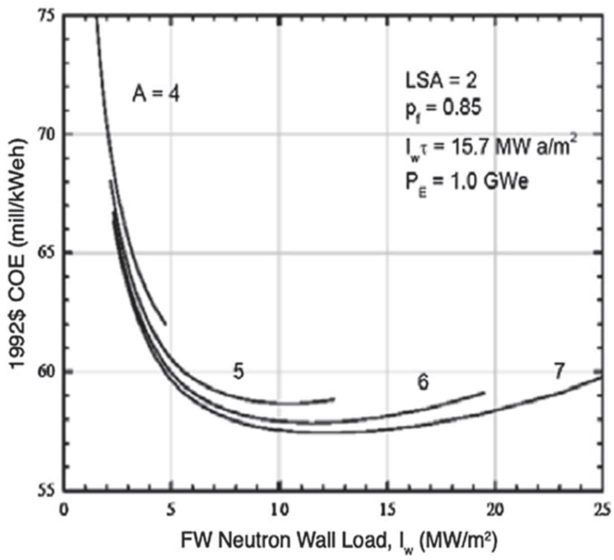

Figure 80. 1 GWe RFP power-plant COE as a function of FW neutron wall load, I_w, for several plasma aspect ratios, $A = R/a$. The plant availability is assumed to be $p_f = 0.85$. [643] 2009, reprinted by permission of the publisher (Taylor & Francis Ltd, http://www.tandfonline.com.)

10.2. Studies on the RFP as a neutron source

The RFP as a neutron source for the development of fusion materials and technology was also discussed in the 1980s. In just the past few years, a renewed interest in the RFP neutron source for a fusion–fission hybrid reactor has emerged [376, 642]. Most of the features that make TITAN attractive carry over immediately for the RFP as a compact neutron source. One difference in operation is the use of conventional pulsed induction with short dwell time between pulses as a way to achieve up to 90% duty cycle, motivated by the fact that the existing RFP database is based almost entirely on pulsed operation and the development path might be faster, considering also that the OFCD is very challenging. Preliminary studies suggest a compact device with $R = 4$ m and $a = 0.8$ m, which could produce 30 MW of fusion power with fusion gain $Q = 0.5$ and a neutron wall load below 1 MW m^{-2} [376, 642]. A suggested three-stage approach for a pilot experiment, mainly based on the extrapolation of the RFX-mod performance to be confirmed by the upgraded device RFX-mod2 [114], could fill the gap between today's experiments and a fusion reactor operating as a neutron source. The first phase would resolve key physics and technology issues by extending operation for plasma current up to $I_p = 9$ MA with 1.5 s pulse duration. In phase 2, superconducting coils for magnetizing and field-shaping windings would be adopted, and operation up to $I_p = 14$ MA with 8 s pulses would be developed. Phase 3 would be a fusion–fission nuclear reactor operating with D-T. The development of a neutron source would validate most of the physics basis and technology required for a pure fusion reactor.

11. Concluding remarks

Over the last three decades research on the RFP magnetic configuration has produced many very important contributions to fusion and plasma science. The potential of the RFP as a fusion power core has been increased, and several fundamental challenges for the RFP are either resolved or better understood. Research on the RFP has also contributed to the science and technology for magnetic fusion more broadly, as well as advanced the physics associated with naturally occurring plasmas, especially in the context of magnetic self-organization. These accomplishments accrued through the successful operation of well-diagnosed experiments coupled closely with comprehensive theory and modelling.

A key transformational result is the experimental demonstration that magnetic fluctuations and stochasticity that challenge confinement are not intrinsic to the RFP configuration. This happens either through inductive control of the plasma current (PPCD) or through magnetic self-organization towards the SH regime which allows RFP sustainment in a state with reduced magnetic fluctuations. Each approach leads to substantially improved confinement. The physics basis for PPCD and SH is now well established, supported by a broad set of nonlinear MHD simulations and theoretical work.

A second transformational achievement for the RFP is the demonstration of reliable control of magnetic instabilities using saddle coils in a feedback process. Active control of MHD stability was pioneered in RFP experiments, and the techniques developed are used within the entire magnetic fusion community, especially in the development of the advanced tokamak. The stabilization of multiple, simultaneously occurring RWMs for pulse duration exceeding many resistive wall times has been routinely achieved. The active control mitigates effects related to magnetic field errors and tearing modes as well, a crucial ingredient for the achievement of long-lived SH states.

RFP research has also been a leading force in the development of modelling of fusion plasmas using a variety of numerical codes and methodologies. This has profoundly influenced our comprehension of RFP physics. They include, for example, nonlinear MHD simulations, tools for the modelling of active control of stability, codes for the three-dimensional reconstruction of helical plasma equilibria, codes for the study of turbulence and micro-instabilities, and codes for the description of the dynamics of fast ions and electrons.

The flexible capabilities and set of experimental and modelling tools developed for active control on RFX-mod as an RFP have also prompted the direct exploration of tokamak scenarios in RFX-mod, where $q(a) < 2$ plasmas have been produced, stimulating similar experiments in the DIII-D tokamak [120]. A second example concerns the observation that a dynamo conversion of poloidal flux to toroidal flux, analogous to the RFP one, can explain the helical core observed in the hybrid mode of operation of the tokamak [143, 223]. Other examples include multi-configuration modelling of the empirical density limit [466] and the pioneering development of advanced diagnostics for fusion plasmas that include high repetition rate Thomson scattering, combined interferometry-polarimetry (Faraday rotation), full-spectrum motional Stark effect, and a number of advanced x-ray diagnostics. Many of these diagnostics are appearing on new fusion facilities, including ITER.

While the progress is substantial, there remain open questions to resolve the potential of the RFP as an attractive fusion power core that can access ohmic ignition, achieve efficient inductive sustainment, and attain compact high power density. These issues can only be addressed with new experiments combined with further advances in theory and modelling. The upgrade to RFX-mod that is currently underway is a major next step to further advance the RFP at 2 MA, and new experiments with yet larger plasma current and additional capabilities will be needed to fully resolve the viability of the RFP for fusion application. Present-day experiments operate with magnetic field strength that is still at least a factor of five smaller than required in a reactor. Hence the scaling of confinement with current and size remains a key issue, with large room for growth. The improved confinement via inductive control and SH self-organization show promising trends for plasmas having temperatures in excess of 1 keV. The limit to the reduction in magnetic fluctuations has not be identified, and in the cases of highest confinement, evidence suggested microturbulence plays an increasingly important role. A key question is, what transport process limits confinement for the RFP?

The development of suitable control of the plasma–boundary interface is the least developed of the key issues for the RFP. A divertor and/or alternative approaches to plasma exhaust must be tested. There are some special constraints, and possibly opportunities, associated with the integration with the helical equilibrium. Boundary control is anticipated to be important for optimization and stationarity of the SH regime. This will be a significant element of the RFX-mod2 programme, taking advantage of the improved magnetic front-end and much smoother boundary.

None of the key issues for the RFP appear to have showstoppers. Some of them originate from uncertainty in the physics that calls for continued fundamental theoretical and experimental work, but others are difficult to advance without new experimental capabilities. The RFP programme is at least one generation behind in development relative to the tokamak, mostly due to the smaller resources invested in RFP research.

The RFP continues to have a valuable role in the scientific and technological path towards fusion electricity, to help completing the fusion grand experiment and to assess its own fusion potential, in particular based on its unique opportunity to exploit the low magnetic field at the magnets, the absence of known limitations on aspect ratio, and the ohmic ignition. These features could be extremely valuable in achieving an economical fusion power plant. The future will tell us whether the community will be able to find efficient and smart ways to exploit the opportunity given by the RFP. Hopefully, keeping in mind the concept expressed by Enrico Fermi in 1947: '…the vocation of the scientist is to move forward the frontiers of our knowledge in all directions, not just along those that promise more immediate rewards or applauses'.

Acknowledgments

The authors greatly appreciate the contribution by D.J. Den Hartog to this paper. We also thank A.F. Almagri, J.K. Anderson, V. Antoni, L. Apolloni, T. Bolzonella, D.L. Brower, P. Brunsell, A. Buffa, L. Carraro, S. Cappello, D. Craig, S. Dal Bello, D.R. Demers, R.N. Dexter, W.X. Ding, G. Fiksel, L. Frassinetti, C.B. Forest, J.A. Goetz, F. Gnesotto, K. Hayase, H. Himura, Y. Hirano, D.J. Holly, M. Iida, R. Ikezoe, P. Innocente, S. Kiyama, H. Koguchi, E. Martines, K.J. McCollam, V.V. Mirnov, N. Mizuguchi, M.D. Nornberg, K. Oki, T. Onchi, S. Ortolani, H. Oshiyama, R. Paccagnella, R. Piovan, S.C. Prager, G. Rostagni, H. Sakakita, A. Sanpei, K.I. Satoh, S. Shiina, T. Shimada, P. Sonato, C.R. Sovinec, G. Spizzo, J.C. Sprott, Y. Suzuki, D. Terranova, P.W. Terry, M. Valisa, M. Wakatani, K.Y. Watanabe, Y. Yagi, P. Zanca, M. Zuin and the EXTRAP-T2R, MST, RELAX and RFX-mod teams. Paolo Piovesan (1977–2019) was a gifted scientist who gave seminal contributions to fusion physics. He had also a

special talent to unite people and blend ideas. We thank and miss him.

ORCID iDs

L. Marrelli https://orcid.org/0000-0001-5370-080X
P. Martin https://orcid.org/0000-0002-4935-3187
M.E. Puiatti https://orcid.org/0000-0001-7608-5993
J.S. Sarff https://orcid.org/0000-0001-8883-6678
B.E. Chapman https://orcid.org/0000-0002-5811-1702
D.F. Escande https://orcid.org/0000-0002-0460-8385
S. Masamune https://orcid.org/0000-0001-6983-5012

References

[1] Bodin H.A.B. 1990 The reversed field pinch *Nucl. Fusion* **30** 1717–37
[2] Bodin H.A.B. and Newton A.A. 1980 Reversed-field-pinch research *Nucl. Fusion* **20** 1255–324
[3] Rechester A.B. and Rosenbluth M.N. 1978 Electron heat transport in a tokamak with destroyed magnetic surfaces *Phys. Rev. Lett.* **40** 38–41
[4] Connor J.W. and Taylor J.B. 1984 Resistive fluid turbulence and energy confinement *Phys. Fluids* **27** 2676
[5] Mercier C. 1960 A necessary condition for hydromagnetic stability of plasma with axial symmetry *Nucl. Fusion* **1** 47
[6] Gnesotto F., Sonato P., Baker W.R., Doria A., Elio F., Fauri M., Fiorentin P., Marchiori G. and Zollino G. 1995 The plasma system of RFX *Fusion Eng. Des.* **25** 335–72
[7] Sonato P. *et al* 2003 Machine modification for active MHD control in RFX *Fusion Eng. Des.* **66–68** 161–8
[8] Dexter R.N., Kerst D.W., Lovell T.W. and Sprott J.C. 1991 The Madison symmetric torus *Fusion Technol.* **19** 131–9
[9] Brunsell P.R., Bergsåker H., Cecconello M., Gravestijn R.M., Hedqvist A. and Malmberg J.-A. 2001 Initial results from the rebuilt EXTRAP T2R RFP device *Plasma Phys. Control. Fusion* **43** 1457
[10] Yagi Y. *et al* 1999 Front-end system of the TPE-RX reversed-field pinch machine *Fusion Eng. Des.* **45** 421–36
[11] Yagi Y. *et al* 1999 Design concept and confinement prediction of TPE-RX reversed-field pinch device *Fusion Eng. Des.* **45** 409–19
[12] Koguchi H., Sakakita H., Kiyama S., Asai T., Hirano Y., Auriemma F., Terranova D. and Innocente P. 2009 High beta and high density operation in TPE-RX *Plasma Fusion Res.* **4** 022
[13] Masamune S., Sanpei A., Ikezoe R., Murata K.-I., Oki K., Shimazu H., Yamashita T. and Himura H. 2007 Characterization of initial low-aspect ratio RFP plasmas in 'RELAX' *J. Phys. Soc. Japan* **76** 123501
[14] Masamune S., Sanpei A., Ikezoe R., Oki K., Yamashita T., Shimazu H., Himura H. and Paccagnella R. 2009 MHD properties of low-aspect ratio RFP in RELAX *J. Fusion Energy* **28** 187–90
[15] Liu W. *et al* 2017 Overview of Keda Torus eXperiment initial results *Nucl. Fusion* **57** 116038
[16] Liu W. *et al* 2014 Progress of the Keda Torus eXperiment project in China: design and mission *Plasma Phys. Control. Fusion* **56** 094009
[17] Zheng J. *et al* 2012 Preliminary design of KTX magnet system *Fusion Eng. Des.* **87** 1853–60
[18] Liu W. *et al* 2019 An overview of diagnostic upgrade and experimental progress in the KTX *Nucl. Fusion* **59** 112013
[19] Marrelli L., Marchiori G., Bettini P., Kapidani B., Grando L., Marconato N., Specogna R. and Voltolina D. 2019 Optimization of RFX-mod2 gap configuration by estimating the magnetic error fields due to the passive structure currents *Fusion Eng. Des.* **146** 680–3
[20] Peruzzo S. *et al* 2017 Design concepts of machine upgrades for the RFX-mod experiment *Fusion Eng. Des.* **123** 59–62
[21] Peruzzo S. *et al* 2019 Technological challenges for the design of the RFX-mod2 experiment *Fusion Eng. Des.* **146** 692–6
[22] Antoni V., Martin P. and Ortolani S. 1989 Mean magnetic field profiles and their dynamics in reversed field pinches *Nucl. Fusion* **29** 1759–67
[23] Antoni V., Merlin D. and Ortolani S. 1986 MHD stability analysis of force-free reversed field pinch configurations *Nucl. Fusion* **26** 1711–7
[24] Ji H., Prager S.C. and Sarff J.S. 1995 Conservation of magnetic helicity during plasma relaxation *Phys. Rev. Lett.* **74** 2945–8
[25] Zanca P. and Terranova D. 2004 Reconstruction of the magnetic perturbation in a toroidal reversed field pinch *Plasma Phys. Control. Fusion* **46** 1115
[26] Terranova D., Auriemma F., Canton A., Lorenzini R. and Innocente P. 2010 Experimental particle transport studies by pellet injection in helical equilibria *Nucl. Fusion* **50** 035006
[27] Anderson J.K., Forest C.B., Biewer T.M. and Wright J.C. 2003 Equilibrium reconstruction in the Madison symmetric torus reversed field pinch *Nucl. Fusion* **44** 162
[28] Guazzotto L. and Paccagnella R. 2009 Magnetic field profiles in fusion plasmas in the presence of equilibrium flow *Plasma Phys. Control. Fusion* **51** 065013
[29] Antoni V., Desideri D., Martines E. and Tramontin L. 1997 Plasma potential well and velocity shear layer at the edge of reversed field pinch plasmas *Phys. Rev. Lett.* **79** 4814–7
[30] Carraro L., Puiatti M.E., Sattin F. and Valisa M. 1998 Toroidal and poloidal plasma rotation in the reversed field pinch RFX *Plasma Phys. Control. Fusion* **40** 1021
[31] Puiatti M.E. *et al* 2001 Plasma rotation and structure of the radial electric field in RFX *J. Nucl. Mater.* **290–293** 696–700
[32] Hutchinson I.H., Malacarne M. and Noonan P. 1984 The structure of magnetic fluctuations in the HBTX-1A reversed field pinch *Nucl. Fusion* **24** 59–74
[33] Holmes J.A., Carreras B.A., Hender T.C., Lynch V.E., An Z.G. and Diamond P.H. 1985 Nonlinear interaction of tearing modes: a comparison between the tokamak and the reversed field pinch configurations *Phys. Fluids* **28** 261–70
[34] Nebel R.A., Caramana E.J. and Schnack D.D. 1989 The role of $m=0$ modal components in the reversed-field-pinch dynamo effect in the single fluid magnetohydrodynamics model *Phys. Fluids* B **1** 1671–4
[35] Schnack D.D., Caramana E.J. and Nebel R.A. 1985 Three-dimensional magnetohydrodynamic studies of the reversed-field pinch *Phys. Fluids* **28** 321–33
[36] Robinson D.C. 1971 High-diffuse pinch configurations *Plasma Phys.* **13** 439
[37] Caramana E.J., Nebel R.A. and Schnack D.D. 1983 Nonlinear, single-helicity magnetic reconnection in the reversed-field pinch *Phys. Fluids* **26** 1305–19
[38] Zanca P. and Terranova D. 2006 MHD linear stability analysis in the setting up phase of the RFX-mod experiment *Plasma Phys. Control. Fusion* **48** 407–17
[39] Ji H., Prager S.C. and Sarff J.S. 1994 Time-resolved observation of discrete and continuous magnetohydrodynamic dynamo in the reversed-field pinch edge *Phys. Rev. Lett.* **73** 668–71
[40] Antoni V., Martin P. and Ortolani S. 1987 Experimental evidence of on axis q oscillations in ETA BETA II *Plasma Phys. Control. Fusion* **29** 279–85

[41] Watt R.G. 1983 Sawteeth, magnetic disturbances, and magnetic flux regeneration in the reversed-field pinch *Phys. Fluids* **26** 1168

[42] Ho Y.L. and Craddock G.G. 1991 Nonlinear dynamics of field maintenance and quasiperiodic relaxation in reversed-field pinches *Phys. Fluids* B **3** 721–34

[43] Cappello S. and Biskamp D. 1996 Reconnection processes and scaling laws in reversed field pinch magnetohydrodynamics *Nucl. Fusion* **36** 571

[44] King J.R., Sovinec C.R. and Mirnov V.V. 2012 First-order finite-Larmor-radius fluid modeling of tearing and relaxation in a plasma pinch *Phys. Plasmas* **19** 055905

[45] Sauppe J.P. and Sovinec C.R. 2016 Two-fluid and finite Larmor radius effects on helicity evolution in a plasma pinch *Phys. Plasmas* **23** 032303

[46] Hattori K., Hirano Y., Shimada T., Maejima Y., Hirota I. and Ogawa K. 1991 Behavior of magnetic field fluctuations during dynamo activity and its effect on energy confinement in a reversed-field pinch *Phys. Fluids* B **3** 3111–24

[47] Verhage A.J.L., Furzer A.S. and Robinson D.C. 1978 Observations of large-amplitude helical kink instabilities and field reversal in a fast pinch experiment (HBTX-1) *Nucl. Fusion* **18** 457–73

[48] Almagri A.F., Assadi S., Prager S.C. and Kerst D.W. 1992 Locked modes and magnetic field errors in the Madison symmetric torus *Phys. Fluids* B **4** 4080–5

[49] Hedin G. 1998 MHD behaviour in a resistive-shell reversed-field pinch *Plasma Phys. Control. Fusion* **40** 1529–39

[50] Hokin S. *et al* 1991 Global confinement and discrete dynamo activity in the MST reversed-field pinch *Phys. Fluids* B **3** 2241–6

[51] Lorenzini R., Auriemma F., Innocente P., Martini S. and Terranova D. 2008 Confinement loss during dynamo relaxation event in RFX-mod *Plasma Phys. Control. Fusion* **50** 035004

[52] Momo B. *et al* 2020 The phenomenology of reconnection events in the reversed field pinch *Nucl. Fusion* **60** 056023

[53] Brower D.L., Ding W.X., Terry S.D. *et al* 2002 Measurement of the current-density profile and plasma dynamics in the reversed-field pinch *Phys. Rev. Lett.* **88** 185005

[54] Howell R.B., Ingraham J.C., Wurden G.A. and Buchenauer C.J. 1987 Asymmetric magnetic flux generation, $m = 1$ activity, and edge phenomena on a reversed-field pinch *Phys. Fluids* **30** 1828

[55] Zuin M., Vianello N., Spolaore M., Bolzonella T., Cavazzana R., Martines E., Serianni G. and Terranova D. 2009 Current sheets during spontaneous reconnection in a current-carrying fusion plasma *Plasma Phys. Control. Fusion* **51** 035012

[56] Crocker N.A., Fiksel G., Prager S.C. *et al* 2003 Measurement of the current sheet during magnetic reconnection in a toroidal plasma *Phys. Rev. Lett.* **90** 035003

[57] Piovesan P., Almagri A., Chapman B.E., Marrelli L., Martin P., Prager S.C. and Sarff J.S. 2008 Filamentary current structures in the Madison symmetric torus *Nucl. Fusion* **48** 095003

[58] Craig D., Martin D., Den Hartog D.J. and Reusch J.A. 2017 Magnetic and velocity fluctuations from nonlinearly coupled tearing modes in the reversed field pinch with and without the reversal surface *Phys. Plasmas* **24** 082308

[59] Jacobson A.R. and Moses R.W. 1984 Sustainment dynamo reexamined: nonlocal electrical conductivity of a plasma in a stochastic magnetic field *Phys. Rev. Lett.* **52** 2041–4

[60] Rusbridge M.G. 1991 The relationship between the 'tangled discharge' and 'dynamo' models of the magnetic relaxation process *Plasma Phys. Control. Fusion* **33** 1381–9

[61] Mattor N. 1996 Scaling of magnetic turbulence with Lundquist number in relaxed state devices *Phys. Plasmas* **3** 1578–84

[62] Stoneking M.R., Chapman J.T., Den Hartog D.J. and Sarff J.S. 1998 Experimental scaling of fluctuations and confinement with Lundquist number in the reversed-field pinch *Phys. Plasmas* **5** 1004–14

[63] Intravaia A. *et al* 1999 Scaling of local core transport with Lundquist number in the reversed field pinch *Phys. Rev. Lett.* **83** 5499–502

[64] Terranova D., Bolzonella T., Cappello S., Marrelli L. and Pasqualotto R. 2000 Study of the scaling of magnetic fluctuations in the RFX reversed field pinch1 *Plasma Phys. Control. Fusion* **42** 843–54

[65] Bolzonella T. and Terranova D. 2002 Magnetic fluctuation spectra and non-linear MHD mode interaction in RFX *Plasma Phys. Control. Fusion* **44** 2569

[66] Nordlund P. and Mazur S. 1994 Nonlinear dynamics of kink-tearing modes and their interaction with the current profiles in a reversed-field pinch *Phys. Plasmas* **1** 4032–42

[67] Sarff J.S. *et al* 1993 Nonlinear coupling of tearing fluctuations in the Madison symmetric torus∗ *Phys. Fluids* B **5** 2540–5

[68] Hansen A.K., Almagri A.F., Craig D., Hegna C.C., Prager S.C. and Sarff J.S. 2000 Momentum transport from nonlinear mode coupling of magnetic fluctuations *Phys. Rev. Lett.* **85** 3408–11

[69] Tamano T., Bard W.D., Chu C., La Haye R.J., Lee P.S., Saito M., Schaffer M.J. and Taylor P.L. 1987 Observation of a new toroidally localized kink mode and its role in reverse-field-pinch plasmas *Phys. Rev. Lett.* **59** 1444–7

[70] Greene P. and Robertson S. 1993 Locking of kink modes in a reversed-field pinch *Phys. Fluids* B **5** 550–5

[71] Brunsell P.R., Yagi Y., Hirano Y. and Shimada T. 1993 Coherent magnetic field fluctuations and locked modes in a reversed-field pinch *Phys. Fluids* B **5** 885–95

[72] Yagi Y., Koguchi H., Sakakita H., Maejima Y., Nilsson J.-A.B., Bolzonella T. and Zanca P. 1999 Mode-locking phenomena in the TPE-RX reversed-field pinch plasma *Phys. Plasmas* **6** 3824–37

[73] Malmberg J.-A., Brunsell P.R. and Yagi Y. 2000 Locked modes in two reversed-field pinch devices of different size and shell system *Phys. Plasmas* **7** 4184–96

[74] Buffa A, Gnesotto F, Antoni V *et al* 1994 Magnetic field configuration and locked modes in RFX *21st EPS Conf. Plasma Physics* (Montpellier, France, 1994) p 458 (http://libero.ipp.mpg.de/libero/PDF/EPS_21_Vol1_1994.pdf)

[75] Zanca P. *et al* 2001 Analysis of phase locking of tearing modes in reversed field pinch plasmas *Phys. Plasmas* **8** 516–24

[76] Martini S., Agostini M., Alessi C. *et al* 2007 Active MHD control at high currents in RFX-mod *Nucl. Fusion* **47** 783

[77] Ortolani S. 2006 Active MHD control experiments in RFX-mod *Plasma Phys. Control. Fusion* **48** B371–81

[78] Valisa M. *et al* 1997 Locked modes induced plasma–wall interactions in RFX *J. Nucl. Mater.* **241–243** 988–92

[79] Zanca P., Terranova D. and Valisa M. 2007 Plasma wall interactions in RFX-mod with virtual magnetic boundary *J. Nucl. Mater.* **363–365** 733–7

[80] Marrelli L., Zanca P., Martin P. and Murari A. 1999 Edge localised asymmetric radiative phenomena in RFX *J. Nucl. Mater.* **266–269** 877–83

[81] Hirano Y., Yagi Y., Maejima Y. and Hirota I. 1997 Self-organization and its effect on confinement in a reversed field pinch plasma *Plasma Phys. Control. Fusion* **39** A393

[82] Sarff J.S., Lanier N.E. and Prager S.C. 1997 Increased confinement and β by inductive poloidal current drive in the reversed field pinch *Phys. Rev. Lett.* **78** 62–5

[83] Martini S., Terranova D. and Innocente P. 1999 Spontaneous and driven reduced turbulence modes in the RFX reversed field pinch *Plasma Phys. Control. Fusion* **41** A315

[84] Martin P. 1999 Magnetic and thermal relaxation in the reversed field pinch *Plasma Phys. Control. Fusion* **41** A247

[85] Paccagnella R., Ortolani S., Zanca P. *et al* 2006 Active-feedback control of the magnetic boundary for magnetohy-

drodynamic stabilization of a fusion plasma *Phys. Rev. Lett.* **97** 075001
[86] Martin P *et al* 2011 Overview of the RFX fusion science program *Nucl. Fusion* **51** 094023
[87] Escande D.F. *et al* 2000 Quasi-single-helicity reversed-field-pinch plasmas *Phys. Rev. Lett.* **85** 1662–5
[88] Martin P. *et al* 2000 Quasi-single helicity states in the reversed field pinch: beyond the standard paradigm *Phys. Plasmas* **7** 1984–92
[89] Marrelli L., Martin P., Spizzo G., Chapman B.E., Craig D., Sarff J.S., Biewer T.M., Prager S.C. and Reardon J.C. 2002 Quasi-single helicity spectra in the Madison symmetric torus *Phys. Plasmas* **9** 2868–71
[90] Piovesan P., Craig D., Marrelli L. *et al* 2004 Measurements of the MHD dynamo in the quasi-single-helicity reversed-field pinch *Phys. Rev. Lett.* **93** 235001
[91] Bergerson W.F., Auriemma F., Chapman B.E. *et al* 2011 Bifurcation to 3D helical magnetic equilibrium in an axisymmetric toroidal device *Phys. Rev. Lett.* **107** 255001
[92] Piovesan P., Spizzo G., Yagi Y., Shimada T., Hirano Y. and Martin P. 2004 Self-organization towards helical states in the toroidal pinch experiment reversed-field pinch *Phys. Plasmas* **11** 151–7
[93] Frassinetti L., Brunsell P.R., Drake J.R. and Cecconello M. 2007 Spontaneous quasi single helicity regimes in EXTRAP T2R reversed-field pinch *Phys. Plasmas* **14** 112510
[94] Ikezoe R., Masamune S., Oki K., Himura H., Onchi T. and Hirose A. 2012 Phase locking and unlocking associated with transition to quasi-single helicity state in the RELAX reversed-field pinch *J. Phys. Soc. Japan* **81** 115001
[95] Hirano Y., Paccagnella R., Koguchi H., Sakakita H., Kiyama S. and Yagi Y. 2005 Quasi-single helicity state at shallow reversal in TPE-RX reversed-field pinch experiment *Phys. Plasmas* **12** 112501
[96] Hirano Y., Koguchi H., Yambe K. and Kiyama S. 2006 Quasi-single helicity state by a small positive pulse of toroidal magnetic field in TPE-RX reversed field pinch experiment *Phys. Plasmas* **13** 122511
[97] Frassinetti L., Yagi Y., Koguchi H., Hirano Y. and Sakakita H. 2006 Toroidally localized soft x-ray expulsion at the termination of the improved confinement regime in the TPE-RX reversed-field pinch experiment *Phys. Plasmas* **13** 042502
[98] Oki K., Fukahori D., Deguchi K., Sanpei A., Himura H., Masamune S. and Paccagnella R. 2012 Characterization of quasi-single-helicity States in a low-aspect-ratio RFP *Plasma Fusion Res.* **7** 1402028
[99] Oki K., Sanpei A. and Himura H. 2013 Dependence of properties of quasi-single-helicity states on field reversal parameter in a low-aspect-ratio reversed field pinch *Fusion Sci. Technol.* **63** 386–8
[100] Sarff J.S., Almagri A.F., Anderson J.K. *et al* 2015 Overview of results from the MST reversed field pinch experiment *Nucl. Fusion* **55** 104006
[101] Martin P. *et al* 2003 Overview of quasi-single helicity experiments in reversed field pinches *Nucl. Fusion* **43** 1855
[102] Valisa M., Bolzonella T., Buratti P. *et al* 2008 High current regimes in RFX-mod *Plasma Phys. Control. Fusion* **50** 124031
[103] Carraro L. *et al* 2013 Advances in understanding RFX-mod helical plasmas *Nucl. Fusion* **53** 073048
[104] Piovesan P. *et al* 2009 Magnetic order and confinement improvement in high-current regimes of RFX-mod with MHD feedback control *Nucl. Fusion* **49** 085036
[105] Sarff J.S., Almagri A.F., Anderson J.K. *et al* 2013 Overview of results from the MST reversed field pinch experiment *Nucl. Fusion* **53** 104017
[106] Martin P., Martini S., Antoni V. *et al* 2002 New insights into MHD dynamics of magnetically confined plasmas from experiments in RFX *Nucl. Fusion* **42** 247
[107] Lorenzini R., Terranova D., Alfier A. *et al* 2008 Single-helical-axis states in reversed-field-pinch plasmas *Phys. Rev. Lett.* **101** 025005
[108] Puiatti M.E., Alfier A., Auriemma F. *et al* 2009 Helical equilibria and magnetic structures in the reversed field pinch and analogies to the tokamak and stellarator *Plasma Phys. Control. Fusion* **51** 124031
[109] Lorenzini R. *et al* 2009 Self-organized helical equilibria as a new paradigm for ohmically heated fusion plasmas *Nat. Phys.* **5** 570–4
[110] Bonomo F., Alfier A., Gobbin M., Franz P., Marrelli L., Pasqualotto R., Spizzo G. and Terranova D. 2009 2D characterization of core thermal topology changes in controlled RFX-mod QSH states *Nucl. Fusion* **49** 045011
[111] Lorenzini R., Agostini M., Alfier A. *et al* 2009 Improvement of the magnetic configuration in the reversed field pinch through successive bifurcationsa *Phys. Plasmas* **16** 056109
[112] Escande D.F., Paccagnella R., Cappello S. and D'Angelo F. 2000 Chaos healing by separatrix disappearance and quasisingle helicity states of the reversed field pinch *Phys. Rev. Lett.* **85** 3169–72
[113] Auriemma F. *et al* 2011 Magnetic reconstruction of nonaxisymmetric quasi-single-helicity configurations in the Madison symmetric torus *Plasma Phys. Control. Fusion* **53** 105006
[114] Marrelli L. *et al* 2019 Upgrades of the RFX-mod reversed field pinch and expected scenario improvements *Nucl. Fusion* **59** 076027
[115] Evans T.E., Moyer R.A., Thomas P.R. *et al* 2004 Suppression of large edge-localized modes in high-confinement DIII-D plasmas with a stochastic magnetic boundary *Phys. Rev. Lett.* **92** 235003
[116] Munaretto S., Chapman B.E., Nornberg M.D., DuBois A.M., Almagri A.F. and Sarff J.S. 2016 Effect of resonant magnetic perturbations on three dimensional equilibria in the Madison symmetric torus reversed-field pinch *Phys. Plasmas* **23** 056104
[117] Munaretto S., Chapman B.E., Holly D.J., Norval R.J., Den Hartog D.J., Goetz J.A. and McCollam K.J. 2015 Control of 3D equilibria with resonant magnetic perturbations in MST *Plasma Phys. Control. Fusion* **57** 104004
[118] Marrelli L., Zanca P., Valisa M. *et al* 2007 Magnetic self organization, MHD active control and confinement in RFX-mod *Plasma Phys. Control. Fusion* **49** B359–69
[119] Piovesan P. *et al* 2011 Influence of external 3D magnetic fields on helical equilibrium and plasma flow in RFX-mod *Plasma Phys. Control. Fusion* **53** 084005
[120] Piovesan P. *et al* 2013 RFX-mod: A multi-configuration fusion facility for three-dimensional physics studies *Phys. Plasmas* **20** 056112
[121] Gobbin M., Franz P., Auriemma F. and Marrelli L. 2015 Spontaneous versus induced hydrogen and deuterium helical shaped plasmas with electron internal transport barriers *Plasma Phys. Control. Fusion* **57** 095004
[122] Frassinetti L., Brunsell P.R. and Drake J.R. 2009 Experiments and modelling of active quasi-single helicity regime generation in a reversed field pinch *Nucl. Fusion* **49** 075019
[123] Veranda M., Bonfiglio D., Cappello S. and Escande D.F. 2013 Impact of helical boundary conditions on nonlinear 3D magnetohydrodynamic simulations of reversed-field pinch *Plasma Phys. Control. Fusion* **55** 074015
[124] Cappello S., Bonfiglio D., Chacon L. *et al* 2012 Nonlinear modeling for helical configurations in toroidal pinch systems *Proc. 24th Int. Conf. on Fusion Energy* (San Diego, CA, 2012) [TH/P2-16] (http://www-naweb.iaea.org/napc/physics/FEC/FEC2012/papers/199_THP216.pdf)
[125] Veranda M. *et al* 2017 Magnetohydrodynamics modelling successfully predicts new helical states in reversed-field pinch fusion plasmas *Nucl. Fusion* **57** 116029

[126] Veranda M., Bonfiglio D., Cappello S. and Escande D.F. 2020 Helically self-organized pinches: dynamical regimes and magnetic chaos healing *Nucl. Fusion* **60** 016007

[127] Spong D.A. 2015 3D toroidal physics: testing the boundaries of symmetry breakinga *Phys. Plasmas* **22** 055602

[128] Newcomb W.A. 1960 Hydromagnetic stability of a diffuse linear pinch *Ann. Phys., NY* **10** 232–67

[129] Robinson D.C. 1978 Tearing-mode-stable diffuse-pinch configurations *Nucl. Fusion* **18** 939–53

[130] White R.B. and Chance M.S. 1984 Hamiltonian guiding center drift orbit calculation for plasmas of arbitrary cross section *Phys. Fluids* **27** 2455–67

[131] Innocente P., Lorenzini R. and Terranova D. 2017 FLiT: a field line trace code for magnetic confinement devices *Plasma Phys. Control. Fusion* **59** 045014

[132] Masamune S., Iida M. and Ohta K. 1998 Magnetic island in helically perturbed force-free equilibrium *J. Phys. Soc. Japan* **67** 2977–80

[133] Masamune S., Iida M., Ohfuji Y. and Oshiyama H. 1998 RFP plasma response to external helical perturbations *Plasma Phys. Control. Fusion* **40** 127–37

[134] Ciaccio G., Veranda M., Bonfiglio D., Spizzo G., Chacón L. and White R.B. 2013 Numerical verification of orbit and nemato codes for magnetic topology diagnosis *Phys. Plasmas* **20** 062505

[135] Franz P. *et al* 2006 Tomographic imaging of resistive mode dynamics in the Madison symmetric torus reversed-field pinch *Phys. Plasmas* **13** 012510

[136] Martines E. *et al* 2011 Equilibrium reconstruction for single helical axis reversed field pinch plasmas *Plasma Phys. Control. Fusion* **53** 035015

[137] Gobbin M. *et al* 2011 Three-dimensional equilibria and transport in RFX-mod: a description using stellarator tools *Phys. Plasmas* **18** 062505

[138] Terranova D., Marrelli L., Hanson J.D., Cianciosa M. and Franz P. 2013 Helical equilibrium reconstruction with V3FIT in the RFX-mod reversed field pinch *Nucl. Fusion* **53** 113014

[139] Gobbin M., Bonfiglio D., Escande D.F., Marrelli L., Alfier A., Martines E., Momo B. and Terranova D. 2011 Vanishing magnetic shear and electron transport barriers in the RFX-Mod reversed field pinch *Phys. Rev. Lett.* **106** 025001

[140] Momo B., Martines E. and Escande D.F. 2011 Magnetic coordinate systems for helical SHAx states in reverse field pinch plasmas *Plasma Phys. Control. Fusion* **53** 125004

[141] Dennis G.R., Hudson S.R., Terranova D. *et al* 2013 Minimally constrained model of self-organized helical states in reversed-field pinches *Phys. Rev. Lett.* **111** 055003

[142] Cooper W.A. *et al* 2013 Bifurcated helical core equilibrium states in tokamaks *Nucl. Fusion* **53** 073021

[143] Jardin S.C., Ferraro N. and Krebs I. 2015 Self-organized stationary states of tokamaks *Phys. Rev. Lett.* **115** 215001

[144] Butt E.P., Carruthers R., Mitchell J.T.D., Pease R.S., Thonemann P.C., Bird M.A., Blears J. and Hartill E.R. 1958 The design and performance of ZETA *Second United Nations International Conference on the Peaceful Uses of Atomic Energy* (Geneva, Switzerland, 1-13 September 1958) [P/1519] (http://cds.cern.ch/record/279634/files/geneva-1958-vol-32.pdf#page=50)

[145] Robinson D.C. and King R.E. 1968 Factor influencing the period of improved stability in zeta *Third International conference on Plasma Physics and Controlled Nuclear Fusion Research* (Novosibirsk, Russian Federation), 1-7 August, 1968) pp 263-76 (https://nds.iaea.org/publications/proceedings/sti-pub-192(v1).pdf#page=279)

[146] Freidberg J.P. 1987 *Ideal Magnetohydrodynamics* (New York: Plenum)

[147] Paccagnella R. 1998 Linear magnetohydrodynamic stability in reversed field pinch with distant and multiple resistive walls *Nucl. Fusion* **38** 1067–81

[148] Hasegawa A. 1985 Self-organization processes in continuous media *Adv. Phys.* **34** 1–42

[149] Taylor J.B. 1986 Relaxation and magnetic reconnection in plasmas *Rev. Mod. Phys.* **58** 741–63

[150] Krebs I., Jardin S.C., Günter S., Hoelzl M., Strumberger E. and Ferraro N. 2017 Magnetic flux pumping in 3D nonlinear magnetohydrodynamic simulations *Phys. Plasmas* **24** 102511

[151] Yamada M. 1999 Review of controlled laboratory experiments on physics of magnetic reconnection *J. Geophys. Res.* **104** 14529–41

[152] Jarboe T.R. 1994 Review of spheromak research *Plasma Phys. Control. Fusion* **36** 945–90

[153] Yamada M., Kulsrud R. and Ji H. 2010 Magnetic reconnection *Rev. Mod. Phys.* **82** 603–64

[154] Taylor J.B. 1974 Relaxation of toroidal plasma and generation of reverse magnetic fields *Phys. Rev. Lett.* **33** 1139–41

[155] Moffatt H.K. 1969 The degree of knottedness of tangled vortex lines *J. Fluid Mech.* **35** 117–29

[156] Woltjer L. 1958 A theorem on force-free magnetic fields *Proc. Natl Acad. Sci.* **44** 489–91

[157] Moffatt H.K. 2015 Magnetic relaxation and the Taylor conjecture *J. Plasma Phys.* **81** 905810608

[158] Prager S.C. 1999 Dynamo and anomalous transport in the reversed field pinch *Plasma Phys. Control. Fusion* **41** A129

[159] Cappello S., Bonfiglio D., Escande D.F. *et al* 2008 The reversed field pinch toward magnetic order: a genuine self-organization *AIP Conf. Proc* **1069** 27

[160] Ortolani S. and Schnack D.D. 1993 *Magnetohydrodynamics of Plasma Relaxation* (Singapore: World Scientific)

[161] Cowling T.G. 1957 The dynamo maintenance of steady magnetic fields *Q. J. Mech. Appl. Math.* **10** 129–36

[162] Moffatt H.K. 1978 *Magnetic Field Generation in Electrically Conducting Fluids* (Cambridge: Cambridge University Press)

[163] Rusbridge M.G., Lees D.J. and Saunders P.A.H. 1962 Electric and magnetic field fluctuations in high-current toroidal discharges *Conference on Plasma Physics and Controlled Nuclear Fusion Research* (Salzburg, Austria, 4-9 September 1961) [CN-10/58] p 895 (http://www-naweb.iaea.org/napc/physics/FEC/1961.pdf#page=814)

[164] Caramana E.J. and Baker D.A. 1984 The dynamo effect in sustained reversed-field pinch discharges *Nucl. Fusion* **24** 423–34

[165] Prager S.C. 1990 Transport and fluctuations in reversed field pinches *Plasma Phys. Control. Fusion* **32** 903–16

[166] Gimblett C.G. and Watkins M.L. 1975 MHD turbulence theory and its implications for the reversed field pinch *7th EPS Conf. Plasma Physics* (Lausanne, Switzerland, 1-5 September 1975) p 103 (http://www-fusion.ciemat.es/media/EPS/EPS_07_Vol1_1975.pdf#page=111)

[167] Ji H. and Prager S.C. 2002 The α dynamo effects in laboratory plasma *Magnetohydrodynamics* **38** 191 (https://arxiv.org/pdf/astro-ph/0110352.pdf)

[168] Sykes A. and Wesson J. 1977 Field reversal in pinches *8th EPS Conf. Plasma Physics* (Prague, Czech Republic, 19-23 September 1977) p 80 (http://www-fusion.ciemat.es/media/EPS/EPS_08_Vol1_1977.pdf#page=82)

[169] Escande D.F. and Bénisti D. 1997 *7th European Fusion Theory Conference* (Jülich, Germany, 8-10 October 1997) p 127

[170] Escande D.F., Cappello S., D'Angelo F., Ortolani S. and Paccagnella R. 2000 Single helicity: a new paradigm for the reversed field pinch *Plasma Phys. Control. Fusion* **42** B243

[171] Caramana E.J., Nebel R.A. and Schnack D.D. 1983 Nonlinear, single-helicity magnetic reconnection in the reversed-field pinch *Phys. Fluids* **26** 1305–19

[172] Aydemir A.Y. and Barnes D.C. 1984 Sustained self-reversal in the reversed-field pinch *Phys. Rev. Lett.* **52** 930–3

[173] Kusano K. and Sato T. 1986 Simulation study of the self-reversal process in the reversed-field pinch based on a non-linearly driven reconnection model *Nucl. Fusion* **26** 1051–61

[174] Schnack D.D., Barnes D.C., Mikic Z. and Caramana E.J. 1987 Semi-implicit magnetohydrodynamic calculations *J. Comput. Phys.* **70** 330–54

[175] Sovinec C.R., Glasser A.H., Gianakon T.A., Nebel R.A., Kruger S.E., Schnack D.D., Plimpton S.J., Tarditi A. and Chu M.S. 2004 Nonlinear magnetohydrodynamics simulation using high-order finite elements *J. Comput. Phys.* **195** 355–86

[176] Chacón L. 2004 A non-staggered, conservative, finite-volume scheme for 3D implicit extended magnetohydrodynamics in curvilinear geometries *Comput. Phys. Commun.* **163** 143–71

[177] Ho Y.L., Prager S.C. and Schnack D.D. 1989 Nonlinear behavior of the reversed field pinch with nonideal boundary conditions *Phys. Rev. Lett.* **62** 1504–7

[178] Anderson J.K., Biewer T.M., Forest C.B., Prager S.C. and Sarff J.S. 2004 Dynamo-free plasma in the reversed field pinch *Phys. Plasmas* **11** L9–L12

[179] Cappello S. and Biskamp D. 1996 Reconnection processes and scaling laws in reversed field pinch magnetohydrodynamics *Nucl. Fusion* **36** 571–81

[180] Cappello S. and Paccagnella R. 1992 Nonlinear plasma evolution and sustainment in the reversed field pinch *Phys. Fluids* B **4** 611–8

[181] Cappello S. and Paccagnella R. 1990 *Proc. Workshop on Theory of Fusion Plasmas* (Varenna, Italy, 27-31 August 1990) p 595

[182] Finn J.M., Nebel R. and Bathke C. 1992 Single and multiple helicity ohmic states in reversed-field pinches *Phys. Fluids* B **4** 1262–79

[183] Cappello S. and Escande D.F. 2000 Bifurcation in viscoresistive MHD: the Hartmann number and the reversed field pinch *Phys. Rev. Lett.* **85** 3838–41

[184] Cappello S. 2004 Bifurcation in the MHD behaviour of a self-organizing system: the reversed field pinch (RFP) *Plasma Phys. Control. Fusion* **46** B313

[185] Chacón L. 2008 An optimal, parallel, fully implicit Newton–Krylov solver for three-dimensional viscoresistive magnetohydrodynamics *Phys. Plasmas* **15** 056103

[186] Bonfiglio D., Chacón L. and Cappello S. 2010 Nonlinear three-dimensional verification of the SPECYL and PIXIE3D magnetohydrodynamics codes for fusion plasmas *Phys. Plasmas* **17** 082501

[187] Zanca P. 2010 Feedback control of dynamo tearing modes in a reversed field pinch: comparison between out-vessel and in-vessel active coils *Plasma Phys. Control. Fusion* **52** 115002

[188] Bonfiglio D., Veranda M., Cappello S. and Chacón L. 2013 Experimental-like helical self-organization in reversed-field pinch modeling *Phys. Rev. Lett.* **111** 085002

[189] Bonfiglio D., Veranda M., Cappello S. and Chacón L. 2015 Helical self-organization in 3D MHD modelling of fusion plasmas *Plasma Phys. Control. Fusion* **57** 044001

[190] Pustovitov V.D. 1982 Evolution equations of a stabilized helical pinch *JETP Lett.* **35** 1 (http://www.jetpletters.ac.ru/ps/1305/article_19719.shtml)

[191] Bonfiglio D., Escande D.F. and Zanca P. 2011 Necessary criterion for magnetic field reversal in the reversed-field pinch *Nucl. Fusion* **51** 063016

[192] Bonfiglio D., Cappello S. and Escande D.F. 2006 Impact of a uniform plasma resistivity in MHD modelling of helical solutions for the reversed field pinch dynamo *Proc. 13th Int. Congress on Plasma Physics* (Kiev, Ukraine, 22-26 May 2006) p 126 (http://icpp2006.kiev.ua/index.html)

[193] Onofri M., Malara F. and Veltri P. 2008 Compressibility effects in the dynamics of the reversed-field pinch *Phys. Rev. Lett.* **101** 255002

[194] Onofri M., Malara F. and Veltri P. 2009 Effects of compressibility and heating in magnetohydrodynamics simulations of a reversed field pinch *Phys. Plasmas* **16** 052508

[195] Onofri M., Malara F. and Veltri P. 2010 Temperature evolution in a magnetohydrodynamics simulation of a reversed-field pinch *Nucl. Fusion* **50** 055003

[196] Ji H., Prager S.C., Almagri A.F., Yagi Y., Hirano Y., Hattori K. and Toyama H. 1996 Measurement of the dynamo effect in a plasma *Phys. Plasmas* **3** 1935–42

[197] Ji H., Toyama H., Fujisawa A. and Miyamoto K. 1992 Fluctuation and edge-current sustainment in a reversed-field pinch *Phys. Rev. Lett.* **69** 616–9

[198] al-Karkhy A., Browning P.K., Cunningham G. and Rusbridge M.G. 1993 Observations of the magnetohydrodynamic dynamo effect in a spheromak plasma *Phys. Rev. Lett.* **70** 1814–7

[199] Shen W. and Prager S.C. 1993 The fluctuation-induced Hall effect *Phys. Fluids* B **5** 1931–3

[200] Kuritsyn A., Fiksel G., Almagri A.F., Ding W.X., Miller M.C., Mirnov V.V., Prager S.C. and Sarff J.S. 2009 Measurements of the momentum and current transport from tearing instability in the Madison symmetric torus reversed-field pinch *Phys. Plasmas* **16** 055903

[201] Ji H., Yagi Y., Hattori K., Prager S.C., Hirano Y., Sarff J.S., Shimada T., Maejima Y. and Hayase K. 1995 Effect of collisionality and diamagnetism on the plasma dynamo *Phys. Rev. Lett.* **75** 1086–9

[202] Ji H. 1999 Turbulent dynamos and magnetic helicity *Phys. Rev. Lett.* **83** 3198–201

[203] Fiksel G., Den Hartog D.J. and Fontana P.W. 1998 An optical probe for local measurements of fast plasma ion dynamics *Rev. Sci. Instrum.* **69** 2024–6

[204] Fontana P.W., Fiksel G. and Prager S.C. 2000 Spectroscopic observation of fluctuation-induced dynamo in the edge of the reversed-field pinch *Phys. Rev. Lett.* **85** 566–9

[205] Den Hartog D.J., Chapman J.T., Craig D., Fontana P.W., Prager S.C. and Sarff J.S. 1999 Measurement of core velocity fluctuations and the dynamo in a reversed-field pinch *Phys. Plasmas* **6** 1813–21

[206] Ennis D.A., Craig D., Gangadhara S., Den Hartog D.J., Ebrahimi F., Fiksel G. and Prager S.C. 2010 Local measurements of tearing mode flows and the magnetohydrodynamic dynamo in the Madison symmetric torus reversed-field pinch *Phys. Plasmas* **17** 082102

[207] Bonomo F. *et al* 2011 Flow measurements and modelling in helical RFX-mod equilibria *Nucl. Fusion* **51** 123007

[208] Scarin P. *et al* 2011 Topology and transport in the edge region of RFX-mod helical regimes *Nucl. Fusion* **51** 073002

[209] Vianello N. *et al* 2015 Magnetic perturbations as a viable tool for edge turbulence modification *Plasma Phys. Control. Fusion* **57** 014027

[210] Agostini M. *et al* 2017 Edge plasma properties with 3D magnetic perturbations in RFX-mod *Nucl. Fusion* **57** 076033

[211] Puiatti M.E. *et al* 2013 Interaction between magnetic boundary and first wall recycling in the reversed field pinch *Plasma Phys. Control. Fusion* **55** 124013

[212] Ding W.X., Brower D.L., Craig D. *et al* 2004 Measurement of the Hall dynamo effect during magnetic reconnection in a high-temperature plasma *Phys. Rev. Lett.* **93** 045002

[213] Mirnov V.V., Hegna C.C. and Prager S.C. 2003 A Hall dynamo effect driven by two-fluid tearing instability *Plasma Phys. Rep.* **29** 566–70

[214] Steinhauer L.C. and Ishida A. 1997 Relaxation of a two-specie magnetofluid *Phys. Rev. Lett.* **79** 3423–6

[215] Hegna C.C. 1998 Self-consistent mean-field forces in turbulent plasmas: current and momentum relaxation *Phys. Plasmas* **5** 2257–63

[216] Ebrahimi F., Prager S.C. and Sovinec C.R. 2007 Momentum transport from current-driven reconnection in the reversed field pinch *Phys. Rev. Lett.* **99** 075003

[217] Sauppe J.P. and Sovinec C.R. 2017 Extended MHD modeling of tearing-driven magnetic relaxation *Phys. Plasmas* **24** 056107

[218] Bonfiglio D., Cappello S. and Escande D.F. 2005 Dominant electrostatic nature of the reversed field pinch dynamo *Phys. Rev. Lett.* **94** 145001

[219] Cappello S., Bonfiglio D. and Escande D.F. 2006 Magnetohydrodynamic dynamo in reversed field pinch plasmas: electrostatic drift nature of the dynamo velocity field *Phys. Plasmas* **13** 056102

[220] Cappello S. *et al* 2011 Equilibrium and transport for quasi-helical reversed field pinches *Nucl. Fusion* **51** 103012

[221] Bonfiglio D., Cappello S. and Escande D. F. 2006 Electrostatic dynamo in reversed field pinch plasmas: simple common fundamental nature of laminar and turbulent regimes *AIP Conf. Proc.* **871** 3

[222] Delzanno G.L., Chacón L. and Finn J.M. 2008 Electrostatic mode associated with the pinch velocity in reversed field pinch simulations *Phys. Plasmas* **15** 122102

[223] Piovesan P. *et al* 2017 Role of a continuous MHD dynamo in the formation of 3D equilibria in fusion plasmas *Nucl. Fusion* **57** 076014

[224] Lapenta G. and Skender M. 2017 Role of electric fields in the MHD evolution of the kink instability *New J. Phys.* **19** 023034

[225] Sovinec C.R., Gianakon T.A., Held E.D. and Schnack D.D. 2003 NIMROD: A computational laboratory for studying nonlinear fusion magnetohydrodynamics *Phys. Plasmas* **10** 1727

[226] Morales J.A., Bos W.J.T. and Schneider K. 2014 The effect of toroidicity on reversed field pinch dynamics *Plasma Phys. Control. Fusion* **56** 095024

[227] King J.R., Sovinec C.R. and Mirnov V.V. 2011 First-order finite-Larmor-radius effects on magnetic tearing in pinch configurations *Phys. Plasmas* **18** 042303

[228] Escande D.F. 2015 What is a reversed field pinch? *Rotation and Momentum Transport in Magnetized Plasmas* Diamond P.H., Garbet X., Ghendrih P. and Sarazin Y. (Singapore: World Scientific)

[229] Onofri M., Malara F. and Veltri P. 2010 Effects of anisotropic thermal conductivity in magnetohydrodynamics simulations of a reversed-field pinch *Phys. Rev. Lett.* **105** 215006

[230] Onofri M. 2011 Single-helicity states in compressible magnetohydrodynamics simulations of the reversed-field pinch with nonuniform resistivity *Nucl. Fusion* **51** 112003

[231] Onofri M. and Malara F. 2013 Effects of the resistivity profile on the formation of a reversed configuration and single helicity states in compressible simulations of the reversed-field pinch *Phys. Plasmas* **20** 102514

[232] Paccagnella R. 2016 Aspect ratio scaling of the single helical states in the reversed field pinch plasmas *Nucl. Fusion* **56** 046010

[233] Paccagnella R. 2016 Relaxation models for single helical reversed field pinch plasmas *Phys. Plasmas* **23** 092512

[234] Bhattacharjee A., Dewar R.L. and Monticello D.A. 1980 Energy principle with global invariants for toroidal plasmas *Phys. Rev. Lett.* **45** 347–50

[235] Tassi E., Militello F. and Porcelli F. 2008 Saturation of tearing modes in reversed field pinches with locally linear force-free magnetic fields and its application to quasi-single-helicity states *Phys. Plasmas* **15** 052104

[236] Terry P.W. and Whelan G.G. 2014 Time-dependent behavior in a transport-barrier model for the quasi-single helcity state *Plasma Phys. Control. Fusion* **56** 094002

[237] Kim J.-H. and Terry P.W. 2012 Magnetic turbulence suppression by a helical mode in a cylindrical geometry *Phys. Plasmas* **19** 122304

[238] Paccagnella R. 2014 Pressure-driven reconnection and quasi periodical oscillations in plasmas *Phys. Plasmas* **21** 032307

[239] Biewer T.M. *et al* 2003 Electron heat transport measured in a stochastic magnetic field *Phys. Rev. Lett.* **91** 045004

[240] Canton A., Hirano Y., Innocente P. and Lorenzini R. 2004 Electron density behaviour in the TPE-RX reversed field pinch experiment and comparison with the particle transport model of the RFX experiment *Plasma Phys. Control. Fusion* **46** 23

[241] Agostini M., Scarin P., Cavazzana R., Alfier A. and Cervaro V. 2010 Optical measurements for turbulence characterization in RFX-mod edge *Rev. Sci. Instrum.* **81** 10D715

[242] Spizzo G., Cappello S., Cravotta A., Predebon I., Marrelli L., Martin P. and White R.B. 2006 Transport barrier inside the reversal surface in the chaotic regime of the reversed-field pinch *Phys. Rev. Lett.* **96** 025001

[243] Vianello N. *et al* 2009 Transport mechanisms in the outer region of RFX-mod *Nucl. Fusion* **49** 045008

[244] Chirikov B.V. 1979 A universal instability of many-dimensional oscillator systems *Phys. Rep.* **52** 263–379

[245] Harvey R.W., McCoy M.G. and Hsu J.Y. 1981 Electron dynamics associated with stochastic magnetic and ambipolar electric fields *Phys. Rev. Lett.* **47** 102–5

[246] Chapman B.E. *et al* 2009 Improved-confinement plasmas at high temperature and high beta in the MST RFP *Nucl. Fusion* **49** 104020

[247] Pegoraro F., Bonfiglio D., Cappello S., Falessi M.V., Grasso D. and Veranda M. 2019 Coherent magnetic structures in self-organized plasmas *Plasma Phys. Control. Fusion* **61** 044003

[248] Di Giannatale G., Falessi M.V., Grasso D., Pegoraro F., Schep T.J., Veranda M., Bonfiglio D. and Cappello S. 2018 Lagrangian coherent structures as a new frame to investigate the particle transport in highly chaotic magnetic systems *J. Phys.: Conf. Ser.* **1125** 012008

[249] Fiksel G. *et al* 1996 Measurement of magnetic fluctuation-induced heat transport in tokamaks and RFP *Plasma Phys. Control. Fusion* **38** A213–25

[250] D'Angelo F and Paccagnella R 1996 The stochastic diffusion process in reversed-field pinch *Phys. Plasmas* **3** 2353

[251] Frassinetti L., Terranova D., Hirano Y., Auriemma F., Yambe K. and Sakakita H. 2007 Cold pulse propagation in a reversed-field pinch *Nucl. Fusion* **47** 135–45

[252] Scheffel J. and Liu D. 1997 Magnetic fluctuation driven cross-field particle transport in the reversed-field pinch *Phys. Plasmas* **4** 3620–8

[253] Scheffel J. and Schnack D.D. 2000 Confinement scaling laws for the conventional reversed-field pinch *Phys. Rev. Lett.* **85** 322–5

[254] Scheffel J. and Schnack D.D. 2000 Numerical studies of confinement scaling in the conventional reversed field pinch *Nucl. Fusion* **40** 1885

[255] Scime E., Cekic M., Den Hartog D.J., Holly D.J. and Watts C. 1992 Ion heating and magnetohydrodynamic dynamo fluctuations in the reversed-field pinch *Phys. Fluids* B **4** 4062–71

[256] Carraro L. *et al* 2009 Improved confinement with internal electron transport barriers in RFX-mod *Nucl. Fusion* **49** 055009

[257] Puiatti M.E. *et al* 2011 Internal and external electron transport barriers in the RFX-mod reversed field pinch *Nucl. Fusion* **51** 073038

[258] Lorenzini R., Auriemma F., Fassina A., Terranova D. and Sattin F. 2016 Internal transport barrier broadening through subdominant mode stabilization in reversed field pinch plasmas *Phys. Rev. Lett.* **116** 185002
[259] Alfier A., Pasqualotto R., Spizzo G., Fassina A. and Frassinetti L. 2008 Electron temperature profiles in RFX-mod *Plasma Phys. Control. Fusion* **50** 035013
[260] Gobbin M., Marrelli L. and Martin P. 2007 Ion and electron local transport inside single helicity islands in the reversed field pinch *Phys. Plasmas* **14** 072305
[261] Terranova D., Alfier A., Bonomo F. *et al* 2007 Enhanced confinement and quasi-single-helicity regimes induced by poloidal current drive *Phys. Rev. Lett.* **99** 095001
[262] Frassinetti L., Koguchi H., Yagi Y., Hirano Y., Sakakita H., Spizzo G. and White R.B. 2006 Improved particle confinement in transition from multiple-helicity to quasi-single-helicity regimes of a reversed-field pinch *Phys. Rev. Lett.* **97** 175001
[263] Stephens H.D., Den Hartog D.J. and Hegna C.C. 2010 Electron thermal transport within magnetic islands in the reversed-field pinch *Phys. Plasmas* **17** 056115
[264] Gobbin M., Franz P., Lorenzini R., Ruzzon A., Fassina A., Marrelli L., Momo B. and Terranova D. 2013 Heat transport in helical RFX-mod plasmas by electron temperature dynamics from soft-x-ray diagnostics *Plasma Phys. Control. Fusion* **55** 105010
[265] Franz P., Gobbin M., Marrelli L., Bonomo F., Fassina A., Martines E. and Spizzo G. 2013 Experimental investigation of electron temperature dynamics of helical states in the RFX-Mod reversed field pinch *Nucl. Fusion* **53** 053011
[266] Fassina A. *et al* 2013 Electron pressure and transport analysis during QSH states in RFX-mod *IEEE Trans. Plasma Sci.* **41** 2–11
[267] Lorenzini R. *et al* 2012 On the energy transport in internal transport barriers of RFP plasmas *Nucl. Fusion* **52** 062004
[268] Hirshman S.P., Shaing K.C., van Rij W.I. and Crume E.C. 1986 Plasma transport coefficients for nonsymmetric toroidal confinement systems *Phys. Fluids* **29** 2951–9
[269] Spong D.A. 2005 Generation and damping of neoclassical plasma flows in stellarators *Phys. Plasmas* **12** 056114
[270] Martin P., Apolloni L., Puiatti M.E. *et al* 2009 Overview of RFX-mod results *Nucl. Fusion* **49** 104019
[271] Puiatti M.E., Bello S.D., Marrelli L. *et al* 2015 Overview of the RFX-mod contribution to the international fusion science program *Nucl. Fusion* **55** 104012
[272] Carraro L. *et al* 2009 Improved confinement with internal electron transport barriers in RFX-mod *Nucl. Fusion* **49** 055009
[273] Innocente P., Alfier A. and Canton A. 2009 Plasma performance and scaling laws in the RFX-mod reversed-field pinch experiment *Nucl. Fusion* **49** 115022
[274] Spizzo G. *et al* 2010 Investigation on the relation between edge radial electric field asymmetries in RFX-mod and density limit *Plasma Phys. Control. Fusion* **52** 095011
[275] Spizzo G. *et al* 2015 Density limit studies in the tokamak and the reversed-field pinch *Nucl. Fusion* **55** 043007
[276] Sattin F., Vianello N., Lorenzini R. and Bonomo F. 2011 Modelling the temperature plateau in RFX-mod single-helical-axis (SHAx) states *Plasma Phys. Control. Fusion* **53** 025013
[277] Innocente P., Martini S. and Canton A. 1997 Upgrade of the RFX CO2 interferometer using in-vessel optics for extended edge resolution *Rev. Sci. Instrum.* **68** 694–7
[278] Gregoratto D., Garzotti L., Innocente P. and Canton A. 1998 Behaviour of electron density profiles and particle transport analysis in the RFX reversed field pinch *Nucl. Fusion* **38** 1199–213
[279] Auriemma F. *et al* 2015 Characterization of particle confinement properties in RFX-mod at a high plasma current *Nucl. Fusion* **55** 043010
[280] Spizzo G., White R.B. and Cappello S. 2007 Chaos generated pinch effect in toroidal confinement devices *Phys. Plasmas* **14** 102310
[281] Spizzo G., White R.B. and Cappello S. 2009 Nonlocal transport in the reversed field pinch *Plasma Phys. Control. Fusion* **51** 124026
[282] Predebon I., Marrelli L., White R.B. *et al* 2004 Particle-transport analysis in reversed field pinch helical states *Phys. Rev. Lett.* **93** 145001
[283] Frassinetti L., Predebon I., Koguchi H. *et al* 2006 Improved particle confinement in transition from multiple-helicity to quasi-single-helicity regimes of a reversed-field pinch *Phys. Rev. Lett.* **97** 175001
[284] Gobbin M., Guazzotto L., Guo S. *et al* 2008 Trapped particles in the reversed field pinch *J. Plasma Fusion Res. Ser.* **8** 1147 (http://www.jspf.or.jp/JPFRS/PDF/Vol8/jpfrs2009_08-1147.pdf)
[285] Gobbin M., Marrelli L. and White R.B. 2009 Numerical studies of transport mechanisms in RFX-mod low magnetic chaos regimes *Plasma Phys. Control. Fusion* **51** 065010
[286] Gobbin M., Spizzo G., Marrelli L. *et al* 2010 Neoclassical transport in the helical reversed-field pinch *Phys. Rev. Lett.* **105** 195006
[287] Barbui T., Carraro L., Franz P., Munaretto S. and Spizzo G. 2015 Light impurity transport studies with solid pellet injections in the RFX-mod reversed-field pinch *Plasma Phys. Control. Fusion* **57** 025006
[288] Carraro L., Costa S., Puiatti M.E., Scarin P. and Valisa M. 2000 Reconstruction of the radiation emitted by the intrinsic impurities in the RFX reversed field pinch *Plasma Phys. Control. Fusion* **42** 731–41
[289] Barbui T., Carraro L., Den Hartog D.J. and Nornberg M. 2014 Impurity transport studies in the Madison symmetric torus reversed-field pinch during standard and pulsed poloidal current drive regimes *Plasma Phys. Control. Fusion* **56** 075012
[290] Gobbin M., Carraro L., Puiatti M.E., Franz P., Momo B. and Terranova D. 2017 Effect of a helical core topology on impurity behavior in RFX-mod plasmas *Plasma Phys. Control. Fusion* **59** 055011
[291] Menmuir S., Carraro L., Alfier A., Fassina A., Spizzo G. and Vianello N. 2010 Impurity transport studies in RFX-mod multiple helicity and enhanced confinement QSH regimes *Plasma Phys. Control. Fusion* **52** 095001
[292] Guo S.C. 2008 Stability threshold of ion temperature gradient driven mode in reversed field pinch plasmas *Phys. Plasmas* **15** 122510
[293] Predebon I., Angioni C. and Guo S.C. 2010 Gyrokinetic simulations of ion temperature gradient modes in the reversed field pinch *Phys. Plasmas* **17** 012304
[294] Sattin F., Garbet X. and Guo S.C. 2010 Study of ion-temperature-gradient modes in RFX-mod using TRB code *Plasma Phys. Control. Fusion* **52** 105002
[295] Predebon I. and Xanthopoulos P. 2015 Ion temperature gradient turbulence in helical and axisymmetric RFP plasmas *Phys. Plasmas* **22** 052308
[296] Liu S.F., Guo S.C., Zhang C.L., Carraro L. and Wang Z.R. 2011 Impurity effects on the ion temperature gradient mode in reversed-field pinch plasmas *Nucl. Fusion* **51** 083021
[297] Predebon I., Carraro L. and Angioni C. 2011 On the mutual effect of ion temperature gradient instabilities and impurity peaking in the reversed field pinch *Plasma Phys. Control. Fusion* **53** 125009

[298] Predebon I., Sattin F., Veranda M. *et al* 2010 Microtearing modes in reversed field pinch plasmas *Phys. Rev. Lett.* **105** 195001

[299] Zuin M. *et al* 2013 Experimental observation of microtearing modes in a toroidal fusion plasma *Phys. Rev. Lett.* **110** 055002

[300] Terry P.W. *et al* 2015 Overview of gyrokinetic studies of finite-β microturbulence *Nucl. Fusion* **55** 104011

[301] Carmody D., Pueschel M.J. and Terry P.W. 2013 Gyrokinetic studies of microinstabilities in the reversed field pinch *Phys. Plasmas* **20** 052110

[302] Williams Z.R., Pueschel M.J. and Terry P.W. 2017 Turbulence, transport, and zonal flows in the Madison symmetric torus reversed-field pinch *Phys. Plasmas* **24** 122309

[303] Zonca F., Chen L. and Dong J.Q. 1999 Existence of ion temperature gradient driven shear Alfvén instabilities in tokamaks *Phys. Plasmas* **6** 1917–24

[304] Predebon I. and Sattin F. 2013 On the linear stability of collisionless microtearing modes *Phys. Plasmas* **20** 040701

[305] Hörling P., Hedin G., Brzozowski J.H. and Mazur S. 1996 Ion temperature, heating and scaling relations at the extrap-T1 reversed-field pinch *Plasma Phys. Control. Fusion* **38** 1725

[306] Gangadhara S., Craig D., Ennis D.A., Fiksel G. and Prager S.C. 2007 Spatially resolved measurements of ion heating during impulsive reconnection in the Madison symmetric torus *Phys. Rev. Lett.* **98** 075001

[307] Gangadhara S., Craig D., Ennis D.A., Fiksel G. and Prager S.C. 2008 Ion heating during reconnection in the Madison symmetric torus reversed field pinch *Phys. Plasmas* **15** 056121

[308] Fiksel G., Almagri A.F., Chapman B.E., Ren Y., Sarff J.S. and Terry P.W. 2009 Mass-dependent ion heating during magnetic reconnection in a laboratory plasma *Phys. Rev. Lett.* **103** 145002

[309] Kumar S.T.A., Almagri A.F., Craig D., Nornberg M.D., Sarff J.S. and Terry P.W. 2013 Charge-to-mass-ratio-dependent ion heating during magnetic reconnection in the MST RFP *Phys. Plasmas* **20** 056501

[310] Magee R.M., Den Hartog D.J., Kumar S.T.A. *et al* 2011 Anisotropic ion heating and tail generation during tearing mode magnetic reconnection in a high-temperature plasma *Phys. Rev. Lett.* **107** 065005

[311] Gatto R. and Terry P.W. 2001 Anomalous ion heating from ambipolar-constrained magnetic fluctuation-induced transport *Phys. Plasmas* **8** 825–35

[312] Tangri V., Terry P.W. and Fiksel G. 2008 Anomalous impurity ion heating from Alfvénic cascade in the reversed field pinch *Phys. Plasmas* **15** 112501

[313] Ren Y., Almagri A.F., Fiksel G. *et al* 2011 Experimental observation of anisotropic magnetic turbulence in a reversed field pinch plasma *Phys. Rev. Lett.* **107** 195002

[314] Terry P.W. *et al* 2012 Dissipation range turbulent cascades in plasmas *Phys. Plasmas* **19** 055906

[315] Thuecks D.J., Almagri A.F. and Sarff J.S. 2017 Evidence for drift waves in the turbulence of reversed field pinch plasmas *Phys. Plasmas* **24** 022309

[316] Svidzinski V.A., Fiksel G. and Mirnov V.V. 2008 Modeling of ion heating from viscous damping of reconnection flows in the reversed field pinch *Phys. Plasmas* **15** 062511

[317] Anderson J.K., Kim J., Bonofiglo P.J., Eilerman S., Nornberg M.D., Sarff J.S. and Sears S.H. 2016 Dynamics of a reconnection-driven runaway ion tail in a reversed field pinch plasma *Phys. Plasmas* **23** 055702

[318] Eilerman S., Anderson J.K., Sarff J.S., Reusch J.A., Nornberg M.D. and Kim J. 2015 Runaway of energetic test ions in a toroidal plasma *Phys. Plasmas* **22** 020702

[319] Frassinetti L., Gobbin M., Marrelli L., Franz P., Martin P. and Chapman B.E. 2005 Perturbative transport studies in the reversed-field pinch *Nucl. Fusion* **45** 1342

[320] Frassinetti L., Gobbin M., Piovesan P., Martin P., Franz P., Chapman B.E., Craig D. and Sarff J.S. 2005 Soft X-ray pulses in the reversed-field pinch *IEEE Trans. Plasma Sci.* **33** 462–3

[321] Frassinetti L., Alfier A., Pasqualotto R. and Innocente P. 2008 Heat diffusivity model and temperature simulations in RFX-mod *Nucl. Fusion* **48** 045007

[322] Frassinetti L., Brunsell P.R. and Cecconello M. 2009 Heat transport modelling in EXTRAP T2R *Nucl. Fusion* **49** 025002

[323] Reusch J.A., Anderson J.K., Den Hartog D.J., Schnack D.D., Stephens H.D. and Forest C.B. 2011 Experimental evidence for a reduction in electron thermal diffusion due to trapped particles *Phys. Rev. Lett.* **107** 155002

[324] Kumar S.T.A. *et al* 2012 Classical confinement and outward convection of impurity ions in the MST RFP *Phys. Plasmas* **19** 056121

[325] Kumar S.T.A., Den Hartog D.J., Caspary K.J., Mirnov V.V., Chapman B.E., Craig D., Fiksel G. and Sarff J.S. 2012 Classical impurity ion confinement in a toroidal magnetized fusion plasma *Phys. Rev. Lett.* **108** 125006

[326] Ding W.X., Brower D.L., Fiksel G. *et al* 2009 Magnetic-fluctuation-induced particle transport and density relaxation in a high-temperature plasma *Phys. Rev. Lett.* **103** 025001

[327] Ding W.X. *et al* 2008 Stochastic magnetic field driven charge transport and zonal flow during magnetic reconnection *Phys. Plasmas* **15** 055901

[328] Ding W.X., Brower D.L., Craig D. *et al* 2007 Nonambipolar magnetic-fluctuation-induced particle transport and plasma flow in the MST reversed-field pinch *Phys. Rev. Lett.* **99** 055004

[329] Agostini M., Scaggion A., Scarin P. and Vianello N. 2012 Interplay between edge magnetic topology, pressure profile and blobs in the edge of RFX-mod *Plasma Phys. Control. Fusion* **54** 065003

[330] Antoni V., Spada E., Vianello N., Cavazzana R., Serianni G. and Martines E. 2005 Shear flows generated by plasma turbulence and their influence on transport *Plasma Phys. Control. Fusion* **47** B13–23

[331] Antoni V., Drake J.R., Spada E., Vianello N., Bergsåker H., Cavazzana R., Cecconello M., Martines E. and Serianni G. 2006 Coherent structures and anomalous transport in reversed field pinch plasmas *Phys. Scr.* T **122** 1–7

[332] Fiksel G., Prager S.C. and Shen W. 1994 Measurement of magnetic fluctuation induced energy transport *Phys. Rev. Lett.* **72** 1028–31

[333] Ji H., Toyama H., Miyamoto K. and Fujisawa A. 1991 Fluctuation and electron-heat transport in a reversed-field-pinch plasma *Phys. Rev. Lett.* **67** 62–5

[334] Rempel T.D., Spragins C.W., Prager S.C., Den Hartog D.J. and Hokin S. 1991 Edge electrostatic fluctuations and transport in a reversed-field pinch *Phys. Rev. Lett.* **67** 1438–41

[335] Terry P.W. *et al* 1996 Ambipolar magnetic fluctuation-induced heat transport in toroidal devices *Phys. Plasmas* **3** 1999–2005

[336] Vianello N., Antoni V., Spada E., Serianni G., Cavazzana R., Bergsåker H., Cecconello M. and Drake J.R. 2005 Reynolds and Maxwell stress measurements in the reversed field pinch experiment Extrap-T2R *Nucl. Fusion* **45** 761–6

[337] Vianello N., Spada E., Antoni V., Serianni G., Regnoli G., Cavazzana R., Bergsåker H. and Drake J.R. 2005 Self-regulation of $E \times B$ flow shear via plasma turbulence *Phys. Rev. Lett.* **94** 135001

[338] Spolaore M., Antoni V., Spada E., Cavazzana R., Drake J.R., Martines E., Regnoli G., Serianni G. and Vianello N. 2004

Vortex-induced diffusivity in reversed field pinch plasmas *Phys. Rev. Lett.* **93** 215003
[339] Sattin F., Scarin P., Agostini M., Serianni G., Spolaore M. and Vianello N. 2006 Statistical features of edge turbulence in RFX-mod from gas puffing imaging *Plasma Phys. Control. Fusion* **48** 1033–51
[340] Vianello N., Spolaore M., Agostini M., De Masi G., Martines E., Momo B., Scarin P., Spagnolo S. and Zuin M. 2016 On the statistics and features of turbulent structures in RFX-mod *Plasma Phys. Control. Fusion* **58** 044009
[341] Spolaore M. *et al* 2015 Electromagnetic turbulent structures: a ubiquitous feature of the edge region of toroidal plasma configurations *Phys. Plasmas* **22** 012310
[342] Ricci P., Halpern F.D., Jolliet S., Mosetto A., Fasoli A., Furno I. and Theiler C. 2012 Simulation of plasma turbulence in scrape-off layer conditions: the GBS code, simulation results and code validation *Plasma Phys. Control. Fusion* **54** 124047
[343] Riva F., Vianello N., Spolaore M., Cavazzana R., Marrelli L. and Spagnolo S. 2018 Three-dimensional simulations of plasma turbulence in the RFX-mod scrape-off layer and comparison with experimental measurements *Phys. Plasmas* **25** 022305
[344] Rea C. *et al* 2015 Comparative studies of electrostatic turbulence induced transport in presence of resonant magnetic perturbations in RFX-mod *Nucl. Fusion* **55** 113021
[345] De Masi G., Martines E., Spolaore M., Cavazzana R., Innocente P., Momo B., Spagnolo S. and Zuin M. 2013 Electrostatic properties and active magnetic topology modification in the RFX-mod edge plasma *Nucl. Fusion* **53** 083026
[346] Scarin P., Agostini M., Spizzo G. and Zanca P. 2019 Helical plasma-wall interaction in the RFX-mod: effects of high-*n* mode locking *Nucl. Fusion* **59** 086008
[347] Zuin M., Dal Bello S., Marrelli L. *et al* 2017 Overview of the RFX-mod fusion science activity *Nucl. Fusion* **57** 102012
[348] Lorenzini R. *et al* 2015 The isotope effect in the RFX-mod experiment *Nucl. Fusion* **55** 043012
[349] Fiksel G., Hudson B., Den Hartog D.J., O'Connell R., Prager S.C., Beklemishev A.D., Davydenko V.I., Ivanov A.A. and Tsidulko Y.A. 2005 Observation of weak impact of a stochastic magnetic field on fast-ion confinement *Phys. Rev. Lett.* **95** 125001
[350] Eilerman S., Anderson J.K., Reusch J.A., Fiksel G., Polosatkin S. and Belykh V. 2012 Time-resolved ion energy distribution measurements using an advanced neutral particle analyzer on the MST reversed-field pinch *Rev. Sci. Instrum.* **83** 10D302
[351] Bonofiglo P.J., Anderson J.K., Gobbin M., Boguski J., Parke E., Kim J. and Egedal J. 2019 Fast ion transport in the quasi-single helical reversed-field pinch *Phys. Plasmas* **26** 022502
[352] García-Muñoz M., Martin P., Fahrbach H.-U., Gobbin M., Günter S., Maraschek M., Marrelli L. and Zohm H. 2007 NTM induced fast ion losses in ASDEX Upgrade *Nucl. Fusion* **47** L10–5
[353] Gobbin M., White R.B. and Marrelli L. 2008 Resonance between passing fast ions and MHD instabilities both in the tokamak and the RFP configurations *Nucl. Fusion* **48** 075002
[354] Waksman J. *et al* 2012 Neutral beam heating of a RFP plasma in MST *Phys. Plasmas* **19** 122505
[355] Parke E., Anderson J.K., Brower D.L., Ding W.X., Johnson C.A. and Lin L. 2016 Current profile redistribution driven by neutral beam injection in a reversed-field pinch *Phys. Plasmas* **23** 056108
[356] Koliner J.J. *et al* 2012 Fast-particle-driven Alfvénic modes in a reversed field pinch *Phys. Rev. Lett.* **109** 115003
[357] Anderson J.K. *et al* 2013 Fast ion confinement and stability in a neutral beam injected reversed field pinch *Phys. Plasmas* **20** 056102
[358] Cook C.R., Hegna C.C., Anderson J.K., Boguski J., Feng R., Koliner J.J., Spong D.A. and Hirshman S.P. 2016 Identification of island-induced Alfvén eigenmodes in a reversed field pinch *Plasma Phys. Control. Fusion* **58** 054004
[359] Lin L. *et al* 2013 Measurement of energetic-particle-driven core magnetic fluctuations and induced fast-ion transport *Phys. Plasmas* **20** 030701
[360] Budny R.V. *et al* 1992 Simulations of deuterium-tritium experiments in TFTR *Nucl. Fusion* **32** 429–47
[361] Lin L. *et al* 2014 Energetic-particle-driven instabilities and induced fast-ion transport in a reversed field pinch *Phys. Plasmas* **21** 056104
[362] Capecchi W., Anderson J.K., Bonofiglo P.J., Magee R.M., McCollam K.J., McConnell R., Parke E. and Sarff J.S. 2019 A measure of fast ion beta at marginal stability in the reversed field pinch *Nucl. Fusion* **59** 086026
[363] Cai H., Lin L., Ding W. and Brower D.L. 2015 Influence of energetic ions on tearing modes in a reversed field pinch *Plasma Phys. Control. Fusion* **57** 025021
[364] Anderson J.K., Capecchi W., Eilerman S., Nornberg M.D., Reusch J.A., Sarff J.S. and Lin L. 2014 Fast ion confinement in the three-dimensional helical reversed-field pinch *Plasma Phys. Control. Fusion* **56** 094006
[365] Bonofiglo P.J., Anderson J.K., Boguski J., Egedal J., Gobbin M., Spong D.A. and Parke E. 2019 Fast ion transport in the three-dimensional reversed-field pinch *Phys. Rev. Lett.* **123** 055001
[366] Antoni V., Bagatin M. and Martines E. 1992 Energy transport and magnetic stochasticity at the edge of a plasma in RFP configuration *Plasma Phys. Control. Fusion* **34** 1639–50
[367] Ingraham J.C., Ellis R.F., Downing J.N., Weber P.G. and Wurden G.A. 1990 Energetic electron measurements in the edge of a reversed-field pinch *Phys. Fluids* B **2** 143–59
[368] Stoneking M.R., Hokin S.A., Prager S.C., Ji H. and Den Hartog D.J. 1994 Particle transport due to magnetic fluctuations *Phys. Rev. Lett.* **73** 549–52
[369] Yagi Y., Antoni V., Bagatin M., Martines E., Serianni G. and Vallone F. 1997 Measurement of superthermal electron flow and temperature in a reversed-field pinch experiment by an electrostatic electron energy analyser *Plasma Phys. Control. Fusion* **39** 1915–27
[370] Yagi Y., Hirano Y., Shimada T., Maejima Y., Hirota I. and Newton A.A. 1991 Plasma current and energetic electrons in the core plasma of a reversed field pinch *Plasma Phys. Control. Fusion* **33** 1391–406
[371] Giruzzi G. and Hokin S. 1996 Superthermal electron generation and transport in the reversed-field pinch *Plasma Phys. Control. Fusion* **38** 1001–9
[372] Giruzzi G. and Martines E. 1994 Kinetic modeling of fast electron dynamics and self-consistent magnetic fields in a reversed field pinch *Phys. Plasmas* **1** 2653–60
[373] Ji H., Toyama H., Yamagishi K., Fujisawa A. and Miyamoto K. 1991 Probe measurements in the REPUTE-1 reversed field pinch *Rev. Sci. Instrum.* **62** 2326–37
[374] Martines E., Bartiromo R. and Shoucri M. 2002 On the origin of superthermal electrons in the edge of RFP plasmas *Plasma Phys. Control. Fusion* **44** 439–49
[375] Clayton D.J. *et al* 2010 Observation of energetic electron confinement in a largely stochastic reversed-field pinch plasma *Phys. Plasmas* **17** 012505
[376] Piovan R., Bettini P., Bustreo C., Cavazzana R., Escande D.F., Puiatti M.E., Valisa M., Zollino G. and Zuin M. 2018 A continuously pulsed reversed field pinch core for an ohmically heated hybrid reactor *Fusion Eng. Des.* **136** 1489–93

[377] Ho Y.L. 1991 Numerical simulation of fluctuation suppression via DC helicity injection in a reversed field pinch *Nucl. Fusion* **31** 341

[378] Sovinec C.R. 1995 *Magnetohydrodynamics Simulations of Noninductive Helicity Injection in the Reversed Field Pinch and Tokamak* (Madison, WI: University of Wisconsin Press) (http://plasma.physics.wisc.edu/uploadedfiles/theses/thesisSovinec69_1995.pdf)

[379] Sovinec C.R. and Prager S.C. 1999 Magnetohydrodynamic effects of current profile control in reversed field pinches *Nucl. Fusion* **39** 777

[380] Sarff J.S., Hokin S.A., Ji H. and Sovinec C.R. 1994 Fluctuation and transport reduction in a reversed field pinch by inductive poloidal current drive *Phys. Rev. Lett.* **72** 3670–3

[381] Svidzinski V.A. and Prager S.C. 2007 On the physics of improved confinement during pulsed poloidal current drive in MST reversed-field pinch *J. Fusion Energy* **26** 215–20

[382] Reynolds J.M., Sovinec C.R. and Prager S.C. 2008 Nonlinear magnetohydrodynamics of pulsed parallel current drive in reversed-field pinches *Phys. Plasmas* **15** 062512

[383] Chapman B.E. *et al* 2002 High confinement plasmas in the Madison symmetric torus reversed-field pinch *Phys. Plasmas* **9** 2061–8

[384] Sarff J.S. *et al* 1995 Transport reduction by current profile control in the reversed-field pinch *Phys. Plasmas* **2** 2440–6

[385] Frassinetti L., Yagi Y., Martin P., Shimada T., Hirano Y., Sakakita H. and Asai T. 2003 Operating conditions to achieve high performance in PPCD in a reversed-field pinch plasma *J. Phys. Soc. Japan* **72** 3297–8

[386] Frassinetti L., Yagi Y., Koguchi H. and Hirano Y. 2004 Performance improvement conditions and their physical origin in the pulsed poloidal current drive regime of the reversed-field pinch device TPE-RX *Phys. Plasmas* **11** 5229–38

[387] Frassinetti L., Yagi Y., Koguchi H., Hirano Y. and Sakakita H. 2005 Role of locked mode in the effectiveness of pulsed poloidal current drive regime in the reversed-field pinch *Phys. Plasmas* **12** 100703

[388] Watterson P. and Gimblett C.G. 1983 Catching voltage prescriptions for the RFP *Theor. Phys. Note* **83** 10

[389] Caramana E.J. and Nebel R.A. 1988 Reversed-field pinch ohmic equilibria during current decay and termination *Phys. Fluids* **31** 3322–9

[390] Nebel R.A., Schnack D.D. and Gianakon T.A. 2002 Self-similar decaying profiles for reversed-field pinches *Phys. Plasmas* **9** 4968–84

[391] Bartiromo R., Antoni V., Bolzonella T., Marrelli L., Martin P., Martines E., Martini S. and Pasqualotto R. 1999 Improved confinement and transport studies in the reversed field experiment (RFX) *Phys. Plasmas* **6** 1830–6

[392] Martines E. and Spagnolo S. 2008 One-dimensional simulations of reversed field pinch discharges *Phys. Plasmas* **15** 122506

[393] Brower D.L., Ding W.X., Terry S.D., Biewer T.M., Chapman B.E., Craig D., Forest C.B., Prager S.C. and Sarff J.S. 2003 Laser polarimetric measurement of equilibrium and fluctuating magnetic fields in a reversed field pinch (invited) *Rev. Sci. Instrum.* **74** 1534–40

[394] Terry S.D. *et al* 2004 Measurement of current profile dynamics in the Madison symmetric torus *Phys. Plasmas* **11** 1079–86

[395] Puiatti M.E., Cappello S., Lorenzini R. *et al* 2003 Analysis and modelling of the magnetic and plasma profiles during PPCD experiments in RFX *Nucl. Fusion* **43** 1057

[396] Chapman B.E. *et al* 2000 Modifications to the edge current profile with auxiliary edge current drive and improved confinement in a reversed-field pinch *Phys. Plasmas* **7** 3491–4

[397] Sarff J.S. *et al* 2003 Tokamak-like confinement at high beta and low field in the reversed field pinch *Plasma Phys. Control. Fusion* **45** A457

[398] Anderson J.K. *et al* 2005 Dynamo-free plasma in the reversed-field pinch: advances in understanding the reversed-field pinch improved confinement mode *Phys. Plasmas* **12** 056118

[399] Sarff J.S. *et al* 2003 Tokamak-like confinement at a high beta and low toroidal field in the MST reversed field pinch *Nucl. Fusion* **43** 1684

[400] Ding W.X., Brower D.L., Terry S.D., Prager S.C., Sarff J.S. and Wright J.C. 2003 Measurement of internal magnetic field fluctuations in a reversed-field pinch by Faraday rotation *Phys. Rev. Lett.* **90** 035002

[401] Lanier N.E., Craig D., Anderson J.K., Chapman B.E., Den Hartog D.J., Forest C.B., Prager S.C., Brower D.L. and Jiang Y. 2000 Control of density fluctuations and electron transport in the reversed-field pinch *Phys. Rev. Lett.* **85** 2120–3

[402] Lanier N.E., Craig D., Anderson J.K., Chapman B.E., Den Hartog D.J., Forest C.B., Prager S.C., Brower D.L. and Jiang Y. 2001 An investigation of density fluctuations and electron transport in the Madison symmetric torus reversed-field pinch *Phys. Plasmas* **8** 3402–10

[403] Lei J., Schoch P.M., Demers D.R., Connor K.A., Anderson J.K. and Crowley T.P. 2002 Core electrostatic fluctuations and particle transport in a reversed-field pinch *Phys. Rev. Lett.* **89** 275001

[404] Chapman B.E. *et al* 1998 $E \times B$ flow shear and enhanced confinement in the Madison symmetric torus reversed-field pinch *Phys. Plasmas* **5** 1848–54

[405] Li G., Drake J.R., Bergsåker H., Hellblom G., Mazur S., Möller A. and Nordlund P. 1995 Correlation between internal tearing modes and edge electrostatic fluctuations in a reversed-field pinch *Phys. Plasmas* **2** 2615–7

[406] Marrelli L., Frassinetti L., Martin P. and Sarff J.S. 2005 Reduced intermittency in the magnetic turbulence of reversed field pinch plasmas *Phys. Plasmas* **12** 030701

[407] Frassinetti L., Yambe K., Kiyama S., Koguchi H. and Sakakita H. 2007 Turbulence and particle confinement in a reversed-field pinch plasma *Plasma Phys. Control. Fusion* **49** 199–209

[408] Franz P., Marrelli L., Piovesan P., Martin P., Predebon I., Spizzo G., White R.B. and Xiao C. 2004 Observations of multiple magnetic islands in the core of a reversed field pinch *Phys. Rev. Lett.* **92** 125001

[409] Zanca P. 2007 Self-similar current decay experiment in RFX-mod *Plasma Phys. Control. Fusion* **49** 113

[410] Bolzonella T., Martin P., Martini S., Pasqualotto R. and Terranova D. 2001 Quasistationary magnetic fluctuation control in the reversed field pinch: a proof of principle experiment *Phys. Rev. Lett.* **87** 195001

[411] Carraro L., Puiatti M.E., Sattin F. and Valisa M. 2002 Impurity transport during pulsed poloidal current drive experiment in the reversed field pinch experiment RFX *Plasma Phys. Control. Fusion* **44** 2135–48

[412] O'Connell R., Hartog D.J.D., Forest C.B. *et al* 2002 Observation of velocity-independent electron transport in the reversed field pinch *Phys. Rev. Lett.* **91** 045002

[413] Hudson B.F. 2006 Fast ion confinement in the reversed field pinch *PhD Thesis* University of Wisconsin–Madison (http://plasma.physics.wisc.edu/uploadedfiles/theses/thesisHudson28_2006.pdf)

[414] Koguchi H., Terranova D., Innocente P., Sakakita H., Asai T., Yagi Y., Hirano Y. and Yambe K. 2006 Deuterium ice pellet injection during pulsed poloidal current drive operation in toroidal pinch experiment-RX reversed-field pinch device *Japan. J. Appl. Phys.* **45** L1124

[415] Auriemma F., Hirano Y., Koguchi H., Innocente P., Lorenzini R., Puiatti M.E., Terranova D. and Sakakita H. 2009 Comparison of particle transport properties in

TPE-RX standard and PPCD plasmas *Plasma Phys. Control. Fusion* **51** 065012

[416] Wyman M.D. *et al* 2008 High-β, improved confinement reversed-field pinch plasmas at high density *Phys. Plasmas* **15** 010701

[417] Wyman M.D. *et al* 2009 Plasma behaviour at high β and high density in the Madison symmetric torus RFP *Nucl. Fusion* **49** 015003

[418] Lorenzini R., Garzotti L., Pégourié B. and Martini S. 2002 Analysis and modelling of plasma response to pellet injection in RFX *Plasma Phys. Control. Fusion* **44** 233–52

[419] Caspary K.J. 2014 Density and beta limits in the madison symmetric torus reversed-field pinch *PhD Thesis* University of Wisconsin– Madison http://plasma.physics.wisc.edu/uploadedfiles/theses/thesisCaspary119_2014.pdf

[420] Kuldkepp M., Brunsell P.R., Cecconello M., Menmuir S. and Rachlew E. 2006 Measurements and modeling of transport and impurity radial profiles in the EXTRAP T2R reversed field pinch *Phys. Plasmas* **13** 092506

[421] Galante M.E., Reusch L.M., Den Hartog D.J., Johnson J.R., McGarry M.B., Nornberg M.D. and Stephens H.D. 2015 Determination of Z_{eff} by integrating measurements from x-ray tomography and charge exchange recombination spectroscopy *Nucl. Fusion* **55** 123016

[422] Stoneking M.R., Lanier N.E., Prager S.C. and Sinitsyn D. 1997 Fivefold confinement time increase in the Madison symmetric torus using inductive poloidal current drive *Phys. Plasmas* **4** 1632–7

[423] Bartiromo R., Bolzonella T., Buffa A., Martini S., Masiello A., Ortolani S., Piovan R., Sonato P. and Zollino G. 1999 Tearing mode rotation by external field in a reversed field pinch *Phys. Rev. Lett.* **83** 1779–82

[424] Chapman B.E., Anderson J.K., Biewer T.M. *et al* 2001 Reduced edge instability and improved confinement in the MST reversed-field pinch *Phys. Rev. Lett.* **87** 205001

[425] Cravotta A., Spizzo G., Terranova D., Franz P., Marrelli L., Martin P., Martini S. and Ortolani S. 2003 A statistical analysis of pulsed poloidal current drive in the reversed field experiment *Phys. Plasmas* **10** 705–12

[426] Yagi Y., Koguchi H., Hirano Y., Sakakita H., Sekine S., Chapman B.E. and Sarff J.S. 2003 Increased confinement improvement in a reversed-field pinch using double-pulsed poloidal current drive *Phys. Plasmas* **10** 2925–31

[427] Telesca G. and Tokar M.Z. 2004 Modelling of PPCD in the reversed field pinch RFX by the transport code RITM *Nucl. Fusion* **44** 303

[428] Chapman B.E. *et al* 2010 Generation and confinement of hot ions and electrons in a reversed-field pinch plasma *Plasma Phys. Control. Fusion* **52** 124048

[429] Yagi Y., Koguchi H., Hirano Y., Shimada T. and Sekine S. 2002 Figure of merit for the improvement of confinement in pulsed poloidal current drive experiments in reversed-field pinch devices *J. Phys. Soc. Japan* **71** 2574–5

[430] Cecconello M., Malmberg J.-A., Spizzo G., Gravestjin R.M., Franz P., Piovesan P., Martin P. and Drake J.R. 2003 Current profile modification experiments in EXTRAP T2R *Plasma Phys. Control. Fusion* **46** 145

[431] ITER Physics Expert Group on Confin 1999 Chapter 2: Plasma confinement and transport *Nucl. Fusion* **39** 2175–249

[432] Yagi Y., Koguchi H., Hirano Y. and Frassinetti L. 2005 An empirical scaling law for improved confinement in reversed-field pinch plasmas *Nucl. Fusion* **45** 138–42

[433] Scheffel J. and Dahlin J.-E. 2006 Confinement scaling in the advanced reversed-field pinch *Plasma Phys. Control. Fusion* **48** L97–L104

[434] Dahlin J.-E. and Scheffel J. 2007 Numerical studies of confinement scalings for the dynamo-free reversed-field pinch *Nucl. Fusion* **47** 9–16

[435] Lin L., Ding W.X., Brower D.L. *et al* 2012 Role of nonlinear coupling and density fluctuations in magnetic-fluctuation-induced particle transport *Phys. Rev. Lett.* **108** 175001

[436] Duff J.R., Williams Z.R., Brower D.L., Ding W.X., Pueschel M.J., Sarff J.S. and Terry P.W. 2018 Observation of trapped-electron-mode microturbulence in reversed field pinch plasmas *Phys. Plasmas* **25** 010701

[437] Carmody D., Pueschel M.J. and Anderson J.K. 2015 Microturbulence studies of pulsed poloidal current drive discharges in the reversed field pinch *Phys. Plasmas* **22** 012504

[438] Nishizawa T., Almagri A.F., Anderson J.K. *et al* 2019 Direct measurement of a toroidally directed zonal flow in a toroidal plasma *Phys. Rev. Lett.* **122** 105001

[439] Nishizawa T., Nornberg M.D., Boguski J. *et al* 2018 Measurements of impurity transport due to drift-wave turbulence in a toroidal plasma *Phys. Rev. Lett.* **121** 165002

[440] Craig D., Fiksel G. and Prager S.C. 2001 Control of magnetic fluctuations in the reversed field pinch with edge current drive *Phys. Plasmas* **8** 1463–6

[441] Uchimoto E., Cekic M., Harvey R.W., Prager S.C., Sarff J.S. and Sovinec C.R. 1994 Lower-hybrid poloidal current drive for fluctuation reduction in a reversed field pinch *Phys. Plasmas* **1** 3517–9

[442] Shiina S., Kondoh Y., Saito K. and Maekawa T. 1995 Theoretical investigation on r.f. current drive in reversed-field pinch plasma *Fusion Eng. Des.* **26** 259–76

[443] Kaufman M.C., Goetz J.A., Thomas M.A., Burke D.R. and Clayton D.J. 2005 Lower hybrid experiments on MST *AIP Conf. Proc.* **933** 309–12

[444] Kaufman M.C., Goetz J.A., Burke D.R., Almagri A.F., Oliva S.P. and Kulpin J.G. 2007 Validating the lower hybrid interdigital-line antenna on MST *AIP Conf. Proc.* **933** 309–12

[445] Burke D.R., Goetz J.A., Kaufman M.C., *et al* 2007 Diagnosis of lower hybrid on MST *AIP Conf. Proc.* **933** 309–12

[446] Forest C.B., Chattopadhyay P.K. and Harvey R.W. 2000 Off-midplane launch of electron Bernstein waves for current drive in overdense plasmas *Phys. Plasmas* **7** 1352–5

[447] Chattopadhyay P.K., Anderson J.K., Biewer T.M., Forest C.B., Harvey R.W. and Smirnov A.P. 2002 Electron Bernstein wave emission from an overdense reversed field pinch plasma *Phys. Plasmas* **9** 752–5

[448] Cengher M., Anderson J.K. and Svidzinski V. 2006 Coupling to the electron Bernstein wave using a phased array of waveguides in MST reversed field pinch *Nucl. Fusion* **46** 521–31

[449] Bilato R., Volpe F., Köhn A., Farina D., Poli E. and Brambilla M. 2009 Feasibility of electron Bernstein wave coupling via O–X–B mode conversion in the RFX-mod reversed field pinch device *Nucl. Fusion* **49** 075020

[450] Seltzman A.H., Anderson J.K., DuBois A.M. and Forest C.B. 2016 X-ray analysis of electron Bernstein wave heating in MST *Rev. Sci. Instrum.* **87** 11E329

[451] Hendries E.R., Anderson J.K., Diem S. *et al* 2014 MHD simulation of RF current drive in MST *AIP Conf. Proc.* **1580** 510–3

[452] Hirano Y., Maejima Y., Shimada T. and Yagi Y. 1996 Improved confinement in a high pinch parameter region of the reversed field pinch plasma *Nucl. Fusion* **36** 721

[453] Chapman B.E., Almagri A.F., Cekic M., Prager S.C. and Sarff J.S. 1996 Sawteeth and energy confinement in the Madison symmetric torus reversed-field pinch *Phys. Plasmas* **3** 709–11

[454] Chapman B.E., Chiang C.-S., Prager S.C. and Stoneking M.R. 1998 Strong $E \times B$ flow shear and reduced fluctuations in a reversed-field pinch *Phys. Rev. Lett.* **80** 2137–40

[455] Yambe K., Hirano Y. and Sakakita H. 2014 Improved confinement region without large magnetohydrodynamic activity

in TPE-RX reversed-field pinch plasma *Phys. Plasmas* **21** 114502

[456] Chapman B.E. 1997 Fluctuation reduction and enhanced confinement in the mst reversed field pinch *PhD Thesis* University of Wisconsin– Madison (http://plasma.physics.wisc.edu/uploadedfiles/theses/thesisChapman85_1997.pdf)

[457] Gatto R., Terry P.W. and Hegna C.C. 2002 Tearing mode stability with equilibrium flows in the reversed-field pinch *Nucl. Fusion* **42** 496–509

[458] Antoni V. *et al* 2000 Experimental measurements and modelling of the structure of the radial electric field in RFX *Czech. J. Phys.* **50** 1387–96

[459] Antoni V., Cavazzana R., Fattorini L., Serianni G., Spolaore M., Tramontin L. and Vianello N. 2000 Effects of pulsed poloidal current drive on the edge region of a reversed field pinch plasma *Plasma Phys. Control. Fusion* **42** 893

[460] Craig D. *et al* 1997 Enhanced confinement with plasma biasing in the MST reversed field pinch *Phys. Rev. Lett.* **79** 1865–8

[461] Antoni V., Martines E., Desideri D., Serianni G., Spolaore M., Tramontin L. and Vianello N. 2000 Electrostatic transport reduction induced by flow shear modification in a reversed field pinch plasma *Plasma Phys. Control. Fusion* **42** 83–90

[462] Sätherblom H.-E., Mazur S. and Nordlund P. 1996 Resistivity profile effects in numerical magnetohydrodynamic simulations of the reversed-field pinch *Plasma Phys. Control. Fusion* **38** 2205–14

[463] Greenwald M. 2002 Density limits in toroidal plasmas *Plasma Phys. Control. Fusion* **44** R27

[464] Sudo S., Takeiri Y., Zushi H., Itoh K., Kondo K. and Iiyoshi A. 1990 Scalings of energy confinement and density limit in stellarator/heliotron devices *Nucl. Fusion* **30** 11–21

[465] Zanca P., Sattin F., Escande D.F. and Tudisco O. 2017 A unified model of density limit in fusion plasmas *Nucl. Fusion* **57** 056010

[466] Zanca P., Sattin F., Escande D.F. *et al* 2019 A power-balance model of the density limit in fusion plasmas: application to the L-mode tokamak *Nucl. Fusion* **59** 126011

[467] Chang Z. 1995 Observation of nonlinear neoclassical pressure-gradient-driven tearing modes in TFTR *Phys. Rev. Lett.* **74** 4663–6

[468] Kislov D.A., Esipchuk Y.V., Kirneva N.A. *et al* 2001 Beta limit due to resistive tearing modes in T-10 *Nucl. Fusion* **41** 1619

[469] Koslowski H.R., Fuchs G., Jaspers R. *et al* 2000 MHD activity at the beta limit in RI mode discharges on TEXTOR-94 *Nucl. Fusion* **40** 821

[470] Weller A. *et al* 2006 Significance of MHD effects in stellarator confinement *Fusion Sci. Technol.* **50** 158–70

[471] Sakakibara S. *et al* 2015 Characteristics of MHD instabilities limiting the beta value in LHD *Nucl. Fusion* **55** 083020

[472] Okamura S. *et al* 1999 Confinement physics study in a small low aspect ratio helical device: CHS *Nucl. Fusion* **39** 1337

[473] Carreras B.A., Lynch V.E., Ichiguchi K. and Tatsuno T. 2001 On the applicability of local asymptotic stability criteria to stellarator stability *Phys. Plasmas* **8** 990–6

[474] Merlin D., Ortolani S. and Paccagnella R. 1989 Linear resistive magnetohydrodynamic stability analysis of reversed field pinch configurations at finite beta *Nucl. Fusion* **29** 1153–60

[475] Ortolani S. and Rostagni G. 1983 Density limits and scaling laws in reversed field pinches *Nucl. Instrum. Methods Phys. Res.* **207** 35–48

[476] Perkins F.W. and Hulse R.A. 1985 On the Murakami density limit in tokamaks and reversed-field pinches *Phys. Fluids* **28** 1837

[477] Valisa M., Auriemma F., Canton A. *et al* 2004 The Greenwald density limit in the reversed field pinch *Proc. 20th Int. Conf. on Fusion Energy* (Vilamoura, Portugal, 2012) [EX/P4-13] (http://www-naweb.iaea.org/napc/physics/fec/fec2004/papers/ex_p4-13.pdf)

[478] Puiatti M.E. *et al* 2009 High density physics in reversed field pinches: comparison with tokamaks and stellarators *Nucl. Fusion* **49** 045012

[479] Wesson J.A. 2004 *Tokamaks* 3rd edn (Oxford: Clarendon) (https://global.oup.com/academic/product/tokamaks-9780199592234?cc=it& lang=en&)

[480] Puiatti M.E. *et al* 2009 High density limit in reversed field pinches *Phys. Plasmas* **16** 012505

[481] Lipschultz B. 1987 Review of MARFE phenomena in tokamaks *J. Nucl. Mater.* **145–147** 15–25

[482] Miyazawa J. *et al* 2006 Detachment phenomena in LHD compared to W7-AS *Fusion Sci. Technol.* **50** 192–200

[483] Bartiromo R., Buffa A., Canton A. *et al* 2000 Analysis of the high density limits in the RFX high current regimes *27th EPS Conf. Plasma Physics* (Budepest, Hungary, 12-16 June 2000) p 1380 (http://epsppd.epfl.ch/Buda/pdf/p4_031.pdf)

[484] Spizzo G., Agostini M., Scarin P., White R.B., Cappello S., Puiatti M.E. and Valisa M. 2012 Edge topology and flows in the reversed-field pinch *Nucl. Fusion* **52** 054015

[485] Agostini M., Scarin P., Cavazzana R., Serianni G., Spolaore M. and Vianello N. 2009 Edge turbulence characterization in RFX-mod with optical diagnostics *Plasma Phys. Control. Fusion* **51** 105003

[486] Spizzo G. *et al* 2014 Edge ambipolar potential in toroidal fusion plasmas *Phys. Plasmas* **21** 056102

[487] Lianghua Y., Dawei Z., Beibin F., Yan Z., Xiaoyu H., Yonggao L., Bucalossi J. and Xuru D. 2010 Comparison of supersonic molecular beam injection from both low field side and high field side of HL-2A *Plasma Sci. Technol.* **12** 529

[488] Stabler A. *et al* 1992 Density limit investigations on ASDEX *Nucl. Fusion* **32** 1557

[489] De Masi G. *et al* 2012 Edge flow and radiation in helium discharges in RFX *39th EPS Conf. Plasma Physics* (Stockholm, Sweden, 2–6 July 2012) [p5.003] (http://ocs.ciemat.es/epsicpp2012pap/pdf/P5.003.pdf)

[490] Sakakita H., Yagi Y., Koguchi H., Shimada T., Canton A.M. and Innocente P. 2004 Electron density control using fast gas puffing in reversed-field pinch device, TPE-RX *Japan. J. Appl. Phys.* **43** L1184

[491] Innocente P., Alfier A., Carraro L., Pasqualotto R. and Terranova D. 2007 Transport and confinement studies in the RFX-mod reversed-field pinch experiment *Nucl. Fusion* **47** 1092

[492] Martini S., *et al* 1999 Oscillating poloidal current drive experiments in RFX *26th EPS Conf. Plasma Physics* (Maastricht, Netherlands, 14-18 June 1999) p 1137-40 (http://epsppd.epfl.ch/Maas/web/pdf/p3049.pdf)

[493] de Aguilera A.M., Castejón F., Ascasíbar E. *et al* 2015 Magnetic well scan and confinement in the TJ-II stellarator *Nucl. Fusion* **55** 113014

[494] Paccagnella R. 2013 Pressure driven tearing and interchange modes in the reversed field pinch *Phys. Plasmas* **20** 012119

[495] Zuin M., Spagnolo S., Paccagnella R., Cavazzana R., Serianni G., Spolaore M. and Vianello N. 2010 Resistiveg-modes in a reversed-field pinch plasma *Nucl. Fusion* **50** 052001

[496] Paccagnella R., Bondeson A. and Lütjens H. 1991 Ideal toroidal stability beta limits and shaping effects for reversed field pinch configurations *Nucl. Fusion* **31** 1899

[497] Guo S.C., Xu X.Y. and Wang Z.R. 2013 Does shaping bring an advantage for reversed field pinch plasmas? *Nucl. Fusion* **53** 113035

[498] Hirshman S.P. 1988 Finite-aspect-ratio effects on the bootstrap current in tokamaks *Phys. Fluids* **31** 3150–2

[499] Sauter O., Angioni C. and Lin-Liu Y.R. 1999 Neoclassical conductivity and bootstrap current formulas for general axisymmetric equilibria and arbitrary collisionality regime *Phys. Plasmas* **6** 2834

[500] Guazzotto L., Betti R. and Manickam J. 2004 Numerical study of tokamak equilibria with arbitrary flow *Phys. Plasmas* **11** 604
[501] Sanpei A. *et al* 2009 Equilibrium reconstruction and estimation of neoclassical effect in low-aspect-ratio reversed field pinch experiments on RELAX *J. Phys. Soc. Japan* **78** 013501
[502] Shiina S. *et al* 2005 Neoclassical reversed-field pinch equilibrium with dominant self-induced plasma current *Phys. Plasmas* **12** 080702
[503] Goforth R.R. *et al* 1986 Reversed-field pinch experiments with a resistive shell *Nucl. Fusion* **26** 515–7
[504] La Haye R.J., Lee P.S., Schaffer M.J. and Taylor P.L. 1988 Magnetic fluctuation measurements in the thin resistive shell OHTE device operated as a reversed field pinch *Nucl. Fusion* **28** 918–22
[505] Greene P. and Robertson S. 1993 Spectra and growth rates of resistive wall modes in a reversed-field pinch *Phys. Fluids* B **5** 556–63
[506] Alper B. *et al* 1989 RFP stability with a resistive shell in HBTX1C *Plasma Phys. Control. Fusion* **31** 205–12
[507] Asakura N., Fujisawa A., Fujita T. *et al* 1987 Experimental studies of reversed field pinch in REPUTE-1 and ultra-low-q discharge *11th International Conference on Plasma Physics and Controlled Nuclear Fusion Research* (Kyoto, Japan, 13-20 November 1986) (https://inis.iaea.org/search/search.aspx?orig_q=RN:18091816)
[508] Asakura N. *et al* 1986 Initial results of RFP experiments in REPUTE-1 *Plasma Phys. Control. Fusion* **28** 805–12
[509] Brunsell P.R., Malmberg J.-A. and Yadikin D. 2003 Resistive wall modes in the EXTRAP T2R reversed-field pinch *Phys. Plasmas* **10** 3823
[510] Alper B. 1990 A review of results from the HBTX reversed field pinch *Phys. Fluids* B **2** 1338–41
[511] Ho Y.L. and Prager S.C. 1988 Stability of a reversed field pinch with resistive and distant boundaries *Phys. Fluids* **31** 1673
[512] Jiang Z.X., Bondeson A. and Paccagnella R. 1995 Stability of current-driven modes in reversed field pinches with resistive walls and plasma rotation *Phys. Plasmas* **2** 442–9
[513] Guo S.C., Freidberg J.P. and Nachtrieb R. 1999 Stability of resistive wall modes in reversed field pinches with longitudinal flow and dissipative effects *Phys. Plasmas* **6** 3868–77
[514] Schnack D.D. and Ortolani S. 1990 Computational modelling of the effect of a resistive shell on the RFX reversed field pinch experiment *Nucl. Fusion* **30** 277–96
[515] Paccagnella R., Schnack D.D. and Chu M.S. 2002 Feedback studies on resistive wall modes in the reversed field pinch *Phys. Plasmas* **9** 234–42
[516] Bolzonella T., Igochine V., Guo S.C. *et al* 2008 Resistive-wall-mode active rotation in the RFX-Mod device *Phys. Rev. Lett.* **101** 165003
[517] Chu M.S. and Okabayashi M. 2010 Stabilization of the external kink and the resistive wall mode *Plasma Phys. Control. Fusion* **52** 123001
[518] Wang Z.R., Guo S.C. and Liu Y.Q. 2012 Drift kinetic effects on the resistive wall mode stability-comparison between reversed field pinches and tokamaks *Phys. Plasmas* **19** 072518
[519] Liu Y., Bondeson A., Gregoratto D., Gribov Y. and Paccagnella R. 2004 Feedback control of resistive wall modes in toroidal devices *Nucl. Fusion* **44** 77–86
[520] Bishop C.M. 1989 An intelligent shell for the toroidal pinch *Plasma Phys. Control. Fusion* **31** 1179–89
[521] Fitzpatrick R. and Yu E.P. 1999 Feedback stabilization of resistive shell modes in a reversed field pinch *Phys. Plasmas* **6** 3536–47
[522] Brunsell P.R. *et al* 2004 Feedback stabilization of multiple resistive wall modes *Phys. Rev. Lett.* **93** 225001
[523] Cavinato M., Manduchi G., Luchetta A. and Taliercio C. 2006 Distributed real time control in RFX-mod nuclear fusion experiment: commissioning and first results *IEEE Trans. Nucl. Sci.* **53** 1015–21
[524] Cavinato M., Manduchi G. and Luchetta A. 2006 General-purpose framework for real time control in nuclear fusion experiments *IEEE Trans. Nucl. Sci.* **53** 1002–8
[525] Drake J.R. *et al* 2005 Experimental and theoretical studies of active control of resistive wall mode growth in the EXTRAP T2R reversed-field pinch *Nucl. Fusion* **45** 557–64
[526] Bolzonella T. *et al* 2007 Feedback control of resistive wall modes by saddle coils in RFX-mod *Fusion Eng. Des.* **82** 1064–72
[527] Paccagnella R., Gregoratto D. and Bondeson A. 2002 Feedback control of resistive wall modes in reversed field pinches *Nucl. Fusion* **42** 1102–9
[528] Bondeson A., Liu Y., Gregoratto D. and Pustovitov V.D. 2002 Active control of resistive wall modes in the large-aspect-ratio tokamak *Nucl. Fusion* **42** 768–79
[529] Zanca P., Marrelli L. and Manduchi G. 2007 Beyond the intelligent shell concept: the clean-mode-control *Nucl. Fusion* **47** 1425–36
[530] Zanca P., Marrelli L., Paccagnella R., Baruzzo M., Bolzonella T., Marchiori G., Martin P. and Piovesan P. 2012 Feedback control model of the $m = 2$, $n = 1$ resistive wall mode in a circular plasma *Plasma Phys. Control. Fusion* **54** 094004
[531] Brunsell P.R. *et al* 2005 Active control of multiple resistive wall modes *Plasma Phys. Control. Fusion* **47** B25–36
[532] Brunsell P.R., Kuldkepp M., Menmuir S., Hedqvist A., Yadikin D., Drake J.R. and Rachlew E. 2006 Reversed field pinch operation with intelligent shell feedback control in EXTRAP T2R *Nucl. Fusion* **46** 904–13
[533] Drake J.R., Bolzonella T., Olofsson K.E.J., *et al* 2008 Reversed-field pinch contributions to resistive wall mode physics and control *Proc. 22nd Int. Conf. on Fusion Energy* (Geneva, Switzerland, 2008) [EX/P9-7] (https://www-pub.iaea.org/MTCD/Meetings/FEC2008/ex_p9-7.pdf)
[534] Zanca P., Marchiori G. and Marrelli L. 2012 Advanced feedback control of magnetohydrodynamic instabilities: comparison of compensation techniques for radial sensors *Plasma Phys. Control. Fusion* **54** 124018
[535] Gregoratto D., Drake J.R., Yadikin D., Paccagnella R., Brunsell P.R., Bolzonella T., Marchiori G. and Cecconello M. 2005 Studies on the response of resistive-wall modes to applied magnetic perturbations in the EXTRAP T2R reversed field pinch *Phys. Plasmas* **12** 092510
[536] Volpe F.A., Frassinetti L., Brunsell P.R. and Olofsson K.E.J. 2013 Error field assessment from driven rotation of stable external kinks at EXTRAP-T2R reversed field pinch *Nucl. Fusion* **53** 043018
[537] Baruzzo M., Bolzonella T., Liu Y.Q., Marchiori G., Soppelsa A., Takechi M. and Villone F. 2012 RWM control studies on RFX-mod with a limited set of active coils *Nucl. Fusion* **52** 103001
[538] Marchiori G., Baruzzo M., Bolzonella T., Soppelsa A. and Villone F. 2012 Dynamic simulator of RWM control for fusion devices: modelling and experimental validation on RFX-mod *Nucl. Fusion* **52** 023020
[539] Olofsson K.E.J., Brunsell P.R. and Drake J.R. 2012 A first attempt at few coils and low-coverage resistive wall mode stabilization of EXTRAP T2R *Plasma Phys. Control. Fusion* **54** 094005
[540] Villone F., Liu Y.Q., Paccagnella R. *et al* 2008 Effects of three-dimensional electromagnetic structures on resistive-wall-mode stability of reversed field pinches *Phys. Rev. Lett.* **100** 255005
[541] Liu Y.Q., Bondeson A., Fransson C.M. and Breitholtz C. 2000 Feedback stabilization of nonaxisymmetric resistive

wall modes in tokamaks. I. Electromagnetic model *Phys. Plasmas* **7** 3681

[542] Portone A., Villone F., Liu Y. and Rubinacci G. 2008 Linearly perturbed MHD equilibria and 3D eddy current coupling via the control surface method *Plasma Phys. Control. Fusion* **50** 085004

[543] Soppelsa A., Marchiori G. and Marrelli L. 2009 Integrated identification of RFX-mod active control system from experimental data and finite element model *Fusion Eng. Des.* **84** 1784–8

[544] Olofsson E., Brunsell P. and Drake J. 2009 Closed-loop direct parametric identification of magnetohydrodynamic normal modes spectra in EXTRAP-T2R reversed-field pinch *IEEE Control Applications* 1449–54

[545] Olofsson K.E.J., Brunsell P.R. and Drake J.R. 2013 Experimental modal analysis of resistive wall toroidal pinch plasma dynamics *Nucl. Fusion* **53** 072003

[546] Olofsson K.E.J., Brunsell P.R., Rojas C.R. and Hjalmarsson H. 2011 Predictor-based multivariable closed-loop system identification of the EXTRAP T2R reversed field pinch external plasma response *Plasma Phys. Control. Fusion* **53** 084003

[547] Olofsson K.E.J., Soppelsa A. and Bolzonella T. 2013 Subspace identification analysis of RFX and T2R reversed-field pinches *Control Eng. Pract.* **21** 917–29

[548] Setiadi A.C., Brunsell P.R. and Frassinetti L. 2015 Implementation of model predictive control for resistive wall mode stabilization on EXTRAP T2R *Plasma Phys. Control. Fusion* **57** 104005

[549] Fitzpatrick R. 1993 Interaction of tearing modes with external structures in cylindrical geometry (plasma) *Nucl. Fusion* **33** 1049–84

[550] Fitzpatrick R., Guo S.C. and Den Hartog D.J. 1999 Effect of a resistive vacuum vessel on dynamo mode rotation in reversed field pinches *Phys. Plasmas* **6** 3878–89

[551] Chapman B.E., Fitzpatrick R., Craig D. and Spizzo G. 2004 Observation of tearing mode deceleration and locking due to eddy currents induced in a conducting shell *Phys. Plasmas* **11** 2156–71

[552] Fitzpatrick R. 1999 Formation and locking of the ‘slinky mode’ in reversed-field pinches *Phys. Plasmas* **6** 1168–93

[553] Werley K.A., Nebel R.A. and Wurden G.A. 1985 Transport description of the rise time of sawtooth oscillations in reversed-field pinches *Phys. Fluids* **28** 1450–3

[554] Fitzpatrick R. and Zanca P. 2002 Phase-locking of tearing modes in the reversed field experiment *Phys. Plasmas* **9** 2707–24

[555] Hansen A.K., Almagri A.F., Den Hartog D.J. and Sarff J.S. 1998 Locking of multiple resonant mode structures in the reversed-field pinch *Phys. Plasmas* **5** 2942–6

[556] Frassinetti L., Sun Y., Fridström R., Olofsson K.E.J., Brunsell P.R., Khan M.W.M., Liang Y. and Drake J.R. 2015 Braking due to non-resonant magnetic perturbations and comparison with neoclassical toroidal viscosity torque in EXTRAP T2R *Nucl. Fusion* **55** 112003

[557] Fridström R., Chapman B.E., Almagri A.F. *et al* 2018 Dependence of perpendicular viscosity on magnetic fluctuations in a stochastic topology *Phys. Rev. Lett.* **120** 225002

[558] Finn J.M., Guzdar P.N. and Chernikov A.A. 1992 Particle transport and rotation damping due to stochastic magnetic field lines *Phys. Fluids* B **4** 1152–5

[559] Guo S.C. and Chu M.S. 2004 Study on wall locking of multiple tearing modes in reversed field pinch plasmas *Phys. Plasmas* **11** 4050–63

[560] Hegna C.C. 1996 Nonlinear tearing mode interactions and mode locking in reversed-field pinches *Phys. Plasmas* **3** 4646–57

[561] Bellina F., Chitarin G., Fiorentin P. *et al* 1996 Feasibility analysis of an active local field control at the poloidal gap of RFX *Fusion Technology* (Amsterdam: Elsevier) pp 771–4

[562] Gaio E., Luchetta A., Manduchi G, *et al* 1999 Upgrade for full control of radial magnetic field errors in RFX poloidal gaps *18th IEEE/NPSS Symposium on Fusion Engineering* (Albuquerque, NM, 1999) pp 579–82

[563] Baker W., Dal Bello S., Marcuzzi D. and Zaccaria P. 2002 Design of a new toroidal shell and support structure for RFX *Fusion Eng. Des.* **63–64** 461–6

[564] Innocente P., Zanca P., Zuin M. and Zaniol B. 2014 Tearing modes transition from slow to fast rotation branch in the presence of magnetic feedback *Nucl. Fusion* **54** 122001

[565] Zanca P. 2009 Avoidance of tearing modes wall-locking in a reversed field pinch with active feedback coils *Plasma Phys. Control. Fusion* **51** 015006

[566] Piron L., Marrelli L. and Piovesan P. 2010 Model-based design of multi-mode feedback control in the RFX-mod experiment *Nucl. Fusion* **50** 115011

[567] Zanca P. and Martini S. 1999 Reconstruction of the plasma surface in a RFP in the presence of non-axisymmetric perturbations *Plasma Phys. Control. Fusion* **41** 1251–75

[568] Valisa M. *et al* 2001 Issues in the plasma wall interactions in RFX *J. Nucl. Mater.* **290–293** 980–4

[569] Carraro L.E., Casarotto M.E., Puiatti P., Scarin P. and Valisa M. 1995 Impurity influxes and production mechanism in RFX *22nd EPS Conf. Plasma Physics* (Bournemouth, United Kingdom, 3-7 July 1995) **19C** 317 (http://libero.ipp.mpg.de/libero/PDF/EPS_22_Vol2_1995.pdf#page=331)

[570] Carraro L., Puiatti M.E., Sattin F., Valisa M. and Mattioli M. 1996 Carbon and oxygen behaviour in the reversed field pinch RFX *Nucl. Fusion* **36** 1623–32

[571] Carraro L., Casarotto E., Pasqualotto R., Sattin F., Scarin P. and Valisa M. 1995 Impurity influx studies in the RFX reversed field pinch *J. Nucl. Mater.* **220–222** 646–9

[572] Carraro L., Costa S., Puiatti M.E., Scarin P., Telesca G., Tokar M.Z., Valisa M., Franz P. and Marrelli L. 2000 Radiation and confinement properties of impurity seeded discharges in the reversed field pinch RFX *Nucl. Fusion* **40** 1983–91

[573] Carraro L., Puiatti M.E., Sattin F., Valisa M., DePol G., Pasqualotto R., Pugno R. and Telesca G. 1999 Impurity screening in the RFX reversed field pinch *J. Nucl. Mater.* **266–269** 446–51

[574] Bergsåker H., Menmuir S., Rachlew E., Frassinetti L. and Drake J.R. 2008 Metal impurity fluxes and plasma–surface interactions in EXTRAP T2R *J. Phys.: Conf. Ser.* **100** 062030

[575] Puiatti M.E. *et al* 2013 Wall conditioning and density control in the reversed field pinch RFX-mod *Nucl. Fusion* **53** 073001

[576] Spizzo G., Franz P., Marrelli L., Murari A., Bolzonella T., Terranova D. and Zanca P. 2001 Mitigation of plasma–wall interaction during quasi-single helicity states in RFX *J. Nucl. Mater.* **290–293** 1018–22

[577] Yagi Y., Shimada T., Hirota I., Hirano Y., Ogawa K., Namiki K. and Ioki K. 1989 Movable limiter experiment on tpe-1rm15 reversed field pinch machine *J. Nucl. Mater.* **162–164** 702–9

[578] Bergsåker H., Möller A., Li G.X., Brzozowski J.H., Emmoth B. and Gudowska I. 1995 Edge plasma conditions and plasma–surface interactions in extrap T1 *J. Nucl. Mater.* **220–222** 712–6

[579] Innocente P., Bufferand H., Canton A. and Visonà N. 2017 Heat flux measurements and modelling in the RFX-mod experiment *Nucl. Mater. Energy* **12** 1199–204

[580] Sonato P., Antoni V., Bagatin M., Peruzzo S., Tramontin L., Zaccaria P. and Zollino G. 1997 Investigation of plasma facing components and vacuum vessel in RFX *J. Nucl. Mater.* **241–243** 982–7

[581] Bergsåker H., Larsson D., Brunsell P. and Tramontin L. 1997 Wall conditioning and particle control in extrap T2 *J. Nucl. Mater.* **241–243** 993–7

[582] Canton A., Dal Bello S., Agostini M., Cavazzana R., Fiameni S., Grando L., Rais B., Spolaore M. and Zuin M. 2013 Studies of spatial uniformity of glow discharge cleaning plasmas on the RFX-mod device *J. Nucl. Mater.* **438** S1164–7

[583] Bettella D., Carraro L., Puiatti M.E., Sattin F., Scarin P., Sonato P., Valisa M. 2000 Hydrogen recycling in the RFX reversed field pinch *Hydrogen Recycling at Plasma Facing Materials* (Dordrecht: Springer) (https://doi.org/10.1007/978-94-011-4331-8_3)

[584] Larsson D., Bergsåker H., Hokin S., Drake J. and Möller A. 1997 Surface modification by solid target boronisation in the extrap T2 experiment *Vacuum* **48** 693–5

[585] Den Hartog D.J., Cekic M., Fiksel G., Kendrick R.D., Prager S.C. and Stoneking M.R. 1993 B4C solid target boronization of the MST reversed-field pinch *J. Nucl. Mater.* **200** 177–83

[586] Den Hartog D.J. and Kendrick R.D. 1995 Solid target boronization of the MST reversed-field pinch during pulsed discharge cleaning *J. Nucl. Mater.* **220–222** 631–5

[587] Ko J., Den Hartog D.J., Goetz J.A. and Limbach S.T. 2013 First gaseous boronization during pulsed discharge cleaning *J. Nucl. Mater.* **432** 146–51

[588] Sonato P. *et al* 1996 Boronization with trimethylboron in the reversed field pinch RFX *J. Nucl. Mater.* **227** 259–65

[589] Sonato P., Antoni V., Carraro L., Serianni G., Scarin P., Spolaore M., Valisa M. and Zaccaria P. 2002 Particle control systems at the edge of RFP experiments *Plasma Phys. Control. Fusion* **44** 627

[590] Barison S., Canton A., Dal Bello S., Innocente P., Alfier A., Munaretto S. and Rossetto F. 2011 Analysis of the interaction between plasmas and the graphite first wall in RFX-mod *J. Nucl. Mater.* **415** S274–7

[591] Fiameni S., Barison S., Canton A., Innocente P., Pagura C., Fabrizio M. and Daolio S. 2013 SIMS analysis of the interaction between plasmas and the graphite first wall in RFX-mod *Surf. Interface Anal.* **45** 423–6

[592] Tramontin L., Antoni V., Bagatin M., Cattaruzza E., Rigato V. and Zandolin S. 1999 Erosion, redeposition and boronization lifetime in RFX *J. Nucl. Mater.* **266–269** 709–13

[593] Bartiromo R., Buffa A., Antoni V. *et al* 1999 Recent progress in reversed field pinch research in the RFX experiment *Nucl. Fusion* **39** 1697

[594] Mansfield D.K. *et al* 1996 Enhancement of tokamak fusion test reactor performance by lithium conditioning *Phys. Plasmas* **3** 1892–7

[595] Mazzitelli G. *et al* 2010 Review of FTU results with the liquid lithium limiter *Fusion Eng. Des.* **85** 896–901

[596] Zuo G.Z., Hu J.S., Zhen S., Mansfield D.K., Cao B., Wu J.H. and Zakharov L.E. 2012 Comparison of various wall conditionings on the reduction of H content and particle recycling in EAST *Plasma Phys. Control. Fusion* **54** 015014

[597] Sánchez J., Acedo M., Alonso A. *et al* 2009 Confinement transitions in TJ-II under Li-coated wall conditions *Nucl. Fusion* **49** 104018

[598] Martin P., Puiatti M.E., Agostinetti P. *et al* 2013 Overview of the RFX-mod fusion science programme *Nucl. Fusion* **53** 104018

[599] Innocente P. *et al* 2015 Lithium wall conditioning by high frequency pellet injection in RFX-mod *J. Nucl. Mater.* **463** 1138–41

[600] Ratynskaia S., Castaldo C. and Bergsåker H. 2011 Diagnostics of mobile dust in scrape-off layer plasmas *Plasma Phys. Control. Fusion* **53** 074009

[601] Rubel M., Cecconello M., Malmberg J.A., Biel W., Drake J.R., Hedqvist A., Huber A. and Philipps V. 2001 Dust particles in controlled fusion devices: morphology, observations in the plasma and influence on the plasma performance *Nucl. Fusion* **41** 1087–99

[602] Bergsåker H., Ratynskaia S., Litnovsky A. and Sahle W. 2011 Studies of mobile dust in scrape-off layer plasmas using silica aerogel collectors *J. Nucl. Mater.* **415** S1089–93

[603] Bykov I., Vignitchouk L., Ratynskaia S., Tolias P., Bergsåker H., Frassinetti L. and Brunsell P.R. 2014 Transport asymmetry and release mechanisms of metal dust in the reversed-field pinch configuration *Plasma Phys. Control. Fusion* **56** 035014

[604] Sarff J.S., Almagri A.F., Assadi S., Dexter R.N., Prager S.C. and Sprott J.C. 1989 Studies of a reversed field pinch in a poloidal divertor configuration *Nucl. Fusion* **29** 104–8

[605] Hattori K., Hayase K. and Sato Y. 1995 First results of the toroidal divertor experiment on the TPE-2M reversed field pinch *Nucl. Fusion* **35** 981–7

[606] Hattori K.-i., Hayase K. and Sato Y. 1994 Poloidal-open divertor experiments on TPE-2M reversed field pinch *J. Phys. Soc. Japan* **63** 2177–84

[607] Iida M., Miyagi T., Ishijima D., Ohta K., Masamune S. and Oshiyama H. 1994 First results from the poloidal divertor experiment in the STE-2 reversed field pinch *Plasma Phys. Control. Fusion* **36** 153–61

[608] Ishijima D., Iida M., Masamune S., Tanonaka A. and Oshiyama H. 1995 Heat flux studies in a poloidal-divertor reversed-field pinch *Plasma Phys. Control. Fusion* **37** 657–66

[609] Loarer T. *et al* 1996 Particle exhaust with a vented pump limiter on Tore Supra *Nucl. Fusion* **36** 225

[610] Martines E., Lorenzini R., Momo B., Innocente P. and Spolaore M. 2010 The plasma boundary in single helical axis RFP plasmas *Nucl. Fusion* **50** 035014

[611] König R., Grigull P., McCormick K. *et al* 2002 The divertor program in stellarators *Plasma Phys. Control. Fusion* **44** 2365

[612] Christiansen J.P. and Roberts K.V. 1982 Power balance in an ohmically heated fusion reactor *Nucl. Fusion* **22** 77–88

[613] Bathke C.G. 1994 A comparison of steady-state ARIES and pulsed PULSAR tokamak power plants *Fusion Technol.* **26** 1163–8

[614] Bellan P.M. 1989 Non-observation of AC helicity injection *Nucl. Fusion* **29** 78

[615] Yamaguchi S., Schaffer M. and Kondoh Y. 1995 Preliminary oscillating fluxes current drive experiment in DIII-D tokamak *Fusion Eng. Des.* **26** 121–32

[616] Sprott J.C. 1988 Electrical circuit modeling of reversed field pinches *Phys. Fluids* **31** 2266–75

[617] Jensen T.H. and Chu M.S. 1984 Current drive and helicity injection *Phys. Fluids* **27** 2881–5

[618] Bevir M.K. and Gray J.W. 1980 Relaxation, flux consumption and quasi steady state pinches *Reversed-Field Pinch Theory Workshop* (Los Alamos National Laboratory, 29 April - 2 May 1980) p 176 (https://inis.iaea.org/collection/NCLCollectionStore/_Public/14/734/14734761.pdf#page=186)

[619] Bellan P.M. 1984 Physical model of current drive by ac helicity injection *Phys. Fluids* **27** 2191–2

[620] Hooper E.B. *et al* 2012 Sustained spheromak physics experiment (SSPX): design and physics results *Plasma Phys. Control. Fusion* **54** 113001

[621] Redd A.J., Nelson B.A., Jarboe T.R., Raman R., Smith R.J. and McCollam K.J. 2002 Current drive experiments in the helicity injected torus (HIT-II) *Phys. Plasmas* **9** 2006

[622] Raman R. *et al* 2001 Non-inductive current generation in NSTX using coaxial helicity injection *Nucl. Fusion* **41** 1081
[623] Fiksel G., Almagri A.F., Craig D., Prager S.C. and Sarff J.S. 1996 High current plasma electron emitter *Plasma Sources Sci. Technol.* **5** 78
[624] Battaglia D.J., Bongard M.W. and Fonck R.J. 2011 Tokamak startup using outboard current injection on the Pegasus toroidal experiment *Nucl. Fusion* **51** 073029
[625] Jarboe T.R. 1999 Steady inductive helicity injection and its application to a high-beta spheromak *Fusion Technol.* **36** 85
[626] Victor B.S. *et al* 2011 Evidence for separatrix formation and sustainment with steady inductive helicity injection *Phys. Rev. Lett.* **107** 165005
[627] Schoenberg K.F., Gribble R.F. and Phillips J.A. 1982 Zero-dimensional simulations of reversed-field pinch experiments *Nucl. Fusion* **22** 1433
[628] Schoenberg K.F., Gribble R.F. and Baker D.A. 1984 Oscillating field current drive for reversed field pinch discharges *J. Appl. Phys.* **56** 2519–29
[629] Ebrahimi F., Prager S.C. and Sarff J.S. 2003 The three-dimensional magnetohydrodynamics of ac helicity injection in the reversed field pinch *Phys. Plasmas* **10** 999–1014
[630] Schoenberg K.F. *et al* 1988 Oscillating field current drive experiments in a reversed field pinch *Phys. Fluids* **31** 2285–91
[631] Nonn P.D., Blair A.P., McCollam K.J. and Stone D.R. 2011 Powered oscillator using ignitron switches *Rev. Sci. Instrum.* **82** 064701
[632] McCollam K.J., Blair A.P., Prager S.C. *et al* 2006 Oscillating-field current-drive experiments in a reversed field pinch *Phys. Rev. Lett.* **96** 035003
[633] McCollam K.J. *et al* 2010 Equilibrium evolution in oscillating-field current-drive experiments *Phys. Plasmas* **17** 082506
[634] Ebrahimi F. and Prager S.C. 2004 Current profile control by alternating current magnetic helicity injection *Phys. Plasmas* **11** 2014–25
[635] Bolzonella T., Terranova D., Zanotto L. *et al* 2006 Oscillating field current drive experiments in RFX-mod *33rd EPS Conference on Plasma Physics* (Rome 19–23 June 2006) vol 301 p P-5.090 http://epsppd.epfl.ch/Roma/pdf/P5_090.pdf
[636] Krakowski R.A., Miller R.L. and Hagenson R.L. 1986 The need and prospects for improved fusion reactors *J. Fusion Energy* **5** 213–30
[637] Krakowski R.A., Hagenson R.L., Schnurr N.M., Bathke C.G., Miller R.L. and Embrechts M.J. 1986 Compact reversed-field pinch reactors (CRFPR) *Nucl. Eng. Des. Fusion* **4** 75–120
[638] Najmabadi F. *et al* 1993 The TITAN-I reversed-field-pinch fusion-power-core design *Fusion Eng. Des.* **23** 81–98
[639] Najmabadi F., Conn R.W., Krakowski R.A. *et al* 1993 Introduction and synopsis of the TITAN reversed-field-pinch fusion-reactor study *Fusion Eng. Des.* **23** 69–80
[640] Najmabadi F. and Conn R.W. The TITAN reversed-field pinch fusion reactor study *The Final Report. UCLA-PPG-1200* (https://inis.iaea.org/collection/NCLCollectionStore/_Public/24/017/24017831.pdf)
[641] Wong C.P.C. *et al* 1993 The TITAN-II reversed-field-pinch fusion-power-core design *Fusion Eng. Des.* **23** 173–200
[642] Piovan R., Agostinetti P., Bustreo C. *et al* 2019 Status and perspectives of a reversed field pinch as a pilot neutron source *IEEE Trans. Plasma Sci.* **48** 1708
[643] Miller R.L. 2009 Power plant considerations for the reversed-field pinch (RFP) *Fusion Sci. Technol.* **56** 940–4
[644] Najmabadi F. *et al* 2006 The ARIES-AT advanced tokamak, advanced technology fusion power plant *Fusion Eng. Des.* **80** 3–23
[645] Raffray A.R., El-Guebaly L., Malang S., Bromberg L., Ihli T., Merrill B. and Waganer L. 2008 Engineering design and analysis of the ARIES-CS power plant *Fusion Sci. Technol.* **54** 725–46
[646] Piron L., Grando L., Marchiori G., Piovesan P., Soppelsa A. and Terranova D. 2011 Dynamic decoupling and multi-mode magnetic feedback for error field correction in RFX-mod *Nucl. Fusion* **51** 063012